On the noise and signal modelling for the search of very-low frequency gravitational waves with International Pulsar Timing Array telescopes

Aurélien Chalumeau

UNIVERSITÉ DE PARIS

ÉCOLE DOCTORALE 560

SCIENCES DE LA TERRE ET DE L'ENVIRONNEMENT ET PHYSIQUE DE L'UNIVERS

AstroParticules et Cosmologie (APC)

groupe Cosmologie et Gravitation

Station de radioastronomie de Nançay (USN)

Laboratoire de Physique et de Chimie de l'Environnement et de l'Espace (LPC2E)

Équipe Astrophysique et Objets Compacts

On the noise and signal modelling for the search of very-low frequency gravitational waves with International Pulsar Timing Array telescopes

---

Par AURÉLIEN CHALUMEAU

Thèse de doctorat D'ASTROPHYSIQUE

Co-dirigée par STANISLAV BABAK
et par GILLES THEUREAU

Présentée et soutenue publiquement le 16 décembre 2021 devant le jury composé de :

ÉRIC CHASSANDE-MOTTIN	Directeur de Recherche (APC)	Président du Jury
CHIARA MINGARELLI	Assistant Professor (University of Connecticut, CCA)	Rapporteur
ANDREA LOMMEN	Professor (Haverford College)	Rapporteur
STANISLAV BABAK	Directeur de Recherche (APC)	Directeur de Thèse
GILLES THEUREAU	Astronome (Observatoire de Paris, LPC2E)	Directeur de Thèse
JONATHAN GAIR	Professor (Albert Einstein Institute)	Examinateur
ALBERTO SESANA	Professor (Università di Milano-Bicocca)	Examinateur
SYLVAIN CHATY	Professeur des Universités (Université de Paris, CEA)	Examinateur

To Rosa María

RÉSUMÉ

La thèse est centrée sur la modélisation des signaux présents dans les données d'un réseau de pulsars chronométrés (Pulsar Timing Array ou PTA) afin d'améliorer la sensibilité pour la recherche d'ondes gravitationnelles de très basses fréquences (du nano-Hz au micro-Hz). Le premier chapitre est une introduction générale du sujet où je présente le contexte scientifique et les méthodes d'analyse utilisés. J'y développe d'abord la notion de modèle de chronométrie des pulsars, en m'appuyant sur un exemple particulier : la caractérisation précise du modèle de rotation du pulsar J1909-3744, avec mise-à-jour des mesures sur l'ensemble des paramètres. Je poursuis avec l'application de cette méthode pour la recherche d'ondes gravitationnelles au nano-Hertz avec PTA, et termine sur les concepts et les outils utilisés dans cette thèse afin de réaliser des analyses de données dans un cadre Bayésien. Le deuxième chapitre porte sur l'optimisation de la prise en compte des bruits intrinsèques à chacun des pulsars, ceci appliqué avec les données récentes de l'EPTA incluant à ce jour six pulsars. Ce travail souligne notamment la grande complexité de l'analyse des données PTA qui combinent des dizaines d'années d'observations de différents pulsars provenant de plusieurs radio téléscopes. Le troisième chapitre présente ma participation aux études récentes sur la recherche d'un fond stochastique d'ondes gravitationnelles (GWB) avec les données de l'European Pulsar Timing Array (EPTA) et celles de l'International Pulsar Timing Array (IPTA), ainsi qu'une évaluation des conséquuences induites par l'optimisation des modèles individuels des pulsars (présentée dans le Chapitre 2) sur la mesure du GWB. Les résultats récents provenant des différentes collaborations sont particulièrement intéressants puisqu'ils convergent sur la présence d'un signal commun entre les pulsars, avec l'amplitude et l'indice spectral attendu, sans toutefois pouvoir confirmer encore sa nature gravitationnelle et donc la détection recherchée. Les collaborations travaillent actuellement sur l'amélioration des lots de données (élongation de la couverture temporelle et augmentation significative du nombre de pulsars) afin d'améliorer la précision des résultats. Le quatrième et dernier chapitre est centré sur la prise en compte des incertitudes des éphémérides du Système solaire (SSE) sur les résultats des PTAs, notamment sur la mesure du GWB. En effet, afin de prendre en compte le mouvement de la Terre dans le Système solaire, les temps d'arrivées des impulsions mesurées sont virtuellement translatés au barycentre de celui-ci, et dont la position est donnée par les SSEs. Une collaboration avec l'Institut de mécanique céleste et de calcul des éphémérides (IMCCE), qui produit les SSE, a permis de construire un modèle (nommé EphemGP) appliqué à PTA et prend en compte des perturbations d'orbite des objets principaux du Système solaire. J'y présente une étude détaillée sur l'efficacité du modèle à réduire l'impact des potentielles erreurs des SSEs pour la recherche du GWB, en incluant une comparaison avec d'autres modèles existants, et termine avec l'application du modèle sur les données récentes de l'EPTA.

Mots clés: Ondes gravitationnelles - Pulsars - Analyse de données

ABSTRACT

The thesis focuses on the noise modelling in pulsar timing data and the search for very-low frequency (from nano-Hz to micro-Hz) gravitational waves with Pulsar Timing Array (PTA). The first chapter gives a general introduction of the subject where I present the scientific context and describe the data analysis methods. I start with the notion of pulsar timing, using a specific example: modelling the timimng data of pulsar J1909-3744, where I also present the updated timing parameters. Then I introduce methodology used in searching for gravitational waves at nano-Hertz with PTA, and conclude with the description of tools used in this thesis to perform data analysis within a Bayesian framework. The second chapter focuses on the single-pulsar noise modelling, applied to six pulsars of the EPTA Data Release 2. In particular, this work highlights the great complexity in the analysis of the PTA data which combine decades of observations of different pulsars from several radio telescopes. The third chapter presents results of the search for a stochastic gravitational wave background (GWB) in the European Pulsar Timing Array (EPTA) and the International Pulsar Timing Array (IPTA) data with a focus on parts with my direct participation. In particular, I present the impact of the custom single-pulsar noise modelling (given in Chapter 2) on the GWB measurement. The recent results from three PTA collaborations are particularly interesting as they converge on the presence of a common red noise signal across considered pulsars with similar amplitude and spectral index, but without being able to confirm yet its gravitational nature and thus the desired GWB detection. Currently, PTAs are working on extending the data sets by adding the latest observations and including more pulsars into analysis to improve the accuracy and uncover the nature of the observed signal. The fourth and last chapter describes the uncertainties in the Solar System Ephemeris (SSE) and their impact on the PTA results, especially on the GWB measurement. We use SSE provided by Institut de mécanique céleste et de calcul des éphémérides (IMCCE) as a basis to construct the model called EphemGP. We demonstrate that this model is efficient at absorbing systematics in the SSE by introducing variations in the orbital parameters of the main planets of the Solar System. The ability to absorb dipolar correlations induced by SSE uncertainties is very import for the robust detection of the GWB. I compare performance of EphemGP to other existing models, and conclude with the application of this model to the recent EPTA data.

Key words: Gravitational waves - Pulsars - Data analysis

Modélisation des avant-plans et sources de bruits corrélés pour la recherche d'ondes gravitationnelles de très basses fréquences avec les radiotélescopes de l'International Pulsar Timing Array

Cette thèse porte sur la modélisation des sources de bruit contenus dans les données de chronométrage de pulsars afin d'optimiser la recherche d'ondes gravitationnelles de très basses fréquences avec Pulsar Timing Arrays (PTA). Elle présente mes travaux effectués durant ces trois dernières années, chacun donnant lieu à une publication publiée, soumise ou bien en cours de rédaction pour publication dans une revue à comité de lecture.

1. Introduction

Cette partie introduit les concepts de base liés aux études effectuées lors de cette thèse: les pulsars, le chronométrage de pulsars, le projet PTA et les méthodes statistiques dans un cadre Bayésien. Elle y présente notamment des résultats publiés dans Liu et al. 2020, qui porte sur le chronométrage du pulsar PSR J1909-3744 en utilisant les données du grand radio télescope de Nançay. Pour cette publication, j'ai participé aux analyses de données liées au chronométrage, et à une partie de la rédaction.

1.1 Étoiles à neutron et pulsars

Les étoiles à neutrons sont des objets compacts pouvant résulter de l'effondrement gravitationnel d'étoiles massives (de 8 à $\sim 20\ M_\odot$, ou masses solaires), donnant lieu à une supernova. Ces objets compacts ont des rayons d'environ $10-12$ km et des masses de l'ordre de $1-2\ M_\odot$. Après l'effondrement gravitationnel, les conservations du moment cinétique et du flux magnétique impliquent respectivement une fréquence rotationnelle élevée (de 1 ms à ~ 10 s) ainsi qu'un champ magnétique intense (de 10^7 à 10^{14} G). La composante dipolaire du champ magnétique est à l'origine d'un faisceau d'émission radio au niveau des pôles magnétiques. Dans le cas d'un non-alignement entre l'axe magnétique et rotationnel, si la trajectoire du faisceau d'émission passe dans la direction de la Terre, il est alors possible d'observer un signal radio périodique donnant lieu au phénomène de *pulsar*.

Les pulsars, bien que majoritairement observés en radio, sont également détectés dans les domaines de l'infra-rouge, de l'optique, des rayons X, et en gamma. La version

la plus récente à ce jour (v.1.65) de l'Australia Telescope National Facility (ATNF) Pulsar Catalogue (Manchester et al. 2005) compte 3177 pulsars, dont 3055 pulsars radio. Chaque pulsar se démarque par son profile (flux en fonction de la phase rotationnelle), souvent intégré en temps et en fréquence radio, qui est différent pour chacun d'entre eux. La plupart des pulsars connus, les *pulsars canoniques*, ont une période rotationnelle de l'ordre de la seconde. D'autres, appelés *pulsars millisecondes* (MSP), se démarquent pour leurs faibles périodes ($<\sim 20$ ms), et sont particulièrement remarquables pour leur haute régularité rotationnelle ($\dot{P} \leq 10^{-18}$ s.s^{-1}). La version 1.65 du catalogue ATNF en dénombre 468. Cette thèse se concentre uniquement sur cette catégorie de pulsars, qui est particulièrement adaptée pour la méthode du chronométrage de pulsars.

1.2 Le chronométrage de pulsar

Le chronométrage de pulsar (pulsar timing en anglais) consiste à dater les temps d'arrivée des impulsions radio provenant des pulsars afin de caractériser tout effet influant sur la régularité du signal. Entre autres, cette méthode permet d'obtenir des informations sur la physique interne des pulsars, leur environnement, d'effectuer des tests de la Relativité Générale (notamment dans le cas de systèmes multiples) ou d'étudier le milieu interstellaire et les vents solaires au travers desquels le signal radio se propage. Les observations de chronométrage durent en général quelques dizaines de minutes et permettent d'évaluer un ou plusieurs *temps d'arrivée* caractéristique (time of arrival, ou ToA), qui est daté à l'aide d'une horloge de référence locale. Chaque ToA est évalué avec une incertitude qui est notamment optimisée pour des pulsars de faible période rotationnelle ayant un faible rapport cyclique (i.e., faible rapport entre largeur de profile et phase rotationnelle). En moyenne, les MSPs sont observés à un rythme hebdomadaire sur plusieurs années. Les ToAs mesurés sont ensuite regroupés afin d'ajuster un *modèle de chronométrage* (timing model en anglais), qui caractérise les principales propriétés mesurables du pulsar.

Le modèle de chronométrage permet de prendre en compte la fréquence rotationnelle du pulsar en fonction du temps (exprimée en série de Taylor) et d'appliquer différentes corrections pour, in fine, estimer le temps d'émission de chaque ToA au référentiel propre du pulsar. Les temps d'arrivée mesurés à l'aide de l'horloge locale sont premièrement transformés à l'echelle temporelle standard appelée temps terrestre (TT), définie à partir du temps atomique international (TAI) qui est évalué et publié régulièrement par le Bureau international des poids et mesures (BIPM) via la combinaison de mesures effectuées par des centaines d'horloges atomiques réparties sur la Terre. Une deuxième correction consiste à transposer les ToAs au barycentre du système solaire afin de compenser le mouvement de la Terre et d'autres effets comme par exemple la dispersion du signal radio due au contenu de l'atmosphère terrestre et du milieu interplanétaire, ou bien des effets relativistes induits par la présence des objets principaux du système solaire (Soleil

ou Jupiter). La troisième correction prend en compte la dispersion causée par le contenu électronique du milieu interstellaire traversé par le signal radio. Cet effet, caractérisé par la mesure de dispersion (DM), entraîne un retard sur les temps d'arrivée proportionnel à l'inverse du carré de la fréquence radio f ($\Delta t \propto 1/f^2$). Enfin, si le pulsar est dans un système binaire, le ToA est transformé depuis le barycentre du système binaire jusqu'au référentiel du pulsar, notamment en tenant compte d'effets relativistes.

En pratique, le modèle de chronométrage est constitué de paramètres ajustés aux ToAs de manière à appliquer les corrections mentionnées ci-dessus. L'ajustement est obtenu via la minimisation de la différence entre les ToAs observés et ceux prédits par le modèle par méthode des moindres carrés. Ces différences sont appelées les *résidus des temps d'arrivée* (timing residuals en anglais), et sont ensuite analysées afin de caractériser d'autres phénomènes non pris en compte, comme la présence d'ondes gravitationnelles de très basses fréquences.

1.3 Application sur PSR J1909-3744 avec le NRT

Le pulsar milliseconde PSR J1909-3744 est l'un des plus stables connus. Il possède une période rotationnelle de 2.95 ms et un rapport cyclique de seulement 1.5%. Situé à environ 1 kpc de la Terre, il possède une naine blanche comme compagnon. Il est chronométré par le grand radiotéléscope de Nançay (NRT) depuis décembre 2004 avec une cadence de l'ordre de la semaine. La publication Liu et al. 2020 rapporte une étude du chronométrage de ce pulsar à partir des observations effectuées par le grand radio télescope de Nançay (NRT), depuis décembre 2004 jusqu'en septembre 2019.

L'analyse de chronométrage est effectuée via une estimation des paramètres du modèle de chronométrie, ainsi que des paramètres du bruit blanc, du bruit rouge achromatique (indépendent de la fréquence radio) et de la variation du DM dans un cadre Bayésien, à l'aide du logiciel TEMPONEST en utlisant le sampler MULTINEST. Les distributions obtenues des paramètres de bruit blanc et de bruits rouges sont comparées avec celles obtenues avec le logiciel ENTERPRISE (Ellis et al. 2019) et l'echantillonneur PTMCMCSAMPLER (Ellis and Haasteren 2017) permettant une estimation des distributions posterieures des paramètres, tout en marginalisant sur les paramètres du modèle de chronométrage.

Le chronométrage appliqué à ce pulsar abouti finalement à une précision des temps d'arrivée de l'ordre de 100 ns sur une période de 15 ans. Entres autres, cette étude a permis d'améliorer la précision sur certains paramètres orbitaux tels que la dérivée de la période orbitale ($\dot{P}_b = 5.1087(13) \times 10^{-13}$) ou la dérivée de la projection du demi-grand axe ($\dot{x} = -2.61(55) \times 10^{-16}$). La mesure du retard lié à l'effet Shapiro permet de déduire la masse du pulsar ($m_p = 1.492 \pm 0.014\ M_\odot$) et celle de son compagnon ($m_c = 0.209 \pm 0.001\ M_\odot$). Enfin, le chronométrage précis de PSR J1909-3744 donne lieu à une mesure de l'eccentricité de son orbite de $e = (1.15 \pm 0.07)^{-7}$, la plus faible valeur connue pour un pulsar à ce jour.

1.4 Pulsar Timing Arrays

Le principe de détection d'ondes gravitationnelles de très basses fréquences (nHz-μHz) via le chronométrage de pulsars, appelé *Pulsar Timing Array* (PTA), a été introduit durant la fin des années 1970 (Sazhin 1978, Detweiler 1979), puis développé jusqu'à la fin du XXème siècle (Foster and Backer 1990, Backer 1995).

Le principe de PTA consiste à sonder la présence d'un signal commun entre les pulsars contenant une corrélation spatiale spécifique aux ondes gravitationnelles. Le signal peut être déterministe. correspondant par exemple à l'orbite d'un système binaire de trous noirs supermassifs, ou bien stochastique, provenant de l'addition d'une multitude de sources faibles en intensité. Cette thèse se concentre uniquement sur le deuxième type: le fond stochastique d'ondes gravitationnelles (GWB), dont la corrélation spatiale attendue suit la courbe de Hellings-Downs (Hellings and Downs 1983). Le principal candidat pour un tel signal est la population de trous noirs supermassifs ($M \geq 10^8 M_\odot$) binaires dans l'Univers local ($z \leq 2$). Pour une population simpliste de systèmes circulaires dont l'évolution est dominée par l'emission d'ondes gravitationnelles, le spectre suit une simple loi de puissance $h_c(t) \propto f^{-2/3}$ (Jaffe and Backer 2003, Chen et al. 2017).

Le paysage des PTAs est divisé en plusieurs collaborations: *Parkes Pulsar Timing Array* (PPTA) en Australie ; l'*European Pulsar Timing Array* (EPTA), regroupant des équipes et instruments situés en Allemagne, en Angleterre, en France, aux Pays-Bas et en Italie ; le *North American Nanohertz Observatory for Gravitational Waves* (NANOGrav) en Amérique du Nord ; l'*Indian Pulsar Timing Array* (InPTA) en Inde ; le *Chinese Pulsar Timing Array* (CPTA) en Chine ; *MeeKAT* en Afrique du Sud. l'*international Pulsar Timing Array* (IPTA) regroupe ces consortia, et permet ainsi de concentrer les efforts pour la recherche d'ondes gravitationnelles, notamment via la combinaison des données des différents PTAs. À ce jour, les membres officiels sont PPTA, l'EPTA, NANOGrav et l'InPTA.

En pratique, les PTAs observent les MSPs les plus stables sur plusieurs dizaines d'années afin d'être sensible aux plus basses fréquences, là où le signal attendu est le plus fort. Les résidus de chronométrage sont ensuite regroupées et analysées afin de rechercher les ondes gravitationnelles. La thèse se concentre en majeure partie sur la modélisation des bruits d'avant-plans à prendre en compte lors de l'analyse des données.

1.5 Analyses Bayésiennes

Les analyses de données effectuées lors de cette thèse suivent une approche Bayésienne, dans laquelle les paramètres à determiner sont considérés comme des variables aléatoires que l'on infère, compte-tenu des données acquises et des informations connues a priori. Elle sont utilisées soit pour effectuer une *estimation de paramètres* (i.e., évaluer les densités de "probabilité des paramètres du modèle sachant le modèle choisi et les données acquises", appelées distributions posterieures), ou bien pour appliquer une *sélection de*

modèle via la détermination de facteur de Bayes. Cet estimateur permet en effet de quantifier à quel point un modèle est statistiquement préféré à un autre pour décrire les données observées. Dans le Chapite 2, nous utilisons l'echelle de Jeffreys (Jeffreys 1961) pour la sélection de modèle, qui propose que, pour comparer deux modèles $\mathcal{M}_a$ et $\mathcal{M}_b$, un facteur de Bayes de $\mathcal{B}^{\mathcal{M}_a}_{\mathcal{M}_b} > 100$ indique une préférence décisive pour le modèle $\mathcal{M}_a$.

L'estimation de paramètre est effectuée par l'application de logiciel permettant un echantillonage via la méthode de Markov Chain Monte Carlo (MCMC), dans laquelle une chaine parcours l'espace des paramètres en maximisant la fonction de vraisemblance (likelihood en anglais). Les logiciels utilsés ici sont PTMCMCSAMPLER et MC^3 (https://gitlab.in2p3.fr/stas/samplermcmc). L'évaluation des facteurs de Bayes est effectuée via le rapport d'évidences (i.e., la probabilité d'obtenir les données observées en supposant que le modèle utilisé est le bon). Nous utilisons un echantilloneur appelé DYNESTY (Speagle 2020, utilisant la méthode de 'nested sampling' permettant de calculer une évidence. Le calcul de facteurs de Bayes peut également se faire via une méthode appelée 'space-product', dans laquelle une chaine MCMC permet de commuter entre différents modèles. Dans notre cas, nous utilisons la classe python "Hypermodel" implémentée dans le logiciel ENTERPRISE_EXTENSIONS (https://github.com/nanograv/enterprise_extensions).

2. Sélection des modèles individuels des pulsar

Cette partie se concentre sur l'application d'une sélection de modèle dans un cadre Bayésien afin d'optimiser le modèle décrivant les processus liés à chacun des pulsars, afin d'améliorer la robustesse des analyses visant à rechercher le fond stochastique d'ondes gravitationnelles. Cette étude est appliquée aux données de la deuxième Data Release de l'EPTA pour six pulsars. Elle a donné lieu à une publication (Chalumeau et al. 2021 en cours d'impression) à la revue Monthly Notices of the Royal Astronomical Society (MNRAS).

L'EPTA Data Release 2 (DR2) - 6 pulsars est un jeu de données comprenant plus de 24 années d'observations de PSRs J0613-0200, J1012+5307, J1600-3053, J1713+0747, J1744-1134 et J1909-3744. Ces observations ont été effectuées par quatre instrument européens: le Radiotélescope d'Effelsberg (EFF) en Allemagne, le Grand Radiotélescope de Nançay (NRT) en France, le télescope Lovell à l'Observatoire de Jodrell Bank (JBO), ainsi que le Westerbork Synthesis Radio Telescope (WSRT) aux Pays-Bas. De plus, l'EPTA DR2 contient des données provenant du Large European Array of Pulsars (LEAP), correspondant aux observation simultanées mensuelles des instruments ci-dessus, en plus du radiotélescope de Sardaigne en Italie. Pour chaque pulsar, les temps d'arrivée mesurés sont accompagnés d'une éphéméride associée au modèle de chronométrage estimé avec le logiciel TEMPO2 (Hobbs et al. 2006).

2.1 Modélisation des signaux dans les données PTA

La modélisation des signaux contenus dans les résidus des temps d'arrivée se fait via la construction de la fonction de vraisemblance, qui correspond à la probabilité $p(\vec{\delta}t|\vec{\theta}_a$ d'observer les n résidus $\vec{\delta}t$ sachant le set de paramètres $\vec{\theta}$. Elle peut s'exprimer comme

$$\begin{aligned} p(\vec{\delta}t|\vec{\theta}) &= p(\vec{\delta}t|\vec{\theta}_d, \mathrm{GP}) \\ &= \frac{\exp\left[-\frac{1}{2}\sum_{\mathrm{ij}}\left(\delta \mathrm{t_i} - \mathrm{d(t_i\,;\,\vec{\theta}_d)}\right)\left(\mathbf{N_{ij}}+\mathbf{C_{ij}}\right)^{-1}\left(\delta \mathrm{t_j} - \mathrm{d(t_j\,;\,\vec{\theta}_d)}\right)\right]}{\sqrt{(2\pi)^n \det(\mathbf{N}+\mathbf{C})}}, \end{aligned} \tag{1}$$

où $i, j = 1, ..., n$, $\mathbf{N}$ est la matrice de covariance contenant les composantes de *bruit blanc*, $\mathbf{C}$ est la matrice de covariance comprenant les *processus Gaussiens* (GP) et $d(t\,;\,\vec{\theta}_d)$ correspond aux signaux *déterministes* représentés par le jeu de paramètres $\vec{\theta}_d$.

Le bruit blanc permet de prendre en compte les possibles erreurs sur l'évaluation de l'incertitude sur les ToAs, via l'utilisation des paramètres EFAC ($\mathrm{E_f}$) et EQUAD ($\mathrm{E_q}$), définis tels $\sigma = \sqrt{\mathrm{E_f^2}\,\sigma_{\mathrm{ToA}}^2 + \mathrm{E_q}^2}$, où σ et σ_{ToA} sont les respectivement les incertitudes corrigées et initiales des ToAs. Ce type de signal peut notamment correspondre à une erreur instrumentale, ou bien au changement de profile du pulsar à court terme. Il s'agit d'un bruit non corrélé entre chacune des observations.

Les autres types de signaux, appelés *bruits rouges*, sont corrélés dans le temps, c'est-à-dire qu'ils induisent des variations à long terme sur les temps d'arrivée. Ces signaux peuvent être stochastiques, et sont dans ce cas généralement décris comme processus Gaussiens (GP), définis par la matrice de covariance $\mathbf{C}$ tel

$$\mathbf{C} = \sum_{a,b} \mathrm{F_a(t)}\mathbf{\Sigma}_{\mathrm{ab}}\mathrm{F_b(t')}, \tag{2}$$

où F est l'ensemble des fonctions de base comprenant une suite de fonctions cosinus et sinus, et $\mathbf{\Sigma}_{ab}$ est la matrice de covariance de covariance dans le domaine fréquenciel, contenant la densité spectral de puissance (PSD), définie comme une simple loi de puissance, comme une loi de puissance brisée, ou bien comme un 'spectre libre' où chaque fréquence est indépendante des autres. Alors que les deux derniers sont utilisés pour mieux comprendre les données, les signaux stochastiques sont plus généralement caractérisés par une loi de puissance dans le domaine spectral, avec des fréquences distribuées telles $1/\mathrm{T}, 2/\mathrm{T}, ..., \mathrm{N/T}$, où T est la durée totale du jeu de données, et N est un entier choisi (typiquement quelques dizaines).

Les signaux rouges stochastiques peuvent être indépendants de la fréquence radio (achromatic red noise, ou RN) ou bien au contraire être chromatiques. Pour le premier cas, il peut s'agir par exemple des variations de fréquence rotationnelle du pulsar à long terme. Pour le deuxième, ceci peut correspondre par exemple aux variations à long terme

de la mesure de dispersion (DM variations, ou DMv), ou bien de la multi-propagation (scattering variations, ou Sv) se produisant dans le milieu interstellaire. Enfin, les signaux rouges stochastiques peuvent correspondre au 'System noise' (SN), décrivant les variations à long terme des temps d'arrivée causée par un défaut de système d'acquisition, ou bien au 'Band noise' (BN), permettant de caractériser toute variation relative à une band de fréquence radio spécifique. Ces deux types de processus sont généralement modélisés comme des signaux achromatiques, à part pour le System noise correspondant au système NUPPI de Nançay, à 1.4 GHz, ou nous avons également considéré une dépendance en fréquence radio correspondant à celle du DM (DM-SN). Chaque observation effectuée avec ce système a été divisée en quatre sous-bandes de fréquence, donnant lieu à quatre ToA, et ainsi une résolution fréquencielle.

Les autres signaux rouges d, dits déterministes, sont définis de manière 'exacte' via leurs paramètres $\vec{\theta}_d$. Il peut s'agir d'une variation annuelle de DM, de scattering, ou bien d'un 'exponential dip', i.e., une chute brutale du contenu électronique dans la ligne de visée du pulsar donnant lieu à une brusque avance chromatique des temps d'arrivée, suivie d'une relaxation exponentielle vers la valeur de départ.

2.2 Sélection de modèles individuels dans l'EPTA DR2

Pour chaque pulsar, la sélection du modèle de bruit est effectuée en plusieurs étapes décrites ci-dessous. Les modèles sont nommés à partir des signaux inclus (hors bruit blanc qui est tout le temps utilisé), en explicitant le nombre de fréquences spectrales utilisées pour caractériser la loi de puissance pour les signaux rouges stochastiques. Le modèle de base utilisé est RN30 DMv100, incluant le bruit blanc et deux bruits rouges stochastiques: le bruit rouge achromatique (RN) et les variations de DM (DMv), modélisés par des processus Gaussiens avec respectivement 30 et 100 fréquences spectrales.

Nous débutons par une optimisation du nombre de fréquences spectrales pour le RN et DMv. Pour ce faire, nous avons appliqué une sélection de modèle via l'évaluation de facteurs de Bayes entre différents modèles candidats. Nous testons des valeurs entre 30 et 100 pour la variation de DM, et entre une valeur minimale et 30 pour le bruit rouge achromatique. Cette valeur minimale est déterminée via une analyse du spectre en utilisant loi de puissance brisée, ou bien comme un 'spectre libre' comme PSD. Pour la plupart des pulsars, nous avons trouvé les valeurs minimales pour le RN (10 ou 15), et une valeur de 100 ou 150 pour DMv, sauf pour PSR J0613-0200, où nous sommes arrivés à la valeur minimale de 30. Nous avons notamment remarqué que le spectre de bruit rouge pour PSR J1909-3744 semble s'aplanir dans les plus basses fréquences. Un tel phénomène pourrait être lié à des processus internes au pulsar, ou bien la présence d'un fond stochastique d'ondes gravitationnelles provenant d'une population de trous noirs supermassifs en systèmes binaires excentriques. Toutefois, nous ne sommes pas en mesure de confirmer ceci

compte tenu de la faible contrainte sur les plus basses fréquences.

La deuxième étape consiste à procéder à une sélection de modèle entre les trois signaux rouges stochastiques physiques appliqués dans cette étude: le bruit rouge achromatique, la variation de DM et la variation de scattering. Nous avons trouvé que le modèle de base, composé de RN et de DMv, est favorable pour la plupart. Le modèle favorisé par les données pour PSR J1600-3053 est composé de DMv et de Sv, ce qui est en accord avec des résultats obtenus dans Main et al. (en préparation), où le pulsar semble montrer une variation de scattering. Pour PSR J1909-3744, le modèle obtenu est contient les trois signaux. Dans cette partie, nous avons reporté la présence de signaux rouges achromatiques à hautes fréquences spectrales pour PSR J1012+5307, ce qui nous a réévaluer le nombre de fréquences spectrales pour RN à 150.

En tenant compte de résultats précédents, nous avons recherché la présence de deux exponential dips pour PSR J1713+0747. Nous avons confirmé leurs présence et rapporté des valeurs d'indice chromatique différent de celle correspondant au DM (valant 2): $\chi_{\mathrm{E}_1} = 4.07^{+1.77}_{-1.13}$ pour le premier et $\chi_{\mathrm{E}_2} = 1.00^{+0.56}_{-1.13}$ pour le deuxième. Nous n'avons cependant pas confirmé la présence de variations annuelles chromatiques pour PSR J0613-0200.

Enfin, nous avons recherché la présence de Band et System noise pour les six pulsars. Le tableau 1 montre les modèles complets obtenu après la sélection de modèle. Il est intéressant de remarquer les modèles sont différents entre les pulsars et que les facteurs de Bayes ont des valeurs très importantes, ce qui souligne l'importance de traiter chaque pulsar de manière unique afin de caractériser proprement les sources de bruit.

3. Recherche d'un GWB avec l'EPTA et l'IPTA

Cette partie présente en premier lieu les résultats obtenus lors de la recherche d'un GWB avec six pulsars de l'EPTA DR2 présentés dans Chen et al. 2021. Puis, l'analyse sur l'impact de la sélection des modèles individuels de pulsars (voir chapitre précédent) sur la recherche d'un GWB est détaillée. Cette section est contenue dans Chalumeau et al. 2021. Enfin, la dernière section présente une partie de l'étude sur la recherche d'un GWB avec la duexième Data Release de l'IPTA (Antoniadis et al. 2022).

3.1 Modélisation des signaux corrélés dans les données PTA

La recherche du GWB nécessite de combiner les données provenant de plusieurs pulsars afin de sonder les corrélations spatiales, et vérifier qu'elles obeissent à la signature décrite par la courbe de Hellings-Downs (Hellings and Downs 1983), caractéristique d'un GWB. En plus d'etre corrélé spatialement, la déformation caractéristique h_c attendue peut être décrite selon une loi de puissance

Table 1: Modèles de bruits obtenus après application de la sélection de modèle pour chacun des six pulsars. La troisième et quatrième colonne montrent la médiane des distributions posterieures de l'amplitude et de l'indice spectral du bruit rouge achromatique, avec un intervalle de confiance de 95%. La cinquième colonne montre les facteurs de Bayes obtenus entre le modèle de base (M1) et celui résultant de la selection de modèle (M2).

Pulsar	Sel. model	A_{RN}	γ_{RN}	$\log_{10} \mathcal{B}^{M2}_{M1}$
J0613-0200	*RN10 DMv30 DMv-SN_NUP_1.4*	$-14.93^{+1.26}_{-1.17}$	$5.07^{+1.83}_{-2.34}$	15.9
J1012+5307	*RN150 DMv30 DMv-SN_NUP_1.4 SN_NUP_2.5*	$-13.03^{+0.08}_{-0.08}$	$1.16^{+0.32}_{-0.29}$	40.7
J1600-3053	*DMv30 Sv150 SN_LEAP_1.4*	-	-	20.0
J1713+0747	*RN15 DMv150 2 Exp. dips DMv-SN_NUP_1.4 SN_JBO_1.5 SN_LEAP_1.4 SN_BON_2.0 BN_Band.3*	$-14.50^{+0.51}_{-0.86}$	$3.94^{+1.82}_{-1.13}$	195.4
J1744-1134	*RN10 DMv100 DMv-SN_NUP_1.4 BN_Band.2*	$-15.31^{+2.03}_{-2.50}$	$3.68^{+3.13}_{-3.46}$	22.6
J1909-3744	*RN10 DMv100 Sv150*	$-14.45^{+0.66}_{-0.85}$	$4.22^{+2.16}_{-1.65}$	2.1

$$h_c(f) = A_{\rm GWB} \left(\frac{f}{\rm yr^{-1}}\right)^{\alpha_{\rm GWB}}, \tag{3}$$

où $A_{\rm GWB}$ et $\alpha_{\rm GWB}$ sont respectivement l'amplitude correspondant à la fréquence $f = 1{\rm yr}^{-1}$ et l'indice spectral. Ce dernier a une valeur attendue de $-2/3$ pour une population simple de systèmes binaires de trous noirs supermassifs.

De la mème manière que pour les analyses de donnée mono-pulsar, l'analyse multi-pulsars fait intervenir l'évaluation d'une fonction de vraisemblance

$$p(\vec{\delta} t|{\rm GP}) = \frac{\exp\left[-\frac{1}{2}\,\vec{\delta}{\rm t}\,\left(\mathbf{N}+\mathbf{C}^{\rm PSRN}+\mathbf{C}^{\rm CRS}\right)^{-1}\,\vec{\delta}{\rm t}\right]}{\sqrt{(2\pi)^n \det(\mathbf{N}+\mathbf{C}^{\rm PSRN}+\mathbf{C}^{\rm CRS})}}, \tag{4}$$

où $\mathbf{N}$, $\mathbf{C}^{\rm PSRN}$ et $\mathbf{C}^{\rm CRS}$ sont les matrices de covariances comprenant respectivement les termes de bruit blanc, de bruits rouges stochastiques intrinsèques à chacun des pulsars, et de signaux rouges stochastiques contenus dans tous les pulsars, appelé Common Red Signal (CRS).

Le CRS est modélisé en processus Gaussiens décris par une loi de puissance spectrale. Dans cette thèse, nous considérons différents types de corrélations spatiales: Le Common Uncorrelated Red Noise (CURN), la corrélation Hellings-Downs (GWB), une corrélation constante égale à 1 (CLK), correspondant à une erreur de correction d'horloge, une corrélation dipolaire (EPH) caractéristique d'erreur sur les éphémérides du Système solaire, ou bien en paramètre libre afin de les mesurer dans les données.

3.2 Recherche d'un GWB dans l'EPTA DR2

La recherche d'un GWB dans l'EPTA DR2 - 6 pulsars (Chen et al. 2021) a abouti aux mêmes conclusions présentés récemment par NANOGrav (Arzoumanian et al. 2020) et PPTA (Goncharov et al. 2021) en reportant la présence d'un signal rouge commun entre les pulsars, mais sans pouvoir confirmer la présence de corrélations Hellings-Downs. Les résultats présentés dans Chen et al. 2021 sont obtenus avec deux logiciels indépendants permettant d'estimer les distributions posterieures des paramètres et d'évaluer des facteurs de Bayes, ENTERPRISE avec PTCMC (EP) et FORTYTWO avec PYMULTINEST ou POLYCHORDLITE (42).

La Figure 1 présente les distributions postérieures obtenues en modélisant le CRS avec une loi de puissance et les corrélations spatiales en paramètres libres. Ces dernières s'avèrent non contraintes, et ne permettent donc pas de confirmer ni d'infirmer la présence d'ondes gravitationnelles. Cependant, un signal commun est présent, avec une amplitude et un indice spectral à $\log_{10} A_{\rm CRS} = -14.32^{+0.31}_{-0.39}$ et $\gamma_{\rm CRS} = 3.83^{+0.82}_{-0.72}$ (médiane et régions crédibles à 95%).

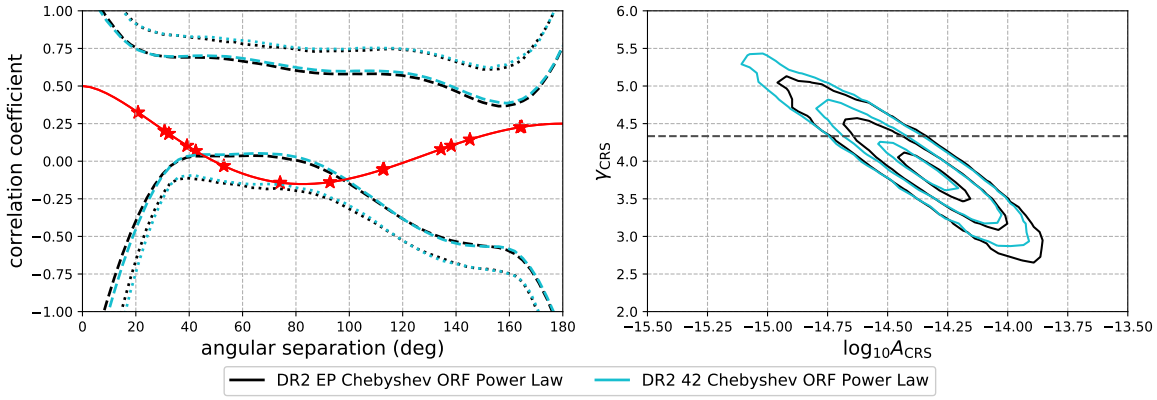

Figure 1: Distributions posterieures des corrélations spatiales (à gauche), et de l'amplitude et de l'indice spectral de la loi de puissance (à droite) décrivant le CRS avec corrélations en paramètres libres obtenues avec l'EPTA DR2 - 6 pulsars, soit avec ENTERPRISE (EN), soit avec FORTYTWO (42). Les courbes en tirets et en pointillés dénotent les régions crédibles respectivement à 95% et 99.7%. La courbe rouge correspond aux corrélations Hellings-Downs théoriques, et les étoiles rouges montrent les séparations angulaires entre les six pulsars considérés.

Le facteur de Bayes obtenu avec ENTERPRISE en faveur du modèle content un CRS sans corrélation spatiale (CURN) contre un modèle sans CRS est de 3.8 en échelle logarithmique, ce qui s'avère hautement significatif. Cependant, le facteur de Bayes entre le modèle incluant les corrélations de Hellings-Downs (GWB) contre le CURN est de 0.4 en faveur du deuxième, ne permettant pas de favoriser l'un des deux modèles. En effet, nous attendons une valeur importante en faveur du GWB pour pouvoir prétendre d'une détection du GWB.

3.3 Impact de la sélection de modèles individuels sur la recherche d'un GWB

La sélection de modèle de bruit individuel présentée précédemment a abouti à des modèles différents pour chacun des pulsars. Cette partie se concentre sur l'impact de cette optimisation sur la mesure du GWB.

La Figure 2 montre un large accord entre les loi de puissance obtenues avec (droite) ou sans (gauche) corrélation angulaire, ce qui permet de confirmer le résultat présenté dans Chen et al. 2021. De plus, nous observons un leger élargissement ainsi qu'un léger décalage des distributions, ce qui montre l'importance d'une telle optimisation pour permettre une caractérisation propre du GWB si présent dans les données.

Figure 2: Distributions postérieures de l'amplitude et de l'indice spectrale de la loi de puissance du CURN (à gauche) et du GWB (à droite), en utilisant les modèles individuels standards (RN DMv) en bleu et ceux obtenus après la selection de modèles en rouge.

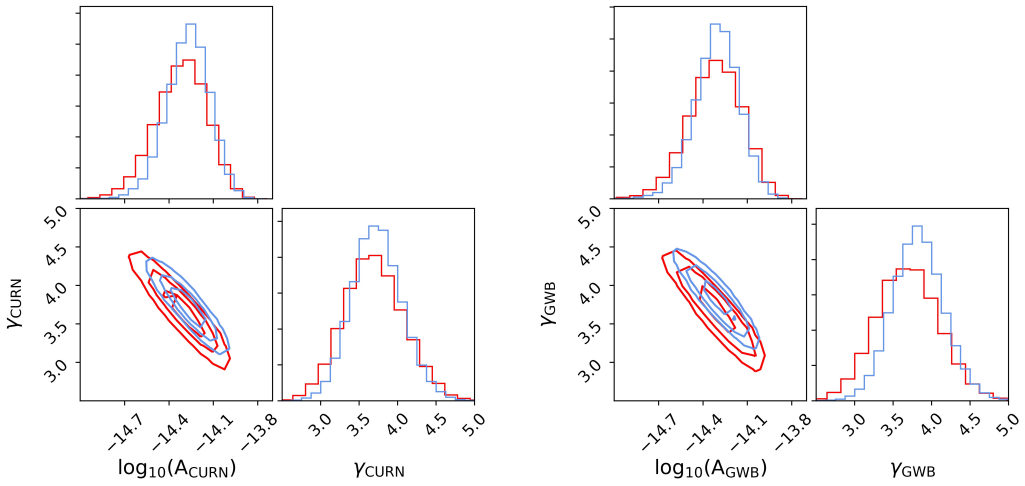

3.4 Évaluation des signaux corrélés dans l'IPTA DR2

L'IPTA Data Release 2 est un jeu de donnée comprenant 65 pulsars provenant de l'EPTA, NANOGrav et PPTA. La publication Antoniadis et al. 2022 présente la recherche du GWB effectuée par l'IPTA dans ces données. Celles-ci sont antérieures aux données utilisées pour les récentes analyses des trois PTAs. Toutefois, la combinaison globale des données a permis une forte amélioration de la sensibilité en ondes gravitationnelles, permettant une mesure d'un signal commun entre les pulsars en accord avec les derniers résultats. Tout comme ces derniers, la corrélation Hellings-Downs n'a pu être reportée.

L'étude est particulièrement focalisée sur l'évaluation des corrélations spatiales dans les données via (1) une estimation des paramètres décrivant une loi de puissance ou bien un 'spectre libre' (2) une sélection de modèle comprenant différentes corrélations, mais aussi en séparant directement les termes corrélés entre les pulsars aux autres dans la fonction de vraisemblance. Ceci corrobore les autres résultats en produisant une limite supérieure sur le signal purement corrélé. La Figure 3 montre la concordance des distributions posterieures des paramètres de la loi de puissance entre les différents jeux de données récents des PTAs et celui de l'IPTA DR2.

4. Modélisation des erreurs des SSEs avec PTA

L'application du modèle de chronométrage implique une transformation des ToAs au référentiel quasi-inertiel du barycentre du Système solaire (SSB). Pour ce faire, nous utilisons la position donnée par les éphémérides du Système solaire (SSEs), régulièrement

Figure 3: Comparaison des spectres (à gauche) et des distributions posterieures de l'amplitude et de l'indice spectral des lois de puissance (à droite) obtenues avec les plus récents jeux de données de NANOGrav, PPTA et l'EPTA, ainsi qu'avec l'IPTA DR2. Figure provenant de Antoniadis et al. 2022.

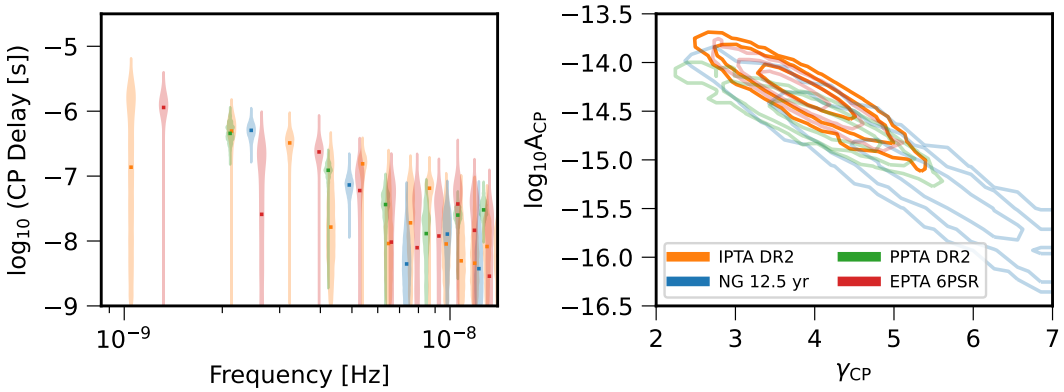

publiée par différentes collaborations telles que l'Institut de Mécanique Céleste et de Calcul des Éphémérides (IMCCE), via Intégrateur Numérique Planétaire de l'Observatoire de Paris (INPOP), ou bien le Jet Propulsion Laboratory (JPL), via les Development Ephemeris (DE). Une erreur sur la position du SSB donnerait lieu à un signal dans les résidus des temps d'arrivée corrélée spatialement, avec une signature dipolaire (Tiburzi et al. 2016). Il est ainsi particulièrement important de prendre en compte les possibles imperfections des SSEs pour assurer une mesure correcte du GWB. Cette partie présente mes travaux sur la construction d'un modèle permettant de décrire les incertitudes des SSEs et son application sur des données simulées et celles de l'EPTA DR2 - 6 pulsars. L'étude de la performance du modèle donne lieu à une publication en cours d'écriture.

4.1 Modélisation des incertitudes dans les SSEs pour PTA

Nous avons construit un modèle nommé *EphemGP* qui permet la description du signal dans les résidus des temps d'arrivée correspondant à la variation de la position du SSB causée par une perturbation des paramètres orbitaux des principaux objets du Système solaire (Jupiter et Saturne dans cette thèse). Le signal est modélisé comme un processus Gaussien, dont les fonctions de bases et la matrice de covariance sont obtenues à partir de données provenant de l'intégration numérique effectuée pour obtenir les éphémérides INPOP (INPOP19a dans notre cas). Ces données ont été partagées par A. Fienga (GEOAZUR) qui dirige la production de ces SSEs. Afin de pouvoir décrire des signaux visibles dans les données PTA, nous avons largement étendu les incertitudes des paramètres orbitaux donnés par INPOP19a.

Dans la suite nous comparons des résultats obtenus avec EPHEMGP à ceux produit

Table 2: Notations simplifiées des différents jeux de donnée simulés et leurs signaux inclus. WN, SSE et GWB dénotent respectivement la présence de bruits blancs, de d'erreur sur les SSEs, et du GWB avec une précision sur l'amplitude.

Data	Signal
'B1'	WN + GWB ($A = 10^{-16}$)
'B2'	WN + GWB ($A = 10^{-15}$)
'A+B1'	WN + SSE + GWB ($A = 10^{-16}$)
'A+B2'	WN + SSE + GWB ($A = 10^{-15}$)

avec un CRS contenant des corrélations dipolaires ou bien avec BAYESEPHEM (Vallisneri et al. 2020), un modèle décrivant la variation de la position du SSB par la perturbation d'orbites et de masses des objets principaux du Système solaire en signaux déterministes.

4.2 Impact des erreurs des SSEs dans la recherche d'un GWB

Cette section présente l'étude de la performance d'EPHEMGP à décrire les systématismes contenu dans les SSEs, et à séparer un tel signal avec celui produit par un GWB. Pour cela, nous avons simulé des temps d'arrivée à partir de données EPTA réelles. Les quatre jeux de données simulés sont présentés dans le Tableau 2.

Le signal d'erreur des SSEs ('A') est simulé en injectant dans les données la différence des résidus des temps d'arrivée obtenus avec deux SSEs différentes. Dans cette étude, nous considérons la différence entre DE438 et INPOP19a.

La Figure 4 montre les distributions postérieures de l'amplitude et de l'indice spectral du CRS avec des corrélations Hellings-Downs obtenues en considérant les jeux de données analysés avec différents modèles décrivant les erreurs des SSEs. En haut, le signal de GWB est injecté avec une amplitude $A = 10^{-16}$ ('B1') relativement faible par rapport au signal 'A' qui induit un faux positif (distributions rouges). Pour les trois modèles d'erreur sur les SSEs, les distributions postérieures (en vert) n'indiquent plus de faux positif. Dans le cas d'un signal fort de GWB avec une amplitude $A = 10^{-15}$ (en bas ; 'B2'), le signal 'A' ne semble pas affecter les distributions posterieures. Ces résultats montrent ainsi que les trois modèles testés permettent d'absorber des potentielles erreurs dans les SSEs, et qu'ils n'ont pas d'impact significatif sur la caractérisation du GWB.

Figure 4: Distributions postérieures des paramètres de la loi de puissance décrivant un signal de GWB obtenues pour les quatre jeux de données simulés pour un GWB avec une amplitude de $A = 10^{-16}$ (en haut), et $A = 10^{-15}$ (en bas). Les erreurs provenant des SSEs sont modélisées avec EPHEMGP (à gauche ; EGP), BAYESEPHEM (au centre ; BFM) et un CRS dipolaire (à droite ; EPH). Les lignes en noir montrent les valeurs de GWB injectées.

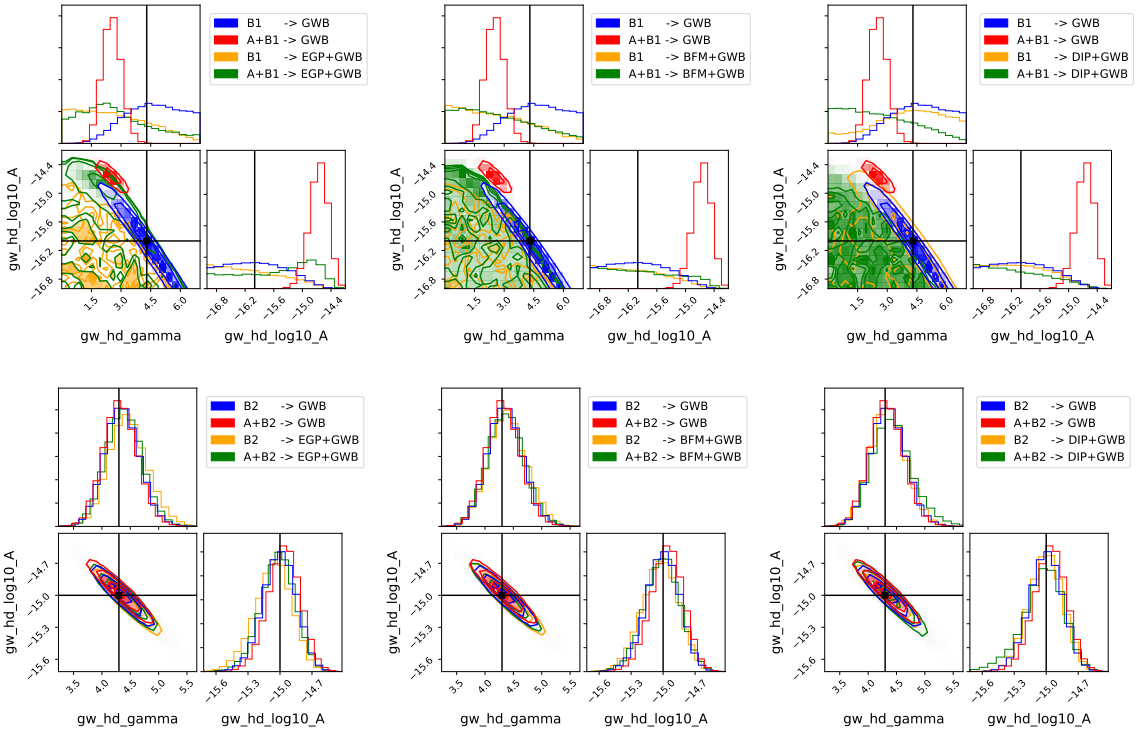

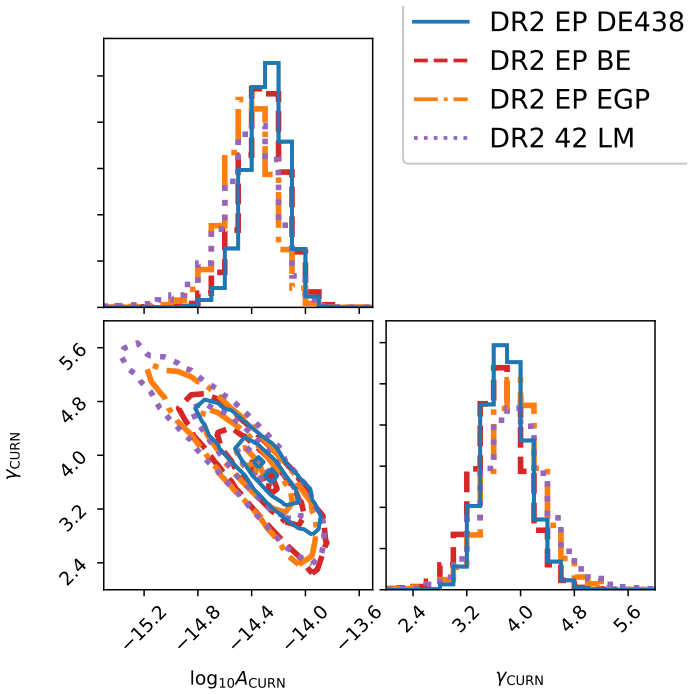

Figure 5: Distributions postérieures de l'amplitude et de l'indice spectral du CURN obtenues sans modèle décrivant les erreurs contenues dans les SSEs (DE438), ou bien en utilisant BAYESEPHEM (BE), EPHEMGP (EGP) ou LINIMOSS (LM).

4.3 Impact sur l'estimation des paramètres du GWB avec l'EPTA DR2

Les résultats publiés dans Chen et al. 2021 contiennent également une partie qui décrit une étude sur l'impact de la modélisation des erreurs des SSEs sur la mesure du signal commun. En plus de considérer EPHEMGP et BAYESEPHEM, le modèle LINIMOSS (Guo et al. 2019) y est également considéré. La Figure 5 montre les distributions postérieures des paramètres décrivant la loi de puissance du signal CURN (sans corrélation spatiale) obtenues avec les différents modèles. Les résultats restent compatibles avec la mesure initiale (en bleu), avec un léger élargissement des distributions. Ainsi, le signal commun mesuré persiste même après l'inclusion des modèles considérés.

5. Conclusion et perspectives

Les travaux effectués lors de cette thèse ont pour objectif commun d'améliorer la description des sources de bruit et signaux contenus dans les données de chronométrage de pulsar, afin d'optimiser la recherche d'ondes gravitationnelles avec PTA. En plus de participer à la recherche du GWB avec l'EPTA et l'IPTA, j'ai étudié l'impact de la modélisation des signaux individuels et des erreurs des éphémérides du Système solaire sur la mesure du GWB. Dans ces travaux, j'ai construit une méthode afin d'optimiser la modélisation des

bruits rouges individuels, et j'ai construit un modèle permettant de prendre en compte les erreurs des SSEs en utilisant des informations provenant des éphémérides INPOP.

Les résultats récents des PTAs sont particulièrement prometteurs pour les prochaines années. Je participe en ce moment aux efforts fournis par la collaboration européenne afin d'effectuer une recherche du GWB avec 25 pulsars dont les résultats sont attendus pour l'année 2022. Cette augmentation du nombre de pulsars devrait permettre une large amélioration pour la recherche des corrélations spatiales. Enfin, la combinaison des données provenant des différents PTAs continentaux au niveau de l'IPTA dans les prochaines années permettra d'obtenir la mesure la plus précise et peut être de confirmer (ou infirmer) la présence d'un fond stochastique d'ondes gravitationnelles.

ACKNOWLEDGEMENTS

I would like to thank to my two supervisors, Gilles Theureau and Stas Babak, for allowing me to discover and take part in the fascinating Pulsar Timing Arrays project. I feel very lucky to have received such a complementary and broad training from you two. I am particularly grateful for the patience, guidance and support you have constantly offered me, and for allowing me to enjoy working with you everyday on pulsar timing and gravitational waves (GWs).

I am very grateful to Lucas Guillemot who taught me so much about pulsars and pulsar timing methods, and who was always there to help me at any time. I also thank Antoine Petiteau for his infinite kindness and all his help, especially in understanding noise modelling and Bayesian techniques. A special thank you to Siyuan Chen who is one of those who helped and advised me the most during these three years. I admire your professionalism and I really enjoyed working with you. I also thank Ismaël Cognard, Jean-Mathias Grießmeier and Louis Bondonneau who were always willing to discuss about pulsars, and in particular their radio emission, the effects of the interstellar and interplanetary medium and the techniques of radio astronomy observation. Thank you very much to all my other colleagues from Orléans: Anaïs Berthereau, Mark Brionne, Raphaël Gros, Musfar Kozhikkal, Cyprien Calmels ; from Paris: Mikel Falxa, Alexandre Toubiana, Léon Vidal, Nam Dam, Étienne Savalle, Nikos Karnesis, Maude Lejeune, Hubert Halloin, Éric Plagnol. It was a real pleasure to discuss with you all about pulsars and GW science. To all my colleagues-friends, I really enjoyed spending time and sharing unforgettable moments together. I look forward to living many more !

I would like to express my deepest gratitude to my colleagues at the European Pulsar Timing Array (EPTA) for their constant support and help. In particular, thanks to Golam Shaifullah, James McKee, Kuo Liu, Caterina Tiburzi and Robert Main for their kindness. They have definitely been part of my education in the science of pulsar timing, and I will certainly learn more from them and other EPTA friends in the future. I am also very grateful to the International Pulsar Timing Array (IPTA), especially for allowing me to meet and collaborate with many colleagues around the world. I am truly convinced that the future of PTAs will be held by IPTA, where the best constraints on very-low frequency gravitational waves can be realized. Special thanks to Boris Goncharov, Stephen Taylor, Michele Vallisneri, Jeffrey Hasboun and Nathan Garver-Daniels for their unique kindness and very significant help in many aspects of this thesis. In addition, I am deeply grateful to Agnès Fienga who helped me a lot during the thesis and still now to understand and deal with the Solar system ephemeris errors in the PTA data.

I would like to adress my gratitude to the president, the referees and the examiners of this thesis: Éric Chassande-Mottin, Chiara Mingarelli, Andrea Lommen, Sylvain Chaty, Alberto Sesana, Jonathan Gair. Your comments allowed a significant improvement of the

manuscript, and I have very much appreciated the question session that raised many interesting points. I am deeply grateful to my two comités de suivi de thèse: Éric Chassande-Mottin and Arache Djannati-Ataï in Paris, Tjarda Roberts and Xavier Vallières in Orléans. I hopefully did not give you too much work to do, but I still learned from your advices for my thesis and for preparing my future in research. I would like to express my gratitude to Arache, who gave me the passion for pulsar science during my Master 1 internship, and who has continued to help me and contribute to my training through my thesis committee, and les Entretiens (an informal and useful meeting where researchers can share their knowledge on pulsars). This thesis would not have been possible without the support of the École doctorale 560 STEP'UP, the Université de Paris, the Île-de-France region via the DIM ACAV+, the AstroParticules et Cosmologie laboratory, the Laboratoire de Physique et de Chimie de l'Environnement et de l'Espace, the Station de Radioastronomie de Nançay and the Centre national de la recherche scientifique. Moreover, I am grateful to the Université de Tours and to the Observatoire de Paris for the very rich and complete training I received in physics and astrophysics, which allowed me to carry out this thesis.

To conclude, I would like to thank to all my family and non-colleague friends, to my mother Claude, to my father Philippe, to Valérie, to my brother and sister Étienne and Clémentine, to my grand parents, Mamine, Papi Jeannot, Mamilène, Papiland, to Yves and Yvette, to my aunt and uncle, Isabelle and Pierre. To the families Chalumeau, Bry, Rossi, Lozada and Secheret. To my closest friends, Boris, Pijule, Maxime F., Lilian, Adrien, Thomas, Maxime S., Victorine, Thibaud, Jordan, Halim, Augustin, Amélie, Jaikhomba, Shinnosuke and many others. To all of you that have been present during these last three years, I can never thank you enough for your support and all the beautiful moments we have lived together. Finally, I dedicate this thesis to my wife, Rosa María, who has given me the strength for the last eight years to accomplish everything I did until this thesis and made me become the person I am today. Nunca te agradeceré lo suficiente por todo lo que hiciste por mí, te amo para siempre.

CONTENTS

List of Figures

LIST OF TABLES

ACRONYMS AND ABBREVIATIONS

Collaborations, projects, databases, etc...

Notation	Description
PTA	Pulsar Timing Array
IPTA	The International Pulsar Timing Array
EPTA	The European Pulsar Timing Array
NANOGrav	The North American Nanohertz Observatory for Gravitational Waves
PPTA	The Parkes Pulsar Timing Array
InPTA	The Indian Pulsar Timing Array
CPTA	The Chinese Pulsar Timing Array
NRT	Nançay Radio Telescope
EFF	Effelsberg
JBO	Jodrell Bank Observatory
WSRT	Westerbork Synthesis Radio Telescope
SRT	Sardinia Radio Telescope
LEAP	Large European Array of Pulsars
VLBI	Very Long Baseline Interferometry
LLR	Lunar Laser Ranging
EPN	European Pulsar Network
ATNF	Australia Telescope National Facility
BIPM	Bureau International des Poids et Mesures
IMCCE	Institut de Mécanique Céleste et de Calcul des Éphémérides
INPOP	Intégrateur Numérique Planétaire de l'Observatoire de Paris
JPL DE	Jet Propulsion Laboratory Development Ephemeris
EPM	Ephemerides of Planets and the Moon

Pulsar timing & Pulsar Timing Array

Notation	Description
PSR	Pulsating Source of Radio
MSP	Millisecond pulsar
CP	Canonical pulsar
SGR	Soft Gamma-ray Repeater
AXP	Anomalous X-ray Pulsar
RRAT	Rotating Radio Transient
ISM	Interstellar Medium
IISM	Ionized Interstellar Medium
ToA	Time of Arrival
TM	Timing model
DM	Dispersion Measure
JD	Julian Date
MJD	Modified Julian Date
GW	Gravitational Waves
GWB	Gravitational Wave Background
SMBHBs	Supermassive Black Hole Binaries
z	Cosmological redshift
TT	Terrestrial Time
UTC	Universal Time Coordinate
GPS	Global Positioning System
TAI	Temps Atomique International
SSE	Solar System Ephemeris
SSB	Solar system Barycenter

Noise models & data analysis

Notation	Description
WN	White Noise
RN	Red Noise
DMv	DM variations
Sv	Scattering variations
FCN	Free-Chromatic Noise
SN	System Noise
BN	Band Noise
E	Exponential dip
Y	Annual chromatic process
PSRN	Single-pulsar noise model only
CRS	Common Red Signal
CURN	Common Uncorrelated Red Noise
CLK	CRS with monopolar spatial correlations
DIP	CRS with dipolar spatial correlations
HD	CRS with spatial correlations following Hellings-Downs curve
BFM	BayesEphem
EGP	EphemGP
rms	root mean square
S/N	Signal-to-Noise Ratio
PSD	Power Spectrum Density
ORF	Overlap Reduction Function
MCMC	Markov Chain Monte Carlo
BF	Bayes Factor
$J-S$ div.	Jensen-Shannon divergence
A^2	Anderson-Darling test
SVD	Singular-Value Decomposition

Constant values

Notation	Description	Value
π	Archimedes constant	~ 3.14159265
G	Gravitational constant	$\sim 6.67430 \times 10^{-11}$ m^3 kg^{-1} s^{-2}
c	Speed of light	299 792 458 m.s^{-1}
k	Dispersion constant	$\sim 4.149 \times 10^3$ MHz^2 cm^3 pc^{-1} s
$M_\odot$	Mass of the Sun	$\sim 1.9884 \times 10^{30}$ kg
JD 0	Julian Date 0	12:00, January the 1st, 4713 BC.
MJD 0	Modified Julian Date 0	JD 0 + 2 400 000.5 days

CHAPTER 1

INTRODUCTION

Abstract

This chapter begins with a presentation of pulsars in general and a focus on millisecond pulsars (MSPs). It is followed by a detailed introduction on pulsar timing methods, including the concepts of Time of Arrival (ToA) and Timing Model. The application to PSR J1909-3744 and some related results published in Liu et al. 2020 are developed. I have contributed to this project in the timing data reduction, the red noise analysis and writing part of the paper. The third section gives a description of the Pulsar Timing Array (PTA) gravitational wave detector principle, a brief review of the related expected sources, and an overview of PTAs in the gravitational wave field. The last section details the concepts, the techniques and tools used to perform Bayesian analyses presented in the next chapters.

1.1 Neutron stars and Pulsars

1.1.1 Overview

Two years after the discovery of the neutron by Chadwick in 1932 (Chadwick 1932), Baade and Zwicky (Baade and Zwicky 1934) proposed the existence of very small and high density objects called neutron stars, resulting from supernovae, i.e., the gravitational collapse of an "ordinary" star. For decades then, these predicted objects have been studied mainly to understand the state of ultra-dense matter (Oppenheimer and Volkoff 1939, Harrison et al. 1958), described by the equation of state. Giacconi and colleagues suggested in 1962 that the first extra-solar X-ray source observed, named Scorpius X-1, was a young and hot neutron star (Giacconi et al. 1962). This proposition was corrected by Shklovsky five years later who concluded that the X-ray signal was emitted by the accretion of matter from a putative neutron star (Shklovsky 1967). In 1964, Hoyle, Narlikar and Wheeler discussed about the existence of a highly magnetized neutron star within the Crab nebula (Hoyle et al. 1964), followed by Pacini in 1967 (Pacini 1967) who designated the hypothetical compact object as the source of energy of the nebula.

In 1967, the Ph.D. student Jocelyn Bell and her supervisor Anthony Hewish observed a regular signal at 19^{h} 19^{m} right ascension and 21 degrees of declination with the Interplanetary Scintillation Array at Cambridge, built to monitor the interplanetary scintillation with high time-resolution. In the same year, an upgrade of the instrumentation allowed them to measure the period of the signal at 1.337 s. Firstly named *LGM-1* (for little green man) with humour, this source was then more seriously called *CP 1919* (CP standing for Cambridge Pulsar) (Hewish et al. 1968). In 1968, Gold proposed an interpretation of radio pulsars to be fastly spinning and highly magnetized neutron stars which lose energy from electromagnetic radiation and emission of relativistic particules (Gold 1968). The discovery of pulsars in Vela (Large et al. 1968) and Crab (Howard et al. 1968) nebulae the same year finally validated the correspondence between pulsars and neutron stars.

1.1.2 General description

Neutron stars are remnant compact objects that are produced (among other processes) from core-collapse supernovae, the violent "death" of stars with masses from 8 to ~ 20 solar masses ($M_{\odot}$). In such events, the degeneracy pressure of electrons and the fusion reactions inside the massive star are not high enough to compensate against the gravitational compression, leading to a cataclysmic implosion forming the neutron star at the core, and an explosion from the rebound of the external matter. Models of internal struc-

tures of neutron stars, which are still in status of active researches, predict masses from 0.5 to 2.5 $M_\odot$ and radii of about 10 – 12 km. Measurements of masses (e.g., from pulsar timing of binary systems) have an average of $1.4 M_\odot$, and only few radii have been evaluated, such as for the double neutron star merger GW170817 with multimessenger observations ($R_1 = R_2 = 11.9^{+1.4}_{-1.4}$) (Abbott et al. 2018), or for the pulsar PSR J0030+0451[1] ($R = 12.71^{+1.14}_{-1.19}$) (Riley et al. 2019), from the Neutron Star Interior Composition Explorer (NICER) X-ray telescope.

After the rapid collapse at the origin of the supernova, the conservations of both angular momentum and magnetic flux imply respectively a fast rotation and an intense magnetic field of the neutron star. The rotating dipolar magnetic field (in the case of non-aligned rotation and magnetic axes) induces a very high electric field, parallel with the magnetic axis, that tears out particules from the compact object which fill the magnetosphere (Goldreich and Julian 1969), and follow the co-rotating magnetic field lines. The "light cylinder" of the neutron star with a period P (see Fig. 1.1) defines an imaginary cylinder aligned with the rotation axis and with a radius $cP/(2\pi)$ at which the magnetic field lines spin at the speed of light. Therefore, the openned lines that reach out of the light cylinder emmit charged particules at the magnetic poles, which produce radio beams from curvature radiation. If the trajectory of (at least) one beam passes through our radiotelescope, we can then detect a pulsated radio signal, and therefore observe the neutron star as a *pulsar* (and in our case, a *radio pulsar*).

Each pulsar act as a cosmic lighthouse with a particular profile, i.e, the flux amplitude as a function of its rotational phase. The observed profiles are subject to change at each rotation of the pulsar, due for instance to the variations of the magnetosphere content. Therefore, we usually consider the average profiles (integrated over many rotations), which then appear most of the time very stable between two observations. The mean profile is the fingerprint of the pulsar, it is unique (see Fig. 1.2) and depend on (1) the distribution of the charged particles in the magnetosphere of the pulsar, (2) the angle between the rotation and magnetic axes of the pulsar, (3) the different effects on the radio beam as it travels from the pulsar to the radio telescope and (4) the angle between the line of sight and the rotation axis of the pulsar.

[1]The conventionnal nomenclature of pulsars is defined as "PSR J" (for Pulsating Source of Radio), followed by the right ascension and declination in equatorian Julian coordinate system (J2000). For the pulsars discovered before the late 1990$'s$, the "J" is often replaced with "B" and the positions are given in the Besselian system (B1950). If several pulsars have the same names, their names end with letter in order to distinguish them, such as PSR J0737-3039A.

[2]http://www.epta.eu.org/epndb/

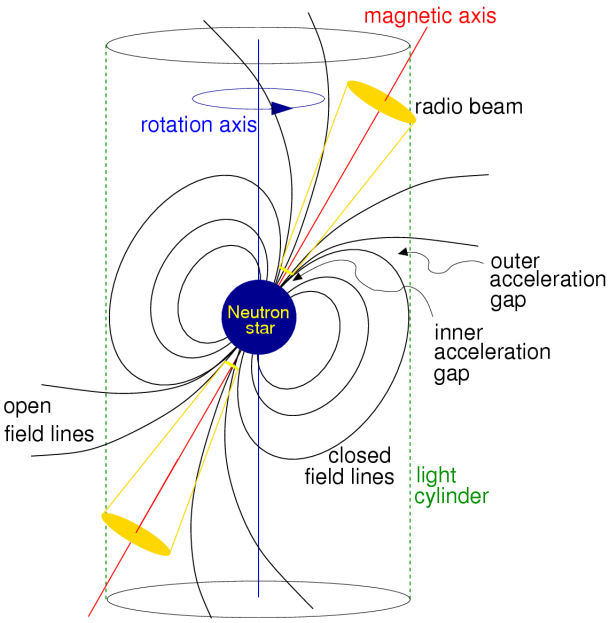

Figure 1.1: Toy-model for the pulsar, with the dipolar magnetosphere, the light cylinder and the radio beam emission (from Lorimer and Kramer 2004).

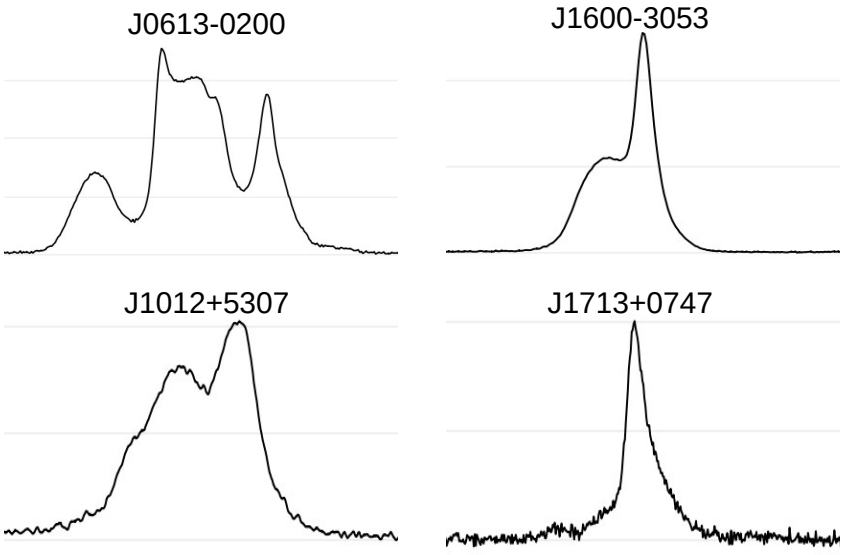

Figure 1.2: Rotational phase fractions of integrated pulse profiles of four different pulsars from the European Pulsar Network[2] (EPN) database.

1.1.3 Millisecond pulsars

The current version (v.1.65, up to December 2020) of the Australia Telescope National Facility (ATNF) Pulsar Catalogue (Manchester et al. 2005) reports 3177 pulsars, including 3055 radio pulsars with periods ranging from 1.4 ms (Hessels et al. 2006) to 23.5 s (Tan et al. 2018). The population of radio pulsars is often represented by the so-called "P-$\dot{\text{P}}$" diagram (see Fig. 1.3), with the spin period P and its first derivative $\dot{\text{P}}$. The majority of pulsars, referred as *canonical pulsars*, have periods between 0.1 and few seconds, and a deceleration rate $\dot{\text{P}}$ between 10^{-17} and 10^{-13} s.s^{-1}. The slowing down due to electromagnetic radiation and particle emission among other processes makes these (usually young) pulsars migrate to the right side of the diagram.

The lower left part of the P-$\dot{\text{P}}$ diagram contains the *millisecond pulsars* (MSPs), with very low periods ($\leq$ 30 ms). In contrast to canonical pulsars, the vast majority of MSPs are located in binary systems. This characteristic can be explained by the following scenario: if the star that originated the pulsar was contained in a binary (or multiple) system that remained from the original supernova, after a certain time, the approaching companion undergoes mass transfer to the pulsar which gains angular momentum from mass accretion (Alpar et al. 1982). These old pulsars are therefore named *recycled pulsars* because they are accelerated by recycling part of their companion.

The v.1.65 of the ATNF Catalogue counts 468 MSPs observed in radio, 276 of which are contained in a binary system. MSPs are remarkable for their high rotational regularity ($\dot{\text{P}} \leq 10^{-18}$ s.s^{-1}), which allows them to be used as cosmic clocks with pulsar timing studies.

1.2 Pulsar Timing

The Pulsar Timing in radio exploits the high rotational stability of millisecond pulsars in order to measure various physical values with very high accuracy. The first indirect detection of gravitational waves (Taylor and Weisberg 1982) have been obtained by timing the first pulsar detected in a binary system, PSR B1913+16, or PSR J1915+1606 (Hulse and Taylor 1975), where the evaluation of the periastron advance of the orbital period is in strong agreement with the prediction of General Relativity. The timing of PSR B1257+12 has enabled to discover the very first exoplanets (Wolszczan and Frail 1992), that induce slight movements of this MSP. Furthermore, the pulsar timing enable to perform tests of general relativity in the strong-field regime with very high accuracy, see for example Kramer et al. 2006 for the double pulsar PSR J0737-3039A/B.

Among many other applications, the pulsar timing also permits to measure masses of pulsars contained in binary systems (Demorest et al. 2010) and therefore induce con-

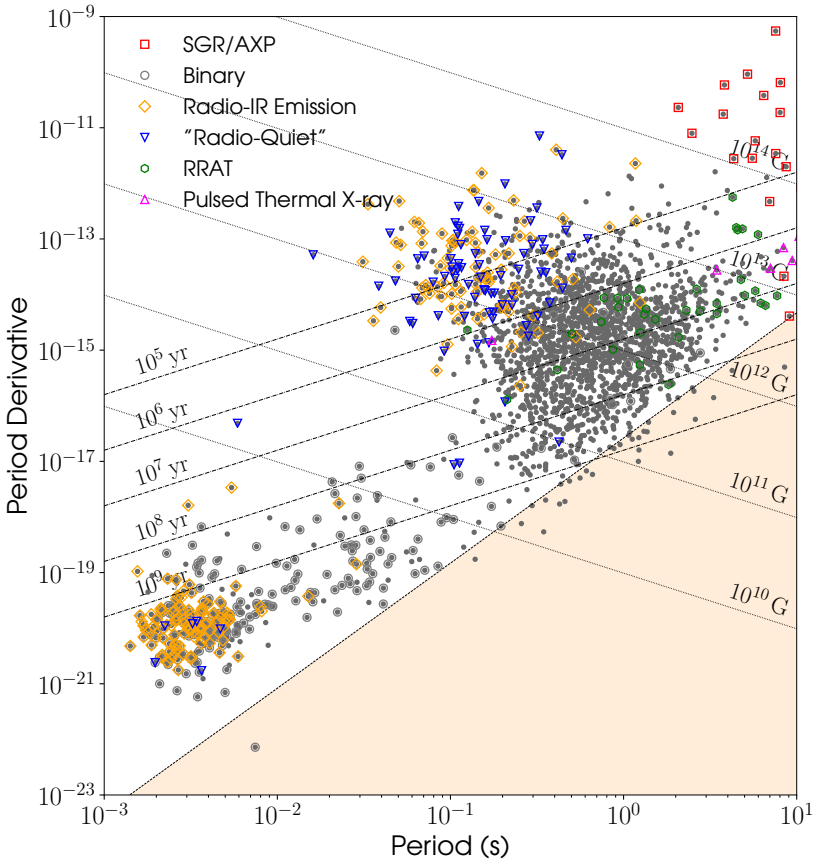

Figure 1.3: The pulsar zoology with the P-$\dot{P}$ diagram obtained from the ATNF Pulsar Catalogue v.1.65. All pulsars are shown with grey dots and different subgroups are represented: soft Gamma-ray repeaters (SGR) and anomalous X-Ray pulsars (AXP) in red squares, those in a binary system with a grey circle, those observed in the infrared in yellow diamonds, those not detected in radio in blue triangle, rotating radio transient sources (RRAT) with intermittent pulsed radio emission in green hexagons and neutron stars with thermal pulsed X-ray emission in pink triangles. The orange shaded region is called the pulsar "graveyard", delimited by the "death line", under which the pulsars are not expected to emmit detectable radio beams because they supposedly cannot support pair production (Chen and Ruderman 1993).

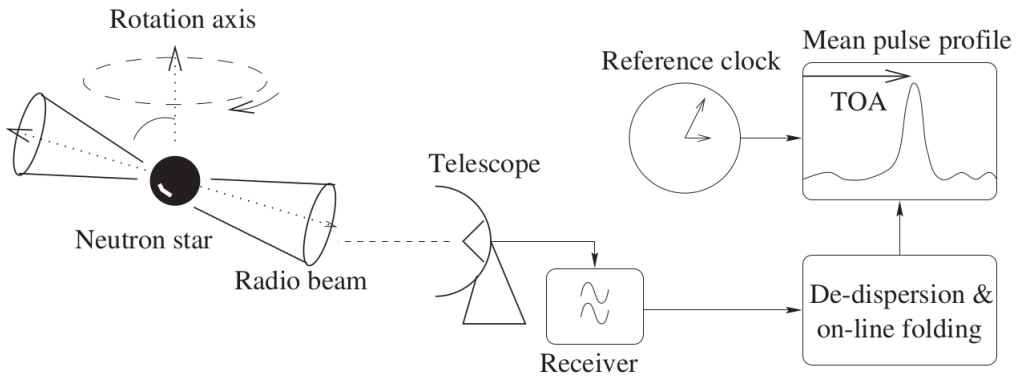

Figure 1.4: Basic concept of a pulsar timing observation (from Lorimer and Kramer 2004).

straints on the equations of state of ultra dense matter.

The millisecond pulsars are weak radio sources and in most of the case it is impossible to detect each single pulse. In practice during a timing observation, the pulses are stacked together in real time for $\sim 1000 - 10000$ rotations in order to increase the signal-to-noise ratio (S/N) and obtain a stable mean pulse profile, this is called the *folding* (see Fig. 1.4). Moreover, the radio signal is affected by the dispersion induced by the free electron content between the pulsar and the telescope. This creates a delay proportional to the inverse of the square radio frequency, i.e., the pulses arrive later for the lower frequencies. The timing observations correct this effect in real-time in order to obtain the most precise folded profiles. This method is called the *dedispersion* (see again Fig. 1.4).

A pulsar timing observation therefore provides a measure of average pulses at several radio frequencies during a given time (usually at the range of an hour). The timing procedure consists of (1) extracting one or several times of arrival (ToA) from each observation and (2) build a *timing model* from a full set of of observations which takes into account the different effects that impact the ToAs.

1.2.1 The Time of Arrival

The Time of arrival is the observed time of a fiducial point in the average profile used to time precisely the pulsar signal. Their conventional unit is the Modified Julian Date[3] (MJD). Usually, the ToAs are produced from an observation fully averaged in time and either fully averaged in radio frequency, or only partially. If the latter is chosen, one has several "sub-bands" ToAs for one observation, each one representing a part of the observed

[3]The MJD is defined as the number of days since midnight on November 17, 1858, exactly 2400000.5 days after day 0 of the Julian Date (JD) calendar that has been proposed in the 16-th century in order to cover all human history (JD 0 corresponds to 12 : 00 on Janurary 1, 4713 BC.).

frequency band. This option is especially useful for wideband observations because it allows to describe possible effects that depend on the radio frequency (i.e., chromatic processes).

The ToAs are determined from the cross-correlation of the observed profile $\mathrm{P_{obs}(t)}$ with a reference "template" profile T(t), usually the smoothed (i.e., noise reduced) addition of several high S/N observations. One can express the observed profile as

$$\mathrm{P_{obs}(t)} = \mathrm{a} + \mathrm{b\ T(t-\tau)} + \mathcal{N}(\mathrm{t}), \tag{1.1}$$

where a, b and $\mathcal{N}$(t) are respectively an arbitrary offset, a scaling factor and Gaussian noise. τ is the time shift between $\mathrm{P_{obs}}$ and T, it permits to evaluate the ToA defined at a fiducial point of the template. The common approach to evaluate ToAs is based on the minimization the difference between both profiles transformed in the Fourier domain (Taylor 1992). The manipulation of observation files, the creation of the profile template and the ToA creation is most of the time performed with the software PSRCHIVE[4].

The uncertainty σ_{ToA} of the ToA depends on the pulse width W and observed signal-to-noise ratio S/N as follows (Lorimer and Kramer 2004)

$$\sigma_{\mathrm{ToA}} \simeq \frac{W}{S/N} \propto \frac{S_{\mathrm{sys}}}{\sqrt{\mathrm{t_{obs}}\,\Delta f}} \times \frac{P\,\delta^{3/2}}{S_{\mathrm{mean}}}, \tag{1.2}$$

where S_{sys} is the "system equivalent flux density", used to characterize the effectiveness of a system, $\mathrm{t_{obs}}$ and Δf are the integration time and the bandwidth of the observation, P is the pulsar spinning period, $\delta = W/P$ is the pulse duty cycle and S_{mean} is the mean flux density of the pulsar. The first term on the right hand side displays the dependence of the precision on the radio telescope and observation quality, which is optimized with an effective instrument (low S_{sys}) observing the pulsar with a wide band (large Δf) for a long duration (large t_{obs}). The second term shows that the ToA accuracy is optimal for bright pulsars (large S_{mean}) with short periods (low P) and small pulse duty cycles (low δ). The millisecond pulsars are therefore particularly adapted to obtain very high quality ToAs.

For wideband observations, the ToA measurement can be significantly impacted by effects that induce variations of the profile with a frequency dependence (i.e., chromatic). As mentionned previously, one can split the full bandwidth in sub-bands and create sub-band ToAs in order to account for chromatic effects afterwards. Another possibility is to use modern methods that extends the common ToA creation procedure shown in Taylor 1992 by considering chromatic processes, such as the dispersion (Liu et al. 2014, Pennucci et al. 2014, Pennucci 2019). This method, often referred as "2D-template" matching, allows to add the radio frequency f information into the cross-correlation as

$$\mathrm{P_{obs}(t,\ }f) = \mathrm{a}(f) + \mathrm{b}(f)\ \mathrm{T}\left(\mathrm{t} - \tau(f),\ f\right) + \mathcal{N}(\mathrm{t},\ f), \tag{1.3}$$

[4] http://psrchive.sourceforge.net

where $\tau(f)$ describes time shifts as function of observational frequency.

1.2.2 The Timing Model

The ToAs obtained for a given pulsar are then combined using the Timing Model (TM), which permits the phase-connection between them, and therefore to study any effect that impacts the arrival time of the pulses at time scales larger than the observation cadence. Most of the MSPs were observed at least once a week for several years, or decades. Note that the cadence and the time span of a timing dataset are important to characterize short and long term processes. Let us now have a look on how the Timing Model is built.

The pulsar spin frequency

First of all, the TM takes into account the change in rotation of a pulsar over time. Its spin frequency ν is expressed as a Taylor expansion (Lorimer and Kramer 2004) :

$$\nu(t) = \nu_0 + \dot{\nu}_0(t - t_0) + \frac{1}{2}\ddot{\nu}_0(t - t_0)^2 + ..., \tag{1.4}$$

where $\nu_0 = \nu(t_0)$, $\dot{\nu}_0 = \dot{\nu}(t_0)$ and $\ddot{\nu}_0 = \ddot{\nu}(t_0)$ are the spin frequency and first two derivatives at a reference epoch t_0. The term $\dddot{\nu}_0$ and higher derivatives are usually too small to be significantly measured. These components are part of the "red noise"(see Chapter 2) that is often treated with analyses post-application of the Timing Model.

The TM permits the phase-connection between the ToAs, which means that every rotations of the pulsar is unambiguously counted. The rate of change of pulse number N can be expressed as (Lorimer and Kramer 2004)

$$N(t) = N_0 + \nu_0(t - t_0) + \frac{1}{2}\dot{\nu}(t - t_0)^2 + \frac{1}{6}\ddot{\nu}(t - t_0)^3 + ..., \tag{1.5}$$

where N_0 is the pulse number at the reference epoch t_0.

Transformation to the pulsar reference frame

The regularity of the observed pulses is also altered by the relative motions of both the pulsar and the Earth, and also by the electron content of the interstellar medium. The Timing Model describes these effects and transforms the "topocentric" ToAs to the pulsar reference frame. The pulse emission time at the pulsar frame t_e^{psr}, related to the arrival time measured at the observatory frame t_a^{obs} and dated with the local observatory clock, is expressed as (Hobbs et al. 2006, Edwards et al. 2006)

$$t_e^{psr} = t_a^{obs} - \Delta_c - \Delta_\odot - \Delta_{ISM} \; (- \Delta_B), \tag{1.6}$$

with the following correction components :

- The clock correction Δ_c:

This term is used to convert the local time measurements to the Terrestrial Time (TT) standard; an ideal clock placed on the geoid, i.e, the Earth surface at mean sea level. In practice, the correction is divided into several stages: the observatory time standard defined by a clock (usually rubidium clock or hydrogen maser) used to measure pulse arrival times is compared with the Universal Time Coordinate (UTC) broadcast by the Global Positioning System (GPS). The UTC is then reduced to the most stable long-term time scale available, the "Temps Atomique International" (TAI), a weighted average of hundreds of atomic clocks given by the Bureau International des Poids et Mesures (BIPM). The TT is finally obtained directly from TAI by adding a constant time. The TT is regularly refined in order to take into account for TAI instabilities and published by the BIPM (Guinot 1988). The most recent release up to October 2021 is TT(BIPM20).

- The Solar-system barycentric correction $\Delta_\odot$:

The ToAs at the telescope frame are transformed to correspond at the arrival time of the pulse wavefront at the quasi-inertial Solar-system barycenter (SSB), in order to correct any effect related to the Earth motion around the SSB, the Solar sytem spacetime curvature and the electron content of the interplanetary medium and the Earth atmosphere. This correction can be expressed as

$$\Delta_\odot = \Delta_A + \Delta_{G\odot} + \Delta_{D\odot} + \Delta_{E\odot} + \Delta_{S\odot}, \tag{1.7}$$

with

→ Δ_A, the atmospheric delay that comes from the radio wave dispersion and refraction in the ionized (ionosphere) and neutral (troposphere) layers of the Earth atmosphere.

→ $\Delta_{G\odot}$, The geometric vacuum delay (Observatory to SSB frame transformation) that compensates for the observatory motion around the SSB frame assuming a vacuum flat space. It is described with the Solar system Roemer delay $\Delta_{R\odot}$ and the annual parallax term Δp (related to the pulse spherical wavefront curvature) :

$$\Delta_{G\odot} = \Delta_{R\odot} + \Delta p, \tag{1.8}$$

The Solar-system Roemer delay is defined as the classical light travel time from the observatory to the SSB frame projected toward the pulsar's direction (Lorimer and Kramer 2004) :

$$\Delta_{R\odot} = -\frac{\vec{r} \,.\, \hat{R}_{BB}}{c}, \tag{1.9}$$

with $\vec{r}$, $\hat{R}_{BB}$ and c respectively the observatory position, the pulsar (or binary barycenter if the pulsar has a companion) position unit vector, usually expressed in SSB frame, and the speed of light. The vector $\vec{r}$ is in practice constructed as the sum of the observatory position in the geocentric frame $\vec{s}$ and the geocentre position in the SSB frame $\vec{r}_{\oplus}$:

$$\Delta_{R\odot} = -\frac{(\vec{s}+\vec{r}_{\oplus})\,.\,\hat{R}_{BB}}{c}, \tag{1.10}$$

The geocentre position $\vec{r}_{\oplus}$ is directly defined by a chosen Solar-system ephemeris (SSE) that gives informations on Solar-system body positions, velocities and masses. They are produced and shared by collaborations such as the french Institut de Mécanique Céleste et de Calcul des Éphémérides (IMCCE), the american Jet Propulsion Laboratory (JPL) or the russian Ephemerides of Planets and the Moon (EPM).

→ $\Delta_{D\odot}$, the dispersion due to the electron content present in the interplanetary medium which affects the pulsar radio signal. It mainly comes from the solar winds.

→ $\Delta_{E\odot}$, the Solar system Einstein delay due to the relativistic time dilation and the gravitational redshift induced by the Solar system objects.

→ $\Delta_{S\odot}$, the Solar system Shapiro delay caused by the spacetime curvature in the Solar system, for which the major contributions come from the Sun and Jupiter.

- The Interstellar medium correction Δ_{ISM}:

The ToAs expressed at the SSB are then subjected to a coordinate transformation to the pulsar frame. This term corrects for the secular distance variations between the pulsar and the SSB, and for the dispersion of the radio signals happening in the interstellar medium (ISM). The ISM dispersion delay of a ToA at the observed frequency f_{obs} can be expressed as

$$\Delta_{D_{ISM}} = \frac{k \times DM}{f_{obs}^2}, \tag{1.11}$$

where DM is the dispersion measure, defined as the integral of the column density of the electron between the reference frame and the pulsar, and $k \simeq 4.149 \times 10^3$ MHz^2 cm^3 pc^{-1} s is the dispersion constant.

- The binary correction Δ_B:

If the pulsar has a companion, which is the case for a good fraction of MSPs, one needs to correct for the geometric delay due to the orbital motion in the binary system and related relativistic effects. In other words, we need to transform the ToA from the binary

barycenter to the pulsar rest frame. The binary correction can be expressed as (Lorimer and Kramer 2004)

$$\Delta_B = \Delta_{RB} + \Delta_{SB} + \Delta_{EB} + \Delta_{AB}, \tag{1.12}$$

with

→ Δ_{RB}, the binary Roemer delay, similar to Solar system Roemer delay, but now to describe the orbital motion of the pulsar in the binary system.

→ Δ_{AB}, the aberration delay that takes into account the variation of the direction of the Earth seen from the pulsar, which affects the observed time of emission along the orbit of the pulsar in the binary system.

→ Δ_{SB}, the binary Shapiro delay due to the curvature of spacetime from the companion.

→ Δ_{EB}, the binary Einstein delay due to the relativistic time dilation and the gravitational redshift in the frame of the pulsar.

The Timing Model parameters

Technically, the Timing Model describes the pulsar spin frequency and the corrections detailed above by fitting parameters to the ToA dataset of a given pulsar. The fitted Timing Model parameters can be grouped as the following :

→ The *rotational parameters*, usually the spin frequency F0 and its first derivative F1, defined at a reference epoch.

→ The *astrometric parameters*, the pulsar position and proper motion at a reference epoch, given by the right ascension RA and declination DEC and their related proper motions PMRA and PMDEC. The positions are derived from the annual variation of the ToAs coming from the Solar system Roemer delay (see Eq. 1.9). Thus, the precision of the position parameters depends strongly on the ecliptic latitude of the pulsar because of the term $\vec{r}\,.\,\hat{R}_{BB}$. The proper motion is also measured from the Roemer delay component. A transverse component of the pulsar velocity related to the SSB might modify the term $\hat{R}_{BB}$, and induce a linear time-dependent trend in the Roemer delay. The annual parallax PX, related to the Δp correction (see Eq. 1.8), can also be evaluated for nearby pulsars.

→ The *dispersion measure parameters* are given by its constant value DM at a reference epoch and the its derivatives (DM1,DM2, ...). Note that the dispersion effect is related to the non homogeneous electron content between the pulsar and the Earth, which varies because their relative motions. Therefore, the dispersion measure variations can either (1) be treated during the timing procedure, with the “DMX“ parameters, that describe

the DM by dividing the total duration into time intervals, or (2) taken as a chromatic "red noise" signal (see Chapter 2), as it is always performed for the results presented in this manuscript.

→ The *orbital parameters*, formed by the Keplerian and post-Keplerian components of the pulsar binary system.

1.2.3 The timing procedure and timing residuals

In practice, only few Timing Model parameters are approximately known just after the discovery of a given pulsar. Building up an observational dataset over time allows to improve their accuracy and estimate other timing parameters. For instance, it is important to have a time span over one year in order to characterize components that are dependent to annual terms, such as the astrometric parameters.

The Timing Model parameters are evaluated using a least-square fitting procedure applied to match the set of the m observed ToAs to pulse numbers shown in Eq. 1.5 namely (Lorimer and Kramer 2004)

$$\chi^2 = \sum_{i=1}^{m} \left(\frac{N(t_i) - n_i}{\sigma_i} \right)^2, \tag{1.13}$$

where n_i is the nearest integer of $N(t_i)$, and σ_i is the uncertainty of the i-th ToA in units of pulse period.

This procedure is performed to obtain a phase-coherent TM solution that minimizes the differences between the observed ToAs and those predicted by the Timing Model, refered as *timing residuals* δt. If the Timing Model accurately describes all processes affecting the arrival times of the pulses, the weighted residuals $\delta t(t) \,/\, \sigma$ should follow a Normal distribution $\mathcal{N}(0,1)$. However, incorrect TM parameter values induce systematics in the post-fit timing residuals with specific structures (see Fig. 1.5). Several processes might not be captured by the Timing model and therefore the timing residuals still contain unmodelled signals, such as intrinsic pulsar red noise, variations of chromatic processes, systematics in the SSEs or very-low frequency gravitational waves. A next step of data analyis is then required in order to account for such processes.

The main software packages that allow to fit for the TM parameters and evaluate timing residuals are TEMPO2 (Hobbs et al. 2006) and (more recent) PINT (Luo et al. 2019). In this work, all timing residuals and TM parameters have been obtained using TEMPO2.

Instead of performing pulsar timing with ToAs, one can directly analyse and characterize signals from the timing observations. Usually referred as "profile domain" pulsar

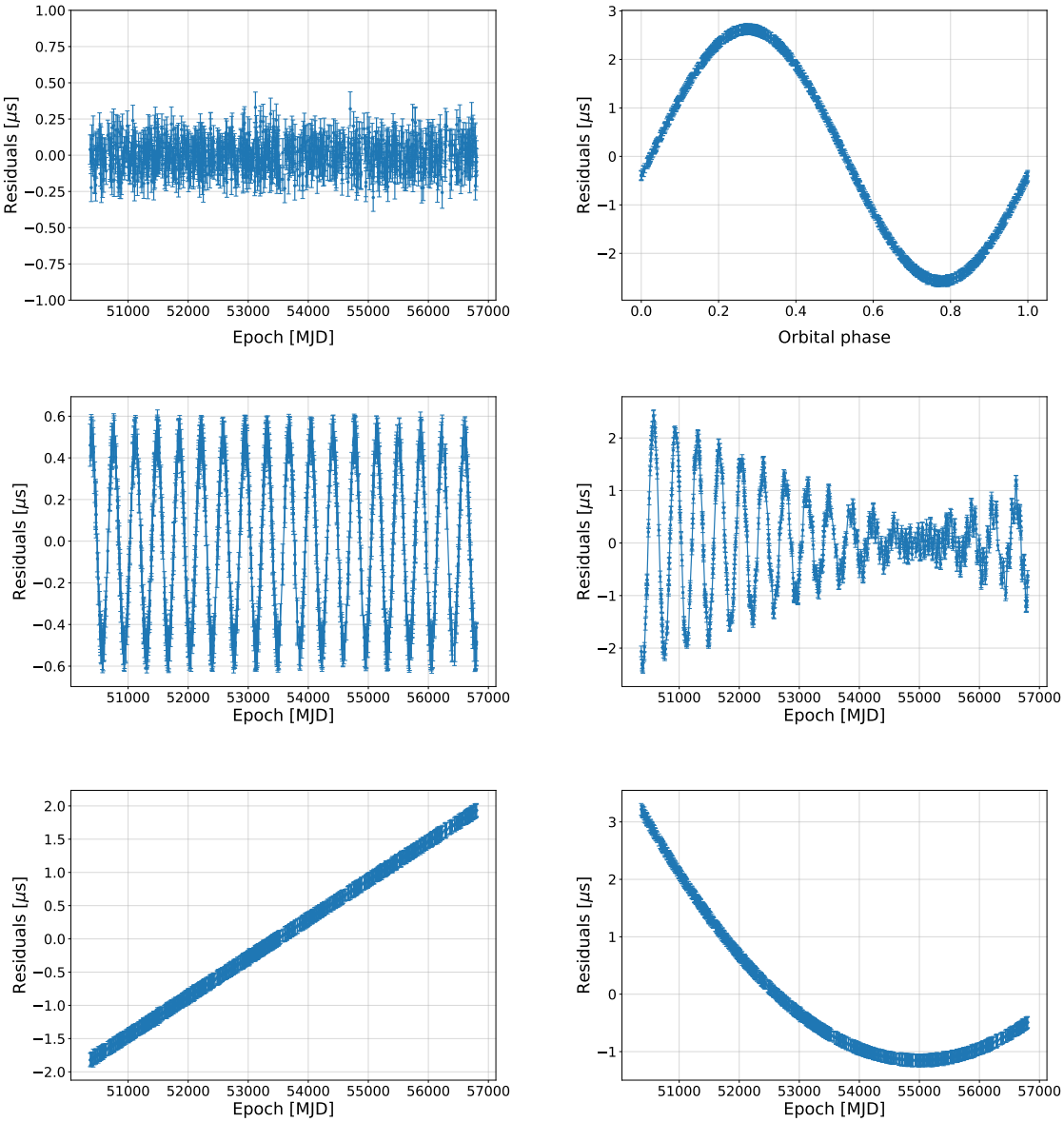

Figure 1.5: Simulated timing residuals for the case of (top left) a perfect TM fit, (top right) error in the projected semi-major axis A1, (second row left) error in positions RAJ and DECJ, (second row right) errors in proper motions PMRA and PMDEC, (lower left) error in frequency F0 and (lower right) error in the frequency derivative F1. The reference epochs for the position and frequency are both at MJD 55000.

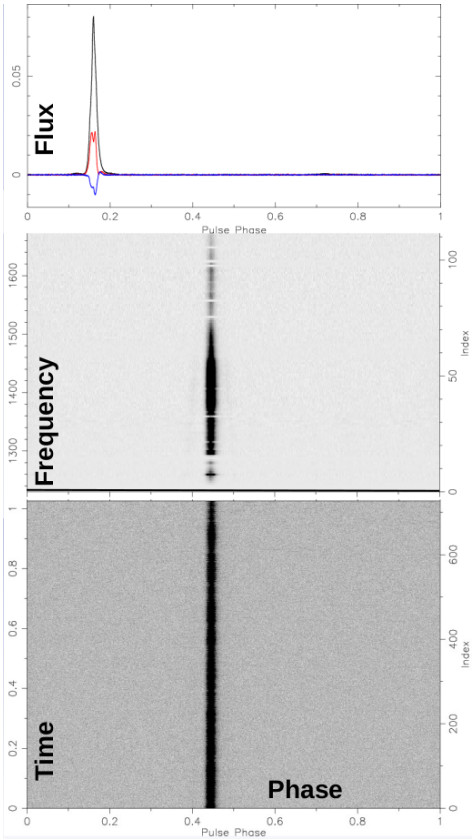

Figure 1.6: L-band observation of PSR J1909-3744 from the Nançay Radio Telescope.

timing (Lentati et al. 2015, Lentati and Shannon 2015, Lentati et al. 2017), such methods are however currently under development.

1.2.4 Application on PSR J1909-3744 with the NRT

Now that the pulsar timing procedure is described, we apply it to PSR J1909-3744 and detailed analysis is given below.

PSR J1909-3744 is a millisecond pulsar with a white dwarf companion. This MSP has been discovered in 2003 (Jacoby et al. 2003) from a survey applied with the Parkes 64-m Radio Telescope in Australia. It is one of the best-timed pulsars, with a timing precision at the level of hundreds of nano-seconds. Indeed, this relatively nearby ($\sim$ 1 kpc) pulsar has a spinning period at approximately 2.95 ms and a profile composed of a single narrow peak (see Fig. 1.6) with a full width at half maximum at about 43 μs ($<$ 1.5% of the phase). According to eq. (1.2), these properties allow to compute ToAs with high accuracy.

A study of this pulsar is published in Liu et al. 2020, which presents a precise timing analysis of this binary system with 15 years of data from the french Nançay Radio Telescope (NRT). For this work, I have participated in the process of the ToA creation, the

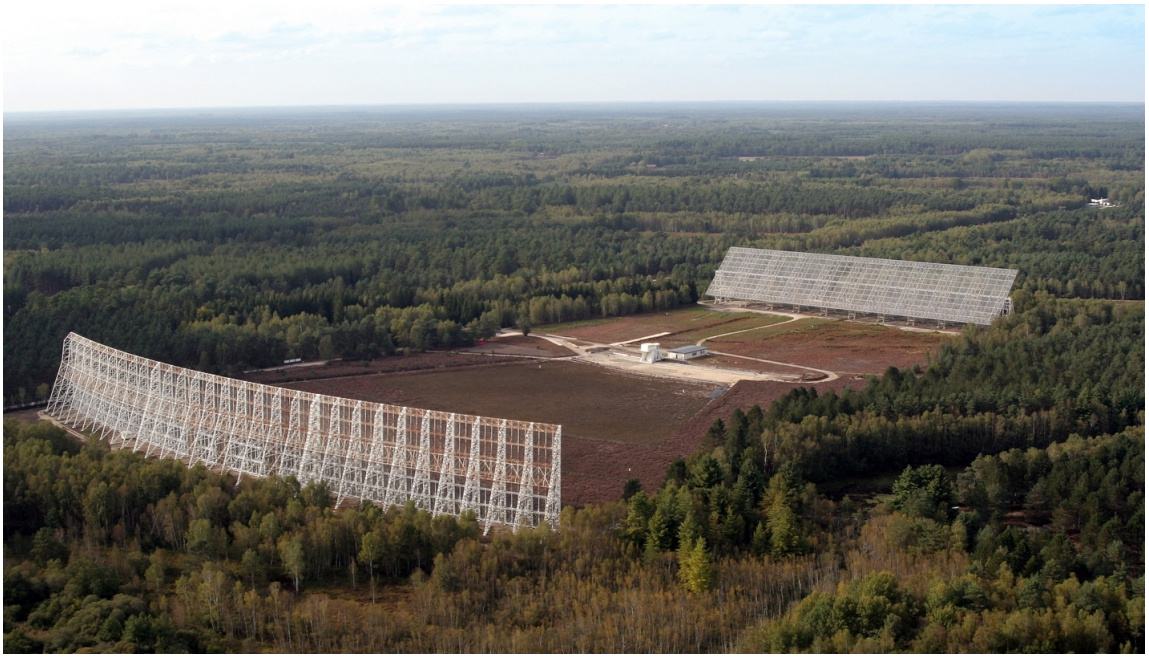

Figure 1.7: The Nançay Radio Telescope.

timing and noise analysis, and writing part of the paper. Let us first introduce the NRT and then present some results of that paper.

The Nançay Radio Telescope

The Nançay Radio Telescope is a meridian Kraus-type instrument inaugurated in 1967, with a flat primary mirror (200 m × 40 m panel at the right of Fig. 1.7) that reflects the radio signal coming from the sky at the meridian toward the spherical secondary mirror (300 m × 35 m spherical structure at the left of Fig. 1.7), which focuses the signal to the focal cart in the center of instrument. The 7000 m^2 collecting area makes it equivalent to a 94-m single dish. The rotating primary mirror permits to observe at all declinations over $-40°$ and the focal cart which carries the receivers can move over 100 m during the observations in order to compensate the Earth's rotation.

There are currently two receivers allowing to observe at L-band (1.1 – 1.8 GHz) and S-Band (1.7 – 3.5) GHz. The recent pulsar timing data from the NRT combines observations performed with two backends : BON (Berkeley-Orléans-Nançay) that observed from 2004 until 2014 with bandwidths of 64 and 128 MHz before and after July 2008, and NUPPI (The Nançay Ultimate Pulsar Processing Instrument) from August 2011 with a bandwidth at 512 MHz separated into 128 frequency channels.

Timing analysis of PSR J1909-3744

The dataset used in Liu et al. 2020 is constituted of 15 years (from December 2004 to September 2019) of weekly cadenced observations performed with both BON and NUPPI backends. The data is first reduced by (1) calibrating the polarizations, (2) applying radio frequency interference (RFI) mitigation methods and (3) removing the top and bottom 16 MHz frequency ranges that are affected by signal reflections in the receiver. In total, the timing dataset contains 615 L-band and 231 S-band ToAs, produced with the standard Fourier domain cross-correlation method Taylor 1992 for BON, and a 2D-Template matching method for NUPPI, using the Channelised Discrete Fourier Transform (CDFT) algorithm presented in Liu et al. 2014.

The timing analysis in this work extends the timing procedure detailed previously. The ToAs are modelled by the Timing Model and stochastic processes (described in details in Chapter 2) that are (1) the Gaussian white noise that corrects for possible errors in the ToA uncertainty evaluation, (2) the time-dependent DM variations and (3) the achromatic red noise that characterizes long-term signals that are independent of the observed radio frequency. The parameters of the TM and the stochastic models are simultaneously evaluated following Bayesian approach (see Section 1.4) with the software TEMPONEST (Lentati et al. 2014), which combines TEMPO2 and the nested sampler MULTINEST (Feroz et al. 2009). The stochastic parameters are also estimated with ENTERPRISE package (Ellis et al. 2019) for a cross check.

It is interesting to notice that the timing residuals before subtracting the stochastic noise signals (upper panel of Fig. 1.8) display a long term variation consistent with Arzoumanian et al. 2018b. The final "whitened" residuals shown in the lower panel of Fig. 1.8 yield to a timing precision of 103 ns weighted root mean square (rms), which is particularly notable for a 15 years of data. The measured and derived Timing Model parameters are shown in Table 1.1 with uncertainties relating to the 68% credible intervals of the 1D marginalized posteriors.

Among other results, the high quality timing analysis allowed to derive the masses of the MSP and white dwarf companion at $m_p = 1.492 \pm 0.014\ M_\odot$ and $m_{wd} = 0.209 \pm 0.001\ M_\odot$ from the measurement of the post-Keplerian parameters s ('shape') and r ('range') that are related with the binary Shapiro delay (see Section 1.2.2). Assuming General Relativity, they can be expressed as (Edwards et al. 2006) $s = \sin(i)$ and $r = G m_2 / c^3$, where i is the inclination orbit with respect to the line of sight and m_2 is the mass of the binary companion. The Figure 1.9 shows the nice consistency with the mass ratio obtained from optical observations of the white dwarf. Also, the orbital eccentricity evaluation $e = \sqrt{\kappa^2 + \eta^2} = (1.15 \pm 0.07) \times 10^{-7}$ is consistent with previous results (Manchester et al.

Table 1.1: Measured and derived timing parameters of PSR J1909-3744 (Liu et al. 2020).

Parameter	Value
MJD range	53368−58693
Number of TOAs	846
Timing residual rms (μs)	0.103
Reference epoch (MJD)	55000
Measured parameter	
Right ascension, α (J2000)	19:09:47.4335812(6)
Declination, δ (J2000)	−37:44:14.51566(2)
Proper motion in α, μ_α (mas yr^{-1})	−9.512(1)
Proper motion in δ, μ_δ (mas yr^{-1})	−35.782(5)
Parallax, π (mas)	0.861(13)
Spin frequency, ν (Hz)	339.315687218483(1)
Spin frequency derivative, $\dot{\nu}$	$-1.614795(7) \times 10^{-15}$
DM (cm^{-3} pc)	10.3928(3)
DM1 (cm^{-3} pc yr^{-1})	−0.00035(5)
DM2 (cm^{-3} pc yr^{-2})	$2.2(7) \times 10^{-5}$
Orbital period, $P_{\rm b}$ (d)	1.533449474305(5)
Epoch of ascending node (MJD), $T_{\rm asc}$	53113.950742009(5)
Projected semi-major axis, x (s)	1.89799111(3)
$\hat{x}$ component of the eccentricity, κ	$4.68(98) \times 10^{-8}$
$\hat{y}$ component of the eccentricity, η	$-1.05(5) \times 10^{-7}$
Orbital period derivative, $\dot{P}_{\rm b}$	$5.1087(13) \times 10^{-13}$
Derivative of x, $\dot{x}$	$-2.61(55) \times 10^{-16}$
Shape of Shapiro delay, s	0.998005(65)
Range of Shapiro delay, r (μs)	1.029(5)
Derived parameter (assuming GR)	
Galactic longitude, l (deg)	359.7
Galactic latitude, b (deg)	−19.6
Longitude of periastron, ω (deg)	156(5)
Orbital eccentricity, e	$1.15(7) \times 10^{-7}$
Pulsar mass, $m_{\rm p}$ ($M_\odot$)	1.492(14)
Companion mass, $m_{\rm c}$ ($M_\odot$)	0.209(1)
Parallax distance, d_π (kpc)	1.16(2)
kinematic distance, $d_{\rm k}$ (kpc)	1.158(3)
Spin period, P (ms)	2.94710806976663(1)
Spin period derivative, $\dot{P}$ ($\times 10^{-21}$)	14.02521(6)
$\dot{P}_{\rm Gal}$ ($\times 10^{-21}$)	0.0587(2)
$\dot{P}_{\rm Shk}$ ($\times 10^{-21}$)	11.36(3)
$\dot{P}_{\rm Int}$ ($\times 10^{-21}$)	2.60(3)
Characteristic age, $\tau_{\rm c}$ (Gyr)	18.0
Surface magnetic field, B (G)	8.9×10^7

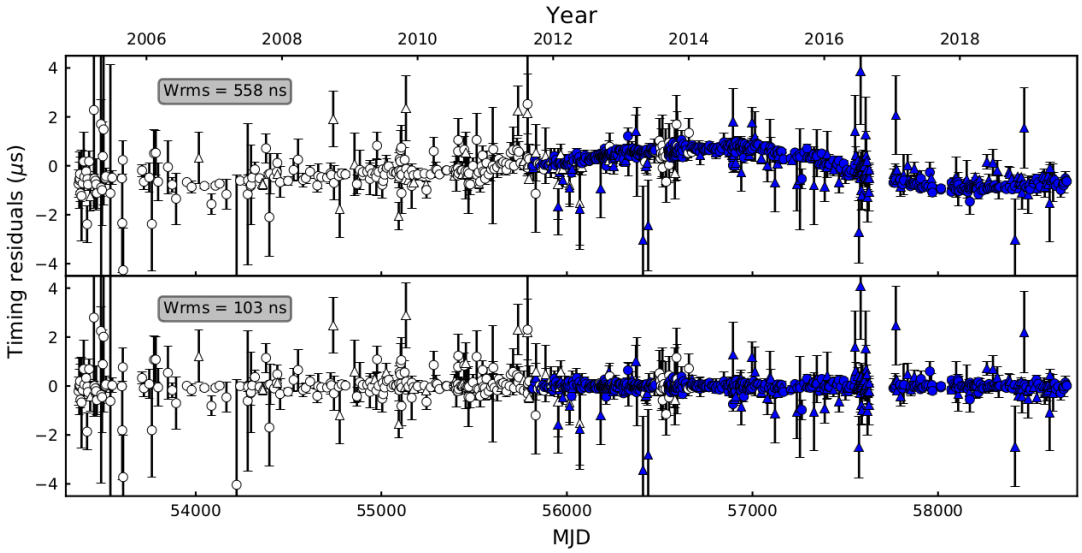

Figure 1.8: Timing residuals of PSR J1909-3744 (Liu et al. 2020) from NRT observations using BON (white) and NUPPI (blue) backends at L-band (circles) and S-band (triangles). The upper panel displays the residuals after fitting for the Timing Model parameters, and the lower panel shows the residuals after subtracting the evaluated stochastic noise delays.

2005), which confirms that PSR J1909-3755 is in the most circular pulsar binary system known so far. Finally, the orbital parameters obtained in this work shown in Table 1.2 appear to be in agreement with other pulsar timing studies on this pulsar.

1.3 Pulsar Timing Arrays

In General Relativity, the spacetime is curved and driven by its matter (mass-energy) content as formulated by Einstein equation. The dynamic aspect of spacetime naturally led Einstein to predict the existence of *gravitational waves* (Einstein 1918), that are 'ripples'

Table 1.2: Comparison of a selection of timing parameters measured in Liu et al. 2020 with previous publications. The values of orbital eccentricity e were calculated from two eccentricity vectors κ, η, except for the case of Reardon et al. 2016 where it was directly fitted for.

	π (mas)	$\dot{P}_b$	$\dot{x}$	$\sin i$	m_c ($M_\odot$)	e
Desvignes et al. 2016	0.87(2)	$5.03(5) \times 10^{-13}$	$-0.6(17) \times 10^{-16}$	0.99771(13)	0.213(2)	$1.22(11) \times 10^{-7}$
Reardon et al. 2016	0.81(3)	$5.03(6) \times 10^{-13}$	-	0.99811(16)	0.2067(19)	$1.14(10) \times 10^{-7}$
Arzoumanian et al. 2018b	0.92(3)	$5.02(5) \times 10^{-13}$	$-4.0(13) \times 10^{-16}$	0.99808(9)	0.208(2)	$1.16(12) \times 10^{-7}$
Perera et al. 2019	0.88(1)	$5.05(3) \times 10^{-13}$	$-3.9(7) \times 10^{-16}$	0.99807(6)	0.209(1)	$1.04(6) \times 10^{-7}$
Alam et al. 2021	0.88(2)	$5.09(3) \times 10^{-13}$	$-2.9(8) \times 10^{-16}$	0.99794(7)	0.210(2)	$1.10(9) \times 10^{-7}$
Liu et al. 2020	0.861(13)	$5.1087(13) \times 10^{-13}$	$-2.61(55) \times 10^{-16}$	0.998005(65)	0.209(1)	$1.15(6) \times 10^{-7}$

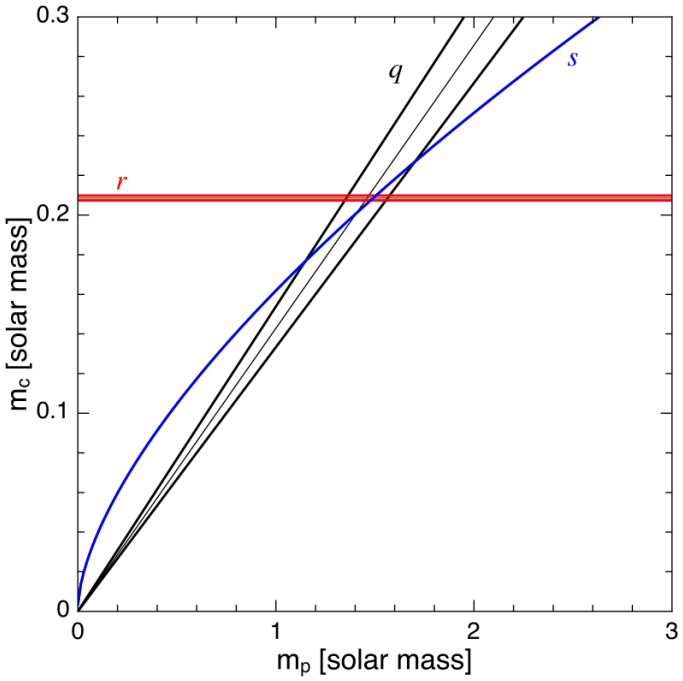

Figure 1.9: Mass–mass diagram of PSR J1909-3744 binary system (Liu et al. 2020). Constraints from r and s parameters are obtained from the pulsar timing analysis and q is obtained from optical observations of the white dwarf companion (Antoniadis 2013).

due to spacetime perturbations propagating at the speed of light.

The idea of detecting gravitational waves from pulsar timing measurements was first proposed in Sazhin 1978, following the method described in Estabrook and Wahlquist 1975 to detect GWs with Doppler spacecraft tracking, and elaborated by Detweiler 1979 who derived an upper-limit on the dimensionless GW amplitude of a stochastic gravitational wave background (GWB). In Hellings and Downs 1983, the correlations in the timing residuals induced by a GWB as function of the angular separation of pulsars in the sky have been formulated (See Chaper 2). The concept of Pulsar Timing Array (PTA), using a combined dataset of several pulsars to probe GWs has been developped in practice since the last years of the 20-th century (Romani 1988, Foster and Backer 1990, Backer 1995).

This part contains a brief discussion of the principle of detecting gravitational waves with a Pulsar Timing Array (PTA), followed by a review of the main expected sources, a brief discussion on PTA sensitivity and an overview of PTAs collaborations.

1.3.1 Detecting gravitational waves with a Pulsar Timing Array

The pulsar timing datasets of ultra-stable millisecond/recycled pulsars consist of decades of weekly cadenced measurements with a precision at the level of hundreds of nano-

seconds. The principle of PTAs is to utilize these measurements to detect very-low frequency (nHz - μHz) GWs that perturb the geodesics followed by the pulsated radio signals from the pulsar to the radio telescope, and therefore induce (long-term) delays on the timing residuals. For a pulsar with a spinning frequency at ν_0, the passage of GWs modulates the measured frequency $\nu(t_a)$, and generates a signal $\delta t_{\rm GW}$ in the timing residuals as (Detweiler 1979)

$$\delta t_{\rm GW}(t_a) = \int_{t_e}^{t_a} \frac{\nu(t') - \nu_0}{\nu_0} dt' = \int_{t_e}^{t_a} \frac{\delta\nu}{\nu_0}(t') dt', \tag{1.14}$$

with t_e and t_a the emission and reception times of the the radio pulses.

If the gravitational wave comes from the direction $\hat{k}$, the term $\delta\nu/\nu_0$ for a pulsar α with a sky position unit vector $\hat{n}_\alpha$ can be expressed as (Anholm et al. 2009)

$$\frac{\delta\nu}{\nu_0} = \frac{\hat{n}^i_\alpha \hat{n}^j_\alpha}{2\,(1 + \hat{n}_\alpha.\hat{k})} \Delta h_{ij}, \tag{1.15}$$

where Δh_{ij} is the difference between the GW characteristic strain at t_e and t_a, respectively defined as the pulsar term $h_{ij}(t_e)$ and the Earth term $h_{ij}(t_a)$, thus

$$\Delta h_{ij} = h_{ij}(t_e) - h_{ij}(t_a), \tag{1.16}$$

And the emission and reception times are related such as

$$t_e = t_a - \frac{L_\alpha}{c}(1 + \hat{n}_\alpha.\hat{k}), \tag{1.17}$$

with L_α the distance between the Earth and the pulsar.

The hunted signal in the residuals depends on the relative sky positions of the GW source and the pulsar, and on the distance between the Earth and the pulsar which is usually of the order of few kilo-parsecs (kpc; $\sim$ 10000 light-years). This means that the pulsar term imprints the GWs emitted tens of thousands of years earlier relative to the Earth term.

In practice, a GW signal cannot be distinguished from intrinsic signals of the pulsar such as stochastic variations of its spin due to internal processes. The idea behind PTAs is to combine of a full array of pulsars and probe for the correlated signals. It is important to note that unlike the pulsar terms, the Earth terms are correlated across all pulsars. For this case, the difference between the signals in timing residuals of two pulsars only depends on their angular separation in the sky.

In summary, PTAs are galactic-sized multi-arm GW dectectors that use (typically tens) MSPs as clocks for which one measures variations on the regularity of the pulse arrival time. To give an idea, the characteristic precision of PTA from a dataset with a time span T = 20 year, a one-week cadence (ΔT) and a timing precision δt = 100 ns can be evaluated as $dt/\mathrm{T} \sim 1.6 \times 10^{-16}$ in dimensionless amplitude, with an observable frequency range at $\Delta f = [1/\mathrm{T} - 1/\Delta\mathrm{T}] \sim \left[10^{-9} - 10^{-6}\right]$ Hz.

1.3.2 GW sources at very-low frequencies

Several sources are expected to emmit GWs in the frequency range of PTAs. Some of the signals are *deterministic*, meaning that the signal $\delta t_{\rm GW}$ expressed in Eq. 1.14 can be exactly calculated from the characteristic strain $h(t)$ related to the source. Alternatively, we could expect *stochastic* (noise-like) GW signals that could be produced either during energetic processes in the early universe or as a superposition of many weak individual (monochromatic) signals. Let us now briefly review different sources seeked by PTAs.

The inspiralling supermassive black hole binaries

The most promising GW sources observable with PTAs are the inspiralling supermassive ($\geq 10^7$ $M_\odot$) black hole binaries (SMBHBs) located at the center of nearby ($z \leq 2$) galaxies. These binary systems are formed by the mergers of galaxies that occur during the history of the Universe.

The nearest and most massive SMBHBs could be seen as continuous GW sources, producing deterministic signals in the data (top right of Fig. 1.10). At PTA frequencies ($10^{-9} - 10^{-6}$ Hz), the detectable systems would have orbital periods of order $\sim 0.1 - 10$ years[5], emitting quasi-monochromatic GWs within the time span of PTA datasets. A detection of continuous waves would permit to characterize properties of sources such as the sky location, the orbital eccentricity, the chirp mass[6] and the luminosity distance. The disentanglement of the last two parameters is in practice challenging and could be achieved either through an independent measurement of the SMBHB distance (e.g., via the distance to the host galaxy), or exploiting the waveform evolution in time, e.g., comparing one or several pulsar terms with the Earth term (see Section 1.3.1) that each correspond to different moment in the system orbital evolution.

Other possible deterministic processes produced by SMBHBs are short-lived GW signals often referred to as GW bursts. For instance, a close encounter of two supermassive black holes would cause a generic burst that might induce a transient effect (~ weeks - months) in the timing residuals (bottom right of Fig. 1.10). Moreover, the merger of a SMBHB might produce a sudden (less than one day; Favata 2010) GW burst with a permanent change of the spacetime metric after the event named burst with memory (Blanchet and Damour 1992). As shown in the bottom left panel of Fig. 1.10, such signal yields to a linear trend that begins at the event epoch (here at day 1500) in the timing residuals,

[5]The frequency of GWs emitted by a circular and GW-driven SMBHB system is equal to twice the orbital frequency.

[6]For a binary system with masses m_1 and m_2, the chirp mass $\mathcal{M}$ is an effective mass derivable from GW measurement and defined as $\mathcal{M} = (m_1\ m_2)^{3/5}\ /\ (m_1 + m_2)^{1/5}$.

due to the different configuration of the metric that is not taken in account by the timing model. The quadratic shaped post-fit residuals (bottom sub-panel) are caused by the inaccurate fit of the pulsar spin and spin derivative parameters affected by the burst signal.

The superposition of all signals from a population of SMBHBs forms a stochastic gravitational wave background (GWB ; top left of Fig. 1.10) that is considered to be the main candidate for detection with PTAs (Rajagopal and Romani 1995, Sesana et al. 2008). The inspiral of SMBHBs get faster as the orbital separation decreases. Therefore, the related spectrum is expected to display higher power at lower frequencies, where most systems are located. For a simplified population of circular and GW-driven orbits, the derived strain using the GW quadrupole formula follows a simple powerlaw $h(f) \propto f^{-2/3}$ (Jaffe and Backer 2003, Chen et al. 2017). Contrary to circular systems, the GW power induced by an eccentric binary is distributed over multiples harmonics of the orbital frequency. With such systems in the population of SMBHBs, part of the power of the stochastic background at the lowest frequencies is therefore shifted to higher frequencies, causing a turnover in the related spectrum. The perturbations of SMBHB orbits via the interactions with the surrounding environment (stars in the core of the host galaxy, circumbinary gaseous disk) are expected to reduce GW power at lower frequencies, but to increase in the orbital energy dissipation and accelerating the orbital evolution. The probability for the presence of a single bright source rising over the total background increases at higher frequencies, making this frequency range attractive for continuous wave searches. Finally, in case of bright but unresolvable single sources, or an excesses of SMBHB in specific regions in the sky (e.g., galaxy clusters), the GWB sky distribution would be anisotropic. We only consider the isotropic component of GWB in this thesis.

Other sources

Besides the GWs from SMBHBs, which are the main focus of this work, we mention briefly other GW sources in the PTA band.

The cosmic strings are one-dimensional macroscopic topological defects that would be produced in the early Universe from phase transitions. After these, a network of cosmic strings would then evolve in time, with interconnections and self-intersections of strings, producing loops that would oscillate and decay via GW emission (Ölmez et al. 2010). Cosmic superstrings predicted from string theory would also produce GWs with similar mechanisms. A stochastic GWB coming from the addition of all sources is expected to contains a flat part at higher frequencies (from loops decaying during the radiation era) and broad peak at lower frequencies (from loops decaying during the radiation-to-matter era transition and the matter era). Cosmic (super)strings are also expected to emmit GW bursts from bend and reconnection mechanisms such as cusps and kinks (Damour and

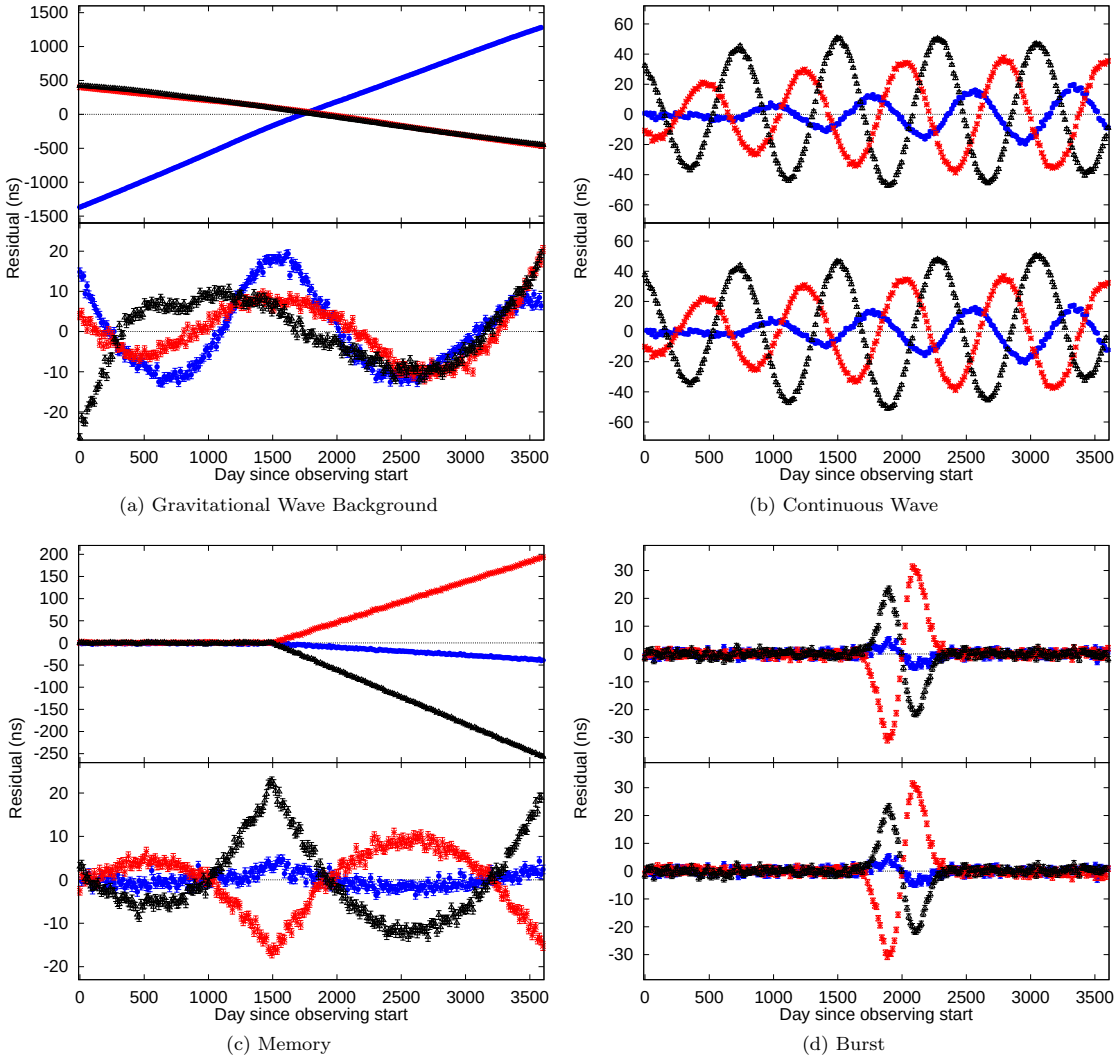

(a) Gravitational Wave Background

(b) Continuous Wave

(c) Memory

(d) Burst

Figure 1.10: Simulated pulsar timing residuals before and after fitting for the TM parameters (resp. top and bottom of each sub-panel) for three pulsars with different sky locations (black, blue and red) that contains signals from (a) a GWB from a SMHBH population, (b) a single SMBHB system, (c) a burst with memory and (d) a generic (Gaussian) burst (from Burke-Spolaor 2015).

Vilenkin 2001, Key and Cornish 2009).

There are other sources expected to emmit GWs in PTA band such as quantum space-time fluctuations at the early stage of the Universe that are amplified by the inflation (Grishchuk 1976, Fabbri and Pollock 1983), or magnetohydrodynamic processes happening at the quantum chromodynamics phase transition (Neronov et al. 2021), which would both produce a stochastic GWB.

1.3.3 Assessing the detectability of GWs with PTAs

Let us now explore the time evolution of the signal-to-noise ratio (S/N) for different types of signals. In this part, we only focus on GWs produced from inspiralling SMBHBs with PTAs.

The S/N of a deterministic GW signal from a circular SMBHB ($\rho_{\rm CW}$) with an amplitude $A_{\rm CW}$ emitted at frequency $f_{\rm CW}$ using an array of M identical MSPs, all observed with a uniform cadence Δt for a total time span T, assuming white noise only (i.e., with a constant power for all frequencies ; see Chapter 2) and considering only the Earth term, can be derived as (Perrodin and Sesana 2018)

$$\rho_{\rm CW} \propto \frac{A_{\rm CW}}{\sigma f_{\rm CW}} \left(\frac{T}{\Delta t} M \right)^{1/2},$$

where σ is the rms of the timing residuals (see Section 1.2.3).

Therefore, the S/N for a single SMBHB increases linearly with the emitted amplitude and decreases linearly with the residuals rms and the GW frequency. Conversely, $\rho_{\rm CW}$ is proportionnal to the square root of the observational time span, the number of pulsars in the array, and the inverse of the observing cadence. Note that the choice of white noise only is relevant since we expect this noise to dominate at high GW frequencies, where the probability of having a single source rising over the background is maximal.

In this thesis, we focus on the stochastic GWB produced by the population of SMBHBs in the local Universe. In the same way as above, we assume only white noise and the GWB to be present in the data. As discussed in Chapter 3, the smoking gun of a GWB detection is given by the Hellings-Downs correlation function that only depends on the angular separation between each pair of MSPs in the case of an isotropic GWB. The S/N of the GWB, $\rho_{\rm GWB}$, can be derived through the evaluation of the cross-correlated power in MSPs. Assume an array composed of M equal pulsars, all observed with a cadence Δt during the total time span T and a timing precision σ, let us consider the expectation value of the S/N $\langle \rho_{\rm GWB} \rangle$ for a GWB signal modelled as a powerlaw power spectral density (see Chapter 2) with a spectral index $\gamma_{\rm GWB}$ and an amplitude $A_{\rm GWB}$ set at $f = 1\ \mathrm{yr}^{-1}$. In the

weak signal regime (GWB spectrum fully under the white noise), the S/N scales with time as (Siemens et al. 2013)

$$\langle \rho_{\rm GWB} \rangle_l \propto M \left(\frac{A_{\rm GWB}}{\sigma \sqrt{\Delta t}} \right)^2 T^{\gamma_{\rm GWB}}. \tag{1.18}$$

Hence, at the low-S/N regime, $\langle \rho_{\rm GWB} \rangle_l$ increases linearly with the number of pulsars and the inverse of the observing cadence, quadratically with the GWB amplitude and the timing residual rms. It is proportional to $T^{\gamma_{\rm GWB}}$, where $\gamma_{\rm GWB} = 13/3$ in case of an idealistic population of circular and GW-driven SMBHBs.

At the intermediate S/N regime (with low frequencies of the GWB spectrum over the white noise level, but highest frequencies below), the average S/N can be written as

$$\langle \rho_{\rm GWB} \rangle_i \propto M \left(\frac{A_{\rm GWB}}{\sigma \sqrt{\Delta t}} \right)^{1/\gamma_{\rm GWB}} T^{1/2}. \tag{1.19}$$

In this case, the S/N has weaker dependence on the GWB amplitude, the cadence and the timing residual rms. Moreover, it is now proportional to the square root of the total duration of observations. The number of pulsars in the array has now the biggest impact on the S/N, with a linear dependence. Given the current timing precision and GWB signal constraints (see Chapter 3), the strong S/N regime (where the signal is all over the white noise) is not realistic and therefore not considered here.

Note that this scaling of S/N has to be taken carefully since only white noise have been involved, while other noise become important at the lowest frequencies (see Chapter 2), which might impact significantly the actual S/N for the GWB. It is also possible to derive scaling laws for more complex GWB spectrum (see e.g., Vigeland and Siemens 2016).

1.3.4 PTAs in the GW landscape

The gravitational waves are also probed at higher frequencies, with different types of detectors that are summarized just below.

→ **The gound-based laser interferometers**:

The ground-based laser interferometers observe gravitational waves at frequencies from 1 to 10^3 Hz (see Fig. 1.11). A laser beam is split into two parts that travel back and forth in two perpendicular four km long arms. The lasers beams are then recombined at the beam splitter and sent to a photodiode. The passage of a GW modifies differently the size of each arms, leading to a phase difference between the two lasers and thus changing the interference pattern at the detector output. The first direct observation of gravitational waves has been accomplished by the two American detectors, the

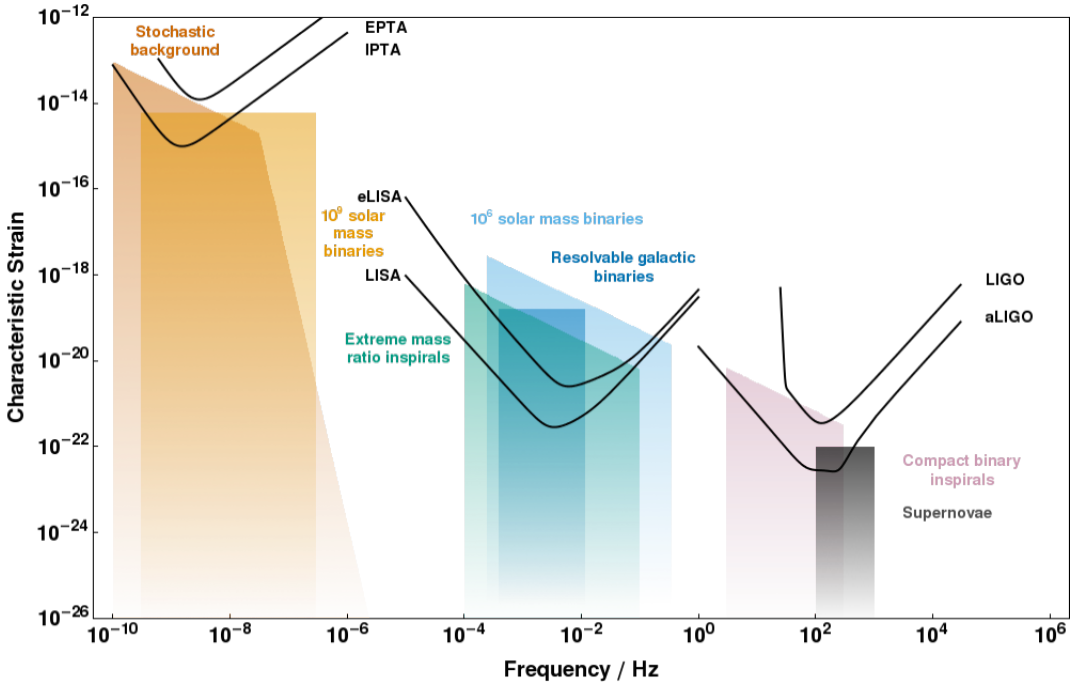

Figure 1.11: The gravitational wave spectrum with the related sources and detectors (from Moore et al. 2014).

Laser Interferometer Gravitational-Wave Observatory (LIGO). The detected signal corresponds to the coalescence of two stellar mass ($\sim 30\ M_\odot$) black holes (Abbott et al. 2016). Since this historic event, three joint observational runs with the European Virgo detector have permitted to detect more than 50 other signals from the coalescence of stellar mass systems (black holes and/or neutron stars). The observational runs are alternated by upgrade phases to improve the sensitivity. Other detectors such as KAGRA in Japan or the future LIGO-India will also join the future observation runs.

→ **The space-based interferometers**:

The Laser Interferometer Space Antenna (LISA) is a future space-based detector planned for launch in 2034 composed of three spacecrafts exchanging laser signals, forming an interferometer of triangle shape with an arm length of 2.5 million kilometers. It will operate in the frequency range $\left[10^{-4} - 10^{-1}\right]$] Hz (see Fig. 1.11), and aims at detecting signals from Galactic low-mass binary systems (for instance composed of two white dwarfs), the coalescence of massive black hole binaries or Extreme Mass Ratio Inspiral (EMRI), formed by a stellar mass object orbiting around a massive black hole. LISA will also study GW backgrounds formed by population of Galactic, extra-Galactic and cosmological sources.

1.3.5 The Pulsar Timing Array collaborations

The detection of gravitational waves with PTA is a long-term task. Each pulsar is observed over many years at different radio frequencies with telescopes that are subject to regular updates. It is also important to combine pulsars that cover an optimal part of the sky in order to probe the presence of spatial correlations. There are several collaborations that time pulsars and work toward the detection of the very-low frequency GWs with PTA (see Fig. 1.12):

→ **The Parkes Pulsar Timing Array** (PPTA) is the Australian project formed in 2004 as a collaboration between Commonwealth Scientific and Industrial Research Organisation (CSIRO) Astronomy and Space Science and Swinburne University of Technology. The main instrument is the 64-m single dish Parkes Radio Telescope.

→ **The European Pulsar Timing Array** (EPTA) is the European collaboration officially established in 2006, connecting groups from France, Germany, Italy, Netherlands and United Kingdom. The EPTA data are collected from the Effelsberg 100-m radio telescope, the Nançay Radio Telescope, the Lovell Telescope at Jodrell Bank Observatory (JBO), the Westerbork Synthesis Radio Telescope (WSRT) and the Sardina Radio Telescope. The Large European Array of Pulsars (LEAP) program also permit to simultaneously time pulsars with a monthly cadence by using a combination of the five radio telescopes as a tied-array telescope (Bassa et al. 2016).

→ **The North American Nanohertz Observatory for Gravitational Waves** (NANOGrav), founded in 2007, is now made of more than 40 institutions in the United States of America and Canada. The two contributor instruments are Green Bank Telescope, and Arecibo Radio Telescope which has been decommissioned because of critical damages happening in late-2020. The Very Large Array and the Canadian Hydrogen Intensity Mapping Experiment (CHIME) are also expected to participate to the pulsar timing datasets.

→ **The Indian Pulsar Timing Array** (InPTA) is the Indian collaboration formally set up in 2019. It combines research groups from the National Centre for Radio Astrophysics, the Tata Institute of Fundamental Research, the Raman Research Institute in India, the Indian Institute of Technology Hyderabad and the Indian Institute of Mathematical Sciences. The instruments are the Ooty Radio Telescope and the upgraded Giant Metrewave Radio Telescope (uGMRT).

→ **MeerKAT** is a South African radio telescope launched in 2018 which comprises 64 13.5-m dishes, and has an total effective area of 9000 m^2. About 60% of the antennas are located in a 1 km diameter circle, and the rest are located around, allowing a maximum baseline of 8 km. It is one of the precursors of the ambitious Square Kilometer Array radio

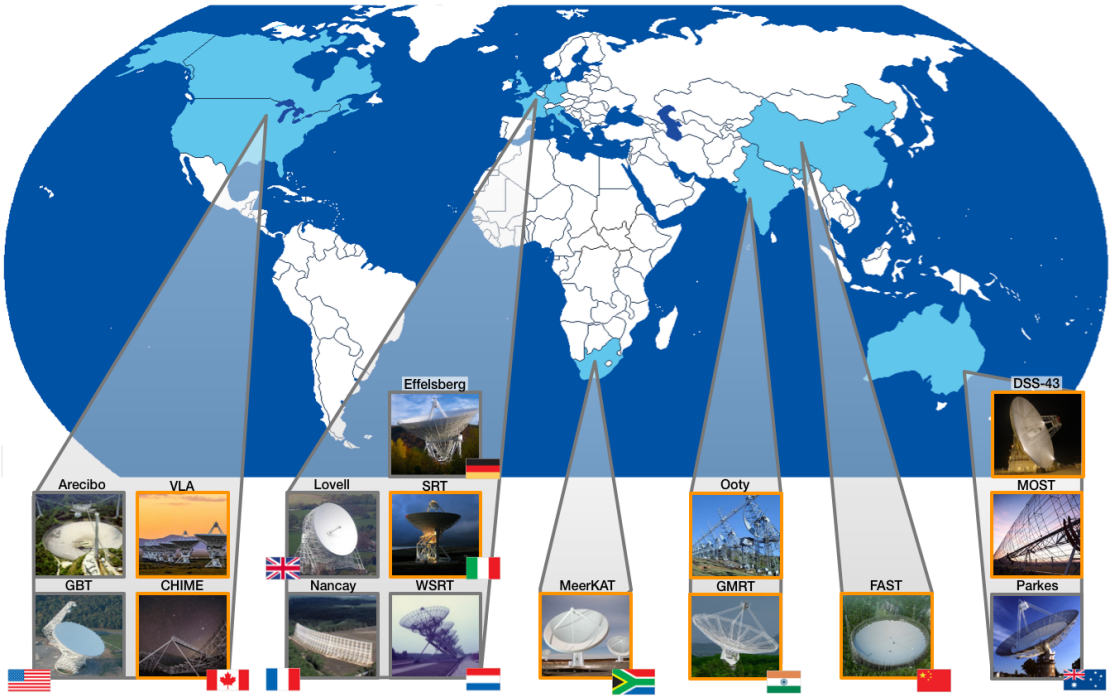

Figure 1.12: The Pulsar Timing Arrays around the world in 2021 (from NANOGrav website[7]). Note that Arecibo radio telescope sadly broke in late-2020.

telescope that is planned to be held in Australia and South Africa. The MeerKAT radio telescope performs timing of over 1000 pulsars (189 MSPs) with very high quality data following the MeerTime project programmed for five years (Bailes et al. 2018) launched since ~ 3 years ago.

→ **The Chinese Pulsar Timing Array** (CPTA) is a Chinese collaboration which is in a process of formation. The main instrument is the Five-hundred-meter Aperture Spherical radio Telescope (FAST) which is officially operating since early-2020. Whereas the 110-m Qitai Radio Telescope and the Jingdong 120-m Pulsar Radio Telescope are both planned to be built in the upcoming years.

→ **The International Pulsar Timing Array** (IPTA) is the consortium of consortia originally formed by EPTA, PPTA and NANOGrav, and joined by the InPTA in early-2021. The main idea behind IPTA is to combine the data from all PTAs and coordinate the worldwide effort on searching for low-frequency GWs.

[7] https://nanograv.github.io/optimalobs/

1.4 Bayesian framework

The data analyses techniques applied to the single-pulsar model selection (Chapter 2), the search of a GWB (Chapter 3) and the study of the impact of Solar system ephemeris errors on GWB searches (Chapter 4) are all performed within a Bayesian framework. This section introduces this framework and describes the methods, the software and the statistical tools used to produce the results in the next chapters.

1.4.1 Basic concepts and methods

The data analyses carried in this thesis are based on a statistical Bayesian approach, where we aim at evaluating noise and signals in the data that are described by parametrized models. In Bayesian inference, the parameters are (1) considered as random variables and (2) evaluated using a priori knowledge, through the parameter priors.

We use conditional probabilities to infer parameter probability distributions (i.e., posteriors) given the data and parameter prior distributions, this is refered as *parameter estimation*. The Bayesian framework also permits to perform *model selection*, where we determine which model is favored by the data among different candidates. Let us now formulate the different quantities and describe the methods chosen to perform the model selection in this thesis.

→ The parameter estimation

The Bayes (or Bayes-Price) theorem (Bayes and Price 1763, Laplace 1812, Kolmogorov 1960) permits to formulate the probability distribution of the parameters $\vec{\theta}_a$ given the observed data (timing residuals in our case) $\vec{\delta t}$ and the model $\mathcal{M}_a$, called posterior distribution, as :

$$\begin{aligned} \mathrm{P}(\vec{\theta}_a|\vec{\delta t},\mathcal{M}_a) &= \frac{\mathrm{P}(\vec{\delta t}|\vec{\theta}_a,\mathcal{M}_a)\ \mathrm{P}(\vec{\theta}_a|\mathcal{M}_a)}{\mathrm{P}(\vec{\delta t}|\mathcal{M}_a)} \\ &= \frac{\mathcal{L}(\vec{\delta t}|\vec{\theta}_a,\mathcal{M}_a)\ \pi(\vec{\theta}_a|\mathcal{M}_a)}{\mathcal{Z}_{\mathcal{M}_a}}, \end{aligned} \tag{1.20}$$

where

- $\mathcal{L}(\vec{\delta t}|\vec{\theta}_a,\mathcal{M}_a)$ is the *likelihood* function of observing $\vec{\delta t}$ given the set of parameters $\vec{\theta}_a$ of the model $\mathcal{M}_a$. Its computation for PTA is detailed in Section 2.3.1.
- $\pi(\vec{\theta}_a|\mathcal{M}_a)$ is the *parameter priors*, the probability distributions of $\vec{\theta}_a$ given $\mathcal{M}_a$ and any knowledge prior to observations.

- $\mathcal{Z}_{\mathcal{M}_a}$ is the *evidence* (or marginal likelihood) associated with $\mathcal{M}_a$, the probability of observing $\vec{\delta t}$ assuming that model $\mathcal{M}_a$ is the correct one. It is often presented as a normalization constant and neglected but it plays a key role in model selection.

Here, the subscript a enumerates the models.

→ The model selection

The Chapter 2 focuses on the noise model selection for each pulsar, with an objective to find the most favored model given the observed data. The probability of a particular model $\mathcal{M}_a$ given $\vec{\delta t}$ is expressed from the Bayes theorem

$$\mathrm{P}(\mathcal{M}_a|\vec{\delta t}) = \frac{\mathrm{P}(\vec{\delta t}|\mathcal{M}_a)\ \mathrm{P}(\mathcal{M}_a)}{\mathrm{P}(\vec{\delta t})} = \frac{\mathcal{Z}_{\mathcal{M}_a}\ \pi_{\mathcal{M}_a}}{\mathrm{P}(\vec{\delta t})}, \tag{1.21}$$

where $\mathcal{Z}_{\mathcal{M}_a}$ is the model evidence, $\pi_{\mathcal{M}_a}$ is the model prior and $\mathrm{P}(\vec{\delta t}) = \sum_b \mathrm{P}(\vec{\delta t}|\mathcal{M}_b)\ \pi_{\mathcal{M}_b}$, the probability of the observed dataset.

Note that the computation of $\mathrm{P}(\vec{\delta t})$ requires to marginalize (i.e., sum up) the quantity $\mathrm{P}(\vec{\delta t}|\mathcal{M}_a)$ over every possible models $\mathcal{M}_a$, which is often unrealizable. For the study in Chapter 2, we have used previously published results as a guidance for selecting models for a given pulsar assuming that all considered models have equal probability (prior) $\mathcal{Z}_{\mathcal{M}_a}$ unless otherwise specified. The model selection between two models $\mathcal{M}_a$ and $\mathcal{M}_b$ is based on the *posterior odds ratio*:

$$\frac{\mathrm{P}(\mathcal{M}_a|\vec{\delta t})}{\mathrm{P}(\mathcal{M}_b|\vec{\delta t})} = \frac{\mathcal{Z}_{\mathcal{M}_a}}{\mathcal{Z}_{\mathcal{M}_b}}\frac{\pi_{\mathcal{M}_a}}{\pi_{\mathcal{M}_b}}, \tag{1.22}$$

Since we use equal (non-informative) priors, the odds ratio reduces to the Bayes factor $\mathcal{B}^{\mathcal{M}_a}_{\mathcal{M}_b} = \mathcal{Z}_{\mathcal{M}_a}/\mathcal{Z}_{\mathcal{M}_b}$ (Gelman et al. 2004).

In order to calculate $\mathcal{B}^{\mathcal{M}_1}_{\mathcal{M}_2}$, one can express the evidence of a given model as a fully marginalized posterior (Sivia and Skilling 2006):

$$\begin{aligned}\mathcal{Z}_{\mathcal{M}_a} = \mathrm{P}(\vec{\delta t}|\mathcal{M}_a) &= \int d\vec{\theta}_a\ \mathrm{P}(\vec{\delta t}|\vec{\theta}_a,\mathcal{M}_a)\ \mathrm{P}(\vec{\theta}_a|\mathcal{M}_a) \\ &= \int d\vec{\theta}_a\ \mathcal{L}(\vec{\delta t}|\vec{\theta}_a,\mathcal{M}_a)\ \pi(\vec{\theta}_a|\mathcal{M}_a),\end{aligned} \tag{1.23}$$

As we involve multi-dimensional parameter spaces, this integral is hard to calculate and requires numerical algorithms such as nested samplers (see the next subsection).

An alternative method called product-space (or hyper-model) is also used to obtain Bayes factors without evidence evaluation. It has been proposed in Carlin and Chib 1995,

extended in Hee et al. 2015 and applied in Taylor et al. 2020. In this approach we sample models and their corresponding parameters using a hyper-parameter that switches between the models.

The decisions for the model selection in Chapter 2 are based on the scale proposed in Jeffreys 1961, that is $\mathcal{B}^{\mathcal{M}_a}_{\mathcal{M}_b} > 100$ indicates a preference for the model $\mathcal{M}_a$ against $\mathcal{M}_b$ with 'decisive' evidence. This interpretation criteria has been set phenomenologically, and revised in Kass and Raftery 1995, which suggests using a threshold value 150 ($\log_{10}\mathcal{B}^{\mathcal{M}_a}_{\mathcal{M}_b} \gtrsim 2.2$). Therefore, we use the range $2 < |\log_{10}\mathcal{B}^{\mathcal{M}_a}_{\mathcal{M}_b}| < 2.2$ as a selection criteria. In case of the non-conclusive Bayes factor we follow Occam principle and select the model with the lowest prior volume (or computational cost).

1.4.2 Data sampling techniques and software

The Bayesian analyses mentionned in this manuscript are carried through numerical evaluation appoaches. The likelihood and parameter posteriors are evaluated with ENTERPRISE package (Ellis et al. 2019).

The parameter estimation is also conducted with Markov chain Monte Carlo (MCMC ; Gilks et al. 1995) sampler software, PTMCMCSAMPLER (Ellis and Haasteren 2017) and MC^3 (`https://gitlab.in2p3.fr/stas/samplermcmc`), both based on Metropolis-Hastings algorithms (Metropolis et al. 1953, Hastings 1970). We perform analyses with the former that is widely used for PTA data analyses as a standard MCMC, with a (long) single chain. The latter is a sampler that runs several chains independently, which permits convergence checks.

The Bayes factors calculated through the ratio of evidences are estimated with the nested algorithms (Skilling 2004, Skilling 2006). They are evaluated either with DYNESTY (Speagle 2020) package in Chapter 2 and Section 3.4, or with MULTINEST (Feroz et al. 2009) or POLYCHORD (Handley et al. 2015) in Section 3.3. The product-space approach is applied with the "Hypermodel" class implemented in ENTERPRISE_EXTENSIONS (`https://github.com/nanograv/enterprise_extensions`) package and used in Chapters 2 and 3.

The following software packages are used to produce the results and figures in this manuscript: NUMPY (Walt et al. 2011), SCIPY (Oliphant 2007), MATPLOTLIB (Hunter 2007), CORNER (Foreman-Mackey 2016), LA FORGE (`https://github.com/Hazboun6/la_forge`) and OUTLIER-UTILS (`https://github.com/c-bata/outlier-utils`).

1.4.3 Statistical tools

→ The Jensen-Shannon divergence

The Jensen-Shannon divergence (JSD ; (Manning and Schütze 1999)), or information radius, is used to compare two posterior distributions. JSD($A||B$) quantifies the similarity of 2 distributions A and B:

$$\mathrm{JSD}(A||B) = \frac{D_{\mathrm{KL}}(A||M)}{2} + \frac{D_{\mathrm{KL}}(M||B)}{2}, \tag{1.24}$$

with $M = (A+B)/2$, and D_{KL}, the Kullback-Leibler divergence (Kullback 1959), based on Shannon entropy

$$D_{\mathrm{KL}}(A||B) = \sum_x A(x) \ \ln\left(\frac{A(x)}{B(x)}\right), \tag{1.25}$$

The Jensen-Shannon divergence has convenient properties, such symmetricity ($\mathrm{JSD}(A||B) = \mathrm{JSD}(B||A)$), and presence of boundaries ($0 < \mathrm{JSD}(A||B) < \ln(2) \sim 0.69$). The consistency between the two compared distributions is high for low values of JSD. In the thesis, we empirically consider that $\mathrm{JSD}(A||B) \leq 10^{-2}$ informs that both distributions are indistinguishables.

→ The Gelman-Rubin ratio

The convergence of MCMC samplers are examined with Gelman-Rubin statistics (Gelman and Rubin 1992, Brooks and Gelman 1998). This estimator quantifies the difference between several MCMC chains. Let's consider a parameter θ sampled with m chains of length n (all equal for simplicity). Let $\hat{\theta}_{i,j}$, the estimated posterior value of θ at the iteration i of the chain j that has a mean μ_j, and the overeall estimated mean $\mu = (1/m)\sum_{j=1}^{m} \mu_j$. Let us define the between-chain variance B/n and within-chain variance W as

$$\frac{B}{n} = \frac{1}{m-1}\sum_{j=1}^{m}(\mu_j - \mu)^2, \tag{1.26}$$

$$W = \frac{1}{m(n-1)}\sum_{j=1}^{m}\sum_{i=1}^{n}(\hat{\theta}_{i,j} - \mu_j)^2 = \frac{1}{m}\sum_{j=1}^{m}\sigma_j^2, \tag{1.27}$$

with σ_j^2, the variance of the chain j.

A pooled posterior variance $\hat{V}$ can be estimated (with sampling variability correction) as

$$\hat{V} = \frac{n-1}{n}W + \frac{m+1}{m}\frac{B}{n}, \tag{1.28}$$

The Gelman-Rubin ratio, also called potential scale reduction factor, is then expressed as

$$\hat{R}_c = \left(\frac{d+3}{d+1} \frac{\hat{V}}{W} \right)^{1/2}, \tag{1.29}$$

where d refers to the degree of freedom (Gelman and Rubin 1992).

The estimator tends to 1 as all MCMC chains explore the full posterior, and become consistent with each other. We follow the interpretation proposed in Brooks and Gelman 1998, which considers that convergence is reached for $\hat{\theta}_{i,j}$ if $\hat{R}_c < 1.2$.

The Gelman-Rubin ratio have been calculated to check for the convergence of posteriors obtained in the model selection study described in Chapter 2.

→ The Anderson-Darling test

As mentionned in Section 1.2.3, the noise subtracted timing residuals divided by ToA errors (i.e., whitenned residuals) should follow a standard Gaussian distribution $\mathcal{N}(0,1)$ if the model describes properly the signals in the data. We use the normality test Anderson-Darling (Anderson and Darling 1952) in Chapter 2 to estimate the performance of the investigated models. The Anderson-Darling statistic evaluates how much a given data sample deviates from a chosen probability distribution. It compares the empirical distribution function F (i.e., cumulative distribution function) of the tested sample with a theoretical function chosen as a null hypothesis. For $\mathcal{N}(0,1)$ and thus with both the mean and variance known, the Anderson-Darling estimator A^2 of a sample x_i (here the whitenned residuals) with $i = 1, ..., n$ can be expressed as

$$A^2 = -n - \sum_{i=1}^{n} \frac{2i-1}{n} \left[\ln(\mathrm{F}(x_i)) + \ln(1 - \mathrm{F}(x_{n+1-i})) \right], \tag{1.30}$$

The likelihood in PTA is based on assuming the Gaussianity of the data. If the data is modelled correctly, a model selection based on Bayes factor allows to choose the best model from a given set, but it doesn't guarantee the goodness of the model. The Anderson-Darling test, permits to complete the Bayesian model selection by evaluating the performance of the model. The Gaussian assumption (i.e., null hypothesis) is rejected at a certain confidence level if A^2 is over a corresponding critical value. For instance, the null hypothesis cannot be excluded at 95% confidence level if $A^2 = 2.5$ (Table 4.2 of D'Agostino and Stephens 1986).

CHAPTER 2

SINGLE-PULSAR NOISE MODEL SELECTION

Abstract

This chapter is dedicated to the optimisation of the single-pulse noise models, with the aim of giving a special treatment for each pulsar given the data and our a priori knowledge. This work is the main content of a publication (Chalumeau et al. 2021) submitted to Monthly Notices of the Royal Astronomical Society journal (MNRAS) journal for which a model selection is performed to six pulsars of the EPTA Data Release 2 (DR2). The chapter begins with a presentation of the EPTA DR2, followed by a description of the method to model single-pulsar noise components in PTAs. It concludes with the full study achieved in order to obtain the most favored single-pulsar noise model for each considered pulsar.

2.1 Introduction

The three following PTA collaborations, PPTA, NANOGrav and EPTA have recently published consistent results on the presence of a red (i.e., time-dependent) signal common among pulsars with their own independently processed datasets (Goncharov et al. 2021, Arzoumanian et al. 2020 and Chen et al. 2021) but still without evidence for Hellings-Downs correlations, which would confirm a detection of the GWB.

The biggest problem with PTA data is the low control on the noise: there are many potential sources which could contribute to the observed data (i.e., timing residuals) which we model in a parametrized (and sometimes simplified) way and include in the "global fit". The high frequency end of PTA data is usually dominated by *measurement white noise*. The low frequency end is expected to be dominated by *red noise processes*. Some of the red noise is expected to be correlated, those are spatial correlations that are a function of angular separation of each pair of pulsars on the sky (Tiburzi et al. 2016). Besides the GWB (see Section 1.3.2) we expect other sources of correlated noise such as errors in the clock time standard (causing monopolar-type correlation) or systematic errors in the Solar-system ephemeris (causing dipolar-type correlations). Moreover, we also expect the presence of uncorrelated red noise which is individual to each pulsar in the array, this is the spin noise (or timing noise) which refers to the rotational variations of the pulsar caused by different possible phenomena (e.g., unmodeled objects in the vicinity of the neutron star, intrinsic processes, etc.). The red noise types described above are commonly referred to as *achromatic* red noise since it is independent of the observing radio frequencies. Most of the PTA data also show the presence of *chromatic* red noise that depends on the radio frequency of observations. In particular there is the long-term variations of dispersion measure, which add time delays to the time of arrival as $\Delta t \propto \nu^{-2}$ and scattering variations ($\Delta t \propto \nu^{-4}$), both caused by the time-varying electrons column density between the pulsar and the radio telescope.

Our ability to detect and characterize GW signals strongly depends on the faithfulness of the pulsar noise model (Hazboun et al. 2020). Due to large choice of possible noise components (we see it as various models of the noise) and their description/parametrization, the search for GWB assumes a common (and usually simplified) noise model that is the same for each pulsar and infers parameters of that model together with characterizing the GWB. It was shown (see, for example, Goncharov et al. 2021 and the references therein) that actual noise model could vary significantly from pulsar to pulsar and could influence detectability of GWB (Hazboun et al. 2020). This is the main motivation in this study, in which we seek for the most favored single-pulsar noise model and compare it with the standard one used for in recent EPTA search for a GWB (Chen et al. 2021). Based on the previous investigations for each pulsar in the EPTA DR2, we suggest a finite set of noise

models and use Bayes factors (cf. Section 1.4) as a ranking statistic for various choices, assuming that all models are equally probable *a priori*. When the Bayes factor is not informative (close to one) we make selection based either on simplicity of the model or on the basis of computational efficiency with very few exceptions which we discuss in the main text explicitly.

The chapter is organized as follows. A brief presentation of EPTA DR2 data in section 2.2 is followed by a detailed description of each noise process that will be used in building the noise model given in Section 2.3. The Section 2.4 presents all the results obtained for the single-pulsar noise model selection with a summary in Section 2.4.4.

2.2 Description of the EPTA Data Release 2

The EPTA Data Release 2 (DR2) – 6-pulsars dataset (Chen et al. 2021) – comprises up to 24 years of high cadence observations of PSRs J0613-0200, J1012+5307, J1600-3053, J1713+0747, J1744-1134 and J1909-3744. These pulsars are observed at four European radio telescopes: the Effelsberg 100-m radio telescope (EFF), the Nançay Radio telescope (NRT), the Lovell Telescope at the Jodrell Bank Observatory (JBO), the Westerbork Synthesis Radio Telescope (WSRT). In addition, we have used data of Large European Array of Pulsars (LEAP), that is the combination of four mentioned telescopes with the Sardinia Radio Telescope (SRT), forming a tied-array telescope (Bassa et al. 2015). The five radio telescopes contribute to all pulsars except PSR J1909-3744, which has a dataset that contains only NRT observations because of its low-declination. Upgrades of telescopes, including improvements in or changes of receivers/backends, have been applied during the observational period, which make the dataset heterogeneous in timing precision and radio frequency coverage. We label the data by the telescope (or observatory) and the system that collected it followed by the radio frequency in MHz (e.g., EFF.P200.1400). Having the multiple systems in PTA datasets is a curse, as we need to combine the data from all systems together taking into account possible systematics, and a blessing as the multi-band observations are required to disentangle and characterize the chromatic noise and the system specific instrumental red noise (e.g., system noise, Lentati et al. 2016).

A characteristic time-of-arrival (ToA) is computed from the time and frequency averaged profile of each observation, except for JBO.ROACH and NRT.NUPPI backends, which use respectively 2 and 4 (radio-frequency) sub-band ToAs per epoch. The ToAs of each pulsar are assembled together and used to fit the timing model (TM) parameters that describe pulsars's sky position and proper-motion, its spin frequency and corresponding derivative, the DM and its two first derivatives. For pulsars in binary systems, the timing model accounts also for the orbital motion including Keplerian and post-Keplerian

parameters. Phase jumps are included in TM for each system and also for each of the JBO.ROACH & NRT.NUPPI.1484 sub-bands. The fit for TM parameters was obtained using TEMPO2 package (Hobbs et al. 2006) with the JPL Solar-system ephemeris DE438 (to transform the local observatory ToAs to the Solar-system barycentre) and with the clock corrections TT(BIPM2019) (time conversion from the observatory time standard to the Terestrial Time (TT) given by the Bureau International des Poids et Mesures (BIPM)). The end result are the *timing residuals*, i.e. the differences between the observed ToAs and the predicted arrival times by the TM, that are then analysed to search for GWs.

2.3 Modelling signals in PTA data

This section presents the likelihood computed for PTAs and the signals related to the single-pulsars components that are either stochastic, defined as *Gaussian processes* (Rasmussen and Williams 2005), or deterministic. The common red-signals related to the GWB and Solar system ephemeris errors will be further developped in the Chapters 3 and 4. The descriptions follow the methods used in the package ENTERPRISE (Ellis et al. 2019) which is employed to compute the likelihood and prior values for most of the analyses presented in the manuscript.

Gaussian processes in a nutshell

Gaussian processes (GPs) are the generalization of multivariate Gaussian distributions in the case of an infinite number of random variables. GPs are particularly convenient to describe random functions $f(x)$ and quantify an uncertainty at any given point x. More formally, a GP is a stochastic process $\{f(x);\ x \in \mathcal{S}\}$ where, for any finite set $\{x_1, x_2, ..., x_n\} \in \mathcal{S}^n$, with $n \in \mathbb{N}$, the random vector $\big(f(x_1), f(x_2), ..., f(x_n)\big)^{\mathrm{T}} \in \mathbb{R}^n$ is distributed as a multivariate Gaussian.

A Gaussian process can be fully characterized by its mean and covariance that are both (continuous) functions (see next section). GPs are often used to solve regression problems, where one wants to predict values of some continuous functions given a set of input data and a chosen covariance function (also referred as kernel). As mentionned previously, this method is very convenient since it provides a value and related errors at any given point using very few assumptions (Gaussian and often stationnary), and allowing irregularly sampled data in any number of dimensions. However, GPs are not sparse (i.e., they require to use all data to perform the prediction), and they cannot be applied for big data sets ($> 10^4$ points).

In PTA noise modelling, we do not use Gaussian processes to perform regression. In-

stead, we model (apparent) stochastic processes (pulsar spin noise, DM variations, gravitational wave background, ...) as GPs with a parametrized kernel for which we want to infer hyperparameters through Bayesian method. As described in the next section, the kernel is built in the frequency domain, using basis functions (expressed as a sum of sine/cosine functions) and a chosen power spectral density. Note that for PTAs, a signal modelled as a GP follows a Gaussian distribution at any given epoch (i.e., observation time), with a zero mean in time domain and where the kernel defines the covariance of the process between each epoch (i.e., the correlation in time between the times of arrival). The kernel is also used to describe covariances between pulsars (e.g., Hellings-Downs correlations), or the radio frequency dependence of the process, also referred as the chromaticity (see Section 2.3.2).

2.3.1 The single-pulsar likelihood

Let us introduce the likelihood for Gaussian processes following Haasteren and Vallisneri 2014. We assume that all noise components are Gaussian and stationary and we separate the white noise component **N** (see below) from the rest. The Gaussian process can be introduced in two equivalent ways:

→ As a sum of deterministic basis functions $\sum_i \mathrm{F_i(t) w_i}$, where w_i are weights – random Gaussian distributed variable $\mathcal{N}(w_i^0, \mathbf{\Sigma}_{ij})$, where w_i^0 is a mean value for each weight, $\mathbf{\Sigma}_{ij}$ is a covariance matrix, and $\mathrm{F_i(t)}$ are basis functions. This is the weight-space view.

→ As a continuous function such that the ensemble average $\mathbb{E}[f(t)] = m(t)$ and the covariance $\mathbb{E}[(f(t) - m(t))(f(t') - m(t'))] = C(t, t')$. This is the function space view.

Those two descriptions are related via

$$\mathbf{C}(t, t') = \sum_{a,b} \mathrm{F_a(t)} \mathbf{\Sigma}_{\mathrm{ab}} \mathrm{F_b(t')}, \tag{2.1}$$

with $a, b = 1, ..., N$.

The red noise covariance matrix $C(t, t')$ described in the following Section was introduced in Haasteren and Levin 2012 and it was approximated using an incomplete Fourier basis (sin, cos) in Lentati et al. 2013. Applying the Gaussian process approach to the PTA likelihood function we get (Haasteren and Vallisneri 2014):

$$p(\vec{\delta t} | w_a, \mathrm{GP}) = \frac{\exp\left[-\frac{1}{2} \sum_{\mathrm{ij}} \left(\delta \mathrm{t_i} - \sum_{\mathrm{a}} \mathrm{F_a(t_i)\, w_a}\right) (\mathbf{N}_{\mathrm{ij}})^{-1} \left(\delta \mathrm{t_j} - \sum_{\mathrm{a}} \mathrm{F_a(t_j)\, w_a}\right)\right]}{\sqrt{(2\pi)^n \det(\mathbf{N})}} \times \frac{\exp\left[-\frac{1}{2} \sum_{\mathrm{a,b}} \mathrm{w_a} \, (\mathbf{\Sigma}_{\mathrm{ab}})^{-1} \, \mathrm{w_b}\right]}{\sqrt{(2\pi)^N \det(\Sigma)}}, \tag{2.2}$$

where δt_i the i-th observed residuals with $i, j = 1, ..., n$. The equivalent representation is given as

$$p(\vec{\delta t}|\mathrm{GP}) = \frac{\exp\left[-\frac{1}{2}\ \sum_{\mathrm{ij}}\ \delta \mathrm{t_i}\ (\mathbf{N_{ij}} + \mathbf{C_{ij}})^{-1}\ \delta \mathrm{t_j}\right]}{\sqrt{(2\pi)^n \det(\mathbf{N}+\mathbf{C})}}, \tag{2.3}$$

where $\mathbf{C_{ij}} = \sum_{\mathrm{a,b}}\ \mathrm{F_a(t_i)}\ \mathbf{\Sigma_{ab}}\ \mathrm{F_b(t_j)}$. The convenience of the latter description is that it can be computed efficiently using the Woodbury equality (Woodbury 1950):

$$\begin{aligned}(\mathbf{N}+\mathbf{C})^{-1} &\simeq (\mathbf{N} + \mathrm{F}\mathbf{\Sigma}\mathrm{F}^{\mathrm{T}})^{-1} \\ &= \mathbf{N}^{-1} - \mathbf{N}^{-1}\mathrm{F}(\mathbf{\Sigma}^{-1} + \mathrm{F}^{\mathrm{T}}\mathbf{N}^{-1}\mathrm{F})^{-1}\mathrm{F}^{\mathrm{T}}\mathbf{N}^{-1},\end{aligned} \tag{2.4}$$

In what follows we consider $\mathbf{C}$ as a combination of several (chromatic and achromatic) red noise components each decomposed in its own set of basis functions.

For a set of n timing residuals δt, the likelihood function describing white noise $\mathbf{N}$, a stochastic red noise as gaussian process with covariance matrix $\mathbf{C}$, and a deterministic signal $d(t\ ;\ \vec{\theta}_d)$, characterised with parameters $\vec{\theta}_d$, is expressed as

$$p(\vec{\delta t}|\vec{\theta}_d, \mathrm{GP}) = \frac{\exp\left[-\frac{1}{2}\ \sum_{\mathrm{ij}}\ \left(\delta \mathrm{t_i} - \mathrm{d(t_i\ ;\ \vec{\theta}_d)}\right)\ \left(\mathbf{N_{ij}} + \mathbf{C_{ij}}\right)^{-1}\ \left(\delta \mathrm{t_j} - \mathrm{d(t_j\ ;\ \vec{\theta}_d)}\right)\right]}{\sqrt{(2\pi)^n \det(\mathbf{N}+\mathbf{C})}}, \tag{2.5}$$

with $i, j = 1, ..., n$.

2.3.2 The single-pulsar noise models

Marginalization over Timing Model parameter errors

Before we introduce the noise components, we should explain how we treat the timing model. We assume that an initial fit of the timing model obtained with LIBSTEMPO (Vallisneri 2020), a python wrapper of TEMPO2, reduces it to a linear model where the coefficients are given by a design matrix $\mathbf{M}$ (made of partial derivatives of timing residuals with respect to timing model parameter errors). The deterministic linearized signal from errors of the p timing model parameters is thus

$$d^{\mathrm{TM}}(t;\ \vec{\xi}) = \mathbf{M}(t)\ \vec{\xi}, \tag{2.6}$$

with $\dim(\mathbf{M}) = (n \times p)$.

The likelihood function given by eq. (2.3) is therefore expressed (in 'matrix' form) as

$$p(\vec{\delta t}|\vec{\xi}, \mathrm{GP}) = \frac{\exp\left[-\frac{1}{2}\ \left(\vec{\delta \mathrm{t}} - \mathbf{M}\vec{\xi}\right)^{\mathrm{T}}\ (\mathbf{N}+\mathbf{C})^{-1}\ \left(\vec{\delta \mathrm{t}} - \mathbf{M}\vec{\xi}\right)\right]}{\sqrt{(2\pi)^n \det(\mathbf{N}+\mathbf{C})}}, \tag{2.7}$$

In each analysis of the manuscript, we analytically marginalize the likelihood over the TM parameter errors (left over from the main fit). The analytic marginalization was first demonstrated in Haasteren et al. 2009 as

$$p(\vec{\delta t}|\mathrm{GP}) = \int d^p\vec{\xi}\; p(\vec{\delta t}|\vec{\xi},\mathrm{GP}) = \frac{\exp\left[-\frac{1}{2}\,(\vec{\delta}\mathrm{t})^{\mathrm{T}}\,\mathbf{K}'\,(\vec{\delta}\mathrm{t})\right]}{\sqrt{(2\pi)^{n-p}\det(\mathbf{K})\,\det(\mathbf{M}^{\mathrm{T}}\mathbf{K}^{-1}\mathbf{M}^{\mathrm{T}})}}, \tag{2.8}$$

with $\mathbf{K} = \mathbf{N} + \mathbf{C}$, and $\mathbf{K}' = \mathbf{K}^{-1} - \mathbf{K}^{-1}\mathbf{M}\left(\mathbf{M}^T\mathbf{K}^{-1}\mathbf{M}\right)^{-1}\mathbf{M}^T\mathbf{K}^{-1}$.

An alternative formulation was proposed after in Haasteren and Levin 2012 as

$$\int d^p\vec{\xi}\; p(\vec{\delta t}|\vec{\xi},\mathrm{GP}) = \frac{\exp\left[-\frac{1}{2}\,(\vec{\delta}\mathrm{t})^{\mathrm{T}}\,\mathbf{G}\,\left(\mathbf{G}^{\mathrm{T}}\mathbf{K}\,\mathbf{G}\right)^{-1}\,\mathbf{G}^{\mathrm{T}}\,(\vec{\delta}\mathrm{t})\right]}{\sqrt{(2\pi)^{n-p}\,\det(\mathbf{G}^{\mathrm{T}}\mathbf{K}^{-1}\mathbf{G}^{\mathrm{T}})}}, \tag{2.9}$$

where $\mathbf{G}$ is obtained after factorising $\mathbf{M}$ with a singular-value decomposition (SVD), such $\mathbf{M} = \mathbf{U}\mathbf{D}\mathbf{V}^*$, with $\mathbf{D}$ the $(n \times p)$ diagonal matrix, and $\mathbf{U}$ and $\mathbf{V}$ respectively the $(n \times n)$ and $(p \times p)$ orthogonal matrices. Then $\mathbf{U} = [\mathbf{F}\;\mathbf{G}]$, with $\mathbf{F}$ the $(n \times p)$ matrix, corresponding to the p first columns of $\mathbf{U}$ and $\mathbf{G}$, the remaining $(n \times (n-p))$ matrix.

Rather, it has been shown in Haasteren and Vallisneri 2014 that these analytic marginalization expressions are equivalent to the marginalization of a corresponding Gaussian process with an improper prior. The implementation of the marginalization in ENTERPRISE (used for all data analyses in the manuscript) utilizes in the equivalence of weight space and function space description of a Gaussian process. The design matrices ($\mathrm{M_a(t_i)}$) are used as basis functions, the covariance for the TM process is given as

$$\mathbf{C}^{\mathrm{TM}} = \sum_{\mathrm{a,b}} \mathrm{M_a(t_i)}\;\mathbf{\Sigma}^{\mathrm{TM}}_{\mathrm{ab}}\;\mathrm{M_b(t_j)}, \tag{2.10}$$

where the prior on the parameter errors is modelled with a prior $\Sigma = \lambda I$ with I being a diagonal unit matrix and λ is a large numerical number (see Haasteren and Vallisneri 2014 for details). In the limit $\lambda \to \infty$ this prior becomes improper, but in this analysis the values of λ are fixed but large so the prior is formally proper. The marginalization over timing errors ("weights") is then performed in a usual way by going from eq. (2.2) to eq. (2.3).

The use of a very wide or improper prior in Bayesian model selection should be taken with great caution especially comparing two models where one of them uses marginalization over the improper prior. The penalization which is embedded in the prior (for being too wide) and propagates into computation of the evidence is lost and reliable results

from evidence-based model selection cannot be guaranteed. However in *all* noise models described below we perform marginalization over the TM parameters which brings them all to the common starting point for further comparison.

The white noise

As mentioned above the white noise dominates the high frequency end of the PTA sensitivity band. The ToA errors ($\sigma_{\rm ToA}$) are estimated within the template-matching method (Taylor 1992) that is used to compute the actual ToAs. This method is based on the Fourier domain cross-correlation of a template profile with the integrated pulse profile at the corresponding epoch (see Section 1.2.1). The uncertainties of each ToA are further modified as

$$\sigma = \sqrt{\mathrm{E_f}^2\,\sigma^2_{\rm ToA} + {\mathrm{E_q}}^2}.$$

EFAC ($\mathrm{E_f}$) is a multiplicative factor that takes into account ToA measurement errors (or radiometer noise). EQUAD ($\mathrm{E_q}$) is added in quadrature to account for any other white noise (such as a stochastic profile variations (Shannon et al. 2014)) and for a possible systematic errors. The white noise model, therefore, is given as

$$\mathbf{N}_{\rm ij} = \left({\mathrm{E_f}}^2\,\sigma^2_{\rm ToA}(\mathrm{t_i}) + {\mathrm{E_q}}^2\right)\delta_{\rm i,j}, \tag{2.11}$$

where i and j indexing the ToAs of the corresponding backend. EFAC and EQUAD are the phenomenological parameters that characterize the white noise for each system and for each pulsar.

The stochastic red signal

It is essential for PTAs to describe properly the intrinsic red noise because of its possible correlation with low-frequency GW signals (Shannon and Cordes 2010). Results from simulations in Hazboun et al. 2020 have clearly demonstrated the impact of red noise modelling on GWB results. The single-pulsar stochastic red noise is a time-correlated signal modelled as a stationary Gaussian process usually with power-law power spectral density (PSD) as

$$S_p(f) = \frac{A^2}{12\pi^2}\left(\frac{f}{\mathrm{yr}^{-1}}\right)^{-\gamma}\ \mathrm{yr}^3, \tag{2.12}$$

where the amplitude A is the normalized value at the frequency of one over one year ($f = 1/\mathrm{yr}$), and γ is the spectral index.

The Fourier cosine transform permits to relate $S_p(f)$ to the time-domain correlation function $\mathbf{C}(\tau_{\rm ij})$ as (Haasteren et al. 2009)

$$\mathbf{C}(\tau_{ij}) = \int_0^\infty df\ P(f)\cos(\tau_{ij}\ f), \tag{2.13}$$

where $\tau_{ij} = 2\pi\,|t_i - t_j|$ contains the time difference between two observations.

After defining a low-frequency cutoff f_L, the stochastic red noise covariance matrix can be expressed as (Haasteren et al. 2009)

$$\mathbf{C}^{\rm SRS}_{ij} = \frac{A^2}{12\pi^2}\left(\frac{f_L}{\rm yr^{-1}}\right)^{1-\gamma}\left[\Gamma(1-\gamma)\sin\left(\frac{\pi\gamma}{2}\right)(f_L\,\tau_{ij})^{\gamma-1} - \sum_{q=0}^{\infty}\frac{(-1)^q\,(f_L\,\tau_{ij})^{2q}}{(2q)!\,(2q+1-\gamma)}\right], \tag{2.14}$$

where Γ is the Euler gamma function.

The analyses applied in the thesis adopt the "weight-space" representation of the Gaussian Process, that is the timing residuals due to red noise at each epoch t_i are approximated as

$$\delta t^{\rm SRS}(t_i) = \sum_{l=1}^{N} X_l\cos\left(2\pi\,t_i f_l\right) + Y_l\sin\left(2\pi\,t_i f_l\right), \tag{2.15}$$

where X_l and Y_l are playing the role of weights and the basis functions are

$$\begin{aligned} \mathrm{F}_{2l-1}(\mathrm{t_i}) &= \cos\left(2\pi\ t_i f_l\right), \\ \mathrm{F}_{2l}(\mathrm{t_i}) &= \sin\left(2\pi\ t_i f_l\right), \end{aligned} \tag{2.16}$$

where $l = 1,...,N$ and $f_l = l/T$ (where T is the duration of the observation). This representation would correspond to the usual Fourier transform if we had regularly spaced epochs, t_i. However the radio observations are quite irregular (besides maybe the last 5 years or so) which makes the Fourier basis not exactly orthogonal. In addition, we do not use a complete set: we usually truncate it at some low frequency as we are interested in modelling the red noise. The optimal choice of frequencies was considered in Haasteren and Vallisneri 2015, however for all results presented here, we have used an evenly spaced $\Delta f = 1/T$ set of frequencies, starting at $f = 1/T$ and truncating at N/T where N is one of the parameters in the model selection.

The covariance matrix Σ for the Fourier coefficients (weights X_l, Y_l) is defined by the PSD, $S(f)$. The simplest model for the PSD of a stochastic red process in a single pulsar data is a power-law $S_{\rm P}(f;A,\gamma)$ (Eq. 2.12). The covariance matrix is given in the frequency domain by

$$\mathbf{\Sigma}_{kl} = S_P(f_k;A,\gamma)\,\delta_{kl}\ /\ T, \tag{2.17}$$

where $k,l = 1,...,N$

An alternative description takes into account that the data is dominated by white noise at high frequencies, and that is captured as a broken power law (Arzoumanian et al. 2020) :

$$S_{\rm BPL}(f; A, \gamma, \delta, f_b, \kappa) = \frac{A^2}{12\pi^2}\left(\frac{f}{\rm yr^{-1}}\right)^{-\gamma}\left(1+\left(\frac{f}{f_b}\right)^{1/\kappa}\right)^{\kappa\ (\gamma-\delta)} {\rm yr}^3, \tag{2.18}$$

with the amplitude A set at $f = \frac{1}{\rm yr}$, f_b the transition frequency, γ and δ, the slopes for f respectively below and above f_b and κ defines the smoothness of transition.

Jumping a bit ahead, the Bayesian analyses of the data applied for the model selection use priors on κ and f_b as uniform $\mathcal{U}(0.01, 0.5)$ and log-uniform $\log_{10}\mathcal{U}(10^{-10}, 10^{-6})$, and the priors on A and γ are the same as for the simple power-laws models given in Table 2.1. The high-frequency spectral index δ is fixed at 0.

A completely different approach is not to impose any particular spectral shape but rather estimate it from the data itself: the free-spectrum method (Lentati et al. 2016), given as

$$S_{\rm FS}(f_i; \rho_i) = \rho_i^2\ T, \tag{2.19}$$

where ρ_i is the spectral amplitude at each frequency, $f_i = i/T$ with $i = 1, ..., N$, in units of residuals. This modelling is particularly convenient to understand the spectral content and to interpret our results for the red noise models given above. The number of parameters in the free-spectrum approach is equal to the number of Fourier bins and, therefore, computationally more expensive. For all analyses here, the priors for each ρ_i will be log-uniform: $\log_{10}\mathcal{U}(10^{-10}, 10^{-4})$.

The rest of this section gives more details on each specific type of red noise that are included in the total noise budget for each pulsar.

- Achromatic red noise

The achromatic red-noise (which we denote as RN) is commonly used in single-pulsar noise models in order to characterize the long-term variability of the pulsar spin. Also referred to as “timing noise” or “spin noise”, this stochastic signal is expected to be present and is caused by internal processes in the neutron star (e.g., interactions between the superfluid and the crust, Cordes and Shannon 2010) or by changes in the pulsar’s magnetosphere (Lyne et al. 2010).

For the model selection, we adopt the power law model as our standard approach, however we also use the free spectrum and broken power law (red noise becomes white after some frequency) to guide selection of the truncation frequency in the sum given

by eq. (2.15). This noise component is unique, independent of the observational radio frequency and uncorrelated in each pulsar data set.

- Chromatic red noise

On the way to receiver, the radio emission passes through and interacts with the ionized interstellar medium (IISM), the Solar-system interplanetary medium and the Earth's ionosphere, which leads to frequency-dependent delays at the observed signal.

An important effect is the interstellar dispersion that induces a delay in the arrival time $\Delta t^{\mathrm{DM}} \propto \nu^{-2}\mathrm{DM}$, where ν is the radio frequency and DM is the path integral of the free-electron density called the dispersion measure (Lorimer and Kramer 2004). This effect is taken into account during the observations and inside the timing model which considers its value at a reference epoch together with its first and second derivatives (see Section 1.2.2). However, pulsars and Solar-system motions in the turbulent and inhomogeneous IISM induce time-dependent DM variations (DMv) that affect the timing residuals as $\delta t^{\mathrm{DMv}} \propto \nu^{-2}$ at the PTA's timescales (You et al. 2007, Keith et al. 2013).

Another result of interaction with IISM is the scattering variations (Sv), corresponding to the multi-path propagation of the radio signal due to diffraction and refraction in the IISM (Lorimer and Kramer 2004, Lyne et al. 2010). This causes a chromatic pulse broadening and a time delay with $\sim \nu^{-4}$ chromaticity. The scattering variations are described as a stochastic red signal such that $\delta t^{\mathrm{Sv}} \propto \nu^{-4}$.

More generally we describe phenomenologically any chromatic red noise (chromatic due to its dependence on the observational radio frequency ν) using the basis functions

$$\mathrm{F}_{\mathrm{j}}^{\mathrm{chrom.}}(\mathrm{t_i}) = \mathrm{F}(\mathrm{t_i}) * \left(\frac{\nu_{\mathrm{j}}}{1.4\ \mathrm{GHz}}\right)^{-\chi}, \tag{2.20}$$

where F is the incomplete set of sin/cos basis functions and ν_j is an observational radio frequency for a corresponding residual at the epoch t_i, and χ is the chromatic index. We use the same covariance matrices for chromatic red noise as for achromatic (power-law, broken power-law, free spectrum). It is essential to have multiband radio observations to disentangle chromatic red noise from the achromatic (otherwise they are completely degenerate).

During the model selection, we will consider the following chromatic red processes: (i) dispersion measurement variations (DMv) with $\chi = 2$, (ii) scattering variations (Sv) with $\chi = 4$, and, (iii) phenomenological model (FCN – 'free chromatic noise') with χ taken to be a free parameter with prior $\mathcal{U}(0,7)$. The FCN was first introduced in (Goncharov et al. 2021) and is used here as a diagnostic to verify the combined noise model.

- System and Band noise

EPTA DR2 dataset is a combination of ToAs produced by five radio telescopes which use different systems observing at radio frequencies ranging from ~ 300 MHz to ~ 5 GHz. Following Lentati et al. 2016 we introduce the "system" and "band" red noise to be applied on the model selection on this dataset. The system noise (SN) is a stochastic red signal specific to a single receiver system. Such a signal could, for example, arise from a miscalibration of polarizations or specific radio frequency interferences. We model this process as stochastic red noise applied to the ToAs of only the considered system. This noise is considered to be achromatic for every system except for NRT.NUPPI.1484 that is divided into 4 sub-bands and it will be probed for presence of both the chromatic red process SN and DMv (labelled as DMv-SN).

The band noise (BN) is a stochastic red noise assigned to a specific radio frequency band. This is to account either for a possible frequency-dependent DM in the amplitude (additional to the overall ν^{-2} factor) caused by multi-path propagation of radio emission (Cordes et al. 2016) or by a frequency-dependent calibration errors (van Straten 2013). Given the frequency coverage of the EPTA DR2 dataset (Chen et al. 2021), we will consider four radio bands for the BN:

- Band.1 : < 1 GHz
- Band.2 : $[1,2]$ GHz
- Band.3 : $[2,3]$ GHz
- Band.4 : > 3 GHz.

The deterministic red processes

In addition to stochastic processes we also consider two types of deterministic signals of non-GW natures for the model selection. We have used prior information about these signals and pulsars where those signals were identified.

- Exponential dip

Several pulsars have displayed exponential dips (E), where the ToAs are suddenly perturbed by a frequency-dependent advance in ToAs. Most relevant for us is that these events have been observed at least twice for PSR J1713+0747, in 2008 (~ MJD 54757) and in 2016 (~ MJD 57510), both those epochs fall into the EPTA DR2 timespan.

The first event, reported in Coles et al. 2015, Zhu et al. 2015 and Desvignes et al. 2016, is interpreted as a "DM event", i.e. a drop in the electron column density along the line-of-sight producing a sudden reduction of DM that returns to the previously observed level exponentially over the time.

The second event, reported in Lam et al. 2018, was accompanied by a pulse shape change and the corresponding chromatic index lower than 2, so it is not compatible with a DM-related process. It was proposed instead (Goncharov et al. 2021) that this event is rather related to processes in the magnetosphere of a pulsar.

We model the exponential dip delay at the epoch t_i and radio frequency ν_k as :

$$d^{\mathrm{E}}(t_i, \nu_k; A_E, \tau, t_0, \chi_E) = \begin{cases} 0, \text{if } t_i < t_0 \\ A_E \left(\dfrac{\nu_k}{1.4\ \mathrm{GHz}}\right)^{-\chi_E} \exp\left(-\dfrac{t_i - t_0}{\tau}\right), \text{if } t_i \geq t_0 \end{cases} \tag{2.21}$$

where A_E is the amplitude in residual units, t_0 the reference epoch of the event, τ the relaxation time and χ_E the chromatic index, either fixed or being a free parameter with prior $\mathcal{U}(0,7)$.

- Annual chromatic signals

The second deterministic signal which could be present in the data is an annual chromatic process (which we label as "Y") that comes from the electron density variations during the Earth motion around the Sun.

The previous investigations (Keith et al. 2013, Main et al. 2020) indicate that this signal is present in PSR J0613-0200, which we model as in (Lentati et al. 2016, Goncharov et al. 2021):

$$d^{\mathrm{Y}}(t_i, f_l; A_Y, \phi, \chi_y) = A_Y \left(\frac{f_l}{1.4\ \mathrm{GHz}}\right)^{-\chi_y} \sin\left(2\pi\ \frac{t_i}{\mathrm{yr}} + \phi\right), \tag{2.22}$$

where A_Y is the characteristic amplitude in residual units, χ_y is the chromatic index and ϕ is the initial phase. We consider either annual DM variations or annual scattering variations, with a chromatic index fixed at 2 or 4 respectively.

The priors of the single-pulsar noise components used for the model selection described in Section 2.4 are given in the Table 2.1.

Table 2.1: Models and priors used for the single-pulsar model selection.

Model (abrev.)	Parameters	Priors (or fixed val.)
White-noise (WN)	EFAC	$\mathcal{U}(0.1,5)$
	EQUAD [s]	$\log_{10}\mathcal{U}(10^{-9},10^{-5})$
Achromatic red-noise (RN)	$A_{\rm RN}$	$\log_{10}\mathcal{U}(10^{-18},10^{-10})$
	$\gamma_{\rm RN}$	$\mathcal{U}(0,7)$
DM variations (DMv)	$A_{\rm DM}$	$\log_{10}\mathcal{U}(10^{-18},10^{-10})$
	$\gamma_{\rm DM}$	$\mathcal{U}(0,7)$
Scattering variations (Sv)	$A_{\rm Sv}$	$\log_{10}\mathcal{U}(10^{-18},10^{-10})$
	$\gamma_{\rm Sv}$	$\mathcal{U}(0,7)$
Free-chromatic noise (FCN)	$A_{\rm FCN}$	$\log_{10}\mathcal{U}(10^{-18},10^{-10})$
	$\gamma_{\rm FCN}$	$\mathcal{U}(0,7)$
	$\chi_{\rm FCN}$	$\mathcal{U}(0,7)$
System-noise (SN or DMv-SN)	$A_{\rm SN}$	$\log_{10}\mathcal{U}(10^{-18},10^{-10})$
	$\gamma_{\rm SN}$	$\mathcal{U}(0,7)$
	$\chi_{\rm SN}$	0 or 2
Band-noise (BN)	$A_{\rm BN}$	$\log_{10}\mathcal{U}(10^{-18},10^{-10})$
	$\gamma_{\rm BN}$	$\mathcal{U}(0,7)$
DM events (E)	$A_{\rm E}$ [s]	$\log_{10}\mathcal{U}(10^{-10},10^{-2})$
	$\tau_{\rm E}$ [day]	$\log_{10}\mathcal{U}(1,10^{2.5})$
	t_0 [MJD]	$\mathcal{U}(54650,54850)$ or $\mathcal{U}(57490,57530)$
	$\chi_{\rm E}$	1, 2, 4 or $\mathcal{U}(0,7)$
Annual chrom. (Y)	$A_{\rm Y}$ [s]	$\log_{10}\mathcal{U}(10^{-10},10^{-2})$
	$\phi_{\rm Y}$	$\mathcal{U}(0,2\pi)$
	$\chi_{\rm y}$	2 or $\mathcal{U}(0,7)$

2.4 Single-pulsar noise model selection with the EPTA DR2

This section describes the selection of the noise model optimised for each pulsar. The selection is done in several steps in a partially iterative way. We start with the base model used in (Chen et al. 2021) that contains only achromatic red noise (RN) and DM variations (DMv). Both these models depend on the number of Fourier frequency bins we use for the basis functions, or, in other words, on the high frequency cut-off that roughly corresponds to the transition from red noise to white noise dominated region. The analysis in (Chen et al. 2021) used 30 and 100 lowest Fourier frequencies (k/T, where $k = 1...30(100)$) for RN amd DMv respectively for *all* 6 pulsars, which is a reasonable (and justifiable) choice.

We start also with those two basic sources of noise and apply Bayesian model selection to find the number of frequency bins for each pulsar. We use a simple power-law model for each red noise, and we use broken power-law and free-spectrum models as guidance to minimize the set of models to try. Next we include stochastic chromatic noise and deterministic signals to the noise budget, and, finally we test for the presence of system and/or band noise.

Each pulsar's noise model always includes white noise and we marginalize over the TM parameter errors (as implemented in ENTERPRISE).

2.4.1 Selection on number of Fourier modes for the achromatic red noise and DM variation

The importance of the choice of spectral binning has been discussed in Haasteren and Vallisneri 2015, where the authors show limitations of the usual Fourier-sum approach with $f_k = \{1/T, ..., N/T\}$ in the presence of linear and/or quadratic signals, or if the stochastic red process spectral index is relatively high (i.e., $\gamma \geq 7$). We do not expect so steeply rising RN and use a prior on the spectral index $\mathcal{U}(0,7)$, and, as we will see later, this prior range is broad enough.We have chosen to use Fourier frequencies f_k in our analysis.

We start with identifying the most favoured number of Fourier bins for each pulsar. We extend short-hand notation for RN and DMv by appending the number of bins (basis functions) used in its description. For example, *RN30_DMv100* refers to a model marginalized over the TM parameter errors, including white-noise parameters, and both achromatic red-noise and DM variations with respectively 30 and 100 Fourier modes.

The RN and DMv could be highly correlated if we lack multi-band observations, therefore we expect that DMv requires the inclusion of more bins to accommodate dispersion information stored at high frequencies. For the RN, we expect that a relatively small

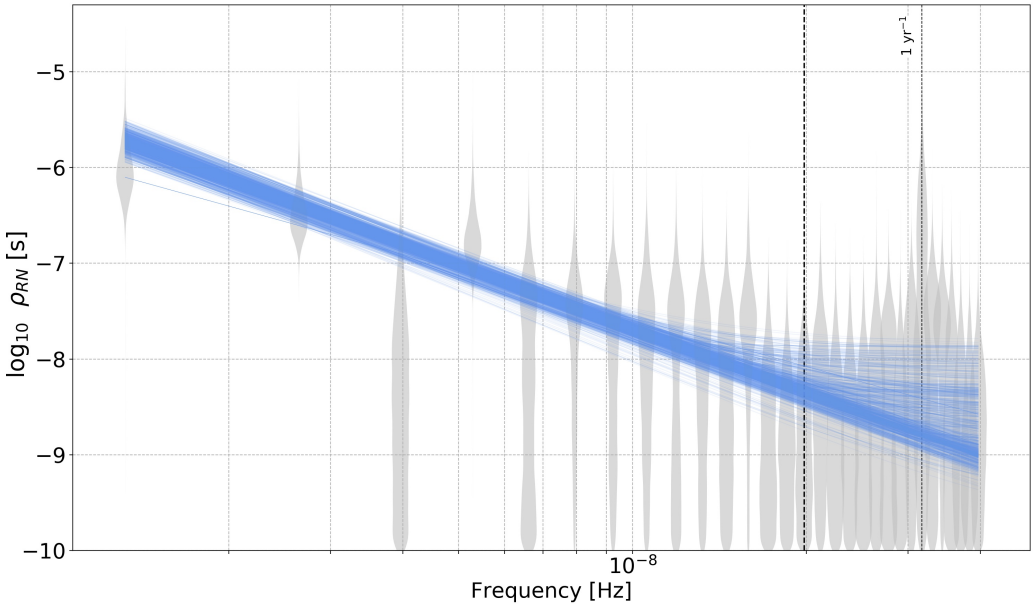

Figure 2.1: Achromatic red-noise spectrum of PSR J1713+0747 using the model *RN30_DMv100*, with free-spectrum PSD (grey violin plot) and broken power-law (blue) PSDs, showing 1000 random realisations of the posterior distribution. The thin dotted line display the 1yr^{-1} frequency and the dashed line show the 15th bin.

number of bins contribute to the analysis before the white noise becomes dominant. Jumping a bit ahead, for example, we have found that use of (what used to be a default choice) *RN30_DMv30* is disfavoured by Bayes factor of more than 10^5 compared to the most favourable model *RN30_DMv100* for PSR J1744-1134. In addition, use of 30 bins shows a very strong cross-model "leakage" in the posterior of RN and DMv parameters, which disappears completely in the favourable model.

We have analysed each pulsar using broken power-law and free-spectrum models in order to get a rough indication on the expected range for the number of Fourier modes. Typical results of such an analysis (for RN) is given in Fig. 2.1 for PSR J1713+0747 where the estimation of power in each bin is given by grey violin-type histograms and we have over-plotted 1000 realizations of the broken power-law randomly drawn from the posterior as blue solid lines. The broken power-law model suggests that the transitional frequency f_b should be above 15 bins (as indicated by a vertical dashed line in Fig. 2.1). Therefore for this pulsar we try 15, 20 and 30 Fourier modes for the RN. Similar analysis could be performed for DMv and we decided to use 30, 50, 70, 100 and 150 modes (to choose from) for every pulsars, which allows us to consider frequencies up to $f_{\rm max} \simeq 1/(2\ \text{months})$ for the longest dataset pulsar (PSR J1713+0747).

We have performed Bayesian model selection across pre-selected number of modes for both RN and DMv. The favourable models are summarized in Table 2.2. It shows that

data supports frequencies higher than $100/T_{span}$ for DMv, except for J0613-0200 which displays no difference neither in evidence nor in the posterior distribution of parameters across the range of N-bins for DMv that we have tried. As expected, for the RN, we require no more than 20 frequency bins for all pulsars except PSR J1012+5307, which remains at 30. In case where there was no clear preference between two (or more) models (Bayes factor less than 10) we preferred the model with lowest number of bins for the reason of computational efficiency.

Let us give a few comments on the results presented in Table 2.2. The quoted Bayes factor compares the selected model for the number of Fourier modes with the model used in (Chen et al. 2021). You can see a significant gain in the Bayes factor for PSRs J1012+5307 and J1713+0747 which is mainly due to the extension of DMv to higher frequencies, in fact all pulsars give slight preference to 150 bins but with the Bayes factor close to one, and following our logic we have chosen to use 100 (30 for PSR J0613-0200) bins to win on the computational cost. The negative (but close to zero) log-Bayes factor for PSRs J1600-3053, J1744-1134, J1909-3744 indicates that the use of 30 modes for RN has only a slight preference (what we would call *inconclusive*) and we have chosen the lowest allowed number of bins to save CPU-time. The residuals in pulsar J0613-0200 data did not favour any particular number of modes. As we are mainly interested in the red noise, we have quantified the difference in the posterior of the red noise between two models by computing Jensen-Shannon divergence. The last column indicates that RN has changed only for J1012+5307: the increase in frequency range of the DMv process constrained RN to lower frequencies (the amplitude of RN has slightly dropped but the spectral index increased) we will revisit the modes selection for this pulsar in Section 2.4.2.

Red noise free-spectrum of PSR J1909-3744

In this paragraph we want to discuss PSR J1909-3744. This is one of the best timers, but it has the shortest observational span (about 11 years) and the data was only acquired by NRT. The free spectrum of the achromatic red noise and the power-law (corresponding to the maximum a posteriori parameters) are plotted in Fig. 2.2 . The blue violin plot shows the power distribution using our standard Fourier modes (i/T_{span}). We performed additional runs (given by different colours) with the scaled down $T_{span} \rightarrow T_{span}/1.2$, $T_{span}/1.45$, $T_{span}/1.7$ to get better resolution at low frequency. Note that those frequency bins are not independent as we have used over-sampling in frequency domain, and the corresponding basis functions are not orthogonal even for evenly spaced data. One can clearly see that the spectrum flattens out and probably bends downwards at the lowest frequency bin. This bend is not very conclusive: the posterior at the lowest bin is poorly constrained, that could be caused by the gaps in the data (214 epochs from 2004 to 2011 with BON vs.

Table 2.2: Favored number of Fourier modes for RN and DMv for the 6 pulsars. The third and fourth columns compare the favored model with *RN30_DMv100*, respectively showing the Bayes factors and the Jensen-Shannon divergences for the RN amplitude (top) and spectral index (bottom). The models for PSR J1713+0747 also include the 2 exponential dips.

Pulsar	Favored NBins	$\log_{10}\mathcal{B}^{\text{Fav.NBins}}_{\textit{RN30\_DMv100}}$	J-S div. A_{RN} / γ_{RN}
J0613-0200	*RN10_DMv30*	0.0	$2.31e-03$
			$1.32e-03$
J1012+5307	*RN30_DMv150*	3.1	$2.68e-02$
			$2.99e-02$
J1600-3053	*RN20_DMv100*	−0.3	$4.44e-03$
			$4.03e-03$
J1713+0747	*RN15_DMv150*	6.3	$2.71e-03$
			$1.04e-03$
J1744-1134	*RN10_DMv100*	−0.3	$4.85e-03$
			$4.66e-03$
J1909-3744	*RN10_DMv100*	−0.1	$3.72e-03$
			$1.98e-03$

695 from 2011 to 2020 with NUPPI backends). If this downturn is true, it could have been caused by the processes intrinsic to the neutron star (Goncharov et al. 2020), or a putative GWB produced by eccentric SMBHBs (Chen et al. 2017). We require longer time span to better constrain the lowest frequencies and refine our interpretation.

2.4.2 Extending model selection for stochastic and deterministic signals

Let us now investigate the different red signals presented in Section 2.3. We start with the pulsar stochastic processes by (1) inspecting the presence of the chromatic signals in the data, and (2) performing a model selection to obtain the most favoured signal combination with RN, DMv and Sv. The number of modes selection for Sv process was done in a manner similar to described in the previous section. We have also checked that the selected number of basis functions for RN and DMv is still optimal and it is the case for all pulsars except PSR J1600-3053 which we will discuss separately. Then we probe for specific deterministic signals chosen from previous investigations. In our case, we inspect for an annual chromatic signal in PSR J0613-0200 data and exponential dips in PSR J1713+0747. Eventually, we search for the presence of system and band noise in each pulsar.

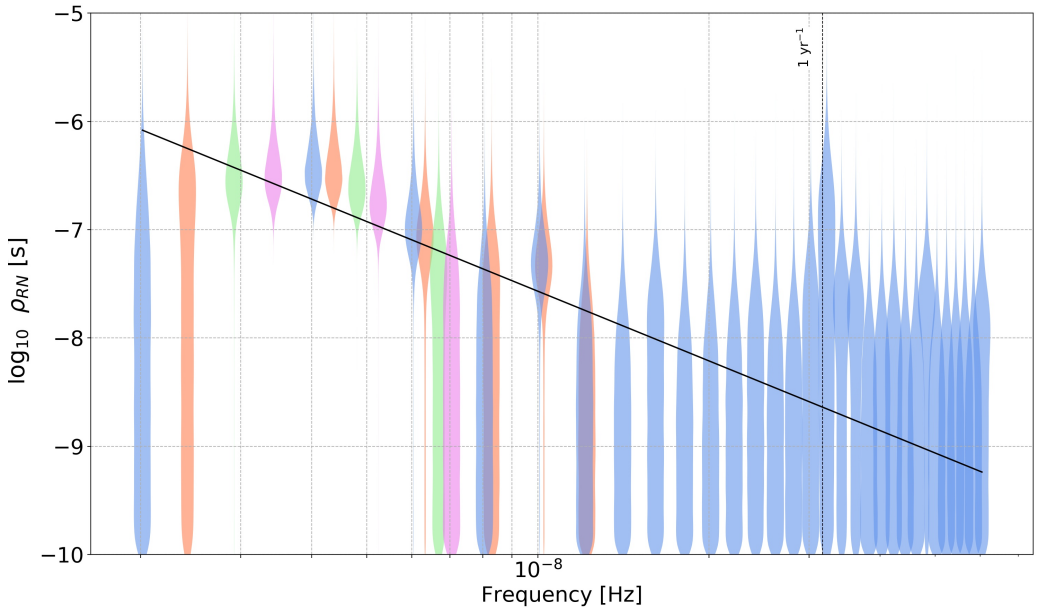

Figure 2.2: Achromatic red-noise spectrum of PSR J1909-3744 using the model *RN30_DMv100*, with a power-law (black solid line drawn with the maximum a posteriori), and four free-spectrum (violin plots) PSDs computed with four different minimum frequencies : $i/\mathrm{T_{span}}$ with $i = 1$ (blue), 1.2 (orange), 1.45 (green) and 1.7 (pink). Here, 30 bins are drawn for the first one, 6 for the second and 3 for the two others.

Stochastic chromatic signals

In the previous subsection we have assumed presence of RN and DMv and concentrated on choosing the number of Fourier modes (basis functions) to describe the noise by a Gaussian Process. Now we fix the number of modes and check if data supports RN, DM and Sv noise components. The probed models and the Bayes factors (with respect to the favourable model given by the bold zeros) are summarized in Table 2.3. Below, we outline the procedure that we have followed.

In parallel to the direct computation of the evidence for each model, we have also conducted the noise diagnostic by using noise model with RN and FCN (free chromatic index), which covers RN (chromatic index $\chi_{\mathrm{FCN}} = 0$), DMv ($\chi_{\mathrm{FCN}} = 2$) and Sv ($\chi_{\mathrm{FCN}} = 4$). The posterior on the chromatic index with *RN_FCN* is given by blue histograms in Fig. 2.3 and in most cases it is centred at 2 indicating presence of DMv, with two exceptions: PSR J1012+5307 (centred at 1.1) and J1909-3744 (centred at 3). We add DMv in our model and repeat analysis with *RN_DMv_FCN*. The FCN captures now the remaining noise not covered by DMv and is presented as red histograms in Fig. 2.3. PSR J1600-3053 shows presence of the scattering noise (spectral index 4). For this pulsar, variable and clumpy scintillation arcs in the secondary spectrum (i.e., power-spectrum of the dynamic spectrum, see e.g., Cordes and Wolszczan 1986) are also seen in L-band in LEAP data (Main

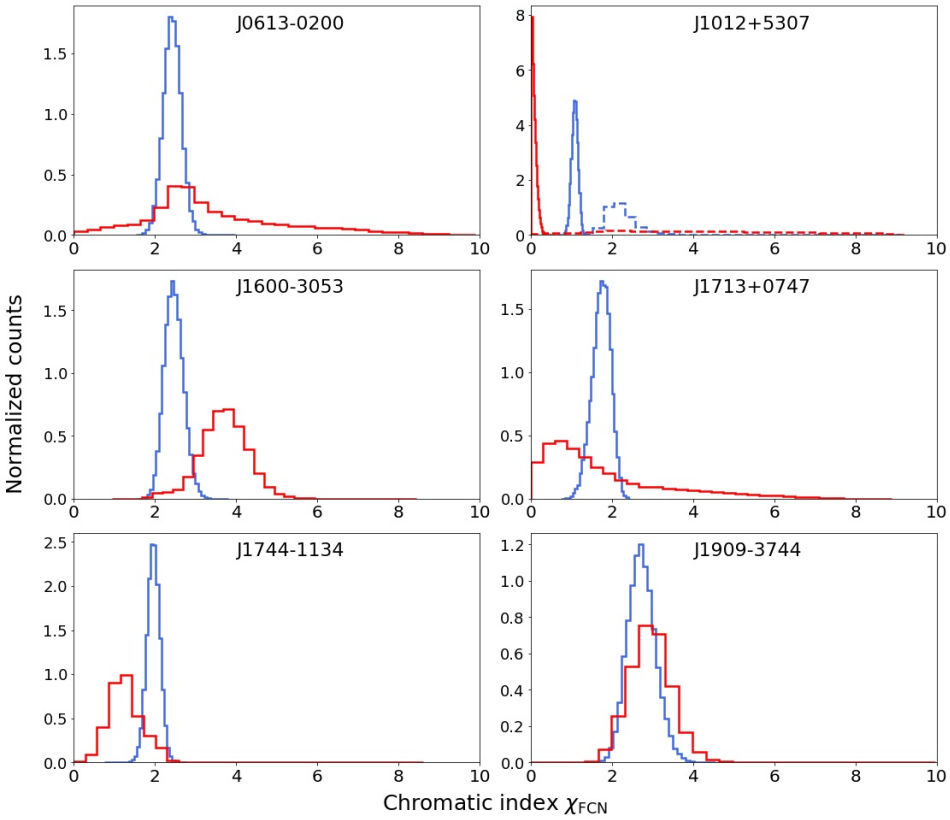

Figure 2.3: Marginalized posterior distributions of chromatic index $\chi_{\rm FCN}$ in *RN_FCN* (solid blue) and *RN_DMv_FCN* (solid red) for the six pulsars. The number of frequency bins for RN and DMv power-law are taken from Table 2.2. For PSR J1012+5307 we performed additional analysis with models *RN150_FCN150* (dashed blue) and *RN150_DMv150_FCN150* (dashed red).

et al. in prep), with power extending up to 16 μs in delay, and averaged time delays at 100ns level. These results add more confidence for the inclusion of this process, and indeed its presence is confirmed by the Bayes factor. However, including Sv into the noise model absorbs most of the red noise and its presence is not conclusive (as indicated in the table). PSRs J0613-0200, J1713+0747 and J1744-1134 show no sign of the scattering variations noise. The chromatic index remains unchanged for J1909-3744, and the model selection indicates (though not very strongly) the presence of both DMv and Sv.

It is important to see how the inclusion of Sv changes the RN properties. In Fig. 2.4 we give the corner plot for the RN parameters for two models *RN_DMv* in blue, *RN_DMv_Sv* in red for the two pulsars favouring Sv. As mentioned above the data is non-informative on the presence of RN in PSR J1600-3053 if we add Sv to the model and this can be seen in the left panel as a poorly constrained posterior (red). For J1909-3744, the inclusion of Sv is less drastic: we see that it absorbs a small part of RN at very low frequencies reducing the spectral index but pushing the amplitude slightly up.

Table 2.3: Model selection for the stochastic chromatic signals. This table contains the log-10-based Bayes factors of the highest evidence model ($\log_{10}\mathcal{B} = 0.0$) over set of other models that we have tried (given in columns). The selected model is indicated in bold. We have used 150 Fourier modes for RN in PSR J1012+5307 and 2 exponential dips are always included in analysis of PSR J1713+0747.

Pulsar	*RN*	*DMν*	*Sν*	*RN_DMν*	*RN_Sν*	*DMν_Sν*	*RN_DMν_Sν*
J0613-0200	−12.5	−10.3	−37.7	**0.0**	−2.2	−1.7	−0.3
J1012+5307	−25.0	−63.0	−143.7	**0.0**	−2.0	−47.5	0.4
J1600-3053	−146.1	−10.2	−59.3	−6.5	−9.1	**0.0**	0.0
J1713+0747	−36.8	−42.6	−125.0	**0.0**	−30.0	−28.5	−0.8
J1744-1134	−12.1	−3.1	−27.9	**0.0**	−10.7	−2.4	−1.8
J1909-3744	−66.7	−82.1	−244.4	−2.1	−3.4	−21.0	**0.0**

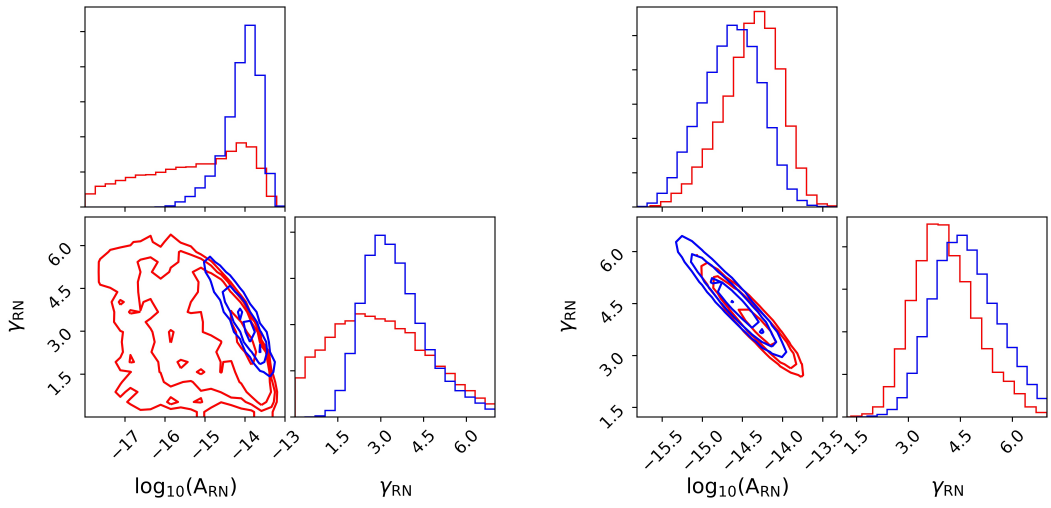

Figure 2.4: 2D distributions of achromatic red-noise amplitude and spectral index. Left plot: J1600-3053, the model *RN_DMν* is in blue and *RN_DMν_Sν* is red ; Right plot: J1909-3744, with *RN_DMν* in blue and *RN_DMν_Sν* (favourable) in red.

Peculiar red noise in PSR J1012+5307

PSR J1012+5307 requires a special investigation given the rather strong signal in model *RN_DMν_FCN* displayed in Fig. 2.3 with chromaticity index close to zero. It turned out to be unaccounted achromatic red noise at high frequencies. In our analysis for the number of Fourier components we have concentrated at the low frequencies (up to 30 bins) for RN and, presently, the FCN in *RN_DMν_FCN* picks up the excess red noise which seems to extend also to high frequencies.

Based on these findings we have revisited the selection of Fourier modes done in Section 2.4.1 for this pulsar by allowing RN to go up to 150 Fourier bins. The favoured model *RN150_DMν30* has a Bayes factor $\log_{10}\mathcal{B}^{RN150\_DM\nu30}_{RN30\_DM\nu150} = 29.8$ over the previous one, and therefore we adopt it in further investigations. In Fig. 2.5 we show the evolution of the red noise parameters (amplitude and spectral index) as we move from *RN30_DMν150* (blue) to the new model *RN150_DMν30* (red). The parameters of the RN process are better constrained, the red noise is significantly shallower (to accommodate the high frequency contribution) but the amplitude is slightly higher. The free spectrum estimation for this pulsar can be seen in Fig, 2.9: second panel from the top, right. One can clearly see the low frequency red noise (well constrained power at three lowest Fourier bins) however we also observe significant fluctuations at higher frequencies. The high frequency red noise is also evident in the time realization of this signal in the left plot. The red noise at high frequencies flattens out the power-law of the overall RN process. However, we do not exclude the possibility of two component red noise of different origin.

Using this number of modes, we have repeated analysis of the data with *RN150_FCN150* and *RN150_DMν30_FCN150* models. The results are presented in Fig. 2.3) as dashed lines confirming that *RN150_DMν30* is sufficient to describe the data. The green histogram in Fig. 2.5 shows that adding Sv does not change properties of RN process..

Deterministic chromatic signals

The scattering and scintillation effects for J0613-0200 have been studied in Main et al. 2020, which also discusses the presence of annual variations of the arc curvatures. Furthermore, Keith et al. 2013 has shown the presence of annual chromatic signals which were reported in Goncharov et al. 2021, suggesting presence of a noise model that contains annual DM process (i.e., $\chi_y = 2$). However we did not find a conclusive evidence for presence of this signal with Bayes factor $\mathcal{B}^{RN\_DM\nu\_AnnualDM}_{RN\_DM\nu} = 8.3$, $\mathcal{B}^{RN\_DM\nu\_AnnualSv}_{RN\_DM\nu} = 7.0$ which we do not consider significant to justify its inclusion in the noise model. Note that (at least part of) annual variations in the timing residuals might be absorbed by the TM parameter fit (through the pulsar sky position and proper motion).

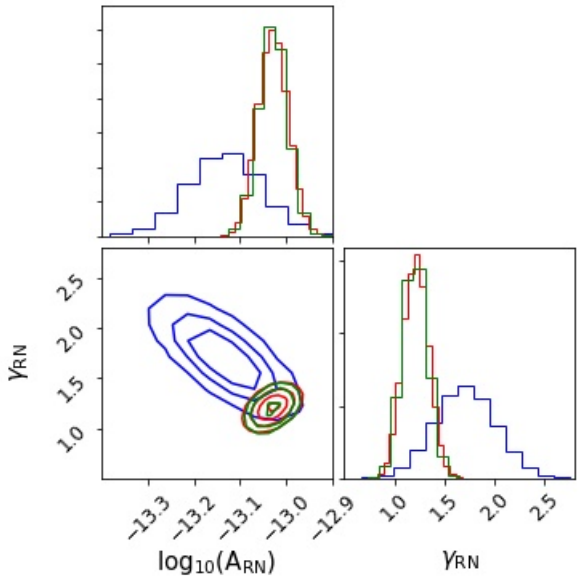

Figure 2.5: 2D distribution of achromatic red-noise amplitude and spectral index for J1012+5307 with the following noise models *RN30_DMv150* (blue), *RN150_DMv30* (red) & *RN150_DMv30_SV150* (green).

As for the exponential dip events, we have found their presence in PSR J1713+0747 data with high statistical confidence: the log-10 Bayes factor is 30.5, 13.9 and 46.8 favouring model that includes respectively one single event at MJD 54757, one single event at MJD 57510 and both those events together. We found a chromatic index very consistent with scattering variations ($\chi_{E_1} = 4.07^{+1.77}_{-1.13}$, error corresponds to 68% confidence interval) for the first event (left panel of Fig. 2.6), and evaluated to $\chi_{E_2} = 1.00^{+0.56}_{-0.49}$ for the second one. The index for the second event is consistent with Goncharov et al. 2021 that reported a profile change for this event and proposed a cause linked with the pulsar's magnetosphere instead of an IISM process. The posteriors for both events are presented in Fig. 2.6. Note that the posteriors of t_0 for both epochs are sharply constrained between the two consecutive ToAs that surround the actual event dates and it is not railing against the prior range (see Table 2.1). For the rest of this work, we fix the chromatic indexes of both events at 4 and 1 as discussed above.

System and Band noise

The dataset for each pulsar is made from the combination of ToAs produced with different receiver systems integrated in different radio telescopes. It might happen that one (or several) of these systems unexpectedly introduce extra noise, the idea of the system-noise

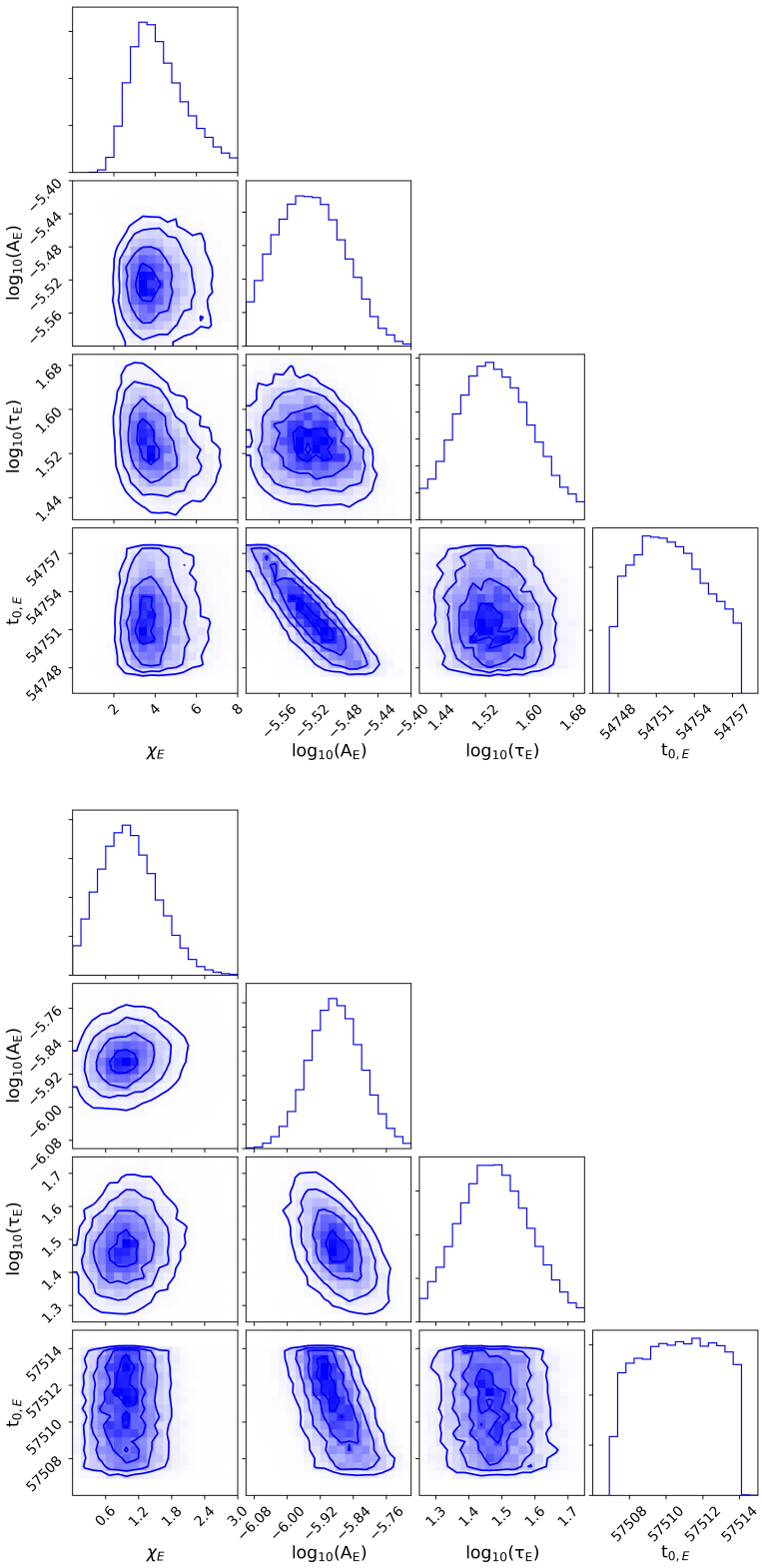

Figure 2.6: Posterior distributions for the exponential dips found in J1713+0747 at MJD 54757 (top) at MJD 57510 (bottom). The chromatic index χ_E was used as a model parameter.

model is to check this hypothesis.

In EPTA we use a large number of systems, checking each of them in turn is computationally prohibitive. Instead we have used an approach based on the hyper-model selection (Hee et al. 2015) to check for the presence of a system noise. We introduce a switch (inclusion) parameter which regulates whether to include or not a particular system noise component in the total model. The posterior of this parameters indicates probability of having red noise across the systems.

For this analysis, we exclude systems that have less than 3 years of time span for any of the 6 pulsars. The selection comprises JBO.DFB.1400, JBO.DFB.1520, WSRT.P1.323.C, WSRT.P1.367.C, WSRT.P1.840.C, WSRT.P1.1380.C, WSRT.P1.1380.1, WSRT.P1.1380.2.C, NRT.BON.1600 and NRT.NUPPI.1854. We also do not investigate NRT.NUPPI.2154, which contributes $\sim$ 2.4 years for J1600-3053 and about 4.7 years for J1909-3744, but with 16 epochs distributed in 1.1 year, and only 2 epochs 4.6 years after.

The dataset of PSR J1909-3744 is composed by ToAs produced only from NRT observations, with three systems (BON backend) before and four (NUPPI backend) after MJD $\sim$ 55812. This means that any possible system red noise is totally correlated with RN and is absorbed in that model.

In Table 2.4 we report the log-10 of the inclusion parameter (which should be proportional to the Bayes factor), where a large number corresponds to a very likely presence of red-like system noise.

We observe three systems NRT.NUPPI.1484, JBO.ROACH.1520 & LEAP.1396 with a significant inclusion factor (10^5, 10^4 and 10^4 respectively). We notice that these three systems observe in the L-band, between 2011 and 2020, which corresponds to the major part of the datasets. The first two of the above mentioned systems (especially NRT.NUPPI.1484) are the largest contributor to EPTA data and LEAP.1396 produces the ToAs with the lowest uncertainties (mean at 1.86 μs for PSR J1012+5307 and lower than 0.55 μs for others). For PSR J1713+0747 two additional systems (EFF.S110.2639 and NRT.BON.2000) show sign of the system noise, and it might also be present in NRT.NUPPI.2539 for PSRs J1012+5307 and J1744-1134.

The systems with an inclusion factor above 10 (presented in bold in Table 2.4) were selected for a detailed analysis of all possible combinations of system noise. We have found that DM-type chromatic system noise (DM-SN) is always favoured (in terms of Bayes factor) over the achromatic SN for NRT.NUPPI.1484 system and it is included in the total noise budget for PSRs J0613-0200, J1012+5307, J1713+0747 and J1744-1134. It is not entirely clear why the data does not support its presence in J1600-3053 (where we have identified SN only in LEAP.1396). One plausible explanation is that NRT.NUPPI.1484

Table 2.4: Inclusion factors values (in decimal log-scale) for the achromatic system noise. Considered systems are given in the second column.

Radio band	System	J0613-0200	J1012+5307	J1600-3053	J1713+0747	J1744-1134	J1909-3744
Band.1 <1 GHz	WSRT.P1.328	−0.18	−0.23	-	-	-	-
	WSRT.P1.328.C	−0.23	−0.07	-	-	-	-
	WSRT.P1.382	−0.07	−0.10	-	-	-	-
	WSRT.P1.382.C	−0.02	−0.01	-	-	-	-
	WSRT.P1.840	-	-	-	−0.15	-	-
	WSRT.P1.840.C	-	-	-	−0.07	-	-
	WSRT.P2.350	-	−0.11	-	−0.16	-	-
Band.2 [1,2] GHz	EFF.EBPP.1360	−0.16	−0.15	-	0.24	−0.23	-
	EFF.EBPP.1410	0.41	−0.16	-	−0.18	−0.36	-
	EFF.P200.1380	-	0.54	-	-	-	-
	EFF.P200.1400	−0.08	-	−0.28	-	-	-
	EFF.P200.1400.np	-	-	-	−0.44	-	-
	EFF.P217.1380	-	0.26	-	-	-	-
	EFF.P217.1400	−0.09	-	−0.29	0.32	−0.14	-
	EFF.P217.1400.np	-	-	-	−0.09	-	-
	JBO.ROACH.1520 (JBO_1.5)	**1.93**	**2.48**	0.01	≥ **5.00**	≥ **5.00**	-
	LEAP.1396 (LEAP_1.4)	≥ **5.00**	0.42	≥ **5.00**	≥ **5.00**	≥ **5.00**	-
	NRT.BON.1400	0.66	−0.23	−0.27	−0.13	0.62	−0.33
	NRT.NUPPI.1484 (NUP_1.4)	≥ **5.00**	**2.65**	**3.80**	≥ **5.00**	≥ **5.00**	−0.41
	WSRT.P1.1380	−0.21	-	-	-	-	-
	WSRT.P1.1380.2	-	−0.18	-	−0.22	-	-
	WSRT.P2.1380	−0.01	−0.13	−0.28	0.56	−0.16	-
Band.3 [2,3] GHz	EFF.EBPP.2639	0.05	−0.29		−0.20	−0.19	-
	EFF.S110.2487	-	−0.30	-	-	−0.17	-
	EFF.S110.2639	0.08	-	−0.25	**2.63**	-	-
	NRT.BON.2000 (BON_2.0)	−0.24	−0.23	−0.01	≥ **5.00**	−0.31	−0.30
	NRT.NUPPI.2539 (NUP_2.5)	−0.23	**1.53**	−0.34	−0.24	**1.48**	−0.40
	WSRT.P1.2273.C	-	-	-	−0.10	-	-
	WSRT.P2.2273	-	-	-	−0.03	-	-
Band.4 >3 GHz	EFF.S60.4850	-	-	-	−0.06	-	-
	EFF.S60.4857	-	−0.16	-	-	0.13	-

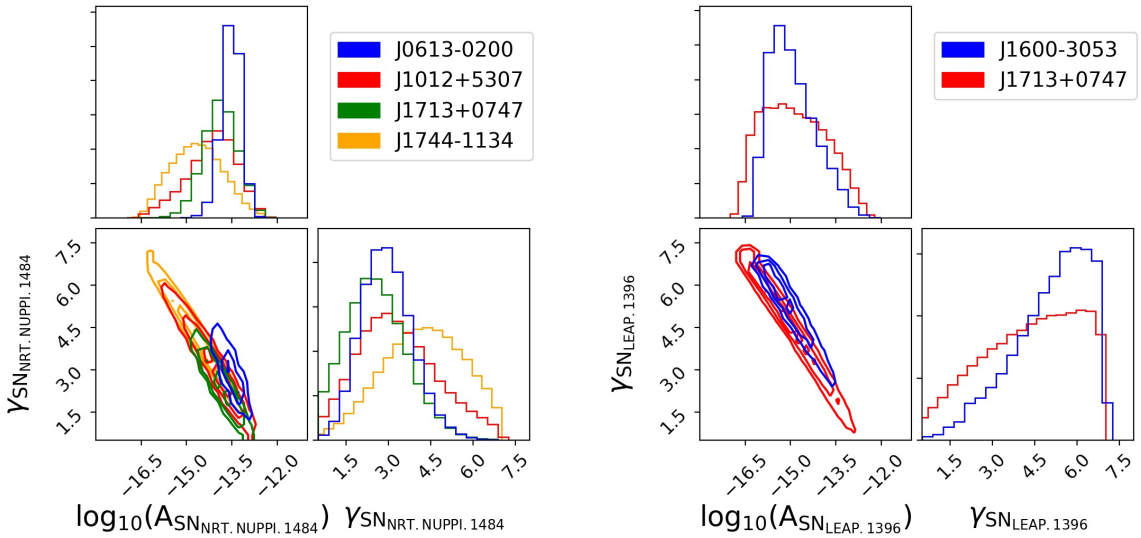

Figure 2.7: 2D distributions of amplitude and spectral slope of NRT.NUPPI.1484 DM-SN (top) and LEAP.1396 SN (bottom), using the final favored model for each pulsar.

ToAs dominate the data of this pulsar and we cannot clearly disentangle SN from RN, we would need the data from other PTAs to test this assumption (that is a plan for the future IPTA data combination).

Polarization calibration errors and radio frequency interferences are possible causes for system noise. Parameter posteriors for SN for NRT.NUPPI.1484 and LEAP.1396 (Figure 2.7) display overall consistency across pulsars, which corroborates for an assumption of a red noise specific to these systems. We should emphasize again the presence of data from other systems (like it is expected in IPTA data) should greatly help to identify the system noise and disentangle it from the RN as it was shown in Lentati et al. 2016 for PSR J1730-2304 using IPTA DR1 dataset.

The results of the system noise selection is given in Table 2.5: inclusion of the system noise lead to log-10 Bayes factors (15.9, 7.4, 13.8, 118.1 & 18.6) for PSRs J0613-0200, J1012+5307, J1600-3053, J1713+0747 and J1744-1134 respectively .

We switch now to the band noise investigation. The main radio frequency bands (cf. Table 2.4) in the datasets are Band.2 and Band.3, which contain the bulk of observations for each pulsar. Band.1 and Band.4 are only covered by one telescope: WSRT and Effelsberg respectively. Like for SN we do not investigate for BN if the corresponding time span of observations is less than three years.

We found evidence of the band noise only in Band.3 of PSRs J1713+0747 and Band.2 of J1744-1134 with corresponding log-10 Bayes factors of 6.5 and 6.2. This result is somewhat

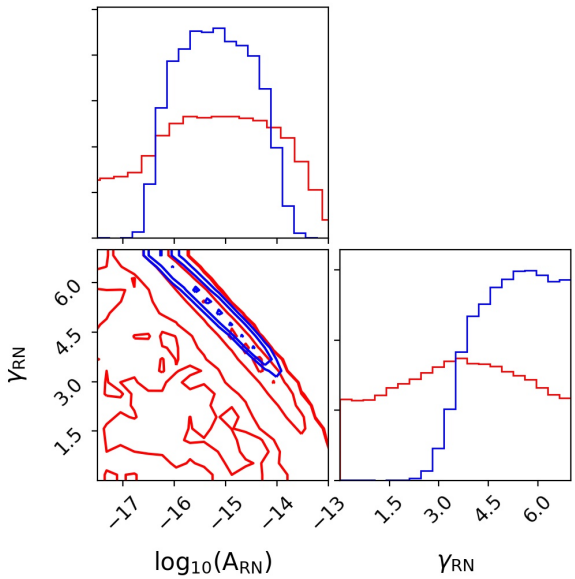

Figure 2.8: 2D posterior distribution of the red-noise parameters for PSR J1744-1134 with models *RN_DMv* (blue) and the most favored, *RN_DMv_SN_BN* (red).

consistent with Goncharov et al. 2021, where Band-noise for both Band,2 and Band.3 were reported for these 2 pulsars. However, we have found that the inclusion of Band.2 for PSR J1713+0747 and Band.3 for PSR J1744-1134 results to insignificant log-10 Bayes factors, 0.6 in both cases. All these again points to the importance of IPTA data combination for the noise analysis. Our results for BN are summarized in Table 2.5.

Poor constraint on RN for PSR J1744-1134

We have revisited Table 2.3 after finding and fixing the set of noise sources in each pulsar. We have noticed that the RN for PSR J1744-1134 becomes poorly constrained using *RN_DMv_SN_BN* model (see red histograms in Fig. 2.8). After further investigation, we have found that the Bayes factor $\mathcal{B}^{RN\_DMv\_SN\_BN}_{DMv\_SN\_BN} = 2$ hardly supports the presence of the RN. Similar result was found in Goncharov et al. 2021, where the RN of this pulsar does not enter the favoured noise model. As another confirmation, the time-domain noise realizations of the red noise signal (see Fig. 2.9) is quite reduced for *RN_DMv_SN_BN* model (light grey) as compared to *RN30_DMv100* (red). We have decided to keep the *RN_DMv_SN_BN* model (as a conservative assumption), however we will address its impact when we discuss the common red noise.

2.4.3 Summary of the model selection

The results of the noise model selection for each pulsar are summarized in Table 2.5. We report the red noise (RN) parameters within each model giving median and 95% confidence interval. We also compare the custom-build noise model (M2) with the default noise model (M1) used in Chen et al. 2021. We quote the log-10 Bayes factors showing strong preference of a custom noise model (ranging from 2 to 195). The biggest impact on the Bayes factor was caused by inclusion of the SN and BN noise components. Finally we have evaluated the Anderson-Darling diagnostics A^2 Anderson and Darling 1952 applied to the whitened residuals. While Bayes factor measures the relative closeness of the whitened residuals to Gaussian distribution, it does not tell us if the final result is actually Gaussian (in other words, if the favoured model is actually good). The Anderson-Darling statistic addresses precisely this question. As a guidance: $A^2 = 2.5$ is a value at which one fails to reject the null hypothesis (i.e., following Gaussian distribution) at 95% confidence interval. A lower value of the statistic corresponds to a better agreement with Gaussian distribution. We see the overall improvement for M2 model. The high values for PSR J1713+0747 could be caused by a few outliers in the whitened residuals. To test this assumption, we recompute the statistic after removing outliers found with Grubbs' test Grubbs 1950 which becomes 3.2 and 2.1 for respectively M1 (with 9 outliers) and M2 (with 6 outliers). The Anderson-Darling statistic for PSR J1744-1134 reduces to 1.0 if we exclude RN from the favourable (M2) model.

In preparation for the next section where we consider common red noise, we investigate how much the white noise parameters impact the measurement of the RN. Following Lentati et al. 2015, we have performed the noise analysis with all white noise parameters fixed to the maximum-likelihood values and compare the RN posteriors with previously obtained results. The results are quoted as Jensen-Shannon divergences (last column of Table 2.5) showing a very good consistency (J-S $div < 3 \times 10^{-3}$), and therefore confirm that we can safely fix white noise parameters for the further investigations.

2.4.4 Conclusion

We used a general Bayesian inference approach to select the most favoured noise model for each pulsar of EPTA DR2. These models are summarized in Table 2.5 and show a significant improvement (in terms of Bayes factor) over the default base model used in Chen et al. 2021. In addition to conventional stochastic processes such as achromatic red noise (RN) and dispersion measurement variations (DMv), we have considered scattering variations (Sv), system noise (both chromatic SN-DMv and achromatic SN), band noise (BN) and two deterministic signals (annual DMv, annual Sv and DM event). Our model selec-

Table 2.5: Final noise models for the six pulsars in EPTA DR2. The third and fourth columns show the median of the RN amplitude (A_{RN}) and spectral slope (γ_{RN}), with corresponding 95% confidence interval. The fifth column displays the $\log_{10}$ Bayes factors of the custom model over the model *RN30_DMv100*. The sixth and seventh columns show the Anderson-Darling statistics applied to the whitened residuals for (1) *RN30_DMv100* and (2) the selected noise model. The last column contains Jensen-Shannon divergences of RN amplitude and spectral index posteriors of the selected noise model with the same model but fixed white-noise parameters.

Pulsar	Sel. model	A_{RN}	γ_{RN}	$\log_{10} \mathcal{B}^{M2}_{M1}$	A^2_{M1}	A^2_{M2}	J-S div_{WNf} A_{RN} / γ_{RN}
J0613-0200	*RN10 DMv30* *DMv-SN_NUP_1.4*	$-14.93^{+1.26}_{-1.17}$	$5.07^{+1.83}_{-2.34}$	15.9	0.4	0.3	$2.36e-03$ $1.82e-03$
J1012+5307	*RN150 DMv30* *DMv-SN_NUP_1.4* *SN_NUP_2.5*	$-13.03^{+0.08}_{-0.08}$	$1.16^{+0.32}_{-0.29}$	40.7	1.8	1.4	$6.60e-04$ $3.80e-04$
J1600-3053	*DMv30 Sv150* *SN_LEAP_1.4*	-	-	20.0	0.3	0.2	- -
J1713+0747	*RN15 DMv150* 2 *Exp. dips* *DMv-SN_NUP_1.4* *SN_JBO_1.5* *SN_LEAP_1.4* *SN_BON_2.0* *BN_Band.3*	$-14.50^{+0.51}_{-0.86}$	$3.94^{+1.82}_{-1.13}$	195.4	5.5	4.1	$1.76e-03$ $1.92e-03$
J1744-1134	*RN10 DMv100* *DMv-SN_NUP_1.4* *BN_Band.2*	$-15.31^{+2.03}_{-2.50}$	$3.68^{+3.13}_{-3.46}$	22.6	1.0	1.2	$4.39e-03$ $1.79e-03$
J1909-3744	*RN10 DMv100 Sv150*	$-14.45^{+0.66}_{-0.85}$	$4.22^{+2.16}_{-1.65}$	2.1	0.8	0.6	$3.10e-04$ $3.20e-04$

tion was guided by previously published investigations or using auxiliary runs that helped to identify the list of models for further consideration.

The process of the model selection has permitted us to obtain several interesting results.

(i) PSR J1909-3744 shows sign of downturn in its spectrum at low frequencies. This feature could be confirmed or disproved with a longer observational span.

(ii) PSR J1012+5307 indicates the presence of high level red noise at high frequencies of unclear origin.

(iii) PSR J1600-3053 and J1744-1134 are not very informative about the presence of achromatic red noise (RN), giving only a small preference to the models with RN.

(iv) We did not observe strong evidence for the annual DNv signal previously reported for PSR J0613-0200.

(v) We found that the first exponential dip of PSR J1713+0747 has a chromatic index consistent with scattering variations, and confirmed the low chromatic index for the second event.

In this work we have emphasized several times the need to combine the data from multiple systems (to disentangle SN and RN processes) and multi-band observations (disentangling achromatic and chromatic red noise). This gives a strong reason for a joint analysis of combined IPTA data.

In the Appendix we show RN free spectrum with the default model *RN30_DM100* and its time-domain realization for each pulsar. We also proved a Table 2.6 with parameters of all noise components.

Appendix A: Achromatic red-noise properties

Here we provide additional plots which demonstrate our main findings about the RN in each pulsar.

We reconstruct time-domain Gaussian process realizations of this signal modelled with a power-law PSD. The left panels of Fig. 2.9 display the 68% confidence interval of 100 random realizations drawn from the posterior distributions of the RN amplitude and spectral index included in two different single-pulsar noise models : the default base *RN30_DMv100* (red) and the "custom" model shown in Table 2.5 (grey). The peculiar high frequency red noise is clearly seen in PSR J1012+5307 (see Section 2.4.2 for detailed discussion). The RN in PSR J1744-1134 is considerably reduced in the "custom" model (see discussion at the end of Section 2.4.2). Note that we did not include RN in the custom

model of PSR J1600-3053. The RN in the default and custom models are quite similar for PSRs J0613-0200, J1713+0747 and J1909-3053.

The right panels of Fig. 2.9 display the spectrum of the achromatic red-noise (using *RN30_DMv100*) for each pulsar computed with (1) a free-spectrum PSD (grey violins), and (2) a broken-power law PSD (blue), where we give 1000 realizations randomly drawn from the posterior distributions.

Appendix B: Single-pulsar noise model parameters

In the Table 2.6 we give median values for each noise component with 68% confidence interval in the custom model of each pulsar.

Figure 2.9: (left panels) 68% confidence interval of 100 time-domain random realizations of the achromatic red-noise included in the default base (*RN30_DM100*) model (red) and the "custom" selected models (light grey) (cf. Table 2.5) for each of the six pulsars. (right panels) Achromatic red-noise spectrum for the corresponding pulsar (noted in left panel) included in the default base model and described with (1) a free-spectrum PSD (grey violins) or (2) a broken power-law (blue), here showing 1000 random realizations drawn from the posterior distributions. The figure continues on the next page.

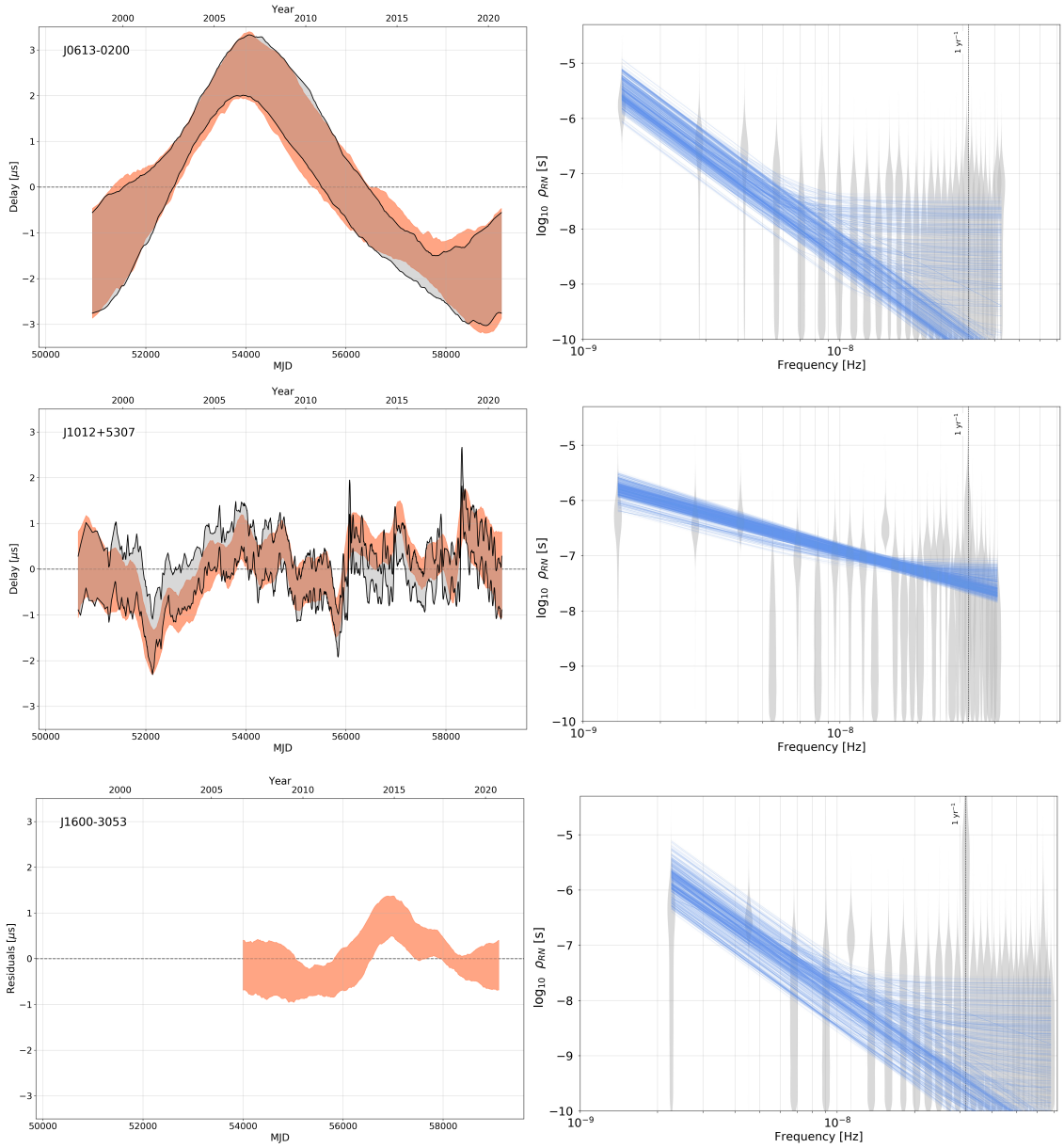

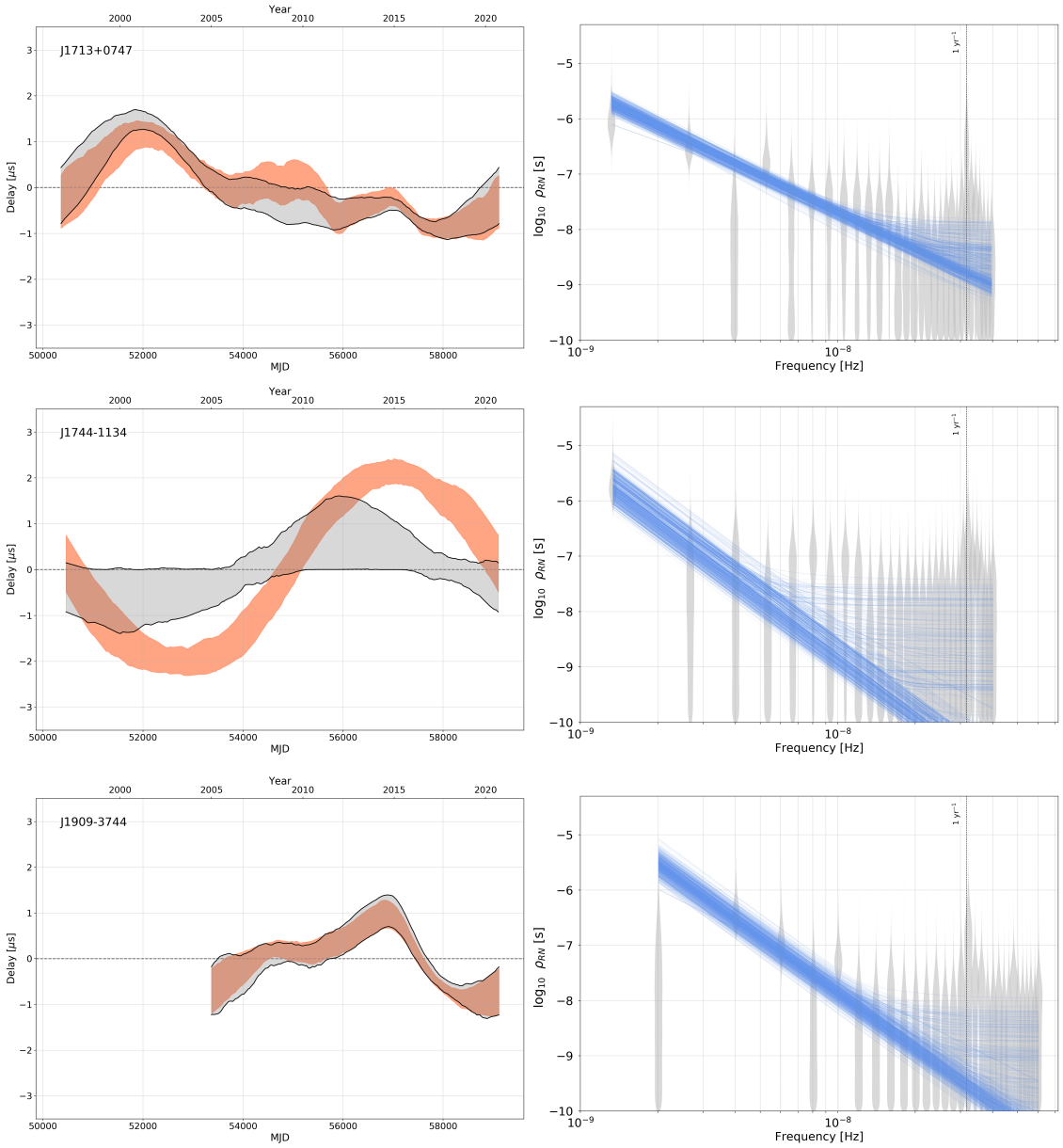
J1713+0747
J1744-1134
J1909-3744
Year
MJD
Delay [μs]
Frequency [Hz]
log10 ρRN [s]
1 yr−1

Table 2.6: Medians and 68% credible intervals of the 1D marginalized posterior distributions of each single-pulsar noise model parameters for (i) the default base models used in Chen et al. 2021 and (ii) the final custom models. Note that *DMν* amplitudes are given with ENTERPRISE normalization.

Model	Signal	parameter	J0613-0200	J1012+5307	J1600-3053	J1713+0747	J1744-1134	J1909-3744
Default	*RN*	$\log_{10}A$	$-14.72^{+0.56}_{-0.60}$	$-13.12^{+0.08}_{-0.08}$	$-14.05^{+0.33}_{-0.53}$	$-14.13^{+0.18}_{-0.19}$	$-15.16^{+0.69}_{-0.72}$	$-14.65^{+0.32}_{-0.37}$
		γ	$4.76^{+1.09}_{-1.04}$	$1.66^{+0.32}_{-0.30}$	$3.50^{+1.22}_{-0.89}$	$3.29^{+0.54}_{-0.47}$	$5.19^{+1.10}_{-1.09}$	$4.65^{+0.96}_{-0.83}$
	DMν	$\log_{10}A$	$-13.75^{+0.21}_{-0.26}$	$-13.36^{+0.05}_{-0.05}$	$-13.09^{+0.04}_{-0.04}$	$-13.47^{+0.04}_{-0.04}$	$-13.33^{+0.05}_{-0.05}$	$-13.56^{+0.04}_{-0.04}$
		γ	$2.89^{+0.66}_{-0.59}$	$1.20^{+0.18}_{-0.16}$	$2.08^{+0.12}_{-0.11}$	$1.49^{+0.20}_{-0.19}$	$1.23^{+0.21}_{-0.21}$	$1.53^{+0.15}_{-0.14}$
Custom	*RN*	$\log_{10}A$	$-14.82^{+0.64}_{-0.67}$	$-13.02^{+0.03}_{-0.03}$	-	$-14.48^{+0.25}_{-0.30}$	$-15.25^{+1.31}_{-1.39}$	$-14.46^{+0.36}_{-0.41}$
		γ	$4.81^{+1.17}_{-1.15}$	$1.19^{+0.13}_{-0.13}$	-	$3.95^{+0.65}_{-0.56}$	$3.67^{+2.17}_{-2.22}$	$4.24^{+1.03}_{-0.88}$
	DMν	$\log_{10}A$	$-13.58^{+0.16}_{-0.21}$	$-13.66^{+0.12}_{-0.14}$	$-14.16^{+0.32}_{-0.41}$	$-13.78^{+0.05}_{-0.06}$	$-13.45^{+0.07}_{-0.07}$	$-13.92^{+0.27}_{-1.21}$
		γ	$2.47^{+0.55}_{-0.47}$	$2.09^{+0.42}_{-0.39}$	$4.69^{+0.92}_{-0.76}$	$1.16^{+0.20}_{-0.21}$	$0.46^{+0.36}_{-0.30}$	$2.64^{+2.67}_{-0.93}$
	Sν	$\log_{10}A$	-	-	$-13.26^{+0.04}_{-0.04}$	-	-	$-13.84^{+0.10}_{-0.19}$
		γ	-	-	$1.48^{+0.14}_{-0.13}$	-	-	$0.78^{+0.31}_{-0.34}$
	Exp. dip 1	$\log_{10}A$ [s]	-	-	-	$-5.54^{+0.05}_{-0.04}$	-	-
		$\log_{10}\tau$ [day]	-	-	-	$1.54^{+0.07}_{-0.07}$	-	-
		t_0 [MJD]	-	-	-	$54752.49^{+3.24}_{-3.17}$	-	-
	Exp. dip 2	$\log_{10}A$ [s]	-	-	-	$-5.89^{+0.05}_{-0.05}$	-	-
		$\log_{10}\tau$ [day]	-	-	-	$1.51^{+0.09}_{-0.09}$	-	-
		t_0 [MJD]	-	-	-	$57510.65^{+2.17}_{-2.20}$	-	-
	SN_BON_2.0	$\log_{10}A$	-	-	-	$-14.78^{+1.03}_{-0.97}$	-	-
		γ	-	-	-	$4.36^{+1.59}_{-1.80}$	-	-
	SN_JBO_1.5	$\log_{10}A$	-	-	-	$-13.10^{+0.21}_{-0.22}$	-	-
		γ	-	-	-	$1.47^{+0.68}_{-0.65}$	-	-
	SN_LEAP_1.4	$\log_{10}A$	-	-	$-14.97^{+0.94}_{-0.66}$	$-13.42^{+0.20}_{-0.21}$	-	-
		γ	-	-	$5.16^{+1.19}_{-1.75}$	$1.70^{+0.60}_{-0.59}$	-	-
	DMν-SN_NUP_1.4	$\log_{10}A$	$-13.52^{+0.29}_{-0.33}$	$-14.10^{+0.72}_{-0.91}$	-	$-14.05^{+0.63}_{-0.64}$	$-14.65^{+0.99}_{-1.03}$	-
		γ	$2.88^{+0.95}_{-0.85}$	$3.17^{+1.60}_{-1.31}$	-	$2.75^{+1.20}_{-1.14}$	$4.23^{+1.68}_{-1.75}$	-
	SN_NUP_2.5	$\log_{10}A$	-	$-13.22^{+0.73}_{-1.03}$	-	-	-	-
		γ	-	$2.50^{+1.84}_{-1.44}$	-	-	-	-
	BN_Band.2	$\log_{10}A$	-	-	-	-	$-13.84^{+0.35}_{-0.42}$	-
		γ	-	-	-	-	$3.02^{+0.86}_{-0.77}$	-
	BN_Band.3	$\log_{10}A$	-	-	-	$-14.32^{+0.37}_{-0.48}$	-	-
		γ	-	-	-	$2.68^{+1.02}_{-0.87}$	-	-

CHAPTER 3

INSPECTING THE PRESENCE OF A STOCHASTIC GWB WITH EPTA AND IPTA DATASETS

Abstract

This Chapter is focused on the search of the GWB with PTAs. It begins with a description of the expected signal from a GWB and a brief historic on the past results, followed by the formulation of the multi-pulsar likelihood and CRS models in PTAs. The third section presents the results reported in Chen et al. 2021 on the search of a GWB with the EPTA DR2, for which I have participated on the data analyses and part of the redaction. The fourth section is the part of Chalumeau et al. 2021 (submitted to MNRAS) which focuses on the application of the single-pulsar noise model selection (see Chapter 2) for the GWB search. The fifth section presents results from Antoniadis et al. 2022 (submitted to MNRAS) which focused on the search of a GWB with the IPTA DR2. I have participated to the data analysis part of this project, and particularly on the application of the phase shift method used to evaluate the correlated signals. The last section briefly describes the promising perspectives toward a detection in the next coming years.

3.1 Introduction

The incoherent superposition of gravitational waves (GWs) from the population of nearby inspiralling supermassive black hole binaries (SMBHBs) should lead to a stochastic gravitational wave background (GWB), the most anticipated GW signal in the nanohertz frequency band (Rajagopal and Romani 1995, Wyithe and Loeb 2003, Sesana et al. 2004). There are other sources of very-low frequency GWB such as cosmic strings (Kibble 1976, Sanidas et al. 2012), first order phase transitions (Caprini et al. 2009) or the 'relic' GWs produced by quantum fluctuations in the early Universe (Grishchuk 1976, Grishchuk 2005). The signal of a very-low frequency GWB imprints specific spatial correlations in the timing residuals. In the case of an isotropic GWB, the correlation pattern predicted by General Relativity is described by the Hellings-Downs (HD) curve (Hellings and Downs 1983) shown in Fig. 3.1. In case of anisotropic GWB, the correlated signal no longer depends on the angular separation between the pulsars, but on the position of each pulsar compared to the anisotropic GWB distribution in the sky (Taylor et al. 2015). In any case, we focus solely on an isotropic stochastic backgroung assuming General Relativity in this manuscript.

The dimensionless characteristic strain spectrum of the GWB is given as a power-law (Jenet et al. 2006) with a reference frequency at 1 yr^{-1}:

$$h_c(f) = A_{\mathrm{GWB}} \left(\frac{f}{\mathrm{yr}^{-1}}\right)^{\alpha_{\mathrm{GWB}}}, \tag{3.1}$$

where A_{GWB} and α_{GWB} are respectively the GWB strain amplitude and spectral index.

One can express the corresponding power-law power spectral density (PSD) $S_P^{\mathrm{GWB}}(f)$ as

$$\begin{aligned} S_P^{\mathrm{GWB}}(f) &= \frac{1}{12\pi^2}\frac{1}{f^3}\, h_c^2(f) \\ &= \frac{A_{\mathrm{GWB}}^2}{12\pi^2}\left(\frac{f}{\mathrm{yr}^{-1}}\right)^{-\gamma_{\mathrm{GWB}}} \mathrm{yr}^3, \end{aligned} \tag{3.2}$$

with $\gamma_{\mathrm{GWB}} = 3 - 2\alpha_{\mathrm{GWB}}$.

The spectrum slope from a population of SMBHBs on circular and GW-driven orbits (Jaffe and Backer 2003, Chen et al. 2017) is expected to be $\alpha_{\mathrm{GWB}} = -2/3$, or $\gamma_{\mathrm{GWB}} = 13/3$. In this thesis, the tilde sign is used to denote the parameters of a power law with a spectral index fixed at 13/3.

A lot of efforts have been made since many years in the PTA community to detect the presence of GWB. In the absence of GW detection, EPTA, NANOGrav and PPTA regularly released upper limits (usually at 95% confidence level) of the dimensionless GW strain

Figure 3.1: The Hellings and Downs curve for an isotropic stochastic GWB following General Relativity (from Jenet and Romano 2015).

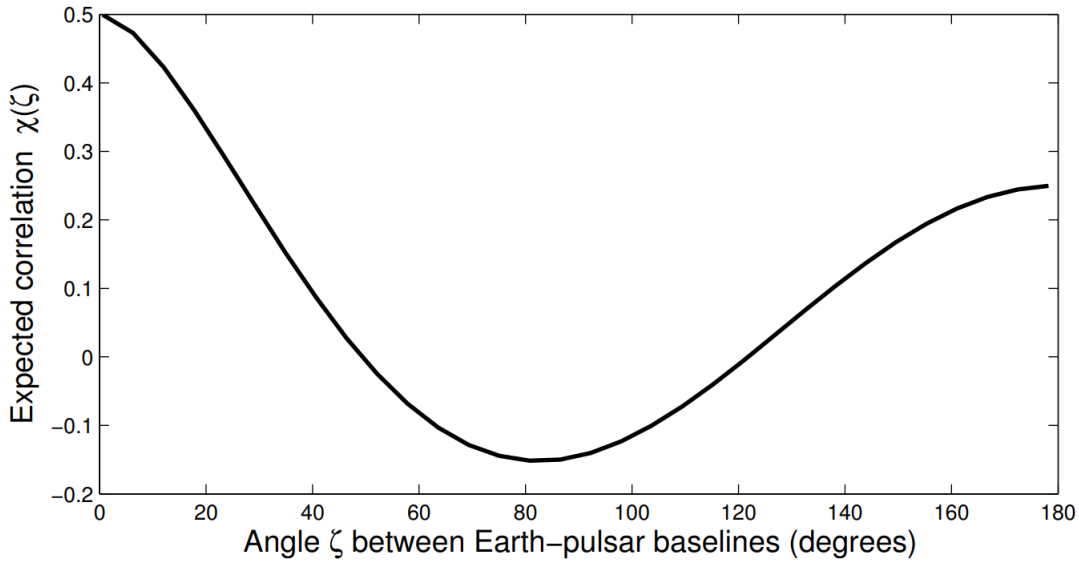

amplitude $A^{95\%}$ set at a reference frequency of 1 yr^{-1} and a spectral index of $\gamma = 13/3$. Here is the chronological evolution of upper limits $A^{95\%}$ from early-2000's: 1.1×10^{-14} (Jenet et al. 2006), 6×10^{-15} (Haasteren et al. 2011), 7.2×10^{-15} (Demorest et al. 2013), 2.4×10^{-15} (Shannon et al. 2013), 1.0×10^{-15} (Shannon et al. 2015), 3.0×10^{-15} (Lentati et al. 2015), 1.5×10^{-15} (Arzoumanian et al. 2016) and 1.45×10^{-15} (Arzoumanian et al. 2018a). The last analysis from NANOGrav (Arzoumanian et al. 2020) have resulted to a measure of $A = 1.92^{+0.75}_{-0.55} \times 10^{-15}$, with a very significant Bayes factor over 10^4. However, the detection of the GWB could not be claimed because the presence of the Hellings-Downs correlations could not be established. This result has been confirmed by measurements from PPTA (Goncharov et al. 2021) and EPTA (Chen et al. 2021), with $A = 2.2^{+0.4}_{-0.3} \times 10^{-15}$ and $A = 2.95^{+0.89}_{-0.72} \times 10^{-15}$ respectively, but again without detecting the spatial correlations.

The second section of this chapter describes how to build the PTA likelihood for a multi-pulsar dataset and to include common signals between several pulsars. The third section presents the analyses and related results of the search for a GWB with six pulsars in the EPTA DR2 (Chen et al. 2021). My contribution to Chen et al. 2021 is in the data analyses of the single-pulsar noise models and the common red signals from a GWB, the investigation of Solar system ephemeris systematics, and a participation in writing the paper. The detailed study related to the Solar system ephemeris errors are included in the Chapter 4 of the thesis. The fourth Section describes the impact of the single-pulsar noise modelling (see Section 2.4) on the GWB searches applied to the EPTA DR2 (Chalumeau et al. 2021). The last part of this chapter presents results from the very recent IPTA GWB analyses (Antoniadis et al. 2022) using the IPTA Data Release 2 submitted to MNRAS journal, where I

have participated in the data analysis process. The section particularly focuses on the investigation of the spatial correlations and the assessment of their statistical significance. The Chapter concludes with a brief discussion on the prospects for a detection of a GWB with the future PTA datasets.

3.2 Modelling correlated signals for PTA

This section expands the formulation of the likelihood given in Section 2.3 to a dataset that combines timing residuals of several pulsars, and it describes the common red signals (CRS) models without any spatial correlation, or with angular correlations corresponding to a signal from a GWB (Hellings-Downs), clock correction errors (monopolar) or systematic errors in the Solar system ephemeris (dipolar).

The PTA likelihood

The PTA likelihood for a dataset that combine several pulsars generalizes the single-pulsar case (Eq. 2.5) and permits to include common signals between pulsars. For a data set of p pulsars with n timing residuals δt in total, the likelihood function describing white noise $\mathbf{N}$, a red noise $\mathbf{C}^{\mathrm{PSRN}}$ for each pulsar and a common red signal $\mathbf{C}^{\mathrm{CRS}}$ is expressed as

$$p(\vec{\delta t}|\mathrm{GP}) = \frac{\exp\left[-\frac{1}{2}\,\sum_{\alpha\beta}\sum_{\mathrm{ij}}\,\delta \mathrm{t}_{\alpha\,\mathrm{i}}\,\left(\mathbf{N}_{\alpha\,\mathrm{i},\beta\mathrm{j}}+\mathbf{C}^{\mathrm{PSRN}}_{\alpha\,\mathrm{i},\beta\mathrm{j}}+\mathbf{C}^{\mathrm{CRS}}_{\alpha\,\mathrm{i},\beta\mathrm{j}}\right)^{-1}\,\delta \mathrm{t}_{\beta\mathrm{j}}\right]}{\sqrt{(2\pi)^n \det(\mathbf{N}+\mathbf{C}^{\mathrm{PSRN}}+\mathbf{C}^{\mathrm{CRS}})}}, \tag{3.3}$$

where the greek letters $\alpha, \beta = 1, ..., p$ enumerate the pulsars and $\delta t_{\alpha\, i}$ is the i-th residual of the pulsar α.

Before we focus on the common red signal, let us re-formulate the components related to the single-pulsar noise models (see Section 2.3.2):

- White noise:

$$\mathbf{N}_{\alpha\,\mathrm{i},\beta\mathrm{j}} = \left[\left(\mathrm{E}_{\mathrm{f},\alpha}\right)^2\,\sigma^2_{\mathrm{ToA},\alpha}(\mathrm{t_i}) + \left(\mathrm{E}_{\mathrm{q},\alpha}\right)^2\right]\,\delta_{\alpha\beta}\,\delta_{\mathrm{ij}}, \tag{3.4}$$

  where $\sigma^2_{\mathrm{ToA},\alpha}(t_i)$ is the uncertainty of the ToA measured at the epoch t_i for the pulsar α, and $\mathrm{E}_{\mathrm{f},\alpha}$ and $\mathrm{E}_{\mathrm{q},\alpha}$ are EFAC and EQUAD parameters attached to each system observing the pulsar α.

- Single-pulsar red noise:

The stochastic red noise components is modelled as Gaussian processes (Eq. 2.15). For the pulsar α, the covariance matric is

$$\mathbf{C}^{\mathrm{PSRN}}_{\alpha\, i,\beta\, j} = \sum_{k,l} \mathrm{F}_{\alpha\, \mathrm{k}}(\mathrm{t_i})\, \mathbf{\Sigma}_{\alpha\, \mathrm{k},\beta \mathrm{l}}\, \mathrm{F}_{\beta \mathrm{l}}(\mathrm{t_j}), \tag{3.5}$$

where F is the incomplete set of N sin/cos basis functions that are indexed with $k, l = 1, ..., N$ and the covariance matrix of the basis weights $\mathbf{\Sigma}^{\mathrm{PSRN}}$ is defined by the PSD $S^{\alpha}(f_k)$:

$$\mathbf{\Sigma}_{\alpha\, k,\beta\, l} = S^{\alpha}(f_k)\, \delta_{kl}\, \delta_{\alpha\beta}\ /\ T, \tag{3.6}$$

The common red signals

As for the single-pulsar noise description, the CRS is also modelled as a Gaussian process using the sin/cos basis functions for the single-pulsar stochastic red signal. The covariance matrix of the CRS is

$$\mathbf{C}^{\mathrm{CRS}}_{\alpha\, i,\beta\, j} = \sum_{k,l} \mathrm{F}_{\alpha\, \mathrm{k}}(\mathrm{t_i})\, \mathbf{\Sigma}_{\alpha\, \mathrm{k},\beta \mathrm{l}}\, \mathrm{F}_{\beta \mathrm{l}}(\mathrm{t_j}), \tag{3.7}$$

where F is the set of basis functions and the covariance matrix of the weights $\mathbf{\Sigma}_{\alpha\, k,\beta\, l}$ depends on a PSD which is the same for all pulsars. Let us describe the common signals considered in PTAs, modelled as a power-law PSD $S_P(f_k; A_{\mathrm{CRS}}, \gamma_{\mathrm{CRS}})$.

→ The common uncorrelated red noise (CURN): The CURN shares spectral properties across all pulsars but does not appear with any particular spatial correlation (random) for each pair of pulsars, its covariance matrix is described as

$$\mathbf{\Sigma}_{\alpha\, k,\beta\, l} = S_P(f_k; A_{\mathrm{CURN}}, \gamma_{\mathrm{CURN}})\, \delta_{kl}\, \delta_{\alpha\beta}\ /\ T, \tag{3.8}$$

where A_{CURN} and γ_{CURN} are the amplitude and the spectral index of the power-law.

The term $\delta_{\alpha\beta}$ implies the block-diagonal structure of the covariance matrix $\mathbf{C}^{\mathrm{CRS}}_{\alpha\, i,\beta\, j}$ and, therefore, describes the 'auto-correlated' processes for every pulsars.

→ The spatially correlated red noise processes: The covariance matrix of a correlated stochastic red signal is given as

$$\mathbf{\Sigma}_{\alpha\, k,\beta\, l} = S_P(f_k; A, \gamma)\, \delta_{kl}\, \Gamma(\theta_{\alpha\beta})\ /\ T, \tag{3.9}$$

where $\theta_{\alpha\beta}$ is the angular separation of a pair of pulsars in the sky and $\Gamma(\theta_{\alpha\beta})$ is the overlap reduction function (ORF ; Finn et al. 2009), which gives the correlation coefficients for each pair of pulsars.

Assuming General Relativity, the ORF used to describe an isotropic stochastic GWB follows the Hellings-Downs curve (Lee et al. 2008):

$$\Gamma_{\rm GWB}(\theta_{\alpha\beta}) = \begin{cases} 1, \text{if } \theta_{\alpha\beta} = 0 \\ x\left(\frac{3}{2}\ln(x) - \frac{1}{4}\right) + \frac{1}{2}, \text{otherwise} \end{cases} \tag{3.10}$$

with $x = [1 - \cos(\theta_{\alpha\beta})]/2$.

In this manuscript, the CRS with 'Hellings-Downs' ORF is referred to as GWB, and characterized by the power-law amplitude and spectral index denoted as $A_{\rm GWB}$ and $\gamma_{\rm GWB}$.

A second spatially correlated red noise could originate from errors in the clock corrections applied by the timing model (Section 1.2.2). If such errors contain long-term processes, a very-low frequency noise would be identically induced in the timing residuals of every pulsars using the same clock correction file (given by the BIPM). The signal (named CLK) would have monopolar correlations with a constant ORF:

$$\Gamma_{\rm CLK}(\theta_{\alpha\beta}) = 1, \tag{3.11}$$

Another correlated signal is the Solar system ephemeris systematics. The time-dependent position of the Earth with respect to the Solar system barycenter used by the timing model (for instance to perform the Solar system Roemer delay) is given by the SSEs (see Section 1.2.2). An error of the Roemer delay produces a signal with dipolar correlation, and ORF is given as (See Appendix A of Tiburzi et al. 2016)

$$\Gamma_{\rm EPH}(\theta_{\alpha\beta}) \propto \cos(\theta_{\alpha\beta}), \tag{3.12}$$

The Chapter 4 of this thesis is specially focused on modelling the SSE errors for robust measurement of a GWB with PTAs. In order to avoid any confusion, the CRS modelled with $\Gamma_{\rm EPH}$ ORF is referred as DIP in all the manuscript.

It is also possible to estimate the ORF given the data. For the method applied in Chen et al. 2021, the ORF is modelled as a Chebyshev polynomial, following the approach proposed in Lentati et al. 2015

$$\Gamma_{\rm Cheb}(x) \simeq c_1 + c_2 x + c_3(2x^2 - 1) + c_4(4x^3 - 3x), \tag{3.13}$$

where $c_{[1,4]}$ are the Chebyshev coefficients used with uniform priors with the range $[-1, 1]$ for each coefficient and $x = (\theta_{\alpha\beta} - \pi/2)/(\pi/2)$.

3.3 Searching for a stochastic GWB with EPTA

The main results reported in Chen et al. 2021 are consistent with those recently obtained by NANOGrav (Arzoumanian et al. 2020) and PPTA (Goncharov et al. 2021) and share the

same conclusion: a significant detection of a common signal across pulsars but no evidence for Hellings-Downs correlation. The dataset is the EPTA DR2 - about 24 years of timing observations performed by the five EPTA radio telescopes for six pulsars: PSRs J0613-0200, J1012+5307, J1600-3053, J1713+0747, J1744-1134, J1909-3744.

In the search for a GWB and other CRSs in the EPTA data, we used two independently developed algorithms for evaluating the likelihood and with independent Monte-Carlo (MC) samplers in order to increase our confidence in the results by having a cross-check for possible bugs and analysis mistakes: ENTERPRISE and FORTYTWO.

We will only focus on results obtained with ENTERPRISE, for which I have participated. The FORTYTWO analyses were performed by another group. We have combined ENTERPRISE with PTMCMCSAMPLER, that allowed us to perform a fully integrated pulsar noise and correlated signals analysis within the same analysis suite. We also used ENTERPRISE_EXTENSIONS that contains additional functionality ENTERPRISE. As in the case of the single-pulsar noise analysis, ENTERPRISE uses the "Gaussian-process" approach to perform the marginalization of the timing model.

In all analyses for common signals, the red-noise and DM-noise parameters are simultaneously sampled with the CRS. The priors for the power-law parameters are $\log_{10}\mathcal{U}(10^{-18}, 10^{-10})$ for $A_{\rm CRS}$ and $\mathcal{U}(0,7)$ for $\gamma_{\rm CRS}$.

In the single-pulsar analysis, we model the white noise with two parameters per observing system. Keeping such a configuration in these CRS analyses would result in a currently unmanageable number of parameters. One approach is to fix the EFAC and EQUAD for each observing system and use a "global EFAC" parameter per pulsar, that acts as a global multiplication factor to regulate each pulsar's white noise level. This has been shown to be a good strategy during the EPTA DR1 GWB analysis, as shown in Lentati et al. 2015, where in all cases the global EFAC was found to be very consistent with unity. This means that the white-noise estimation during single-pulsar analysis is very robust. In the analyses presented in this work, we have verified that the global EFAC values are also close to unity, allowing us to fix the pulsar white-noise parameters from the single-pulsar analysis without significant loss of accuracy in CRS analysis. The analysis described in this section are all performed with a fixed Solar system ephemeris, using DE438.

3.3.1 Evaluating the correlations of the CRS

Figure 3.2 shows the results of the general CRS search by sampling angular correlation coefficients using Chebyshev polynomial. The analyses clearly recover a common signal with two giving providing very consistent results. The left panel shows the estimation of the ORF curve and the right panel shows the posterior distributions for the spec-

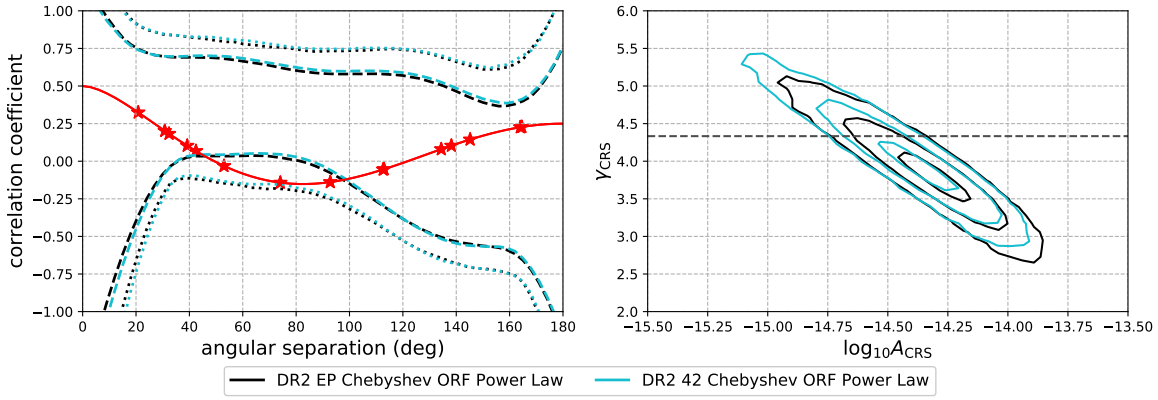

Figure 3.2: ENTERPRISE (EP) and FORTYTWO (42) results from a search for a CRS modelled with a single-power-law spectrum simultaneously sampled with the ORF using the EPTA DR2 6-pulsars. The ORF is approximated with a 4th-order Chebyshev polynomial. Left: The posterior distribution for the angular correlation curve of the CRS, shown as boundaries of the credible regions. The dashed and dotted lines denote the 95% and 99.7% credible regions, respectively. The theoretical Hellings-Downs curve is overplotted for comparison as a solid red line. The red stars denote the angular separations of the pulsars used in this study. Right: Two-dimensional posterior distribution of the spectral parameters for the single-power-law CRS model with the dashed line indicating the expected $\gamma = 13/3$ from a GWB from SMBHBs.

tral parameters. The median and 95% credible intervals for the spectral parameters are $\log_{10} A_{\rm CRS} = -14.32^{+0.31}_{-0.39}$ (or $A_{\rm CRS} = 4.79^{+4.99}_{-2.84} \times 10^{-15}$) and $\gamma_{\rm CRS} = 3.83^{+0.82}_{-0.72}$. The ORF figure shows the 95% and 99.7% credible regions. The boundary encompasses the probability for ORF to be the HD curve, however other possibilities remain.

We have applied Bayesian model selection to DR2 to investigate which model of CRS is preferred. The base model to which we make the model comparisons is one where the pulsar TOAs only have independent, uncorrelated individual pulsar noise (we denote this as PSRN), without any measurable commonality in the spectral properties of the different pulsars. We compare this base model to models that add only one CRS, namely either CURN, GWB, CLK and DIP, as well as models which add two CRSs, i.e. a combination of CURN with one of the remaining three ORFs. The models are listed in Table 3.1. Given the uncertainty on the ORF, we do not expect this analysis to be fully conclusive, but can provide indications on whether some of these CRS models are more supported by the present data set.

The evaluations of Bayes Factors with ENTERPRISE were performed through a hypermodel structure. Table 3.1 shows a summary of the Bayes Factors for the different models. According to the criteria from Kass and Raftery 1995, the addition of either of the CURN, GWB or DIP signals to the base PSRN signal is decisively favoured with a $\log_{10}$ Bayes Factor

Table 3.1: Results from model selection analysis, in logarithmic (base 10) Bayes Factors ($\log_{10}$BF), for different CRS models and with fixed SSE (DE438) using the EPTA DR2 6-pulsars. The model-components acronyms are: (i) PSRN = individual Pulsar noise only, (ii) CURN = Common uncorrelated red noise, (iii) GWB = isotropic GWB with quadrupolar, Hellings-Downs, angular correlation, (iv) CLK = common signal with monopolar spatial correlation, as expected from a clock error, (v) DIP = common signal with dipolar spatial correlation, as expected from SSE errors. PSRN has no $\log_{10}$BF values as it serves as the base model.

Model	$\log_{10}$BF	
	ENTERPRISE	FORTYTWO
PSRN	–	–
PSRN + CURN	3.8	3.6
PSRN + GWB	3.4	3.2
PSRN + CLK	0.6	0.8
PSRN + DIP	2.1	2.1
PSRN + CURN + GWB	3.6	3.7
PSRN + CURN + CLK	3.7	3.4
PSRN + CURN + DIP	3.7	3.4

($\log_{10}$BF) > 2. The strongest Bayes Factor is for the CURN model, although the evidence for the GWB is only lower by $\log_{10}\text{BF} \approx 0.4$. This difference provides only a marginal advantage to the CURN, barely disfavouring the GWB signal. The DIP model, however, is clearly less favoured with an $\log_{10}$BF difference to CURN or the GWB of order ~ 1, which is a substantial difference. In contrast to the three models discussed above, the monopolar correlation is only mildly favoured with respect to the PSRN base model.

Since the CURN model has the strongest evidence of the models with a single CRS, we can compare it against models which include another additional common process. The idea is to test whether there may be evidence for several physically motivated common processes coexisting in the data. In general, none of the three spatially correlated processes add substantial evidence to the single CURN. The ability to distinguish between different spatial correlations could be improved by using more than 6 pulsars in the analysis. We thus plan to expand the analysis to include a larger number of MSPs in the future.

3.3.2 Analysing the spectrum properties

In order to further investigate our results, we use the case of the CURN to investigate the CRS spectrum modelling. We therefore proceed to also perform the analysis with an alternative approach to the power-law spectrum model, where the power of each individual CRS-spectrum frequency bin is sampled independently. This approach has been employed in Lentati et al. 2015 and Arzoumanian et al. 2020, and was first discussed in Lentati et al. 2013. We refer to this as the 'free spectrum' analysis. We conducted the analysis employing both ENTEPRISE and FORTYTWO, which provided fully consistent results. The left panel of Figure 3.3 shows the power of the CURN at each frequency, the free spectrum, with the straight lines indicating the median values of A and γ of their respective posterior distributions from the power-law spectral analysis from ENTERPRISE. The full 2D posterior contours for the power-law parameters are shown on the right panel.

The free spectrum figure in general has two features. At high frequencies the power is white-noise dominated and can thus be modelled with a flat horizontal line. The presence of red noise becomes obvious at the lowest frequency bins and appears to be dominant for about 10 frequency bins.

The median value and 95% confidence interval for CRS parameters are $\log_{10} A = -14.29^{+0.26}_{-0.33}$ (or $A_{\rm CURN} = 5.13^{+4.20}_{-2.73} \times 10^{-15}$) and $\gamma = 3.78^{+0.69}_{-0.59}$.

3.4 Impact of the single-pulsar noise modelling on the GWB searches

This part is based on the last section of Chalumeau et al. 2021 which uses the single-pulsar noise model selection presented in Chapter 2. Now, we investigate how the custom single-pulsar noise model affects the results of the common red signal (CRS) analyses given above. We consider here the CRS either with Hellings-Downs spatial correlations (GWB) or without (CURN).

We denote the default "base" noise model used for all pulsars in Chen et al. 2021 $RN30\_DMv100$ as M1, and label the custom models (summarized in Table 2.5) for each pulsar as M2. For this analysis we fix the parameters of the white noise to their maximum likelihood values (in the corresponding models). We model the common red noise using 30 uniformly spaced Fourier modes $f_k = k/\mathrm{T_{tot}}$, $k = 1...30$, where $\mathrm{T_{tot}}$ is the time span between the lowest and highest epoch from the data of all pulsars.

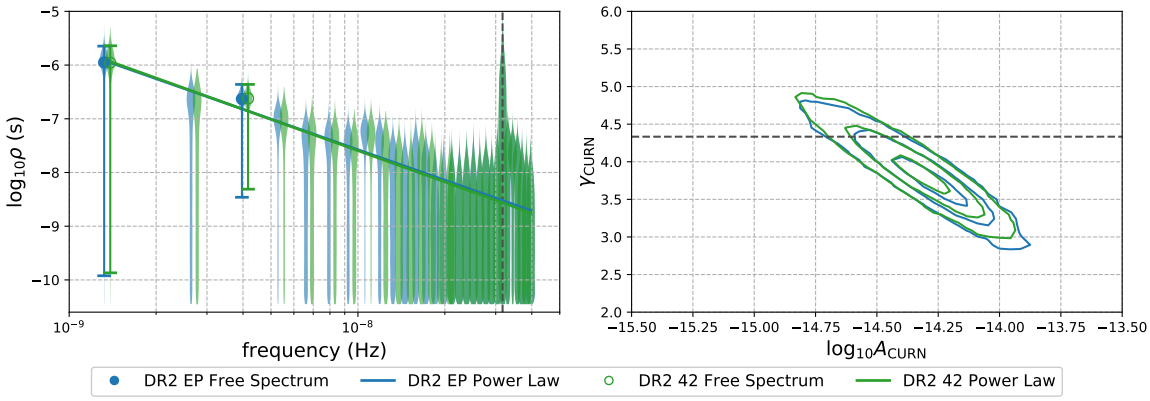

Figure 3.3: Results from CURN analysis using ENTERPRISE (EP) and FORTYTWO (42) with the EPTA DR2 6-pulsars, both for the free-spectrum (left panel) and the single power-law (right panel) analyses. The left plot shows the posterior distribution for the amplitude of the power at each frequency bin using violin plots. Where the inference provides good measurement of the power, we denote the median with a circle and the 95% uncertainties. We consider the measurement good, if more than 95% of the posterior probability lies above the lowest 6.25% of the prior. As the results of the two algorithms are almost identical, we slightly shift the 42 distributions of the lowest 15 frequency bins for easier visual comparison. The right plot shows the two-dimensional posterior distribution for the CURN power-law amplitude and spectral index with the dashed line indicating the expected $\gamma = 13/3$ from a GWB from SMBHBs. The two analysis pipelines have produced consistent results.

3.4.1 Contribution of each pulsar to the CRS

Following Arzoumanian et al. 2020, Goncharov et al. 2021 and Chen et al. 2021, we study the contribution of each pulsar dataset to a common process using dropout analysis. One additional parameter is added to the model for each pulsar, with a uniform prior, and these are sampled as part of the model. When the parameter is one, the common red signal is included in the model for that pulsar used in the likelihood and when it is zero it is not. The dropout factor is the ratio of the fraction of posterior samples when the CRS is included to the fraction when it is not included.

The resulting dropout factors (see Fig. 3.4, blue hollow circles) with M1+CURN are very similar to those presented in Figure 5 in Chen et al. 2021. The dropout factor for PSR J1012+5307 is around 1 (consistent with the results of Arzoumanian et al. 2020) and most likely caused by abnormal red noise at high frequency (see discussion in 2.4.2) .

The contribution of each pulsar to the common red noise has decreased for the custom model M2+CURN with the biggest drop shown for PSR J1600-3053 (the one which did not support RN). Despite that the overall result remains: pulsars support presence of CURN. Interestingly, if we discard RN from M2+CURN model of PSR J1744-1134 (see discussion in subsection 2.4.2) it is picked up by CURN leading to increase in the drop-out factor (see hollow red circle in Fig. 3.4). Note that this poorly constrained (and poorly understood) signal could potentially affect the sensitivity to the GWB. Our choice to keep RN inside the M2 model for PSR J1744-1134 was a conservative choice.

3.4.2 Spectral properties of the CRS

The Figure 3.5 and Table 3.2 summarize the spectral properties of CURN and GWB. We do not see significant changes in the new results (red) from the previously found blue, Chen et al. 2021. The amplitude of both CURN and GWB is slightly lower and the spectral index is a bit shallower with the M2 model. The median amplitude is reduced from $A_{\rm CURN,M1} = 5.42^{+4.48}_{-2.81} \times 10^{-15}$ to $A_{\rm CURN,M2} = 4.88^{+4.94}_{-2.85} \times 10^{-15}$ (95% credible interval) and the uncertainties of the spectral index are somewhat larger. This slight shift and broadening might be caused by partial absorption of the common red signals by the new noise models. Similarly for the GWB we have $A_{\rm GWB,M1} = 5.01^{+4.34}_{-2.63} \times 10^{-15}$ and $A_{\rm GWB,M2} = 4.87^{+5.26}_{-2.88} \times 10^{-15}$. Note that the amplitude of CRS in M2 is the same for CURN and GWB.

We observe no changes in the CURN amplitude and spectral index posteriors using M2 with or without RN for PSR J1744-1134, with corresponding Jensen-Shannon divergences 2.95×10^{-3} and 1.84×10^{-3}.

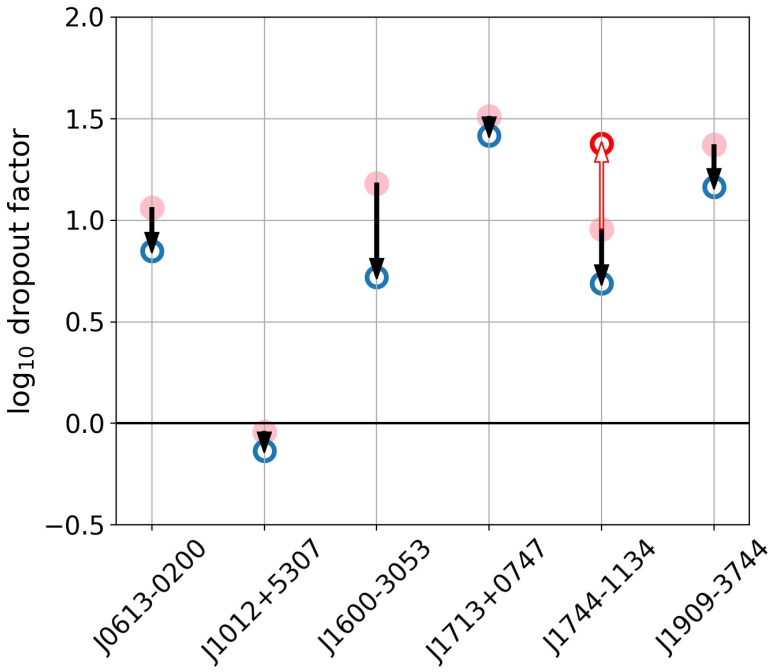

Figure 3.4: Dropout score for the contribution of each pulsar to the CURN model with M1 (pink dots) or M2 (empty blue dots) using the EPTA DR2 6-pulsars. The same analysis for PSR J1744-1134 but without intrinsic red-noise for this pulsar is also shown (empty red dot).

Figure 3.5: 2D posterior distributions of the CURN (left) and Hellings-Down correlated GWB (right) power-law parameters with M1 (blue) and M2 (red) single-pulsar noise models using the EPTA DR2 6-pulsars.

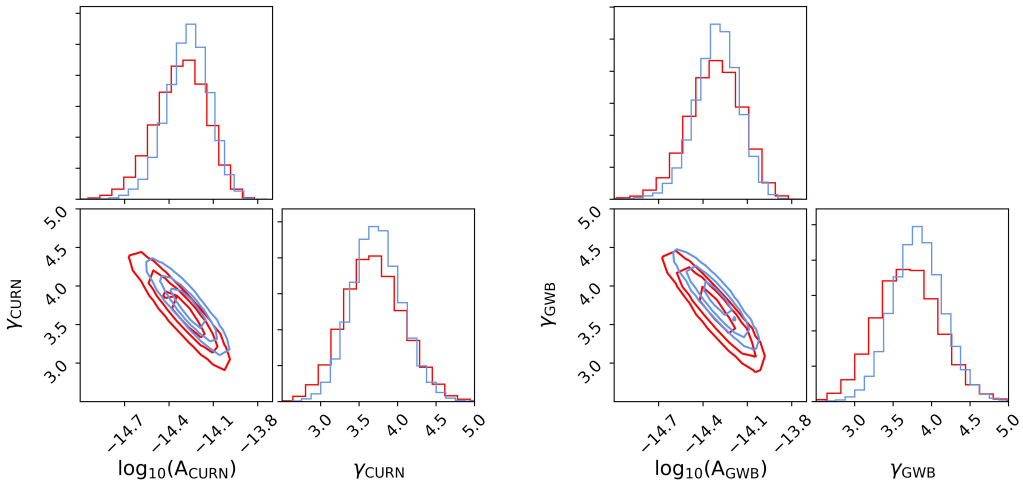

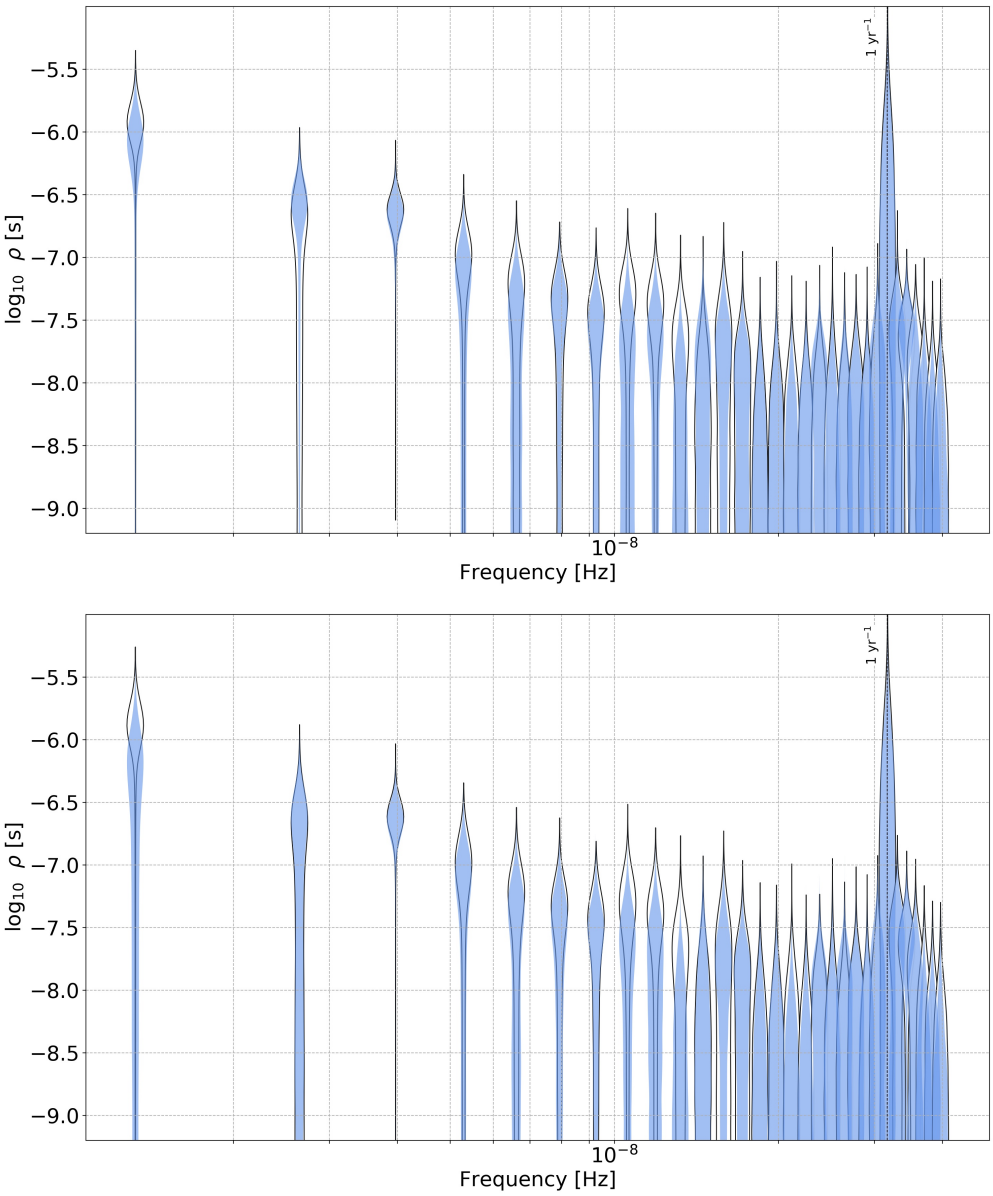

Figure 3.6: Free-spectrum of the CURN (top) and the GWB (bottom) signals using the EPTA DR2 6-pulsars, either with M1 (empty black violin) or M2 (filled blue violin) single-pulsar noise models.

Table 3.2: Median of amplitude and spectral index posterior (and 95% credible interval) of both uncorrelated (CURN) and Hellings-Down (GWB) common processes computed with M1 and M2 using the EPTA DR2 6-pulsars. Two last columns contain Jensen-Shannon divergences values that compare posteriors of CRS added to M1 and M2.

Model	$\log_{10} A$	γ	JS div. A	JS div. γ
M1 + CURN	$-14.27^{+0.26}_{-0.32}$	$3.73^{+0.68}_{-0.61}$	0	0
M2 + CURN	$-14.31^{+0.30}_{-0.38}$	$3.68^{+0.81}_{-0.72}$	$1.55e-02$	$9.40e-03$
M1 + GWB	$-14.30^{+0.27}_{-0.32}$	$3.82^{+0.70}_{-0.65}$	0	0
M2 + GWB	$-14.31^{+0.32}_{-0.39}$	$3.69^{+0.84}_{-0.78}$	$8.73e-03$	$2.60e-02$

We have also considered a free-spectrum model for CRS and plot it in Fig. 3.6. The M1+CRS model is presented by the hollow violins and we plot M2+CRS by filled blue violins. The left plot shows addition of CURN to M1 and M2 noise models. We notice the slight drop in the amplitude at the lowest frequency and slightly better constrain of amplitude at the second frequency bin. The free spectrum for GWB (right plot) shows a slight drop in power at the lowest frequency. These results nicely confirm our main findings with the power-law model of a decreased amplitude and shallower spectral index with M2 compared to M1.

3.4.3 Statistical significance of the CRS with custom noise models

Finally, we evaluate Bayes factors checking for presence of the common processes, considering M1/M2+CURN/GWB against pulsar noise models with no common process (PSRN), M1/M2.

The results are summarized in Table 3.3. We have used two method to compute Bayes factors (Dynesty 'Dyn.' and HyperModel 'Hyp') for cross checking. First of all we have rederived the results of Chen et al. 2021 for the M1 model: we observe a strong presence of a common red process but the data is not informative about its nature (could equally be CURN or GWB). Analysis with the custom noise model built in this work *confirms* these findings. It is quite remarkable that even though the custom noise models used are very different from the standard ones, we can still confirm the presence of CRS. This gives an additional confidence in presence of CRS in the EPTA DR2 data. This is the main result of this paper.

Table 3.3: Bayes factors in favor of CRS signals (CURN or GWB) inclusion in M1 or M2 single-pulsar noise models using the EPTA DR2 6-pulsars. Estimations are performed either through evidence ratios (Dyn.) or using the product-space method (Hyp.).

CRS Model	$\log_{10}$ BF			
	$M1_{Dyn.}$	$M1_{Hyp.}$	$M2_{Dyn.}$	$M2_{Hyp.}$
PSRN	0	0	0	0
PSRN + CURN	3.6	3.8	2.9	3.3
PSRN + GWB	3.4	3.6	3.0	3.6

3.4.4 Summary

The main result of this work is that we confirm the presence of a common red noise in EPTA DR2 despite the use of much more complicated single-pulsar noise models. The data is not informative on the presence of Hellings-Downs spatial correlations, which is not surprising given that we have analysed only the 6 best EPTA pulsars.

3.5 Evaluating the presence of correlations with IPTA data

This section presents results reported in Antoniadis et al. 2022 (submitted to MNRAS) on the search for a GWB with the IPTA Data Release 2 (Perera et al. 2019), the most recent IPTA dataset today. For this paper, I have participated to the data analyses and in particular contributed to the false-alarm study.

3.5.1 The IPTA Data Release 2

IPTA DR2 includes a combination of timing data from the following individual PTA data releases: the EPTA data release 1.0 (Desvignes et al. 2016, the NANOGrav 9-year data set (NANOGrav Collaboration et al. 2015), and the PPTA first data release (Manchester et al. 2013) and its extended version (Reardon et al. 2016). The EPTA data set includes high-precision timing data from 42 MSPs obtained with the largest radio telescopes in Europe – Effelsberg telescope, Lovell telescope, Nançay telescope, and Westerbork Synthesis telescope – covering data from 1996 to 2015 with a time baseline between 7–18 yr. In addition to these data, archival timing data of PSR J1939+2134 since 1994 was included. The NANOGrav 9-year data set includes high-precision timing observations from 37 MSPs obtained with the Robert C. Byrd Green Bank Telescope and the Arecibo telescope, spanning

a time baseline between 0.6–9.2 yr, covering the data from 2004 to 2013. In addition, the long-term timing data of PSR J1713+0747 from (Zhu et al. 2015) and the data of PSRs J1857+0943 and J1939+2134 from 1984 through 1992 (Kaspi et al. 1994) were included. The PPTA data set includes high-precision timing observations from 20 MSPs obtained with the Parkes radio telescope (also known as *Murriyang*) from 2004 to 2011. IPTA DR2 also included single frequency band (1.4 GHz/L-band) Parkes telescope legacy data obtained since 1994. The additional 3.0 GHz timing data reported in Shannon et al. 2015 for PSRs J0437−4715, J1744−1134, J1713+0747, and J1909−3744 were also included in the data set. In total, the timing data from 65 MSPs were included in IPTA DR2, which has 21 more source than the IPTA DR1 (Verbiest et al. 2016). There are 27 and 7 MSPs in IPTA DR2 with a timing baseline >10 yr and >20 yr, respectively. All pulsars were observed at multiple frequencies. All EPTA and PPTA observations were averaged in time and frequency to obtain a single time-of-arrival (TOA) for each receiver and observation. The NANOGrav observations were averaged in time and included sub-band information, i.e., averaged in frequency to maintain a frequency resolution ranging from 1.5 to 12.5 MHz depending on the receiver and backend instrument combination, resulted in a single TOA for each frequency channel. More details about the constituent PTA data sets can be found in Perera et al. 2019.

IPTA DR2, being the combination of data from multiple telescopes and many observing systems, has larger model parameter space than its constituent data sets. The large number of model parameters and TOAs increases the computational complexity of the analysis. As we searched for long-term processes, such as the GWB, we limited our analysis to pulsars whose observation time exceeded 3 years. This reduced the number of pulsars from the full 65 in DR2 to 53.

3.5.2 Evidence for the CRS

Figure 3.7 compares the results when using two different ORFs: one that uses only the diagonal 'auto correlation' terms (i.e., CURN) and one with both 'auto' and 'cross' correlation terms (i.e., GWB). A small shift towards lower amplitudes and higher spectral index can be seen when using the GWB model. Using the CURN, we find $A_{\rm CP} = 5.1^{+6.7}_{-3.1} \times 10^{-15}$ and $\gamma_{\rm CP} = 3.9 \pm 0.9$, where the errors represent 95% credible regions. Using the GWB we can constrain the common process power law to $A_{\rm CP} = 3.9^{+6.3}_{-2.5} \times 10^{-15}$ and $\gamma_{\rm CP} = 4.0 \pm 0.9$.

The CURN model is very strongly favored over a model with only intrinsic pulsar noise and no common-spectrum process with $\log_{10}$ Bayes factor of 8.2 (see Table 3.4). Despite the large Bayes factor in favour of the CURN, this does not suffice to claim a GWB detection, as we have only used the auto-correlations. This strong evidence only indicates that

Table 3.4: Decimal log-scale Bayes factors obtained with the IPTA DR2 comparing the different CRS models investigated over a model that only include single-pulsar noise models (named PSRN).

Model	$\log_{10}$ BF
PSRN	–
PSRN + CURN	8.2
PSRN + GWB	8.5
PSRN + CLK	3.5
PSRN + DIP	5.9

a number of pulsars have red noise with similar spectral characteristics. We must turn on the cross-correlations to determine if this common process is 'Hellings-Downs' correlated as a GWB should be. Using the GWB ORF, we find only middling evidence in favour of the GWB compared to the CURN model ($\log_{10}\mathcal{B}^{\text{GWB}}_{\text{CURN}} = 0.3$).

3.5.3 Extended analysis on the spatial correlations

Similar to how we may consider the auto-correlation parts of the ORF alone, the full ORF can be split into two independent parts. In this case the auto-correlation and the cross-correlation parts each have their own independent amplitude, as was done in Arzoumanian et al. 2020. For the 'cross-correlation only' model, the covariance matrix $\mathbf{C}^{\text{CRS}}_{\alpha i,\beta j}$ in Eq. 3.7 is computed for $\alpha \neq \beta$, with α, β indexing pulsars. In the GWB ORF the auto-correlation part is $\Gamma_{aa} = 1$ and the cross-correlation parts are suppressed by at least a factor of 2, $\Gamma_{ab} < 0.5$. This makes the cross-correlations harder to constrain. Figure 3.8 shows the posteriors for the two amplitudes of a split ORF analysis for fixed $\gamma = 13/3$, compared to the full auto+cross-correlation model. The cross-correlations do not have sufficient precision to place constraints on the amplitude of the GWB. However, they do place an upper limit of $\sim 2.15 \times 10^{-15}$ on the amplitude of the GWB, which is consistent with the lower range of the amplitude derived using the full auto- and cross-correlation model in Fig. 3.8. The auto-correlation terms are much more informative. Combining the information from both shifts the amplitude towards lower values. This shows that the cross-terms can contribute to the full GWB search, even if they provide less information. The auto-correlations are more likely to be affected by intrinsic pulsar noise. Using a more sophisticated noise model for each pulsar can help to produce a more robust estimate on the amplitude of any common process.

Figure 3.7: 2D marginalized posterior distributions of the power-law amplitude and spectral index for the common process (CP) modelled as a CURN (Auto correlations only) or a GWB (Auto + cross correlations) with the IPTA DR2. The green lines indicate $A_{CP} = 2.8 \times 10^{-15}$ and $\gamma_{\rm SMBHB} = 13/3$.

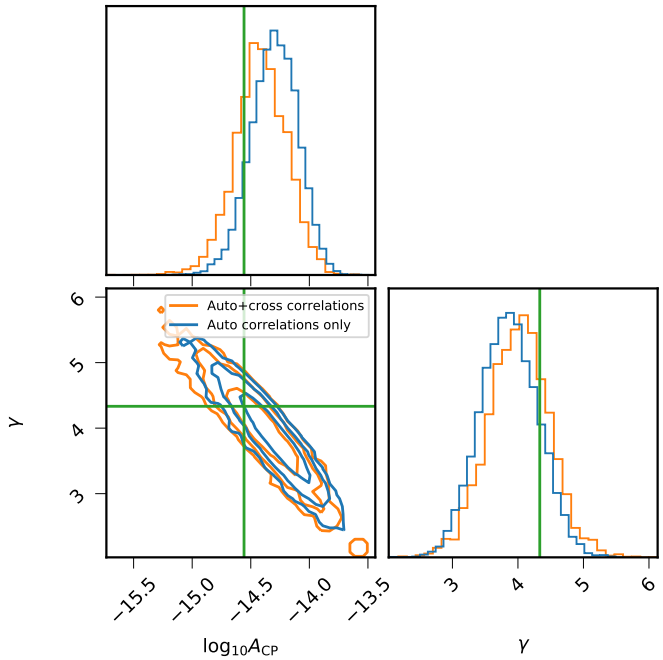

Figure 3.8: Marginalized posterior distributions of the amplitude A of power-laws with fixed spectral index at $\gamma = 13/3$ for the CURN (blue), the GWB (orange) and the cross correlation only (green) CRS models using the IPTA DR2.

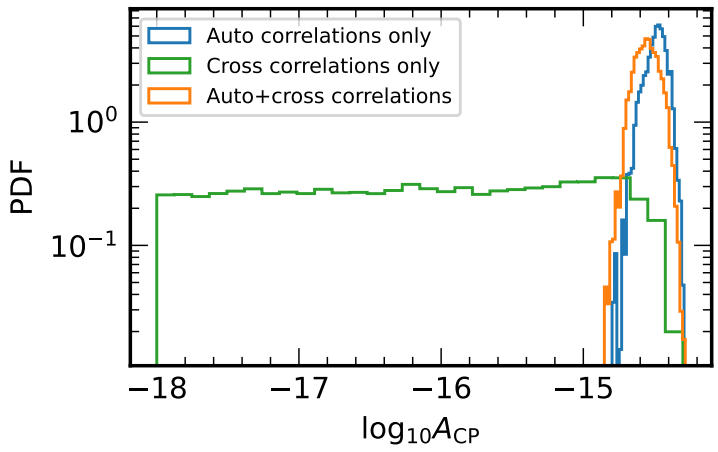

Data was also analysed using the frequentist *optimal statistic* (OS) estimator (Anholm et al. 2009, Demorest et al. 2013, Chamberlin et al. 2015), which evaluates the amplitude and a signal-to-noise ration S/N of a correlated common process. The method used follows the approach proposed in Vigeland et al. 2018, where the accuracy of the statistic is improved by marginalizing on the single-pulsar red noise parameters using their Bayesian posteriors distributions. Figure 3.9 shows the amplitudes and signal-to-noise ratio (S/N) that are recovered by the pulsar noise marginalized optimal statistic (OS) method, which uses cross-correlations only. We find no evidence for a dipolar correlated process, as the amplitude and S/N for this model are centered on 0. SSE systematics are expected to manifest at specific frequencies related to orbital motion of the celestial bodies. The IPTA DR2 data set is long enough to probe lower frequencies that should be less affected by SSE errors Vallisneri et al. 2020. The S/N = $0.6^{+1.2}_{-0.8}$ for the Hellings-Downs correlation is insufficient to claim a detection. This is consistent with the Bayesian model selection. The HD amplitude from the OS seems to be in tension with the Bayesian results for the auto-correlated CP, but consistent with the Bayesian results for the full HD model. This strengthens the case that the cross-terms have a significant role to play in parameter estimation as well as detection confidence. Finally, the OS has the largest S/N = $2.0^{+1.8}_{-1.4}$ for a monopole with a small amplitude. This can be due to the complexity of IPTA DR2 and some amount of unmodeled noise.

The significance of the S/N for the correlated signals have been tested with the two false alarm studies: the *phase-shift* and *sky scrambles* methods (Cornish and Sampson 2016, Taylor et al. 2017). In order to evaluate the significance of a GWB signal, we would like to compare the S/N measurement of the observed dataset $S/N^{\rm obs}$ with values derived from realisations of datasets without any GWB signal. We could then compute a p-value to get the 'probability of getting $S/N^{\rm obs}$ assuming a null hypothesis (i.e., no correlation)'. A very low value would then permit to reject the null hypothesis, and confirm the detection of a GWB. The idea of the false alarm studies is to destroy any spatial correlations, either by modifying the pulsar sky locations (sky scrambles) or including a phase shifting to destroy the coherence of the GWB between pulsars, but preserving the noise in the data.

For this work, the phase shifts are introduced in the CRS model, adding a random phase in the sin/cos functions of the Gaussian process basis functions described in Eq. 2.16, this is the 'Model-driven' approach (Taylor et al. 2017). The sky scramble method requires to make assumptions on the nature of the correlations of the signal. The pulsar positions are set to minimize the match statistic $\bar{M}$, which defines the overlap between the ORF of the assumed correlation to destroy $\Gamma^{\rm init}$ (here Hellings-Downs), and the

Figure 3.9: Amplitude A^2 (top) and S/N (bottom) obtained from the noise marginalized optimal statistic applied for a CRS modelled with monopolar (blue), dipolar (green) or Hellings-Downs correlations using the IPTA DR2. The amplitudes obtained from Bayesian analysis are also plotted (top) for the CURN (black line) and the cross correlation only (black dashed-lines).

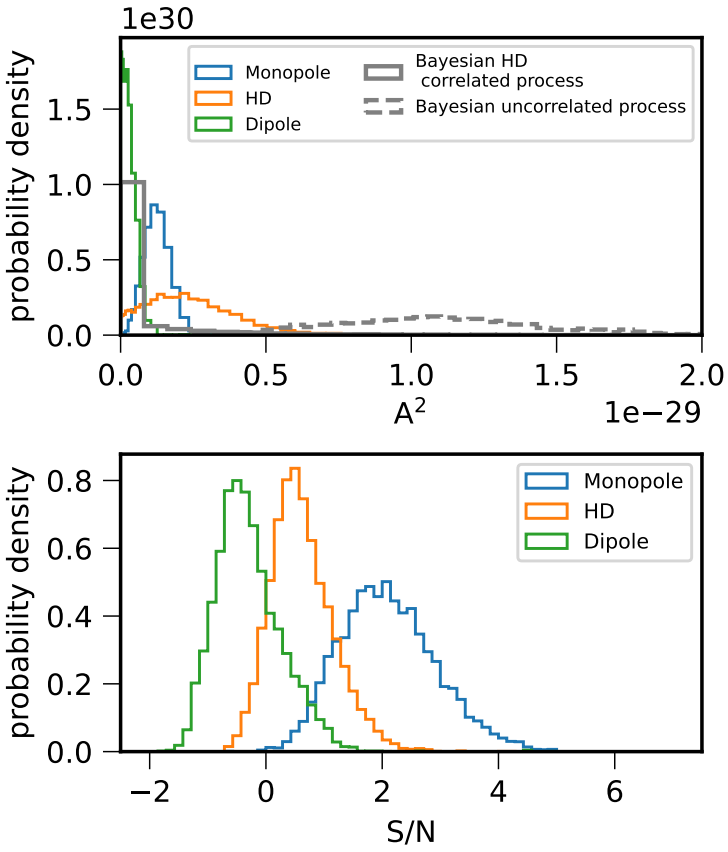

Table 3.5: p-values calculated for the false alarm analyses using the IPTA DR2. The measured S/N value using Hellings-Downs (HD ORF) or monopolar correlations is compared with the S/N distribution obtained after removing correlations either with phase shift or sky scrambles methods (10k random realizations).

	p, phase shift	p, sky scramble
HD ORF	0.25	0.24
Monopole	0.03	–

'scrambled' ORF Γ, as (Taylor et al. 2017)

$$\bar{M} = \frac{\sum_{a,b\neq a} \Gamma^{\text{init}}_{ab}\, \Gamma_{ab}}{\sqrt{\sum_{a,b\neq a} \Gamma^{\text{init}}_{ab}\, \Gamma^{\text{init}}_{ab} \times \sum_{a,b\neq a} \Gamma_{ab}\, \Gamma_{ab}}}, \tag{3.14}$$

Note that the monopolar correlations can't be removed with sky scrambles because it is fully uniform in the sky and therefore independent from the pulsar angular separations.

The phase-shift analysis has been applied to the Hellings-Downs and monopolar correlations, and the sky scrambles on the Hellings-Downs. The p-values obtained are shown in Table 3.5. The very low p-value at 0.03 for the monopolar correlations is consistent with the high S/N shown in Fig. 3.9. However, the Hellings-Downs p-values at 0.25 for phase shift and 0.24 for sky scrambles are too high to reject the null hypothesis and report the measurement of a significant GWB.

3.6 Future prospects toward a detection

The recent results obtained independently from NANOGrav, PPTA and EPTA have provided evidence of a common signal among pulsars. The challenge now is to determine whether this is the signature of a stochastic GWB by improving the sensitivity of the current PTAs. This section is a brief discussion about different aspects related to the improvement of the current GWB measurements in the coming years.

Eliminating non-GW candidates

Apart from GW, there are various sources that could potentially induce very low frequency signals in the timing residuals.

Unmodelled processes for the single-pulsar red noise with similar spectra could be interpreted as an uncorrelated common process (CURN) as demonstrated in Goncharov et al. 2021 via simulations. Moreover, the study on the single-pulsar model selection in Chapter 2 has shown that the each pulsar dataset requires quite specific treatment and

yields to different noise models because of the possible complexity of the intrinsic red noise (PSR J1012+5307), unmodelled chromatic processes such as scattering variations (PSR J1600-3053) and exponential dips (PSR J1713+0747) or long-term noise related to instrumental effects (system noise). Using custom single-pulsar noise models, the power-law of both the CURN and the common red signal with Hellings-Downs (GWB) models have been slightly shifted to lower amplitudes but still remain consistent with main findings (Arzoumanian et al. 2020, Goncharov et al. 2021, Chen et al. 2021). In addition, it is necessary to ensure that the common signal does not come from errors in clock correction or Solar system ephemeris with analyses on the correlations of the signal and advanced modelling. The Chapter 4 focuses on the modelling of Solar system ephemeris uncertainties.

Improvement of the datasets

The recent results published by NANOGrav (Arzoumanian et al. 2020), PPTA (Goncharov et al. 2021) and EPTA (Chen et al. 2021) were obtained using respectively about 12.5, 15 and 24 years of timing data of 45, 26 and 6 MSPs. It is planned in the coming years to include additional ToAs for NANOGrav and PPTA to extend the time span of their datasets and to include more pulsars for EPTA (at least 25) to improve significantly the evaluation of the spatial correlations.

The GWB analyses with the IPTA DR2 (Antoniadis et al. 2022) have particularly shown the important improvement of the data combination. It has permit to obtain a measurement of a common process consistent with the results from the three continental PTAs (see Fig. 3.10), whereas no such tight constraints was found from its constituent datasets. The combination of the future releases with others datasets from InPTA or MeerKAT might therefore permit to complete a search with the best sensitivity available.

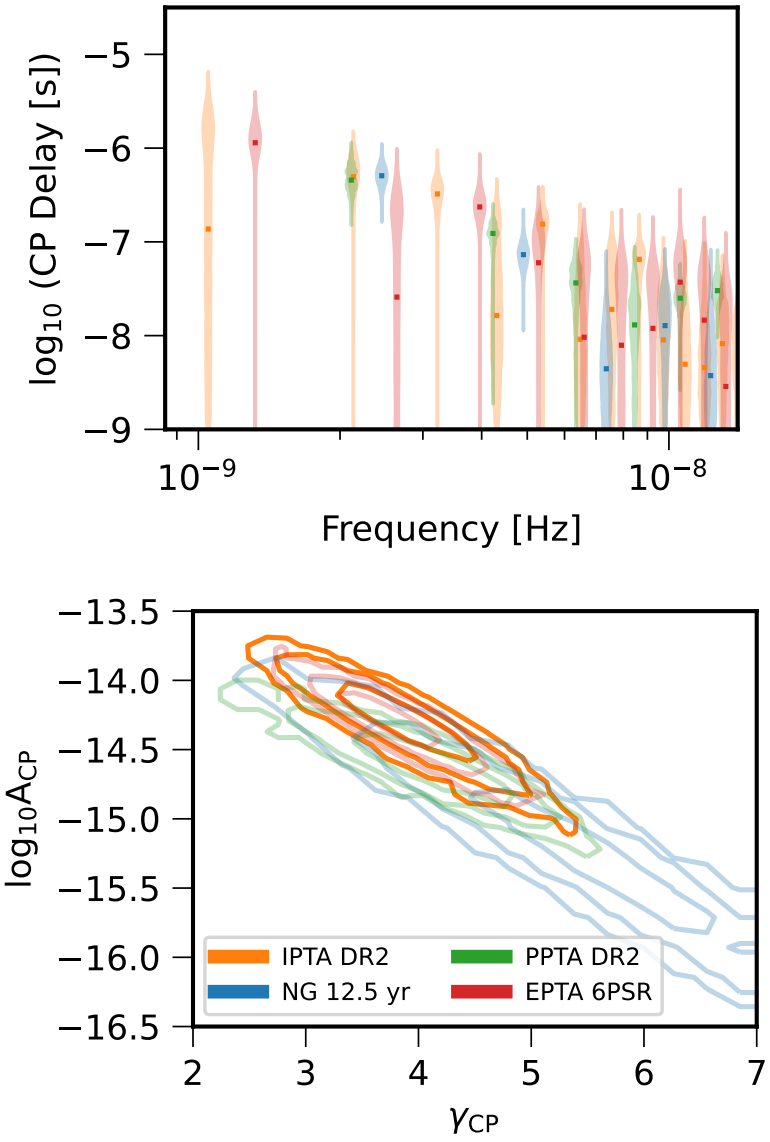

Figure 3.10: Comparison of the CRS modelled with a free-spectrum (top) or a power-law PSD (bottom) between the following datasets: IPTA DR2 (orange; Perera et al. 2019), NANOGrav 12.5 years dataset (blue; Alam et al. 2021), PPTA DR2 (green; Kerr et al. 2020) and six pulsars from EPTA DR2. Note that even if the datasets of the three continental PTAs include more recent ToAs than the IPTA DR2, the time span of the latter if bigger because it contains legacy data with observations performed in the 1980's. Figure from Antoniadis et al. 2022.

CHAPTER 4

MODELLING THE SOLAR-SYSTEM EPHEMERIS ERRORS TOWARD THE SEARCH FOR A GWB

Abstract

This chapter describes our work on the modelling of the Solar System ephemeris (SSE) uncertainties for the search of a GWB with PTAs. The first two sections give a background on the study of SSE errors with PTA, and describe the methods used to take this signal into account. It contains a detailed presentation of EPHEMGP, a new model that we developped and implemented which is based on from the ephemeris numerical integrator *Intégrateur Numérique Planétaire de l'Observatoire de Paris* (INPOP). This work is the result of a near collaboration with A. Fienga (GeoAzur), who contributes to the elaboration of INPOP ephemeris. The third section details the study performed to evaluate EPHEMGP and compare its performances with existing models. It is the subject of a publication to be submitted in the coming weeks (Chalumeau et al. 2021b in prep.). The last section presents the application of EPHEMGP (and other models) to study the impact of SSE error modelling on the parameter estimation of the common red signal detected with EPTA DR2. This work is a full part of Chen et al. 2021, for which I contributed to the noise analyses and the redaction.

4.1 Introduction

The analysis presented in Chapter 3 strongly supports the presence of a CRS, however the PTA data provides no significant evidence for or against Hellings-Downs correlations. In addition to the preparation of the best possible data sets (see section 3.6), a lot of effort is put into the optimization of the noise modelling for improving the robustness of the results (see Chapter 2). It is important to confidently detect quadrupolar correlations in PTA data to claim GW detection. Errors in the Solar system ephemeris (SSE) also produce a correlated signal but with a dipolar pattern (bottom in Fig. 4.1).

It has been demonstrated in Arzoumanian et al. 2018b and Vallisneri et al. 2020 that the measurement of the GWB could depend on the choice of the SSE. The errors in SSE would introduce systematic errors in the GWB measurement, or even can be mistaken for a GWB signal. The Figure 4.2 shows that the peaked GWB amplitude posteriors obtained with different SSE versions (dashed lines) become all consistent with upper-limit distributions (solid lines) after accounting for SSE uncertainties in the noise model, using BAYESEPHEM algorithm (Vallisneri et al. 2020).

This chapter is centered on modelling the SSE uncertainties in the search for GWB with PTAs. The second section contains the impact of SSE errors on pulsar timing and PTAs, followed by a description of the existing models of SSE uncertainties implemented in ENTERPRISE package. Next we give a detailed description of our own independent model, named EPHEMGP, developped and implemented within a collaboration with the *Institut de Mécanique Céleste et de Calcul des Éphémérides* (IMCCE). The third section is a preliminary study of the performance of EPHEMGP using a simulated dataset based on EPTA DR2, compared with other models. This study will be the subject of a publication that is currently in preparation. The last section presents the application of EPHEMGP and other models on the EPTA DR2 dataset, with particular focus on the CRS parameter estimation.

4.2 Modelling SSE errors for PTA

Let us first describe the impact of SSE errors on PTA data.

4.2.1 The SSE errors in PTA

In the pulsar timing procedure, the set of measured topocentric ToAs are transformed to the quasi-inertial Solar system barycenter (SSB) frame to take into account the complex motion of the Earth in the Solar system (see Section 1.2.2). The Solar system barycentric

Figure 4.1: Angular separation pairs of pulsars pair vs. correlation coefficient in the presence of GWB (top) and Solar system Roemer delay error (bottom) which is injected as a stochastic dipolar signal (from Tiburzi et al. 2016).

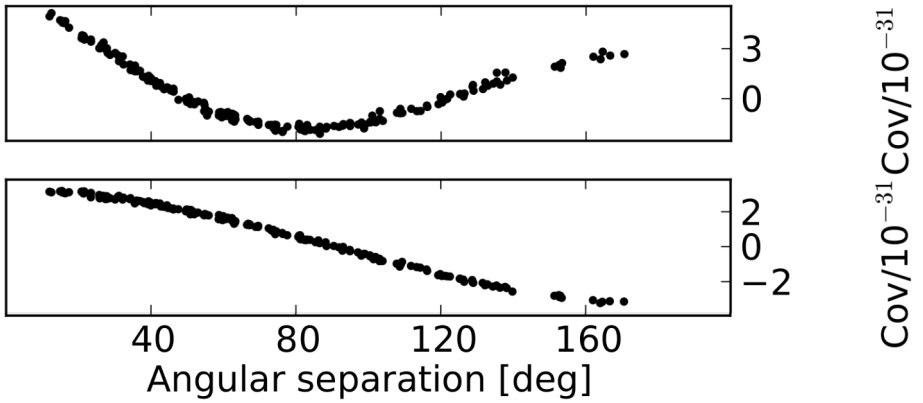

Figure 4.2: Marginalized posterior distribution of the power-law amplitude A_{GWB} (set at $f = 1$ yr^{-1}) of a CRS model with a fixed spectral index at $\gamma = 13/3$ and Hellings-Downs correlations (GWB) using the NANOGrav 11-year dataset and including (solid lines) or not (dashed lines) a model named BAYESEPHEM that takes into account SSE uncertainties (from Vallisneri et al. 2020). The colors denote different choice of JPL ephemeris used by the timing model.

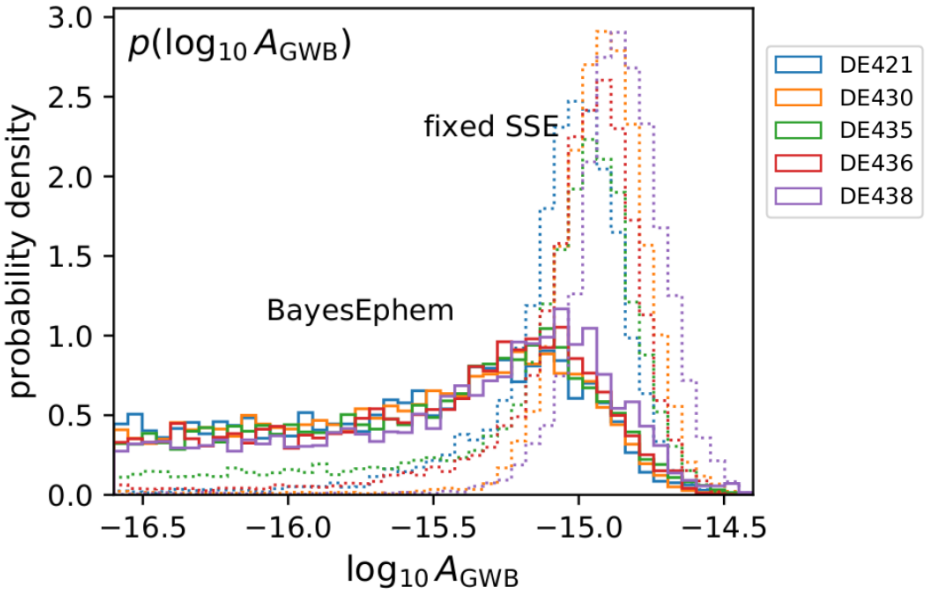

correction includes the Roemer delay $\Delta_{R\odot}$: the vacuum light travel time between the observatory and the SSB. If we ignore the observatory-to-geocentre term, one can express the Solar system Roemer delay as (Eq. 1.10)

$$\Delta_{R\odot} = -\frac{\vec{r}_{\oplus} \,.\, \hat{R}_{BB}}{c}, \tag{4.1}$$

where c is the speed of light, $\hat{R}_{BB}$ is the pulsar position unit vector in the SSB frame obtained and fitted by the timing model, and $\vec{r}_{\oplus}$ is the geocentre position in the SSB frame, fixed in the timing model and given by a chosen SSE.

The Solar system ephemerides provide the Solar system body trajectories (positions and velocities) and masses. They are produced and regularly updated by several collaborations such as the IMCCE with the *Intégrateur Numérique Planétaire de l'Observatoire de Paris* (INPOP), the *Jet Propulsion Laboratory* (JPL) with the *Development Ephemeris* (DE) or the *Russian Institute for Applied Astronomy* of the *Russian Academy of Sciences* with the *Ephemerides of Planets and the Moon* (EPM). The ephemerides are computed from a numerical integration of the equation of motions. Initial conditions of positions and velocities of celestial bodies are used as parameters, which are obtained by fitting integrated orbits to the observational data. One of the difficulties is to assign realistic uncertainties to the heterogeneous sets of data used to generate the SSEs. The observational data come from measurements obtained from space missions (e.g., very long baseline interferometry (VLBI) or spacecraft ranging and Doppler tracking) or other methods such as Lunar Laser Ranging (LLR) or radar ranging. Often the latest SSE superseeds in accuracy the preceding as it is based on extended and, often, more precise observational data. However, SSE produced by different groups might use different data and/or use different fitting and numerical methods which could lead to unaccounted systematic errors. The main idea of this study is to introduce a Gaussian process that absorbs those (possible) systematics leaving GW signal unaffected.

In this manuscript, we consider the two SSEs, JPL DE438 (Folkner and Park 2018) and INPOP19a (Fienga et al. 2019), which have been derived with comparable datasets, both using refined data of Cassini mission for Saturn and range and VLBI tracking of Juno mission perijoves (6 with DE438 and 9 with INPOP19a) for Jupiter.

An error of the geocentre position $\delta\vec{r}_{\odot}$ with respect to the SSB given by the ephemeris would cause a systematic error in the timing residuals expressed from the Solar system Roemer (Eq. 4.1):

$$\delta t_{R_{\odot}} = -\frac{1}{c}\delta\vec{r}_{\odot} \cdot \hat{R}_{BB}, \tag{4.2}$$

The error in the Roemer delay is also expected to be dipolar-correlated among pulsar

angular separation, with an overlap reduction function $\Gamma_{\rm SSE}(\theta_{\alpha\beta})$ as (Tiburzi et al. 2016)

$$\Gamma_{\rm EPH}(\theta_{\alpha\beta}) \propto \cos(\theta_{\alpha\beta}), \tag{4.3}$$

where $\theta_{\alpha\beta}$ is the angle between the positions of two pulsars denoted α and β. Note that other terms of the Solar system barycentric correction use the SSB position given SSEs such as the Shapiro and Einstein delays, but the Roemer delay appears to be the dominant term to impact the timing residuals.

The sensitivity of PTAs strongly depends on the ability to separate SSE systematics and the GWB signal, by including enough pulsars well spaced in the sky (Roebber 2019).

4.2.2 Describing the SSE uncertainties

Several models have been proposed to account for SSE uncertainties in PTA data analysis to apply robust analysis for the search of very-low frequency GWs (Tiburzi et al. 2016, Guo et al. 2019, Vallisneri et al. 2020), which is the objective of this work. We consider here the models implemented in ENTERPRISE software: a common red signal (CRS) with dipolar correlations, BAYESEPEHEM (Vallisneri et al. 2020), and our model named EPHEMGP.

The dipolar CRS, is modelled as a Gaussian process with a simple power-law and an ORF as $\Gamma_{\rm DIP}(\theta_{\alpha\beta}) = \cos(\theta_{\alpha\beta})$.

The model BAYESEPHEM includes SSE errors as deterministic signals to describe linear deviations of masses of Jupiter, Saturn, Uranus and Neptune (4 parameters), Jupiter and Saturn average orbital elements perturbations (12 parameters) and a rotation rate about the ecliptic pole (1 parameters). As explained in Vallisneri 2020, the rotation rate should not have any impact on GW posteriors since its related signal is expected to be absorbed in the pulsar astrometric parameters during the timing model fitting procedure (see Chapter 1).

Let us now present EPHEMGP that we have developped to model the Roemer delay errors as Gaussian processes, using INPOP orbital partials derived from the numerical integration as basis functions. The model do not vary the masses of planets, for which the values given by INPOP are derived from space mission measurements and considered to be accurate enough to have any impact on pulsar timing at current precisions. We vary instead the non-singular orbital elements of planets. Those parameters are related to the Keplerian parameters:

- **a :** semi major axis
- **l :** mean longitude of the planet in the orbit

- **k = e cos(π)**, with **e** as the eccentricity and π as the longitude of perihelion.
- **h = e sin(π)**
- **q = sin $\left(\frac{i}{2}\right)$ cos(Ω)**, with **i** as the inclination and Ω as the longitude of the ascending node
- **p = sin $\left(\frac{i}{2}\right)$ sin(Ω).**

EPHEMGP is included in the PTA likelihood (see Section 3.2) using the 'weight-space view' Gaussian process approach (see Section 2.3.1) as

$$\delta t^{\mathrm{EGP}} = \sum_a \Phi_a^{\mathrm{EGP}}(t)\, \delta\lambda_a,$$

where $\Phi_a^{\mathrm{EGP}}(t)$ is the basis functions computed from INPOP numerical partials and λ_a are the deviations of the non-singular orbital elements.

Currently, the model uses numerical partials produced for INPOP19A solution and provided by our collaborator A. Fienga. The basis functions correspond to the numerical partials of the Earth-Moon barycenter $\frac{\partial \vec{x}_{\mathrm{EMB}}}{\partial \lambda_a}$ projected onto the Roemer delay which gives us variation in $\delta t_{R_\odot}$ as

$$\Phi_a^{\mathrm{EGP}}(t) = \frac{\partial \delta t_{R_\odot}}{\partial \lambda_a}(t) = \left(-\frac{\hat{\mathrm{R}}_{\mathrm{BB}}}{c} \cdot \frac{\partial \vec{x}_{\mathrm{EMB}}}{\partial \lambda_a} \right)(t),$$

The Earth-Moon distance errors are considered negligible compared to the SSB position uncertainties.

The PTA results are particularly sensitive to the long term variations of $\delta \vec{r}_\odot$, and therefore mainly to variations in Jupiter or Saturn orbits, which have orbital periods of respectively ~ 12 and ~ 29 years. With their long orbital periods, Uranus (~ 84 yrs) and Neptune (~ 165 yrs) impacts are expected to be lighter on current PTA results which use ~ 20 years of data. Moreover, the impact of inner planets on the SSB positions are also expected to be negligible compared with giant planets. EPHEMGP is currently used to describe **Jupiter** and **Saturn** orbital variations and therefore includes 12 parameters. The inclusion of trans-Neptunian objects actually might be important but we did not consider it and left this to future investigations. The parameter uncertainties given by the covariance matrix and derived from INPOP19a reflects the uncertainties in this solution given the overall set up (observational dataset, equations of motion, number and distribution of asteroids, etc). This covariance matrix can be used for the multivariate Gaussian prior for the "weights" in EPHEMGP. However, the typical errors suggested by covariance matrix

Table 4.1: Prior ranges centered around zero for all EPHEMGP parameters.

	parameter	Prior range
Jupiter	δa	$\pm 1.37 \times 10^{-4}$
	δl	$\pm 4.07 \times 10^{-5}$
	δk	$\pm 2.54 \times 10^{-4}$
	δh	$\pm 1.64 \times 10^{-5}$
	δq	$\pm 5.19 \times 10^{-6}$
	δp	$\pm 4.06 \times 10^{-6}$
Saturn	δa	$\pm 8.54 \times 10^{-4}$
	δl	$\pm 8.17 \times 10^{-4}$
	δk	$\pm 6.14 \times 10^{-4}$
	δh	$\pm 6.08 \times 10^{-4}$
	δq	$\pm 1.02 \times 10^{-4}$
	δp	$\pm 6.83 \times 10^{-4}$

are too small to have measurable impact on ToAs and therefore on the GW search. The covariance matrix is a local estimation (in vicinity of the best found INPOP19A solution) and does not take into account (i) possibility of having another, alternative to INPOP19A, solution which still fits the observations; (ii) possible systematics caused by particular choice of set up (see above) used to obtain INPOP19A ephemeris. We have phenomenologically expanded the priors by several orders of magnitude to permit the absorption of possible SSE systematic errors and correspond to variations in PTA data at the level of tens of μs. The current priors for each SSE parameter are uniform, centered around zero, with ranges given in Table 4.1.

4.3 Impact of SSE errors on the GWB searches

In this section, we study the efficiency of EPHEMGP to absorb any SSE systematics in the search for GWB. We simulate a PTA dataset injecting SSE systematics and/or a GWB signal. We perform GWB search with or without EPHEMGP. We also compare the performance of EPHEMGP with BAYESEPHEM and a CRS with dipolar spatial correlations. This work is currently in the final stage and will be reported in a future publication (Chalumeau et al. 2021b in prep.).

4.3.1 Methods

We perform noise analysis on simulated (but realistic) datasets that contain real timing parameters, epochs and ToA errors of 25 pulsars from the EPTA Data Release 1 (Desvignes et al. 2016) and extended NRT data, using NUPPI observations until late-2020. We have simulated the data with LIBSTEMPO package (Vallisneri 2020) by applying the following procedure. First we have set all residuals to zero, which means that the timing model alone describes perfectly the observations. Then we have modified residuals by adding the noise (or deterministic signal) according to one or several models ("injecting" the signal according to the set of models) listed below.

- **White noise**: We simulate white noise as random injection for each observing system via the common PTA white noise parameters, EFAC and EQUAD, using the functions 'add_efac' and 'add_equad' from LIBSTEMPO. The signal is input to the residuals δt as:

  $$\delta t^{\mathrm{WN}}(t) = \delta t(t) + \mathrm{EFAC} \times \mathrm{ToAerr}(t) \times \mathcal{N}(0,1) + \mathrm{EQUAD} \times \mathcal{N}(0,1),$$

  where ToAerr relates to the ToA uncertainties, and $\mathcal{N}(0,1)$ is the standard normal distribution.

  The white noise parameters are set to values obtained from single-pulsar analysis on real data.

- **DE438 vs INPOP19a**: We simulate planetary ephemeris systematic errors using the difference between two solar-system ephemeris solutions, here DE438 and INPOP19A. The difference is translated into the timing residuals and added as a deterministic signal. In practice, the data is simulated as if DE438 would be the true ephemeris solution for the solar-system and processed with INPOP19A.

- **GWB signal**: The stochastic gravitational wave background is simulated (using the function 'createGWB' from LIBSTEMPO) according to a power-law model with a given amplitude (set at 1 yr^{-1}) and a slope fixed at $\gamma = 13/3$, assuming an emission from an isotropic population of supermassive black hole binaries. In this work, we simulate the GWB with two possible amplitudes, $A = 10^{-16}$ or 10^{-15}, in order to consider respectively the 'low' and the 'high' S/N regimes, where the signal is poorly or easily recoverable given our dataset.

The white noise is included to all simulated data, and we will add other signals (GWB and/or SSE systematics) in turn checking at each step the correct recovery of the parameters characterizing the data. The Figure 4.3 displays simulated timing residuals for PSR

Figure 4.3: Simulated timing residuals of PSR J1909-3744 with (a) no red signal, (b) the 'DE438 vs. INPOP19a' SSE systematic, (c) a GWB with an amplitude at $A = 10^{-16}$ and (d) idem with $A = 10^{-16}$. For each figure, the residuals are shown before (top) and after (bottom) fitting for the timing model.

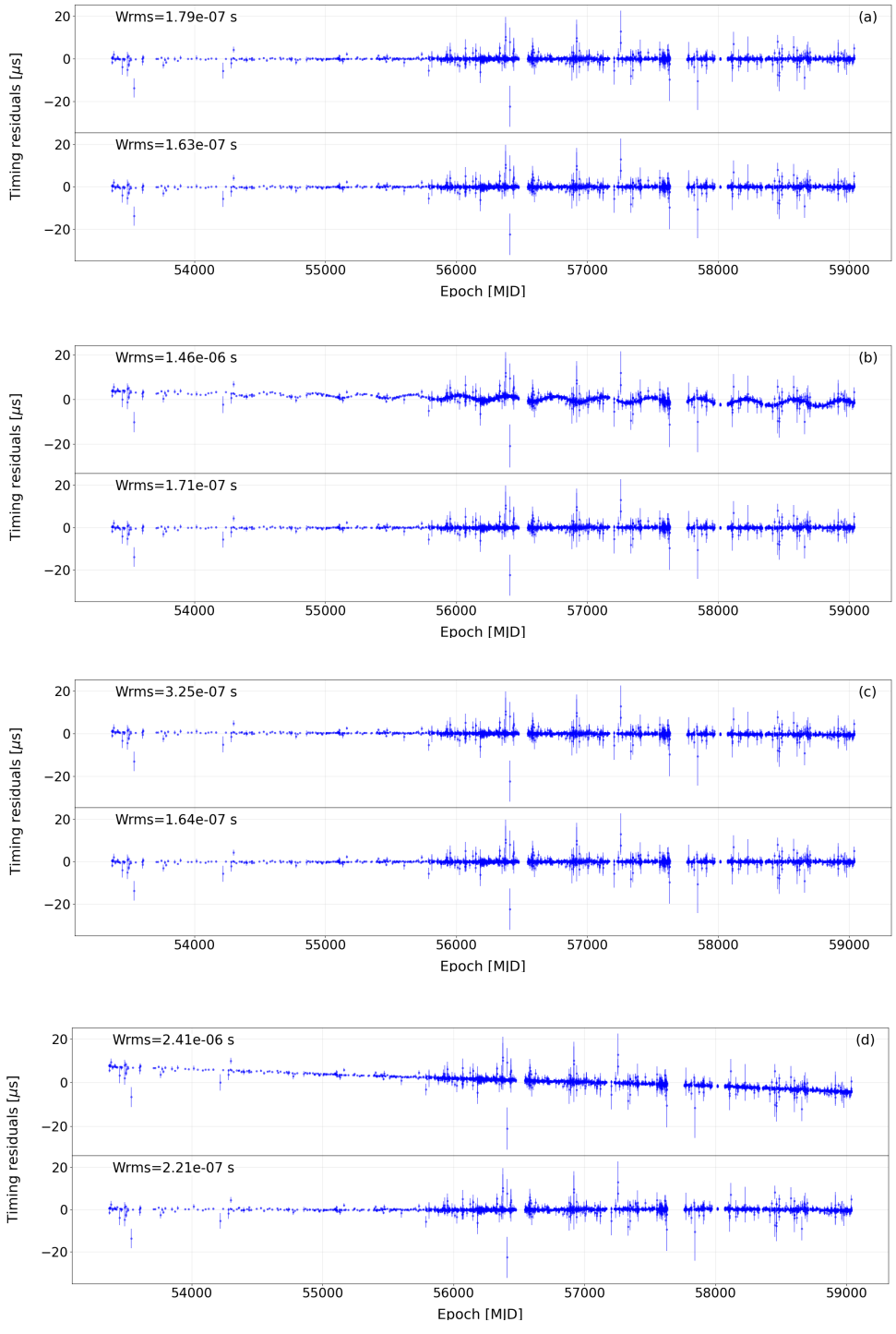

Table 4.2: Short-hand notations and related injected signals for the simulated datasets used to study EPHEMGP. WN refers to white noise, SSE to the DE438 vs. IN19a systematic, and the GWB signal is injected at the given amplitude.

Data	Signal
'A'	WN + SSE
'B1'	WN + GWB ($A = 10^{-16}$)
'B2'	WN + GWB ($A = 10^{-15}$)
'A+B1'	WN + SSE + GWB ($A = 10^{-16}$)
'A+B2'	WN + SSE + GWB ($A = 10^{-15}$)

J1909-3744 with the different signals. For each GWB signal level, the same seed have been used for the random realisation of white noise and GWB to permit fair comparisons between the different noise models.

Within Bayesian analyses we have used ENTERPRISE to evaluate the likelihood and priors, and the Markov Chain Monte Carlo (MCMC) sampler PTMCMCSAMPLER (Ellis and Haasteren 2017) to carry the parameter estimation. For every analyses, we marginalize over timing model parameters following the 'Gaussian process' approach as described in Section 2.3.2. We also keep EFAC and EQUAD parameters fixed as for the standard multi-pulsar noise analyses in PTAs. Depending on the analysis, we then include on the timing residuals a chosen sub-list of the two following signals :

- **Solar-system ephemeris uncertainties/systematics**: Described either by a CRS with dipolar correlations modelled with a power-law PSD, BAYESEPHEM or EPHEMGP, respectively referred as DIP, BFM and EGP.

- **GWB model**: Modelled as a CRS with Hellings-Downs correlations.

In order to simplify the text, we introduce short-hand notations for the signal injection of SSE systematics or GWB with an amplitude at 10^{-16} and one at 10^{-15} repectively as 'A', 'B1' and 'B2' (see Table 4.2). For the data analysis part, the model of a CRS with Hellings-Downs correlations is named GWB, the dipolar CRS, BAYESEPHEM and EPHEMGP are respectively labelled DIP, BFM and EGP.

4.3.2 Impact of unmodelled SSE systematics on the GWB measurement

We first investigate the effect of SSE systematics on the GWB without including any SSE model.

The left panel of Figure 4.4 dislays the GWB power-law amplitude and spectral index posterior distributions applied to the dataset with only 'A' - simulated with only SSE systematics. The signal is well constrained with 1D marginalized distribution medians at $A = 3.77^{+3.22}_{-2.06} \times 10^{-15}$ and $\gamma = 2.15^{+0.88}_{-0.77}$ given with 95% confidence intervals. This first measurement confims the possibility of a false positive GWB detection in presence of SSE systematics. However, the spectral index posterior is lower and not consistent with 13/3, the expected value from a population of SMBHBs.

The center and right panels of Fig. 4.4 compare the posterior distibution of the power-law parameters for datasets that are simulated either only with a gravitational wave backrgound signal (red) or with both a SSE systematics and a GWB signal. For the dataset with 'B1' only (middle panel), the GWB signal is poorly constrained, leading to an amplitude upper-limit measured at $A^{95\%} = 1.42 \times 10^{-15}$ and spectral index constrained from the low, $\gamma^{95\%} = 1.99$. For 'B2' only (right panel), the GWB parameters are constrained with medians at $A = 9.99^{+9.59}_{-5.26} \times 10^{-16}$ and $\gamma = 4.35^{+0.62}_{-0.57}$, and therefore recovering very well the injected signal (black solid lines given injected values). For 'A+B1', the SSE systematic signal dominates 'B1' and the GWB power-law parameters are constrained at $A = 2.25^{+2.68}_{-1.38} \times 10^{-15}$ and $\gamma = 2.52^{+0.99}_{-0.90}$, consitent with the results obtained with the dataset 'A' only. Finally, the posteriors for 'A+B2' are in solid agreement with the results obtained with 'B2' only, with medians at $A = 1.09^{+0.99}_{-0.56} \times 10^{-15}$ and $\gamma = 4.31^{+0.61}_{-0.55}$. For this case, the high-S/N GWB signal 'B2' dominates over SSE systematics.

These results confirm the non-negligible effect of SSE systematics on the GW analysis, in particular the possibly to mistake SSE error for GWB signal in the case of the low-S/N regime. However, the strong GWB signal is correctly recovered and separated from the SSE systematics that has different spatial correlations and spectral properties.

4.3.3 Describing SSE systematics with EphemGP

The two solutions DE438 and INPOP19a give different SSB positions, leading to a systematic Roemer delay error seen as DE438 vs. INPOP19a signal, namely 'A'. In this section, we study this signal with EPHEMGP (EGP) model.

The figure 4.5 shows that the recovered EPHEMGP posteriors are quite gaussian and off-diagonal panels show the correlation between parameters. Almost all parameters are well constrained and all of them (except for $q_{\rm Jup}$, $p_{\rm Jup}$, $k_{\rm Sat}$ and $p_{\rm Sat}$) are not consistent

Figure 4.4: 2D marginalized posterior distribution of the GWB model power-law amplitude and spectral index applied on different simulated datasets. In the left panel, the data contains injection of SSE systematics only. In the center panel, it contains either SSE systematics + GWB (blue) or GWB only (red), both with GWB amplitude $A = 10^{-16}$. In the right panel, the dataset contains either SSE systematics + GWB (blue) or GWB only (red) at $A = 10^{-15}$ (right). The black solid lines indicate the injected amplitude and spectral index of the GWB power-law.

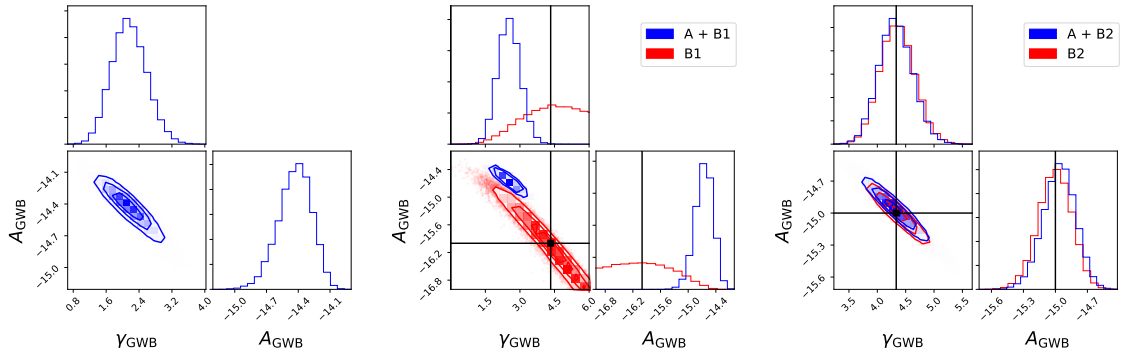

with zero, manifesting absorption of systematic errors. We also observe a strong correlation between some parameter, for example a_{Sat} and k_{Sat}. Note, that the correlations observed here are very different from those observed in the local covariance matrix (Fig. 4.6), in particular, we clearly observe some correlation between orbital elements of Jupiter and orbital elements of Saturn (interplanetary).

A question which emerges from this analysis is if the INPOP19a solution is unique? Assuming that the equations, data and solvers are compatible between JPL and INPOP, we might interprete our results as a non-unique solution: we might recover DE438 ephemeris if we assume the values displayed in the table 4.3 as initial conditions for the INPOP solver. Of course the caveats here are that we do not provide possible values for other parameters, and/or our assumption about compatibility of JPL and INPOP settings could be wrong. Moreover the median values are several orders of magnitude larger than typical r.m.s. predicted by local covariance matrix.

4.3.4 SSE error mitigation in presence of a GWB

The main objective of this study is to inspect EPHEMGP (and other models of SSE error) performance to (1) avoid false detection of GWB due to the presence of SSE systematics and (2) allow correct recovery of GWB.

In case of the weak GW signal (top panels of fig. 4.7) the need to include SSE uncertainties in the analysis (in form of EGP, BFM or DIP) is quite obvious: the analysis lead to false

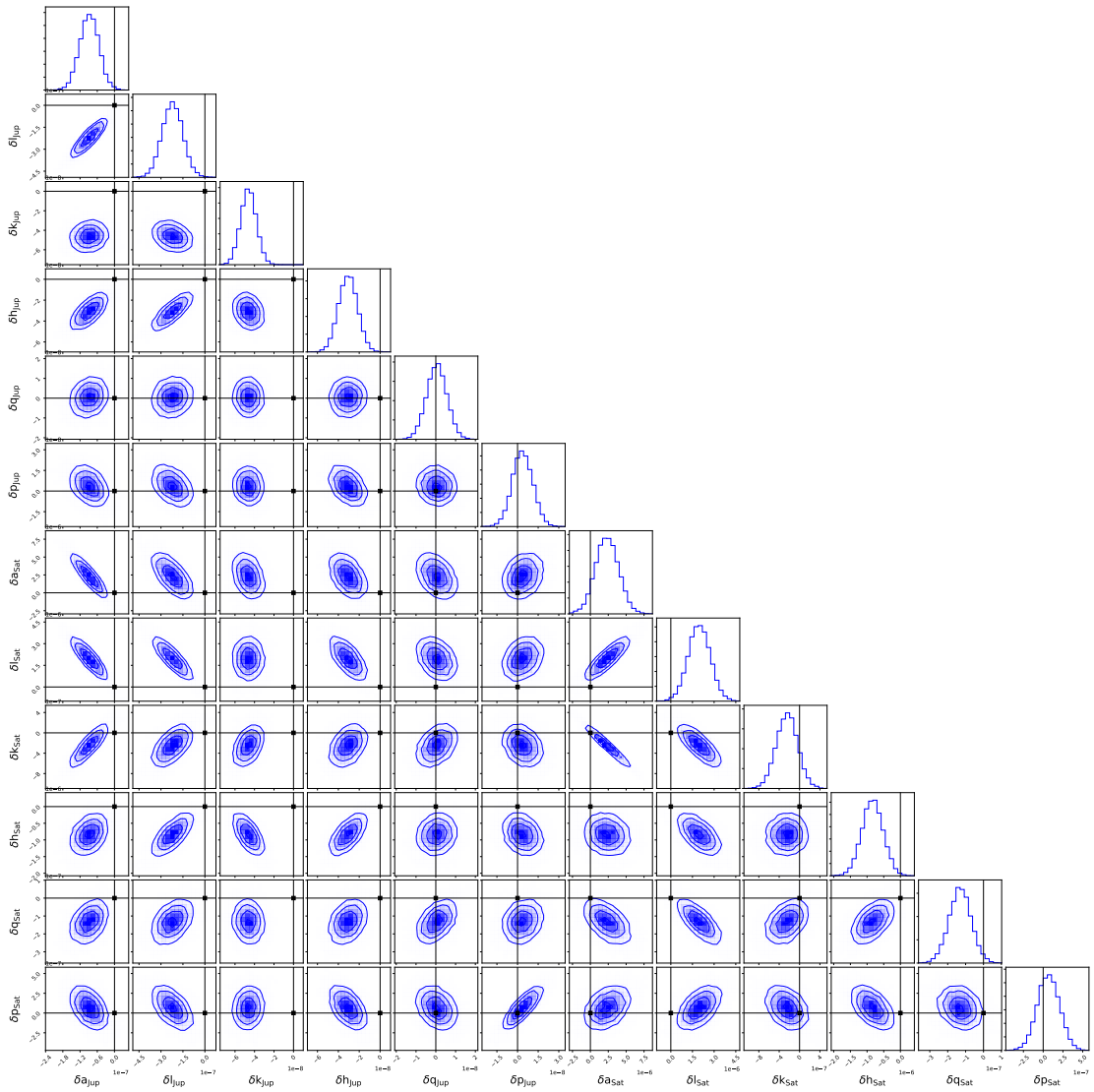

Figure 4.5: Posterior distributions of EPHEMGP parameters applied on the dataset including the signal A only. The black solid lines indicate the zero value for each parameter.

Table 4.3: The 'EGP Posterior' column displays EPHEMGP parameters posterior 1D marginalized medians given with 95% confidence intervals, obtained on data with DE438 vs INPOP19a systematic injection. The last column display the standard variation of each EPHEMGP parameter given by the covariance matrix derived from INPOP19a fit.

	parameter	EGP Posterior	σ_{IN19a}
Jupiter	δa	$-8.75^{+6.63}_{-6.59} \times 10^{-8}$	1.37×10^{-11}
	δl	$-2.21^{+1.40}_{-0.14} \times 10^{-7}$	4.07×10^{-11}
	δk	$-4.62^{+1.57}_{-1.55} \times 10^{-8}$	2.54×10^{-12}
	δh	$-3.07^{+1.77}_{-1.77} \times 10^{-8}$	1.64×10^{-12}
	δq	$0.05^{+1.00}_{-1.01} \times 10^{-8}$	5.19×10^{-11}
	δp	$0.35^{+1.46}_{-1.43} \times 10^{-8}$	4.06×10^{-11}
Saturn	δa	$2.32^{+3.21}_{-3.15} \times 10^{-6}$	8.54×10^{-12}
	δl	$1.96^{+1.52}_{-1.50} \times 10^{-6}$	8.17×10^{-12}
	δk	$-2.45^{+4.08}_{-4.20} \times 10^{-7}$	6.14×10^{-13}
	δh	$-8.36^{+6.19}_{-6.22} \times 10^{-7}$	6.08×10^{-13}
	δq	$-1.31^{+1.22}_{-1.23} \times 10^{-7}$	1.02×10^{-11}
	δp	$0.67^{+2.73}_{-2.73} \times 10^{-7}$	6.83×10^{-12}

Figure 4.6: Color map of the Jupiter and Saturn non-singular orbital element covariance matrix given by INPOP19a. For each body, the parameters are a,l,k,h,q,p.

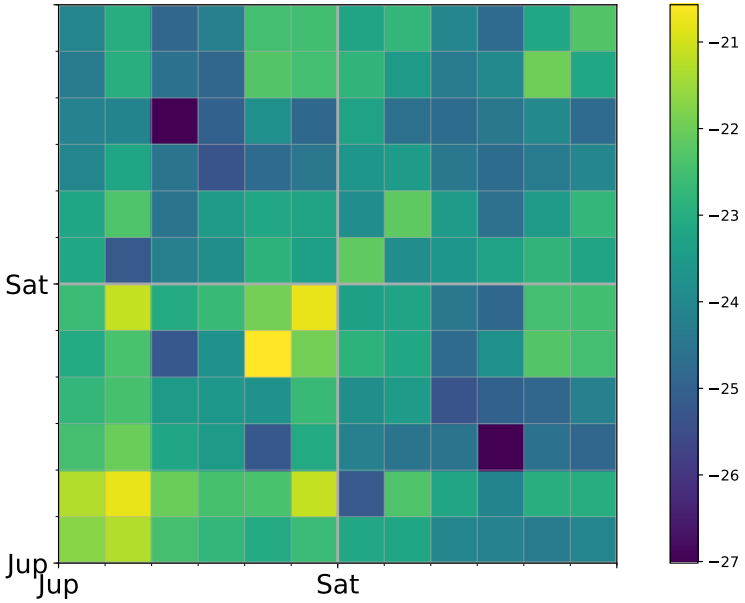

positive (red) which dominates the 'upper-limit' constraints obtained without SSE systematics (blue). The use of GWB and EGP (green in left panel) gives the expected results showing rather an upper-limit GWB amplitude distribution. However, EGP does not fully absorb the SSE systematics (in this particular realisation of the data), which leads to a mild "bump" of the GWB amplitude posterior at the level of the SSE systematic. The suppression of the false positive is also observed for BFM (green in center panel) and DIP (green in right panel) with upper-limit amplitudes consistent with the results obtained with the dataset with 'B1' only (blue). If we consider a model with both GWB and a SSE error model applied on the dataset 'B1' only (orange), the results are similar from a dataset with both 'A+B1' with one exception: the model DIP recovers the spectral index constraint, unlike the two others which lead to broad distributions favoring lower values.

In case of the strong (detectable) GWB (lower panel of fig. 4.7) all analyses detect GW signal, with or without presence of 'A'. The models EGP+GWB, BFM+GWB and DIP+GWB allow GWB measurements that are consistent with the injected value. We also observe that the inclusion of (any of the three) SSE error model lead to very slight widening of the 2D GWB posterior at low A and high γ. Nevertheless, the three SSE models have comparable performances, allowing to detect a GWB at the level of the measurements recently reported by PTA collaborations ($A \sim 10^{-15}$).

4.4 Effects on the parameter estimation of the CRS with EPTA DR2

This section describes the application of the SSE error models to the search for a GWB on EPTA DR2. This section was published as part of Chen et al. 2021, wbere we describe the impact of the SSE uncertainties and its mitigation the parameter estimation of the common uncorrelated red noise (CURN). My contribution to this work was in the data using EPHEMGP.

In this study, three independently developped models have been applied to CRS search to describe the SSE uncertainties: LINIMOSS (Guo et al. 2019), BAYESEPHEM (Vallisneri et al. 2020) and EPHEMGP (Chalumeau et al. 2021b in prep.). LINIMOSS is a fully dynamical model of the major Solar system bodies implemented in FORTYTWO software. It is used to analytically marginalize the mass and orbital parameters for Jupiter and Saturn together with the rest of the timing models during the search for CRS. The two other models (see Section 4.2.2) are computed with ENTERPRISE. In the analyses presented below, the timing models of six pulsars are fitted using the JPL DE438 solution, and the noise models include marginalized errors on timing model parameters, single-pulsar achromatic red noise, DM variations and a CURN.

Figure 4.7: Comparison of the three investigated SSE error models: EGP (left), BFM (center) and DIP (right). The figures display the GWB amplitude and spectral index posterior distributions obtained with different datasets processed with different noise models. All simulations involve a GWB signal at (top panels) low-S/N regime ('B1' : $A = 10^{-16}$) or high S/N regime ('B1' : $A = 10^{-15}$). For each plot, the legend indicates the injected signals ('B1' or 'B2' with or without 'A'), and the related noise model (GWB with or without SSE error). The black solid lines show the injected GWB value.

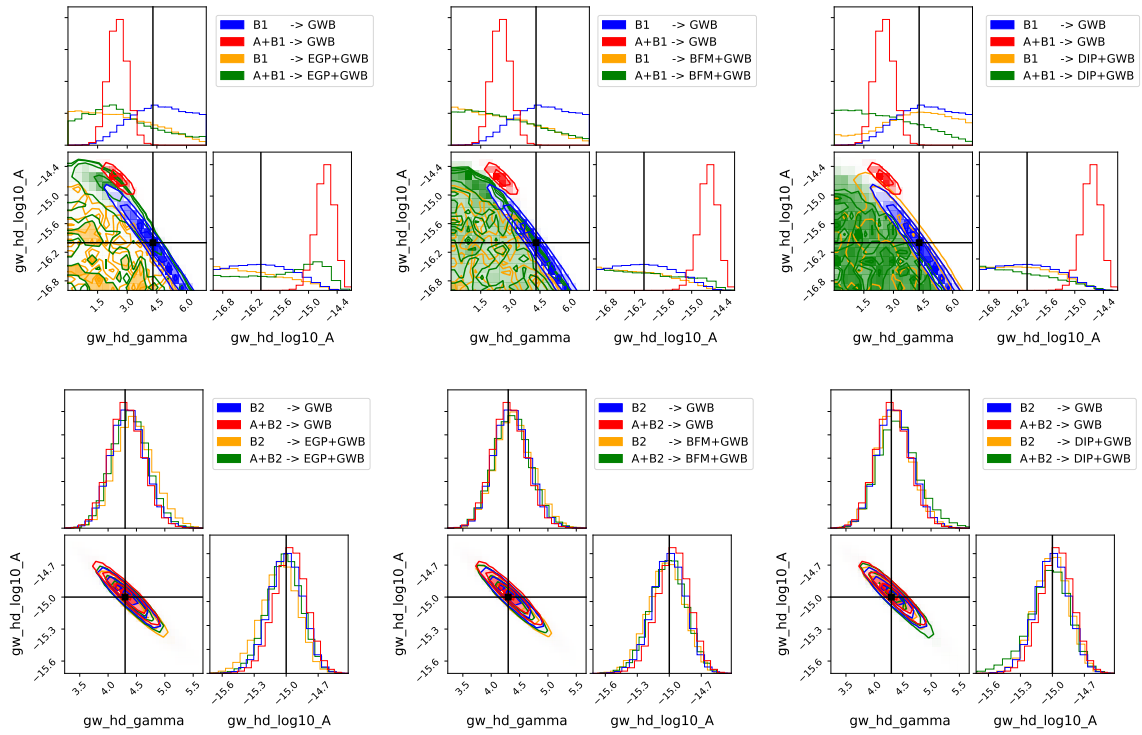

The analyses with BAYESEPHEM and EPHEMGP perform MCMC sampling on the SSE parameters and priors are therefore carefully defined. Both methods determine the prior range phenomenologically by allowing the parameters to vary enough to cover differences between various SSE models, as well as keeping the resulting residuals of the pulsar TOAs below a certain threshold to stay within the linear regime. For BAYESEPHEM the delays are limited to about μs level, while EPHEMGP allows for delays from SSE systematics up to about 100 μs. Both use uniform priors for the orbital elements, BAYESEPHEM uses Gaussian priors for the planetary masses, while they are held fixed in this analysis with EPHEMGP, after confirming that no mass-error signals could be detected by the pulsar data. LINIMOSS analysis performs analytical marginalization of planetary masses and orbital elements together with the pulsar timing model using uniform infinite improper priors.

Figure 4.8 shows the comparison of the ENTERPRISE results without any SSE fitting, and with the use of BAYESEPHEM, EPHEMGP and LINIMOSS (while the LINIMOSS analysis uses FORTYTWO). We can see that all three methods show consistent posterior distributions. The inclusion of the SSE models slightly increases the uncertainties in the recovered parameters, while still keeping them highly confined. As expected, the contours become progressively broader than the contour with fixed SSE at DE438, as the allowed prior increases from BAYESEPHEM to EPHEMGP, to the full marginalization in LINIMOSS.

The approach of sampling the SSE parameters requires careful prior choices as it may leave some dipolar signal unmodelled, potentially affecting the measurement of parameters and detection significance of a true GWB signal. These issues can be reduced significantly by including more pulsars, and therefore better covering the angular separations and disentengle Hellings-Downs and dipolar correlations.

4.5 Summary

We have implemented a new model (EPHEMGP; EGP) that permits to vary orbital elements of Jupiter and Saturn which propagate into the Roemer delay and allows us to absorb SSE systematics and perform a robust search for the GWB. This model is currently based on INPOP19a data, it could be updated with new INPOP releases such as INPOP21a or future versions, and its parametererization could be further extended if needed to any subset of parameters used by INPOP.

The model has been tested on the simulated datasets and compared against other existing SSE error models available in ENTERPRISE: BAYESEPHEM (BFM) and a CRS with dipolar spatial correlations (DIP). For this, we simulate GWB using LIBSTEMPO and SSE systematics from the difference between two SSE releases (here DE438 vs. INPOP19a). In

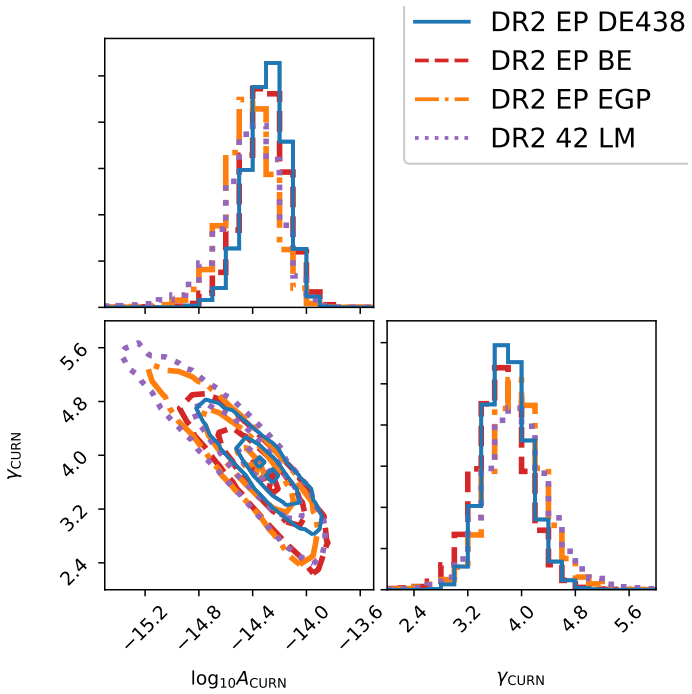

Figure 4.8: Posterior distributions of CURN power-law parameters using ENTERPRISE with (i) fixed DE438 SSE, (ii) BAYESEPHEM (BE),(iii) EPHEMGP (EGP) and FORTYTWO with LINIMOSS (LM). Figure from Chen et al. 2021.

case of low amplitude GWB ($A = 10^{-16}$), all three models allow to avoid a false detection of GWB by absorbing the SSE systematics. With weak GWB and without any SSE systematic in the data, the model DIP permits a better recovery of the GWB spectral index than two other models. For a relatively strong GWB with $A \sim 10^{-15}$ (the same as CRS detected by PTAs, see Chapter 3), all three SSE error models allow the detection of the GWB with only small distortion in parameter estimation (due to small absorption of GWB).

For completeness, we are currently performing the same tests over several realizations of the simulated data in order to avoid the effects of randomness. This study might also be improved in the future by considering more realistic datasets, for instance by including single-pulsar red noise and DM variations, and investigated using other SSE systematics (e.g., differences between other SSE solutions).

CHAPTER 5

SUMMARY AND PERSPECTIVES

The work described in this Ph.D. thesis contributes toward the detection of a very low frequency stochastic gravitational waves background (GWB) with Pulsar Timing Arrays (PTA). The study presented here aims at enabling robust search for the GWB, addressing different aspects such as the timing model (Chapter 1), the single-pulsar noise models (Chapter 2) and the uncertainties of the Solar system ephemeris (Chapter 4).

Chapter 1 presents results on the timing analysis of PSR J1909-3744 using data from the Nançay Radio Telescope (Liu et al. 2020). For this work, I have contributed to the noise analysis, where a simultaneous fit of the timing model and the stochastic noise parameters has been performed to obtain high precision timing measurements. Chapter 2 is based on the single-pulsar noise model selection applied to the EPTA DR2. This study is part of an EPTA project that I led, and which resulted in a publication (Chalumeau et al. 2021) that has been submitted to MNRAS journal. In this paper, we emphasize the importance of treating the noise individually for each pulsar to permit the robust search for GWB. Chapter 3 combines materials from three publications. It first describes the work reported in Chen et al. 2021 (accepted by MNRAS journal) which focused on the search of a GWB with six pulsars of the EPTA DR2. This study confirmed the results recently obtained by other PTAs, with a strong evidence for the presence of a common red signal (CRS) between pulsars, but inconclusive measurements of the spatial correlations needed to claim for a detection of a GWB. For this paper, I participated to the noise analyses performed with ENTERPRISE software, and contributed to the paper writing. This Chapter also describes the last section of Chalumeau et al. 2021, in which the noise model selection performed in Chapter 2 is applied to the search for a GWB, and compared against the results with the standard (simple) noise models. This study led to the same conclusions as in Chen et al. 2021, emphasizing the robustness of CRS signal in EPTA data. The last part of Chapter 3 describes the GWB analysis applied on the IPTA DR2 (Antoniadis et al. 2022, submitted to MNRAS), which also confirms the recent PTA results, and, in particular demonstrates the high potential of the data combination from several collaborations to improve the sensitivity of PTA. This project is the achievement of more than two years of work, where I participated to the discussions and the noise analyses namely in the false alarm study used to evaluate the significance of the correlations. Finally, Chapter 4 is focused on the impact of the systematic errors of the Solar system ephemeris on

PTA results. We built our own model (EPHEMGP) based on INPOP data to absorb the dipolar-correlated signal induced by SSE errors and allow a more robust detection of the quadrupolar GWB. EPHEMGP has been tested on simulated data for different levels of GWB amplitudes, and compared against other existing models. This work is currently being finalised and should be submitted for publication in the coming weeks. The Chapter ends with the application of EPHEMGP and other SSE models to the EPTA DR2 to study the robustness of the measured CRS. This investigation has been reported in Chen et al. 2021, where I analysed EPTA DR2 using EPHEMGP and participated in the writing.

Thanks to the massive work performed in the last three years to (1) build high precision pulsar timing datasets and (2) use complete data analysis pipelines, we are currently in a very interesting period for Pulsar Timing Arrays. The consistency in the measurements of a common red signal across the different PTA collaborations gives a big hope for the presence of a GWB. The EPTA, PPTA and NANOGrav have agreed on a shared timeline to improve their own dataset and perform a search for a GWB with their best sensitivity in the coming years. The improvement for EPTA measurement is particularly promising because the dataset will go from 6 to 25 pulsars specifically chosen to optimize the search for correlations induced by a GWB. I will be co-lead of EPTA effort on the single-pulsar noise analysis of 25 pulsars, and also contribute to the search for GWB. In addition, this work will be the opportunity to apply a single-pulsar noise model selection approach given in Chapter 2, and use EPHEMGP in advanced GWB analysis. Following the publication of these future results, an analysis at IPTA level will eventually allow to perform the search and the characterization of a GWB on the most sensitive (combined) data.

BIBLIOGRAPHY

[1] B. P. Abbott, R. Abbott, T. D. Abbott, F. Acernese, K. Ackley, C. Adams, T. Adams, P. Addesso, R. X. Adhikari, V. B. Adya, C. Affeldt, B. Agarwal, M. Agathos, K. Agatsuma, N. Aggarwal, O. D. Aguiar, L. Aiello, et al.
"GW170817: Measurements of Neutron Star Radii and Equation of State"
Physical Review Letters 121.16, 161101 (Oct. 2018), p. 161101.

[2] B. P. Abbott, R. Abbott, T. D. Abbott, M. R. Abernathy, F. Acernese, K. Ackley, C. Adams, T. Adams, P. Addesso, R. X. Adhikari, V. B. Adya, C. Affeldt, M. Agathos, K. Agatsuma, N. Aggarwal, O. D. Aguiar, L. Aiello, et al.
"Observation of Gravitational Waves from a Binary Black Hole Merger"
Physical Review Letters 116.6, 061102 (Feb. 2016), p. 061102.

[3] M. F. Alam, Z. Arzoumanian, P. T. Baker, H. Blumer, K. E. Bohler, A. Brazier, P. R. Brook, S. Burke-Spolaor, K. Caballero, R. S. Camuccio, R. L. Chamberlain, S. Chatterjee, J. M. Cordes, N. J. Cornish, F. Crawford, H. T. Cromartie, M. E. Decesar, et al.
"The NANOGrav 12.5 yr Data Set: Observations and Narrowband Timing of 47 Millisecond Pulsars"
ApJS 252.1, 4 (Jan. 2021), p. 4.

[4] M. A. Alpar, A. F. Cheng, M. A. Ruderman, and J. Shaham
"A new class of radio pulsars"
Nature 300.5894 (Dec. 1982), pp. 728–730.

[5] T. W. Anderson and D. A. Darling
"Asymptotic Theory of Certain "Goodness of Fit" Criteria Based on Stochastic Processes"
The Annals of Mathematical Statistics 23.2 (1952), pp. 193–212.

[6] M. Anholm, S. Ballmer, J. D. E. Creighton, L. R. Price, and X. Siemens
"Optimal strategies for gravitational wave stochastic background searches in pulsar timing data"
Phys. Rev. D 79.8, 084030 (Apr. 2009), p. 084030.

[7] J Antoniadis, Z Arzoumanian, S Babak, M Bailes, A.-S. B. Nielsen, P. T. Baker, C. G. Bassa, B Bécsy, A Berthereau, M Bonetti, A Brazier, P. R. Brook, M Burgay, S Burke-Spolaor, R. N. Caballero, J. A. Casey-Clyde, A Chalumeau, et al.
"The International Pulsar Timing Array second data release: Search for an isotropic Gravitational Wave Background"
Monthly Notices of the Royal Astronomical Society (Jan. 2022). stab3418.

[8] J. I. Antoniadis
"Multi-wavelength studies of pulsars and their companions"
PhD thesis. University of Bonn, 2013.

[9] Z. Arzoumanian, P. T. Baker, A. Brazier, S. Burke-Spolaor, S. J. Chamberlin, S. Chatterjee, B. Christy, J. M. Cordes, N. J. Cornish, F. Crawford, H. Thankful Cromartie, K. Crowter, M. DeCesar, P. B. Demorest, T. Dolch, J. A. Ellis, R. D. Ferdman, et al.
"The NANOGrav 11 Year Data Set: Pulsar-timing Constraints on the Stochastic Gravitational-wave Background"
ApJ 859.1, 47 (May 2018), p. 47.

[10] Z. Arzoumanian, A. Brazier, S. Burke-Spolaor, S. J. Chamberlin, S. Chatterjee, B. Christy, J. M. Cordes, N. J. Cornish, K. Crowter, P. B. Demorest, X. Deng, T. Dolch, J. A. Ellis, R. D. Ferdman, E. Fonseca, N. Garver-Daniels, M. E. Gonzalez, et al.
"The NANOGrav Nine-year Data Set: Limits on the Isotropic Stochastic Gravitational Wave Background"
ApJ 821.1, 13 (Apr. 2016), p. 13.

[11] Z. Arzoumanian, A. Brazier, S. Burke-Spolaor, S. Chamberlin, S. Chatterjee, B. Christy, J. M. Cordes, N. J. Cornish, F. Crawford, H. Thankful Cromartie, K. Crowter, M. E. DeCesar, P. B. Demorest, T. Dolch, J. A. Ellis, R. D. Ferdman, E. C. Ferrara, et al.
"The NANOGrav 11-year Data Set: High-precision Timing of 45 Millisecond Pulsars"
ApJS 235.2, 37 (Apr. 2018), p. 37.

[12] Z. Arzoumanian, P. T. Baker, H. Blumer, B. Bécsy, A. Brazier, P. R. Brook, S. Burke-Spolaor, S. Chatterjee, S. Chen, J. M. Cordes, and et al.
"The NANOGrav 12.5 yr Data Set: Search for an Isotropic Stochastic Gravitational-wave Background"
The Astrophysical Journal Letters 905.2 (2020), p. L34.

[13] W. Baade and F. Zwicky
"On Super-novae"
Proceedings of the National Academy of Science 20.5 (1934), pp. 254–259.

[14] D. C. Backer
"Millisecond pulsar radiation properties."
Journal of Astrophysics and Astronomy 16 (June 1995), pp. 165–171.

[15] M. Bailes, E. Barr, N. D. R. Bhat, J. Brink, S. Buchner, M. Burgay, F. Camilo, D. J. Champion, J. Hessels, G. H. Janssen, A. Jameson, S. Johnston, A. Karastergiou, R. Karuppusamy, V. Kaspi, M. J. Keith, M. Kramer, et al.
MeerTime - the MeerKAT Key Science Program on Pulsar Timing
2018.

[16] C. G. Bassa, G. H. Janssen, B. W. Stappers, T. M. Tauris, T. Wevers, P. G. Jonker, L. Lentati, J. P. W. Verbiest, G. Desvignes, E. Graikou, L. Guillemot, P. C. C. Freire, P. Lazarus, R. N. Caballero, D. J. Champion, I. Cognard, A. Jessner, et al.
"A millisecond pulsar in an extremely wide binary system"
Monthly Notices of the Royal Astronomical Society 460.2 (May 2016), pp. 2207–2222.

[17] C. G. Bassa, G. H. Janssen, R. Karuppusamy, M. Kramer, K. J. Lee, K. Liu, J. McKee, D. Perrodin, M. Purver, S. Sanidas, R. Smits, and B. W. Stappers
"LEAP: the Large European Array for Pulsars"
Monthly Notices of the Royal Astronomical Society 456.2 (Dec. 2015), pp. 2196–2209.

[18] T. Bayes and R. Price
"An essay towards solving a problem in the doctrine of chances"
Phil. Trans. of the Royal Soc. of London 53 (1763), pp. 370–418.

[19] L. Blanchet and T. Damour
"Hereditary effects in gravitational radiation"
Phys. Rev. D 46.10 (Nov. 1992), pp. 4304–4319.

[20] S. P. Brooks and A. Gelman
"General Methods for Monitoring Convergence of Iterative Simulations"
Journal of Computational and Graphical Statistics 7.4 (1998), pp. 434–455.

[21] S. Burke-Spolaor
Gravitational-Wave Detection and Astrophysics with Pulsar Timing Arrays
2015.

[22] C. Caprini, R. Durrer, and G. Servant
"The stochastic gravitational wave background from turbulence and magnetic fields generated by a first-order phase transition"
Journal of Cosmology and Astroparticle Physics 2009.12 (2009), pp. 024–024.

[23] B. P. Carlin and S. Chib
"Bayesian Model Choice Via Markov Chain Monte Carlo Methods"
Journal of the Royal Statistical Society: Series B (Methodological) 57.3 (1995), pp. 473–484.

[24] J. Chadwick
"The Existence of a Neutron"
Proceedings of the Royal Society of London Series A 136.830 (June 1932), pp. 692–708.

[25] A Chalumeau, S Babak, A Petiteau, S Chen, A Samajdar, R. N. Caballero, G Theureau, L Guillemot, G Desvignes, A Parthasarathy, K Liu, G Shaifullah, H Hu, E van der Wateren, J Antoniadis, A.-S. Bak Nielsen, C. G. Bassa, et al.
"Noise analysis in the European Pulsar Timing Array data release 2 and its implications on the gravitational-wave background search"
Monthly Notices of the Royal Astronomical Society 509.4 (Nov. 2021), pp. 5538–5558.

[26] S. J. Chamberlin, J. D. E. Creighton, X. Siemens, P. Demorest, J. Ellis, L. R. Price, and J. D. Romano
"Time-domain implementation of the optimal cross-correlation statistic for stochastic gravitational-wave background searches in pulsar timing data"
Phys. Rev. D 91 (4 2015), p. 044048.

[27] K. Chen and M. Ruderman
"Pulsar Death Lines and Death Valley"
ApJ 402 (Jan. 1993), p. 264.

[28] S. Chen, R. N. Caballero, Y. J. Guo, A. Chalumeau, K. Liu, G. Shaifullah, K. J. Lee, S. Babak, G. Desvignes, A. Parthasarathy, H. Hu, and E. van der Wateren
"Common-red-signal analysis with 24-yr high-precision timing of the European Pulsar Timing Array: Inferences in the stochastic gravitational-wave background search"
Monthly Notices of the Royal Astronomical Society ... (2021), p. ...

[29] S. Chen, A. Sesana, and W. Del Pozzo
"Efficient computation of the gravitational wave spectrum emitted by eccentric massive black hole binaries in stellar environments"
Monthly Notices of the Royal Astronomical Society 470.2 (May 2017), pp. 1738–1749.

[30] W. A. Coles, M. Kerr, R. M. Shannon, G. B. Hobbs, R. N. Manchester, X. P. You, M. Bailes, N. D. R. Bhat, S. Burke-Spolaor, S. Dai, M. J. Keith, Y. Levin, S. Osłowski, V. Ravi, D. Reardon, L. Toomey, W. van Straten, et al.
"Pulsar Observations of Extreme Scattering Events"
ApJ 808.2, 113 (Aug. 2015), p. 113.

[31] J. M. Cordes and R. M. Shannon
A Measurement Model for Precision Pulsar Timing
2010.

[32] J. M. Cordes and A. Wolszczan
"Multiple Imaging of Pulsars by Refraction in the Interstellar Medium"
ApJ 307 (Aug. 1986), p. L27.

[33] J. M. Cordes, R. M. Shannon, and D. R. Stinebring
"Frequency-dependent Dispersion Measures and Implications for Pulsar Timing"
ApJ 817.1, 16 (Jan. 2016), p. 16.

[34] N. J. Cornish and L. Sampson
"Towards robust gravitational wave detection with pulsar timing arrays"
Phys. Rev. D 93 (10 2016), p. 104047.

[35] R. B. D'Agostino and M. A. Stephens
Goodness-of-Fit Techniques
USA: Marcel Dekker, Inc., 1986.

[36] T. Damour and A. Vilenkin
"Gravitational wave bursts from cusps and kinks on cosmic strings"
Physical Review D 64.6 (2001).

[37] P. B. Demorest, T. Pennucci, S. M. Ransom, M. S. E. Roberts, and J. W. T. Hessels
"A two-solar-mass neutron star measured using Shapiro delay"
Nature 467.7319 (Oct. 2010), pp. 1081–1083.

[38] P. B. Demorest, R. D. Ferdman, M. E. Gonzalez, D. Nice, S. Ransom, I. H. Stairs, Z. Arzoumanian, A. Brazier, S. Burke-Spolaor, S. J. Chamberlin, J. M. Cordes, J. Ellis, L. S. Finn, P. Freire, S. Giampanis, F. Jenet, V. M. Kaspi, et al.
"Limits on the Stochastic Gravitational Wave Background from the North American Nanohertz Observatory for Gravitational Waves"
ApJ 762.2, 94 (Jan. 2013), p. 94.

[39] G. Desvignes, R. N. Caballero, L. Lentati, J. P. W. Verbiest, D. J. Champion, B. W. Stappers, G. H. Janssen, P. Lazarus, S. Osłowski, S. Babak, C. G. Bassa, P. Brem, M. Burgay, I. Cognard, J. R. Gair, E. Graikou, L. Guillemot, et al.
"High-precision timing of 42 millisecond pulsars with the European Pulsar Timing Array"
MNRAS 458.3 (May 2016), pp. 3341–3380.

[40] S. Detweiler
"Pulsar timing measurements and the search for gravitational waves"
ApJ 234 (Dec. 1979), pp. 1100–1104.

[41] R. T. Edwards, G. B. Hobbs, and R. N. Manchester
"TEMPO2, a new pulsar timing package - II. The timing model and precision estimates"
MNRAS 372.4 (Nov. 2006), pp. 1549–1574.

[42] A. Einstein
"Über Gravitationswellen"
Sitzungsberichte der Königlich Preußischen Akademie der Wissenschaften (Berlin (Jan. 1918), pp. 154–167.

[43] J. Ellis and R. van Haasteren
jellis18/PTMCMCSampler: Official Release
Oct. 2017.

[44] J. A. Ellis, M. Vallisneri, S. R. Taylor, and P. T. Baker
ENTERPRISE: Enhanced Numerical Toolbox Enabling a Robust PulsaR Inference SuitE
Dec. 2019.

[45] F. B. Estabrook and H. D. Wahlquist
"Response of Doppler spacecraft tracking to gravitational radiation."
General Relativity and Gravitation 6.5 (Oct. 1975), pp. 439–447.

[46] R. Fabbri and M. D. Pollock
"The effect of primordially produced gravitons upon the anisotropy of the cosmological microwave background radiation"
Physics Letters B 125.6 (June 1983), pp. 445–448.

[47] M. Favata
"The gravitational-wave memory effect"
Classical and Quantum Gravity 27.8 (2010), p. 084036.

[48] F. Feroz, M. P. Hobson, and M. Bridges
"MULTINEST: an efficient and robust Bayesian inference tool for cosmology and particle physics"
MNRAS 398.4 (Oct. 2009), pp. 1601–1614.

[49] A. Fienga, P. Deram, V. Viswanathan, A. Di Ruscio, L. Bernus, D. Durante, M. Gastineau, and J. Laskar
"INPOP19a planetary ephemerides"
Notes Scientifiques et Techniques de l'Institut de Mecanique Celeste 109 (Dec. 2019).

[50] L. S. Finn, S. L. Larson, and J. D. Romano
"Detecting a stochastic gravitational-wave background: The overlap reduction function"
Phys. Rev. D 79.6, 062003 (Mar. 2009), p. 062003.

[51] W. M. Folkner and R. S. Park
"Planetary ephemeris DE438 for Juno"
IOM 392R-18-004 (2018).

[52] D. Foreman-Mackey
"corner.py: Scatterplot matrices in Python"
The Journal of Open Source Software 1.2 (2016), p. 24.

[53] R. S. Foster and D. C. Backer
"Constructing a Pulsar Timing Array"
ApJ 361 (Sept. 1990), p. 300.

[54] A. Gelman and D. B. Rubin
"Inference from Iterative Simulation Using Multiple Sequences"
Statistical Science 7.4 (1992), pp. 457 –472.

[55] A. Gelman, J. B. Carlin, H. S. Stern, and D. B. Rubin
Bayesian Data Analysis
2nd ed. Chapman and Hall/CRC, 2004.

[56] R. Giacconi, H. Gursky, F. R. Paolini, and B. B. Rossi
"Evidence for x Rays From Sources Outside the Solar System"
Phys. Rev. Lett. 9 (11 1962), pp. 439–443.

[57] W. Gilks, S. Richardson, and D. Spiegelhalter
Markov Chain Monte Carlo in Practice
Chapman & Hall/CRC Interdisciplinary Statistics. Taylor & Francis, 1995.

[58] T. Gold
"Rotating Neutron Stars as the Origin of the Pulsating Radio Sources"
Nature 218.5143 (May 1968), pp. 731–732.

[59] P. Goldreich and W. H. Julian
"Pulsar Electrodynamics"
ApJ 157 (Aug. 1969), p. 869.

[60] B. Goncharov, D. J. Reardon, R. M. Shannon, X.-J. Zhu, E. Thrane, M. Bailes, N. D. R. Bhat, S. Dai, G. Hobbs, M. Kerr, R. N. Manchester, S. Osłowski, A. Parthasarathy, C. J. Russell, R. Spiewak, N. Thyagarajan, and J. B. Wang
"Identifying and mitigating noise sources in precision pulsar timing data sets"
MNRAS 502.1 (Mar. 2021), pp. 478–493.

[61] B. Goncharov, X.-J. Zhu, and E. Thrane
"Is there a spectral turnover in the spin noise of millisecond pulsars?"
Monthly Notices of the Royal Astronomical Society 497.3 (Aug. 2020), pp. 3264–3272.

[62] B. Goncharov, R. M. Shannon, D. J. Reardon, G. Hobbs, A. Zic, M. Bailes, M. Curyło, S. Dai, M. Kerr, M. E. Lower, R. N. Manchester, R. Mandow, H. Middleton, M. T. Miles, A. Parthasarathy, E. Thrane, N. Thyagarajan, et al.
"On the Evidence for a Common-spectrum Process in the Search for the Nanohertz Gravitational-wave Background with the Parkes Pulsar Timing Array"
The Astrophysical Journal Letters 917.2 (2021), p. L19.

[63] L. P. Grishchuk
"Primordial gravitons and possibility of their observation"
ZhETF Pisma Redaktsiiu 23 (Mar. 1976), p. 326.

[64] L. P. Grishchuk
"Relic gravitational waves and cosmology"
Physics-Uspekhi 48.12 (2005), 1235–1247.

[65] F. E. Grubbs
"Sample Criteria for Testing Outlying Observations"
The Annals of Mathematical Statistics 21.1 (1950), pp. 27 –58.

[66] B. Guinot
"Atomic time scales for pulsar studies and other demanding applications"
Astronomy and Astrophysics 192 (Feb. 1988), pp. 370–373.

[67] Y. J. Guo, G. Y. Li, K. J. Lee, and R. N. Caballero
"Studying the Solar system dynamics using pulsar timing arrays and the LINIMOSS dynamical model"
Mon. Not. Roy. Astron. Soc. 489.4 (2019), pp. 5573–5581.

[68] R. van Haasteren, Y. Levin, G. H. Janssen, K. Lazaridis, M. Kramer, B. W. Stappers, G. Desvignes, M. B. Purver, A. G. Lyne, R. D. Ferdman, A. Jessner, I. Cognard, G. Theureau, N. D'Amico, A. Possenti, M. Burgay, A. Corongiu, et al.
"Placing limits on the stochastic gravitational-wave background using European Pulsar Timing Array data"
Monthly Notices of the Royal Astronomical Society 414.4 (July 2011), pp. 3117–3128.

[69] R. van Haasteren and Y. Levin
"Understanding and analysing time-correlated stochastic signals in pulsar timing"
Monthly Notices of the Royal Astronomical Society 428.2 (Oct. 2012), pp. 1147–1159.

[70] R. van Haasteren and M. Vallisneri
"Low-rank approximations for large stationary covariance matrices, as used in the Bayesian and generalized-least-squares analysis of pulsar-timing data"
Monthly Notices of the Royal Astronomical Society 446.2 (Nov. 2015), pp. 1170–1174.

[71] R. van Haasteren and M. Vallisneri
"New advances in the Gaussian-process approach to pulsar-timing data analysis"
Phys. Rev. D 90 (10 2014), p. 104012.

[72] R. van Haasteren, Y. Levin, P. McDonald, and T. Lu
"On measuring the gravitational-wave background using Pulsar Timing Arrays"
Monthly Notices of the Royal Astronomical Society 395.2 (Apr. 2009), pp. 1005–1014.

[73] W. J. Handley, M. P. Hobson, and A. N. Lasenby
"polychord: nested sampling for cosmology"
Monthly Notices of the Royal Astronomical Society: Letters 450.1 (2015), L61–L65.

[74] K. Harrison, M. Wakano, and J. A. Wheeler
"The Degenerate Superdense Gas of Elementary Particles"
Onzième Conseil de Physique Solvay (1958), pp. 124,247.

[75] W. K. Hastings
"Monte Carlo sampling methods using Markov chains and their applications"
Biometrika 57.1 (Apr. 1970), pp. 97–109.

[76] J. S. Hazboun, J. Simon, X. Siemens, and J. D. Romano
"Model Dependence of Bayesian Gravitational-wave Background Statistics for Pulsar Timing Arrays"
ApJ 905.1, L6 (Dec. 2020), p. L6.

[77] S. Hee, W. J. Handley, M. P. Hobson, and A. N. Lasenby
"Bayesian model selection without evidences: application to the dark energy equation-of-state"
Monthly Notices of the Royal Astronomical Society 455.3 (Nov. 2015), pp. 2461–2473.

[78] R. W. Hellings and G. S. Downs
"Upper limits on the isotropic gravitational radiation background from pulsar timing analysis."
ApJ 265 (Feb. 1983), pp. L39–L42.

[79] J. W. T. Hessels, S. M. Ransom, I. H. Stairs, P. C. C. Freire, V. M. Kaspi, and F. Camilo
"A Radio Pulsar Spinning at 716 Hz"
Science 311.5769 (Mar. 2006), pp. 1901–1904.

[80] A. Hewish, S. J. Bell, J. D. H. Pilkington, P. F. Scott, and R. A. Collins
"Observation of a Rapidly Pulsating Radio Source"
Nature 217.5130 (Feb. 1968), pp. 709–713.

[81] G. B. Hobbs, R. T. Edwards, and R. N. Manchester
"TEMPO2, a new pulsar-timing package - I. An overview"
MNRAS 369.2 (June 2006), pp. 655–672.

[82] W. E. Howard, D. H. Staelin, and E. C. Reifenstein
"Pulsating radio sources near Crab Nebula."
IAU Cirulars 2110 (Jan. 1968), p. 2.

[83] F. Hoyle, J. V. Narlikar, and J. A. Wheeler
"Electromagnetic Waves from Very Dense Stars"
Nature 203.4948 (Aug. 1964), pp. 914–916.

[84] R. A. Hulse and J. H. Taylor
"Discovery of a pulsar in a binary system."
ApJ 195 (Jan. 1975), pp. L51–L53.

[85] J. D. Hunter
"Matplotlib: A 2D Graphics Environment"
Computing in Science Engineering 9.3 (2007), pp. 90–95.

[86] B. A. Jacoby, M. Bailes, M. H. van Kerkwijk, S. Ord, A. Hotan, S. R. Kulkarni, and S. B. Anderson
"PSR J1909-3744: A Binary Millisecond Pulsar with a Very Small Duty Cycle"
ApJ 599.2 (Dec. 2003), pp. L99–L102.

[87] A. H. Jaffe and D. C. Backer
"Gravitational Waves Probe the Coalescence Rate of Massive Black Hole Binaries"
ApJ 583.2 (Feb. 2003), pp. 616–631.

[88] H. Jeffreys
Theory of Probability
Third. Oxford, England: Oxford, 1961.

[89] F. A. Jenet, G. B. Hobbs, W. van Straten, R. N. Manchester, M. Bailes, J. P. W. Verbiest, R. T. Edwards, A. W. Hotan, J. M. Sarkissian, and S. M. Ord
"Upper Bounds on the Low-Frequency Stochastic Gravitational Wave Background from Pulsar Timing Observations: Current Limits and Future Prospects"
ApJ 653.2 (Dec. 2006), pp. 1571–1576.

[90] F. A. Jenet and J. D. Romano
Understanding the gravitational-wave Hellings and Downs curve for pulsar timing arrays in terms of sound and electromagnetic waves
2015.

[91] V. M. Kaspi, J. H. Taylor, and M. F. Ryba
"High-Precision Timing of Millisecond Pulsars. III. Long-Term Monitoring of PSRs B1855+09 and B1937+21"
ApJ 428 (June 1994), p. 713.

[92] R. E. Kass and A. E. Raftery
"Bayes Factors"
Journal of the American Statistical Association 90.430 (1995), pp. 773–795.

[93] M. J. Keith, W. Coles, R. M. Shannon, G. B. Hobbs, R. N. Manchester, M. Bailes, N. D. R. Bhat, S. Burke-Spolaor, D. J. Champion, A. Chaudhary, A. W. Hotan, J. Khoo, J. Kocz, S. Osłowski, V. Ravi, J. E. Reynolds, J. Sarkissian, et al.
"Measurement and correction of variations in interstellar dispersion in high-precision pulsar timing"
MNRAS 429.3 (Mar. 2013), pp. 2161–2174.

[94] M. Kerr, D. J. Reardon, G. Hobbs, R. M. Shannon, R. N. Manchester, S. Dai, C. J. Russell, S. Zhang, W. van Straten, S. Osłowski, A. Parthasarathy, R. Spiewak, M. Bailes, N. D. R. Bhat, A. D. Cameron, W. A. Coles, J. Dempsey, et al.
"The Parkes Pulsar Timing Array project: second data release"
Publications of the Astron. Soc. of Australia 37, e020 (June 2020), e020.

[95] J. S. Key and N. J. Cornish
"Characterizing the gravitational wave signature from cosmic string cusps"
Physical Review D 79.4 (2009).

[96] T. W. B. Kibble
"Topology of cosmic domains and strings"
Journal of Physics A Mathematical General 9.8 (Aug. 1976), pp. 1387–1398.

[97] A. N. Kolmogorov
Foundations of the Theory of Probability
2nd ed. Chelsea Pub Co, June 1960.

[98] M. Kramer, I. H. Stairs, R. N. Manchester, M. A. McLaughlin, A. G. Lyne, R. D. Ferdman, M. Burgay, D. R. Lorimer, A. Possenti, N. D'Amico, and et al.
"Tests of General Relativity from Timing the Double Pulsar"
Science 314.5796 (2006), 97–102.

[99] S. Kullback
Information Theory and Statistics
New York: Wiley, 1959.

[100] M. T. Lam, J. A. Ellis, G. Grillo, M. L. Jones, J. S. Hazboun, P. R. Brook, J. E. Turner, S. Chatterjee, J. M. Cordes, T. J. W. Lazio, M. E. DeCesar, Z. Arzoumanian, H. Blumer, H. T. Cromartie, P. B. Demorest, T. Dolch, R. D. Ferdman, et al.
"A Second Chromatic Timing Event of Interstellar Origin toward PSR J1713+0747"
ApJ 861.2, 132 (July 2018), p. 132.

[101] P. Laplace
Théorie analytique des probabilités
Paris: Courcier, 1812.

[102] M. I. Large, A. E. Vaughan, and B. Y. Mills
"A Pulsar Supernova Association?"
Nature 220.5165 (1968), pp. 340–341.

[103] K. J. Lee, F. A. Jenet, and R. H. Price
"Pulsar Timing as a Probe of Non-Einsteinian Polarizations of Gravitational Waves"
The Astrophysical Journal 685.2 (2008), pp. 1304–1319.

[104] L. Lentati and R. M. Shannon
"Profile stochasticity in PSR J1909-3744"
Monthly Notices of the Royal Astronomical Society 454.1 (Sept. 2015), pp. 1058–1072.

[105] L. Lentati, S. R. Taylor, C. M. F. Mingarelli, A. Sesana, S. A. Sanidas, A. Vecchio, R. N. Caballero, K. J. Lee, R. van Haasteren, S. Babak, C. G. Bassa, P. Brem, M. Burgay, D. J. Champion, I. Cognard, G. Desvignes, J. R. Gair, et al.
"European Pulsar Timing Array limits on an isotropic stochastic gravitational-wave background"
MNRAS 453.3 (Nov. 2015), pp. 2576–2598.

[106] L. Lentati, R. M. Shannon, W. A. Coles, J. P. W. Verbiest, R. van Haasteren, J. A. Ellis, R. N. Caballero, R. N. Manchester, Z. Arzoumanian, S. Babak, C. G. Bassa, N. D. R. Bhat, P. Brem, M. Burgay, S. Burke-Spolaor, D. Champion, S. Chatterjee, et al.
"From spin noise to systematics: stochastic processes in the first International Pulsar Timing Array data release"
MNRAS 458.2 (May 2016), pp. 2161–2187.

[107] L. Lentati, P. Alexander, and M. P. Hobson
"Generative pulsar timing analysis"
Monthly Notices of the Royal Astronomical Society 447.3 (Jan. 2015), pp. 2159–2168.

[108] L. Lentati, P. Alexander, M. P. Hobson, F. Feroz, R. van Haasteren, K. J. Lee, and R. M. Shannon
"TEMPONEST: a Bayesian approach to pulsar timing analysis"
MNRAS 437.3 (Jan. 2014), pp. 3004–3023.

[109] L. Lentati, P. Alexander, M. P. Hobson, S. Taylor, J. Gair, S. T. Balan, and R. van Haasteren
"Hyper-efficient model-independent Bayesian method for the analysis of pulsar timing data"
Physical Review D 87.10 (2013).

[110] L. Lentati, M. Kerr, S. Dai, M. P. Hobson, R. M. Shannon, G. Hobbs, M. Bailes, N. D. R. Bhat, S. Burke-Spolaor, W. A. Coles, J. Dempsey, P. D. Lasky, Y. Levin, R. N. Manchester, S. Osłowski, V. Ravi, D. J. Reardon, et al.
"Wide-band profile domain pulsar timing analysis"
Monthly Notices of the Royal Astronomical Society 466 (2017), pp. 3706–3727.

[111] K Liu, L Guillemot, A. G. Istrate, L Shao, T. M. Tauris, N Wex, J Antoniadis, A Chalumeau, I Cognard, G Desvignes, and et al.
"A revisit of PSR J1909-3744 with 15-yr high-precision timing"
Monthly Notices of the Royal Astronomical Society 499.2 (2020), 2276–2291.

[112] K. Liu, G. Desvignes, I. Cognard, B. W. Stappers, J. P. W. Verbiest, K. J. Lee, D. J. Champion, M. Kramer, P. C. C. Freire, and R. Karuppusamy
"Measuring pulse times of arrival from broad-band pulsar observations"
MNRAS 443.4 (Oct. 2014), pp. 3752–3760.

[113] D. R. Lorimer and M. Kramer
Handbook of Pulsar Astronomy
Vol. 4. 2004.

[114] J. Luo, S. Ransom, P. Demorest, R. van Haasteren, P. Ray, K. Stovall, M. Bachetti, A. Archibald, M. Kerr, J. Colen, and F. Jenet
PINT: High-precision pulsar timing analysis package
Feb. 2019.

[115] A. Lyne, G. Hobbs, M. Kramer, I. Stairs, and B. Stappers
"Switched Magnetospheric Regulation of Pulsar Spin-Down"
Science 329.5990 (July 2010), p. 408.

[116] R. A. Main, S. A. Sanidas, J Antoniadis, C Bassa, S Chen, I Cognard, M Gaikwad, H Hu, G. H. Janssen, R Karuppusamy, M Kramer, K. J. Lee, K Liu, G Mall, J. W. McKee, M. B. Mickaliger, D Perrodin, et al.
"Measuring interstellar delays of PSR J0613-0200 over 7 yr, using the Large European Array for Pulsars"
Monthly Notices of the Royal Astronomical Society 499.1 (Sept. 2020), pp. 1468–1479.

[117] R. N. Manchester, G. B. Hobbs, A. Teoh, and M. Hobbs
"The Australia Telescope National Facility Pulsar Catalogue"
The Astronomical Journal 129.4 (2005), 1993–2006.

[118] R. N. Manchester, G. Hobbs, M. Bailes, W. A. Coles, W. van Straten, M. J. Keith, R. M. Shannon, N. D. R. Bhat, A. Brown, S. G. Burke-Spolaor, D. J. Champion, A. Chaudhary, R. T. Edwards, G. Hampson, A. W. Hotan, A. Jameson, F. A. Jenet, et al.
"The Parkes Pulsar Timing Array Project"
Publications of the Astron. Soc. of Australia 30, e017 (Jan. 2013), e017.

[119] C. D. Manning and H. Schütze
Foundations of Statistical Natural Language Processing
Cambridge, Massachusetts: The MIT Press, 1999.

[120] N. Metropolis, A. W. Rosenbluth, M. N. Rosenbluth, A. H. Teller, and E. Teller
"Equation of State Calculations by Fast Computing Machines"
Journal of Chemical Physics 21.6 (June 1953), pp. 1087–1092.

[121] C. J. Moore, R. H. Cole, and C. P. L. Berry
"Gravitational-wave sensitivity curves"
Classical and Quantum Gravity 32.1 (2014), p. 015014.

[122] NANOGrav Collaboration, Z. Arzoumanian, A. Brazier, S. Burke-Spolaor, S. Chamberlin, S. Chatterjee, B. Christy, J. M. Cordes, N. Cornish, K. Crowter, P. B. Demorest, T. Dolch, J. A. Ellis, R. D. Ferdman, E. Fonseca, N. Garver-Daniels, M. E. Gonzalez, et al.
"The NANOGrav Nine-year Data Set: Observations, Arrival Time Measurements, and Analysis of 37 Millisecond Pulsars"
ApJ 813.1, 65 (Nov. 2015), p. 65.

[123] A. Neronov, A. R. Pol, C. Caprini, and D. Semikoz
"NANOGrav signal from magnetohydrodynamic turbulence at the QCD phase transition in the early Universe"
Physical Review D 103.4 (2021).

[124] T. E. Oliphant
"Python for Scientific Computing"
Computing in Science Engineering 9.3 (2007), pp. 10–20.

[125] S. Ölmez, V. Mandic, and X. Siemens
"Gravitational-wave stochastic background from kinks and cusps on cosmic strings"
Physical Review D 81.10 (2010).

[126] J. R. Oppenheimer and G. M. Volkoff
"On Massive Neutron Cores"
Phys. Rev. 55 (4 1939), pp. 374–381.

[127] F. Pacini
"Energy Emission from a Neutron Star"
Nature 216.5115 (Nov. 1967), pp. 567–568.

[128] T. T. Pennucci
"Frequency-dependent Template Profiles for High-precision Pulsar Timing"
ApJ 871.1, 34 (Jan. 2019), p. 34.

[129] T. T. Pennucci, P. B. Demorest, and S. M. Ransom
"Elementary Wideband Timing of Radio Pulsars"
ApJ 790.2, 93 (Aug. 2014), p. 93.

[130] B. B. P. Perera, M. E. DeCesar, P. B. Demorest, M Kerr, L Lentati, D. J. Nice, S Osłowski, S. M. Ransom, M. J. Keith, Z Arzoumanian, M Bailes, P. T. Baker, C. G. Bassa, N. D. R. Bhat, A Brazier, M Burgay, S Burke-Spolaor, et al.
"The International Pulsar Timing Array: second data release"
Monthly Notices of the Royal Astronomical Society 490.4 (Oct. 2019), pp. 4666–4687.

[131] D. Perrodin and A. Sesana
"Radio Pulsars: Testing Gravity and Detecting Gravitational Waves"
Astrophysics and Space Science Library (2018), 95–148.

[132] M. Rajagopal and R. W. Romani
"Ultra–Low-Frequency Gravitational Radiation from Massive Black Hole Binaries"
ApJ 446 (June 1995), p. 543.

[133] C. E. Rasmussen and C. K. I. Williams
Gaussian Processes for Machine Learning (Adaptive Computation and Machine Learning)
The MIT Press, 2005.

[134] D. J. Reardon, G. Hobbs, W. Coles, Y. Levin, M. J. Keith, M. Bailes, N. D. R. Bhat, S. Burke-Spolaor, S. Dai, M. Kerr, P. D. Lasky, R. N. Manchester, S. Osłowski, V. Ravi, R. M. Shannon, W. van Straten, L. Toomey, et al.
"Timing analysis for 20 millisecond pulsars in the Parkes Pulsar Timing Array"
MNRAS 455.2 (Jan. 2016), pp. 1751–1769.

[135] T. Riley, A. Watts, S. Bogdanov, P. Ray, R. Ludlam, S. Guillot, Z. Arzoumanian, C. Baker, A. Bilous, D. Chakrabarty, K. Gendreau, A. Harding, W. Ho, J. Lattimer, S. Morsink, and T. Strohmayer
"A NICER view of PSR J0030+0451: Millisecond pulsar parameter estimation"
Astrophysical Journal Letters 887 (Dec. 2019).

[136] E. Roebber
"Ephemeris Errors and the Gravitational-wave Signal: Harmonic Mode Coupling in Pulsar Timing Array Searches"
The Astrophysical Journal 876.1 (2019), p. 55.

[137] R. W. Romani
"Low frequency gravity wave spectra generated by cosmic strings"
Physics Letters B 215.3 (1988), pp. 477–482.

[138] S. A. Sanidas, R. A. Battye, and B. W. Stappers
"Constraints on cosmic string tension imposed by the limit on the stochastic gravitational wave background from the European Pulsar Timing Array"
Phys. Rev. D 85.12, 122003 (June 2012), p. 122003.

[139] M. V. Sazhin
"Opportunities for detecting ultralong gravitational waves"
Soviet Astronomy 22 (Feb. 1978), pp. 36–38.

[140] A. Sesana, A. Vecchio, and C. N. Colacino
"The stochastic gravitational-wave background from massive black hole binary systems: implications for observations with Pulsar Timing Arrays"
MNRAS 390.1 (Oct. 2008), pp. 192–209.

[141] A. Sesana, F. Haardt, P. Madau, and M. Volonteri
"Low-Frequency Gravitational Radiation from Coalescing Massive Black Hole Binaries in Hierarchical Cosmologies"
The Astrophysical Journal 611.2 (2004), pp. 623–632.

[142] R. M. Shannon, V. Ravi, W. A. Coles, G. Hobbs, M. J. Keith, R. N. Manchester, J. S. B. Wyithe, M. Bailes, N. D. R. Bhat, S. Burke-Spolaor, J. Khoo, Y. Levin, S. Oslowski, J. M. Sarkissian, W. van Straten, J. P. W. Verbiest, and J. B. Wang
"Gravitational-wave limits from pulsar timing constrain supermassive black hole evolution."
Science 342 (Oct. 2013), pp. 334–337.

[143] R. M. Shannon, V. Ravi, L. T. Lentati, P. D. Lasky, G. Hobbs, M. Kerr, R. N. Manchester, W. A. Coles, Y. Levin, M. Bailes, N. D. R. Bhat, S. Burke-Spolaor, S. Dai, M. J. Keith, S. Osłowski, D. J. Reardon, W. van Straten, et al.
"Gravitational waves from binary supermassive black holes missing in pulsar observations"
Science 349.6255 (Sept. 2015), pp. 1522–1525.

[144] R. M. Shannon, S. Osłowski, S. Dai, M. Bailes, G. Hobbs, R. N. Manchester, W. van Straten, C. A. Raithel, V. Ravi, L. Toomey, N. D. R. Bhat, S. Burke-Spolaor, W. A. Coles, M. J. Keith, M. Kerr, Y. Levin, J. M. Sarkissian, et al.
"Limitations in timing precision due to single-pulse shape variability in millisecond pulsars"
Monthly Notices of the Royal Astronomical Society 443.2 (July 2014), pp. 1463–1481.

[145] R. M. Shannon and J. M. Cordes
"ASSESSING THE ROLE OF SPIN NOISE IN THE PRECISION TIMING OF MILLISECOND PULSARS"
The Astrophysical Journal 725.2 (2010), pp. 1607–1619.

[146] I. S. Shklovsky
"On the Nature of the Source of X-Ray Emission of Sco XR-1."
The Astrophysical Journal Letters 148 (Apr. 1967), p. L1.

[147] X. Siemens, J. Ellis, F. Jenet, and J. D. Romano
"The stochastic background: Scaling laws and time to detection for pulsar timing arrays"
Classical and Quantum Gravity 30 (May 2013).

[148] D. S. Sivia and J. Skilling
Data Analysis - A Bayesian Tutorial
2nd. Oxford Science Publications. Oxford University Press, 2006.

[149] J. Skilling
"Nested Sampling"
In: *Bayesian Inference and Maximum Entropy Methods in Science and Engineering: 24th International Workshop on Bayesian Inference and Maximum Entropy Methods in Science and Engineering*. Ed. by R. Fischer, R. Preuss, and U. V. Toussaint. Vol. 735. American Institute of Physics Conference Series. Nov. 2004, pp. 395–405.

[150] J. Skilling
"Nested sampling for general Bayesian computation"
Bayesian Analysis 1.4 (2006), pp. 833 –859.

[151] J. S. Speagle
"DYNESTY: a dynamic nested sampling package for estimating Bayesian posteriors and evidences"
MNRAS 493.3 (Apr. 2020), pp. 3132–3158.

[152] C. M. Tan, C. G. Bassa, S. Cooper, T. J. Dijkema, P. Esposito, J. W. T. Hessels, V. I. Kondratiev, M. Kramer, D. Michilli, S. Sanidas, T. W. Shimwell, B. W. Stappers, J. van Leeuwen, I. Cognard, J. M. Grießmeier, A. Karastergiou, E. F. Keane, et al.
"LOFAR Discovery of a 23.5 s Radio Pulsar"
ApJ 866.1, 54 (Oct. 2018), p. 54.

[153] J. H. Taylor
"Pulsar Timing and Relativistic Gravity"
Philosophical Transactions of the Royal Society of London Series A 341.1660 (Oct. 1992), pp. 117–134.

[154] J. H. Taylor and J. M. Weisberg
"A new test of general relativity - Gravitational radiation and the binary pulsar PSR 1913+16"
ApJ 253 (Feb. 1982), pp. 908–920.

[155] S. R. Taylor, L. Lentati, S. Babak, P. Brem, J. R. Gair, A. Sesana, and A. Vecchio
"All correlations must die: Assessing the significance of a stochastic gravitational-wave background in pulsar timing arrays"
Phys. Rev. D 95.4, 042002 (Feb. 2017), p. 042002.

[156] S. R. Taylor, C. M. F. Mingarelli, J. R. Gair, A. Sesana, G. Theureau, S. Babak, C. G. Bassa, P. Brem, M. Burgay, R. N. Caballero, D. J. Champion, I. Cognard, G. Desvignes, L. Guillemot, J. W. T. Hessels, G. H. Janssen, R. Karuppusamy, et al.
"Limits on Anisotropy in the Nanohertz Stochastic Gravitational Wave Background"
Physical Review Letters 115.4, 041101 (July 2015), p. 041101.

[157] S. R. Taylor, R. van Haasteren, and A. Sesana
"From bright binaries to bumpy backgrounds: Mapping realistic gravitational wave skies with pulsar-timing arrays"
Physical Review D 102.8 (2020).

[158] C. Tiburzi, G. Hobbs, M. Kerr, W. A. Coles, S. Dai, R. N. Manchester, A. Possenti, R. M. Shannon, and X. P. You
"A study of spatial correlations in pulsar timing array data"
MNRAS 455.4 (Feb. 2016), pp. 4339–4350.

[159] M. Vallisneri, S. R. Taylor, J. Simon, W. M. Folkner, R. S. Park, C. Cutler, J. A. Ellis, T. J. W. Lazio, S. J. Vigeland, K. Aggarwal, Z. Arzoumanian, P. T. Baker, A. Brazier, P. R. Brook, S. Burke-Spolaor, S. Chatterjee, J. M. Cordes, et al.
"Modeling the Uncertainties of Solar System Ephemerides for Robust Gravitational-wave Searches with Pulsar-timing Arrays"
ApJ 893.2, 112 (Apr. 2020), p. 112.

[160] M. Vallisneri
libstempo: Python wrapper for Tempo2
Feb. 2020.

[161] W. van Straten
"High-fidelity Radio Astronomical Polarimetry Using a Millisecond Pulsar as a Polarized Reference Source"
ApJS 204.1, 13 (Jan. 2013), p. 13.

[162] J. P. W. Verbiest, L. Lentati, G. Hobbs, R. van Haasteren, P. B. Demorest, G. H. Janssen, J. B. Wang, G. Desvignes, R. N. Caballero, M. J. Keith, D. J. Champion, Z. Arzoumanian, S. Babak, C. G. Bassa, N. D. R. Bhat, A. Brazier, P. Brem, et al.
"The International Pulsar Timing Array: First data release"
MNRAS 458.2 (May 2016), pp. 1267–1288.

[163] S. J. Vigeland and X. Siemens
"Supermassive black hole binary environments: Effects on the scaling laws and time to detection for the stochastic background"
Phys. Rev. D 94.12, 123003 (Dec. 2016), p. 123003.

[164] S. J. Vigeland, K. Islo, S. R. Taylor, and J. A. Ellis
"Noise-marginalized optimal statistic: A robust hybrid frequentist-Bayesian statistic for the stochastic gravitational-wave background in pulsar timing arrays"
Phys. Rev. D 98.4, 044003 (Aug. 2018), p. 044003.

[165] S. van der Walt, S. C. Colbert, and G. Varoquaux
"The NumPy Array: A Structure for Efficient Numerical Computation"
Computing in Science Engineering 13.2 (2011), pp. 22–30.

[166] A. Wolszczan and D. A. Frail
"A planetary system around the millisecond pulsar PSR1257 + 12"
Nature 355.6356 (Jan. 1992), pp. 145–147.

[167] M. A. Woodbury
"Inverting modified matrices"
Princeton University, Princeton, NJ, Memorandum Rept. 42 4 (1950).

[168] J. S. B. Wyithe and A. Loeb
"Low-Frequency Gravitational Waves from Massive Black Hole Binaries: Predictions forLISAand Pulsar Timing Arrays"
The Astrophysical Journal 590.2 (2003).

[169] X. P. You, G. Hobbs, W. A. Coles, R. N. Manchester, R. Edwards, M. Bailes, J. Sarkissian, J. P. W. Verbiest, W. Van Straten, A. Hotan, S. Ord, F. Jenet, N. D. R. Bhat, and A. Teoh "Dispersion measure variations and their effect on precision pulsar timing" *Monthly Notices of the Royal Astronomical Society* 378.2 (May 2007), pp. 493–506.

[170] W. W. Zhu, I. H. Stairs, P. B. Demorest, D. J. Nice, J. A. Ellis, S. M. Ransom, Z. Arzoumanian, K. Crowter, T. Dolch, R. D. Ferdman, E. Fonseca, M. E. Gonzalez, G. Jones, M. L. Jones, M. T. Lam, L. Levin, M. A. McLaughlin, et al. "Testing Theories of Gravitation Using 21-Year Timing of Pulsar Binary J1713+0747" *ApJ* 809.1, 41 (Aug. 2015), p. 41.